The bowed string and its playability: Theory, simulation and analysis

Hossein Mansour

Department of Music Research
McGill University
Montréal, Québec, Canada

June 2016

A dissertation submitted to McGill University in partial fulfillment of the requirements for the degree of Doctor of Philosophy in Music Technology

Abstract

This thesis describes the development of a highly refined physics-based model of a bowed string and its subsequent use to investigate several aspects of a bowed string, particularly its playability. Different components of a previously reported model are replaced by more accurate solutions, and several new features are added to make the model more realistic. Plucked-string simulations are described first, followed by enhancements to include the bow and the bowing process. Several properties of the simulated plucked response are compared to their designed values and to their experimental counterparts, which confirms the accuracy of the model and its parameters.

An initial application of the model is focused on the minimum bow force above which the Helmholtz motion is sustainable. The Helmholtz motion is associated with the "speaking" sound of a bowed string, as opposed to its "whistling" or "crunching" sounds. An earlier theoretical relation for the minimum bow force is re-derived starting from a more robust assumption of an ideal stick-slip at the bowing point rather than a perfect sawtooth-shaped excitation force at the bridge. Simulations are used to evaluate and validate the improved accuracy of the new formulation. The revised relation makes some fundamentally different predictions that are confirmed by the simulations. Among those predictions is an upward shift in the frequency of the peaks in the minimum bow force plot with respect to the frequency of the body modes causing those peaks. The extent of that shift is shown to be a function of the bow-bridge distance which has important implications for the playability of an instrument close to its "wolf note".

Extending the scope of our analysis and acknowledging the fact that our model is still a few steps away from making predictions in quantitative agreement with measurements, it has been cautiously used to predict the trend and the relative strength of outcome when different physical details are included or excluded from the model. The features that are investigated are the minimum and the maximum bow force, the increase in the slip-to-stick ratio compared to its theoretical value, the spectral centroid, the pitch flattening, and the rate of occurrence for two special vibration regimes called the "ALF notes" and the "S-motion". The initial transients of the bowed string are also analyzed in the bow force versus bow acceleration plane (a.k.a. the Guettler diagram).

Résumé

Cette thèse décrit le développement et l'utilisation d'un modèle physique très raffiné de corde frottée qui permet l'étude de plusieurs aspects de la corde frottée, en particulier de sa jouabilité. On a remplacé les éléments d'un modèle précédemment décrit par des solutions plus précises et de nouveaux éléments ont été ajoutés pour rendre le modèle plus réaliste. On décrit tout d'abord des simulations de corde pincée puis les améliorations permettant d'inclure l'archet et le processus d'excitation par l'archet. Plusieurs propriétés de la réponse simulée de la corde pincée sont comparées aux valeurs désignées et expérimentales, ce qui confirme la précision du modèle et de ses paramètres.

Une première application du modèle se concentre sur la force minimum fournie par l'archet au-dessus de laquelle le mouvement de Helmholtz est stable. Le mouvement de Helmholtz est associé au son "parlé" d'une corde frottée, en opposition avec son "sifflé" ou "craquant". On reprend une relation théorique précédemment établie pour la force minimum de fournie par l'archet, avec pour point de départ une hypothèse plus robuste de mouvement idéal au point de contact entre la corde et l'archet plutôt que l'hypothèse d'une excitation parfaitement en dents de scie au niveau du chevalet. Les simulations sont utilisées pour évaluer et valider les améliorations apportées par la nouvelle formulation en matière de précision. La relation révisée permet de faire des prédictions fondamentalement différentes, qui sont validées par les simulations. Parmi ces prédictions on trouve une augmentation des fréquences des pics dans le graphique de la force minimum fournie par l'archet par rapport aux fréquences des modes de corps responsables de ces pics. On montre que l'ampleur de l'augmentation fréquentielle est fonction de la distance entre le chevalet et le point de contact corde/archet, ce qui a d'importantes conséquences sur la jouabilité d'un instrument au voisinage de la "note du loup".

En élargissant notre analyse et en restant conscient qu'il reste des améliorations à apporter pour que notre modèle puisse faire des prédictions quantitatives en accord avec les mesures, on a utilisé avec précautions le modèle pour prédire des tendances et les l'ampleur relative des résultats lorsqu'on ajoute ou retire du modèle certains détails physiques. On étudie la force minimum et la force maximum de l'archet, l'augmentation du rapport entre glissement et adhérence comparée à sa valeur théorique, le centre de gravité spectral, l'abaissement de la hauteur de jeu et le taux d'occurrences de deux régimes spéciaux de vibration appelés "les notes ALF" et le "mouvement-S". Les transitoires d'attaque sont également analysés dans le plan force de l'archet / accélération de l'archet (diagramme de Guettler).

Acknowledgements

First and foremost, I would like to thank my supervisor Gary Scavone. His openness for new ideas gave me freedom to explore a wide range of topics while he was always there to give me constructive feedback when it mattered most. The better part of my PhD studies was done remotely and Gary did a lot to make it as smooth as it could be. This work would have not been possible without his continued support, technical and otherwise.

I'm tremendously grateful to Jim Woodhouse whose contribution to this work has been invaluable. I had the pleasure of working with him over two multi-month trips to Cambridge which set important milestones in my academic career.

I would like to extend my gratitude to Colin Gough, and his wife Sophie, for their hospitality over a week of dense and very fruitful discussions in Birmingham.

Special thanks to Anders Askenfelt for carefully reviewing my thesis and for his insightful comments on the draft.

My sincere thanks to Fan Tao for providing various data on string properties, and for patiently responding to my questions with great insight.

A big thanks is due to Paul Galluzzo for his encouragements and for sharing with me a large amount of data.

Many thanks to Darryl Cameron for his technical support and to Yves Méthot, Julien Boissinot, Jacqueline Bednar, and Harold Kilanski for their assistance in conducting my experiments in the Centre for Interdisciplinary Research in Music Media and Technology (CIRMMT). I had the pleasure of serving as the student representative to the board in CIRMMT for a year, during which I had close collaborations with CIRMMT director, Marcelo Wanderley. I would like to thank him for his guidance during that period, and for his support and advice regarding motion capturing and high-speed video recording.

In the course of this study I had the fortune of receiving valuable input from many people including, but certainly not limited to: Julius Smith, George Bissinger, Gabriel Weinreich, George Stoppani, Claudia Fritz, Evan Davis, Frank Fahy, Knut Guettler, Chris Waltham, and my colleagues at the Music Technology area, Charalampos Saitis, Esteban Maestre, Bertrand Scherrer, Erika Donald, and Vincent Fréour. I would like to thank them all for

their contribution to this work. Special thanks to Arthur Paté and to Indiana Wollman for helping with the French version of the thesis abstract.

This research has been funded by the Natural Sciences and Engineering Research Council of Canada (NSERC Vanier scholarship, Michael Smith foreign study scholarship, NSERC Engage), Dr. Richard H. Tomlinson (R. H. Tomlinson doctoral fellowship), CIRMMT (student award, exchange student scholarship), and Schulich School of Music (graduate excellence fellowship, mobility award, GREAT award). The generous support by these organizations allowed me to focus on my studies without being worried about financial concerns, for which I'm extremely grateful.

And above all, I would like to thank my mother Parvin, my father Ali, my sister Leila, and my wife Nazanin for their continued support and encouragement.

"[...] The trouble is that the nature of research is forever to be doing something that we do not know how to do and, as soon as we have learned how to do it, to stop doing it and look for a new problem; this means that a researcher's mind is forever fixed on what has not been achieved which, by the standards of the world, means being condemned to a life of perpetual discouragement. That this is not the way that we researchers perceive it is one of the great miracles of human creativity, and the primary reason that we love our work as much as we do."
Gabriel Weinreich [1]

To Nazanin
for understanding my obsessions
and for her support in times of frustration.

Contents

Nomenclature

α	Decay rate
β	Non-dimensional bow position, defined as (bow-bridge distance)/(string length)
β_{bow}	Distance from the contact point to the frog divided by the full length of the hair ribbon
δ_T	Static increase in the tension due to the transverse force
δ_r	Thickness of the contact patch between bow and string
$\dot{m}$	Mass flow rate of rosin into or out of the contact patch
η	Loss factor of an oscillator
γ	Viscosity of rosin
κ	Radius of gyration
μ	Coefficient of friction, equal to F_F/F_N
μ'_d	Asymptotic value of the dynamic friction force
μ_d	Friction coefficient at the maximum sliding speed within the cycle
μ_s	Maximum possible coefficient of friction, at the limit of static friction
ω_0	Frequency of first transverse string mode (rad/s)
Ω_k	Complex natural frequency of the k^{th} body mode
ω_{Mk}	Natural frequency of the k^{th} body mode (rad/s)
ϕ	Angular displacement of the string
ψ	Coupling strength

ρ	Density
ρ_r	Density of rosin
$\square_k$	Subscript means relevant to the k^{th} body mode
$\square_n$	Subscript means relevant to the transverse string mode number n
$\square_X$	Subscript means in parallel-to-the-plate direction for the guitar and tangent-to-the-bridge-crown direction for the violin
$\square_Y$	Subscript means in perpendicular direction to both the X-direction and the string axis
$\square_b$	Subscript means relevant to the bow hair ribbon
$\square_{sym}$	Subscript means relevant to the sympathetic strings
θ_{Mk}	Spatial angle of the k^{th} body mode at the bridge
Θ	Temperature of the rosin in the contact patch
θ'_{Mk}	Angle of the k^{th} body mode at the bridge with respect to the excitation direction
$\triangle f$	Half-power bandwidth
ς	Damping ratio
ξ	Longitudinal displacement of the string
ζ	Correction factor showing the deviation of the bridge excitation force from being a perfect sawtooth wave
A	Area of the contact patch between bow and string
a	Bow acceleration
a_k	Complex amplitude of the k^{th} body mode
$A_{k,i}$	Complex velocity amplitude of the k^{th} at time-step i
B	inharmonicity coefficient
c	Frequency-dependent transverse wave propagation speed
c_0	Propagation speed of transverse waves on a perfectly flexible string

c_B	Bulk wave speed
c_R	Propagation speed of rotational waves
c_{pr}	Thermal heat capacity of rosin
D	Amplitude of the bridge displacement
E	Effective Young's modulus of the string
f	Frequency (Hz)
f_0'	Frequency of first longitudinal string mode (Hz)
f_0	Frequency of first transverse string mode (Hz)
F_a	Force at point a
F_b	Force at point b
F_F	Excitation (Friction) force at the bowing point
F_M	Bridge force
F_N	Normal force with which the bow presses into the string
F_T	Transverse force applied at the bowing point
F_{max}	Maximum bow force
F_{min}	Minimum bow force
F_{pert}	Perturbation force at the bowing point
F_{Mk}	Excitation force applied by the string(s) to the k^{th} mode
G	Shear modulus
g	Velocity response to a unit impulse force (Green's function) at the excitation point
g_Θ	Green's function for thermal heat conduction
G_1	Gain of the bridge-side loop filter as a function of frequency
h	Time-step of the simulations
h_1	Bridge-side reflection function

h_2	Finger-side reflection function
I	Second moment of area
I_R	polar moment of inertia per unit length of the string
K	"veering" identifier
k	Frequency-dependent wave number
K_0	Integration constant in the calculation of the bowing-point perturbation force
K_R	Torsional stiffness of the string
K_s	Bulk modulus
k_b	wave number of the bowhair for its transverse vibrations
k_y	Shear yield strength of rosin
L	Singing length of the string
l	longitudinal string mode number
L_b	Length of the bowhair ribbon
M_k	Equivalent mass of the k^{th} body mode at the bridge
m_s	Mass per unit length of the string
P	Time period of oscillation of the string in its fundamental transverse mode
Q	Quality(Q) factor
Q^*	Q factor associated with the intrinsic damping of the string
Q_s	Frequency-continuous Q factor of the string
Q_{Mk}	Q factor of the k^{th} body mode
R	Resistive impedance
r	Radius of the string
S	Cross-sectional area of the string
T	Time- and space-varying tension of the string

t	Time
T_0	Static tension of the string
u_k	Mode shape of the k^{th} body mode
v	Physical velocity at the excitation point
V_a	Velocity at point a
V_b	Velocity at point b
v_b	Velocity of the bow
v_h	Combined magnitude of velocity waves impinging on the bowing point of the string
V_M	Bridge velocity
v_{i1}	Magnitude of transverse velocity wave approaching the bowing point from the bridge side
v_{i2}	Magnitude of transverse velocity wave approaching the bowing point from the finger side
v_{o1}	Magnitude of transverse velocity wave sent towards the bridge from the bowing point
v_{o2}	Magnitude of transverse velocity wave sent towards the finger from the bowing point
V_r	Volume of rosin in the contact patch between the bow and the string
x	Distance along the string
x_0	Bow-bridge distance
x_{0b}	Distance from the contact point on the bowhair to the frog
$x_{1,2}$	Amplitude ratio for two successive periods
y	Transverse displacement of the string
Y_M	Admittance matrix at the bridge
Z_1'	Impedance at the bridge side evaluated at point b, assuming the bridge is a rigid termination
Z_1	Impedance at the bridge side evaluated at point b

Z_2 Impedance at the finger side evaluated at point b

Z_a Impedance evaluated at point a

Z_b Impedance evaluated at point b

Z_M Bridge impedance, $Z_M = 1/Y_M$

Z_{0b} Characteristic impedance of the bowhair in its transverse direction

Z_{0R} Characteristic impedance of the string in torsional direction

Z_{0T} Characteristic impedance of the string in its transverse direction

Z_{bow} Transverse impedance of the bowhair at its contact point to the string

Z_{Meff} Bridge impedance, taking into account the effect of the sympathetic strings

Z_{tot} Effective characteristic impedance of the string defined as $\frac{1}{Z_{tot}} = \frac{1}{Z_{0T}} + \frac{1}{Z_{0R}}$

η_A Aerodynamic loss coefficient

η_B Bending loss coefficient

η_F Friction loss coefficient

$\Omega_\pm$ Frequencies of the normal coupled string-body modes (rad/s)

u_{Mk}^2 Amplitude of the mass-normalized mode at the bridge

Contribution of authors

This thesis, and the research to which it refers, is the candidate's own original work except for commonly understood and accepted ideas or where explicit reference to the work of other people, published or otherwise, is made. The dissertation is formatted as a monograph comprising six chapters and includes contents from the following conference publications:

1. H. Mansour, J. Woodhouse, G. Scavone, "Enhanced simulation of the bowed cello string", in Proceedings of Stockholm Music Acoustics Conference (SMAC), pp. 94-100, 2013

2. H. Mansour, J. Woodhouse, G. Scavone, "Time-domain simulation of the bowed cello string: dual-polarization effect", International Congress on Acoustics, Montreal, 2013

The candidate was responsible for conducting the experiments, developing the numerical model, data analysis, and preparing manuscripts for all the publications listed above unless otherwise stated.

The above articles present some preliminary results of the model that will be thoroughly discussed throughout this thesis. The original version of the model and lots of feedback was provided by J. Woodhouse. G. Scavone provided supervision, equipment, and space. He also helped in the review of the manuscripts.

Chapter 1

Introduction

I have often been approached by colleagues in science and engineering disciplines asking questions such as:

- Is your research concerned with the design of an optimal violin?
- What exactly are you trying to figure out about the violin?
- Why don't you pick an excellent violin and reverse engineer it?
- Once you find the secret of Stradivari, can you mass-produce professional-level instruments?

Although not completely within the scope of this thesis, it seems appropriate to start by addressing some of those questions and to clarify the scope of violin research, and more generally musical acoustics.

1.1 What can musical acoustics do – and what can it not?

Violin research has been an active field of study, at least for the last 150 years [2]. The basic idea is to combine our knowledge of psycho-acoustics, physics, and engineering with the experience of the makers and the expectations of the players to better understand how the violin works, and ideally to figure out what distinguishes "good" from "bad" instruments. Like many other fundamental research areas, curiosity is the main drive behind this line of research. There are some fundamental differences between musical acoustics and the majority of topics in science and engineering, which should be understood before offering solutions.

- Violin research combines, and has in some occasions advanced, many fields of study including noise and vibrations, acoustics, psychoacoustics, nonlinear dynamics, tribology, wood science, signal processing, experimental physics, and music performance. It is both challenging and rewarding to study such an intertwined set of diverse topics.

- Violin research deals with a collection of subtle, yet important, details that are perceptible to musicians. *"In most engineering problems concerning frictional vibration, and indeed vibration in general, the overriding concern is to understand the behavior only well enough to design measures which will reduce the vibration and associated noise nuisance. In musical acoustics, things are very different: the essence of music, and in particular of quality judgments by musicians, lies in fine details of vibration and sound. Any two violins of reasonable quality are about as similar to each other, in terms of measured vibration behavior, as two nominally identical car bodies coming off a production line. The remarkable range of market values of violins depends on relatively subtle differences of mechanical behavior"*[1] [3]. Such extreme sensitivity of musicians was echoed by a rigorous analysis of 17 quality rated violins conducted by Bissinger, who was unable to find any reliable discriminator to distinguish the very best violins from the worst ones [4].

- It is practically impossible to make exact replicates of a particular instrument, simply by copying its geometrical properties.[2] It has been shown [5, 6] that minor changes (as small as 25 μm) to the thickness of the top plate can make audible changes in the final sound of an instrument, even perceivable by non-musician subjects. Constructional tolerances in making musical instruments are typically much larger than this. Combining this with the random properties of the wood annihilates any hope of achieving a product consistently within the discrimination thresholds of musicians, simply by following the same manufacturing process. Final adjustment is therefore a key ingredient of making consistent high quality instruments.[3]

- Violin adjustment relies on the perceptual and intuitive knowledge of makers. Makers

[1] Let's assume, at least, a weak correlation between the price of a violin and its quality.

[2] Schleske, a professional violin maker, introduced the concept of tonal copies, as opposed to geometrical copies, in which he tries to match some vibrational properties of a new instrument with those of a reference instrument. It is believed by many violinists that he is quite successful in making very similar instruments in terms of their playing characteristics.

[3] Selling the instruments that end up being of a lower quality for a cheaper price is, of course, a simple alternative. A smarter alternative would be to use the "sorting and mating" approach that is common in applications for which the manufacturing inconsistencies exceed the required precision. This approach can be used either in a sense that the instruments are cascaded into different quality classes, hence different price ranges, once they are made nominally identical, or in a sense that they are cascaded into different perceptual categories based on their playing characteristics, hence be bought by players with matching preferences [6]

have mental models of vibration and sound which may work well enough most of the time – though not always for the reasons the makers think they do [7]. But sometimes their model is simply wrong and that can lead to irreversible faulty adjustments. Having a science-based and reliable model can make the adjustment procedure faster, cheaper, and more insightful. The model does not need to be very accurate or sophisticated as it only needs to predict the right trend or to find the right underlying physics in its general form. Gough [8, 9] has recently used a relatively simplistic finite element model of the violin to investigate the ways different substructures are coupled to form the so-called "signature" modes of a fully assembled violin, and to find their significance in the radiated sound by the instrument. In another notable series of articles, Bissinger [10] provided a "dynamic filter" model to relate the violin's radiativity profile to a discrete set of measurable properties. These approaches are somehow different from common applications of numerical models in engineering problems that are mostly concerned with virtual product development (VPD), or with optimization.

- Our auditory perception is sensitive to the details of the sound in a broad range of frequencies that typically covers a few hundred structural modes, and roughly the same number of modes for the internal air cavity [11].[4] *"Assembling these numbers, it is clear that an accurate synthesis method may have to account correctly for several hundred degrees of freedom. It may come as a surprise to learn that very few vibration predictions of this degree of complexity have ever been confirmed in detail by experiment. Although very large finite-element models are routinely used for vibration prediction of industrial structures of many kinds, where these have been checked against measurements they rarely give full agreement in detail beyond the first few modes"*[11]. This contributes to the fact that making good-enough numerical models for musical applications is a challenging task and often times alternative approaches should be utilized for the modeling of different aspects of it. An example of such alternative approaches is "statistical energy analysis," which has been used to investigate the high-frequency response of violins [12].

- Optimization, in its conventional sense, cannot be applied to the design of the violin. The most significant barrier in that regard is the lack of a well-defined objective function, which is an essential component in any form of optimization[5] (classic or heuristic, discrete or continuous). Even if such an optimal design is available, dimensional vari-

[4] These numbers were originally reported for a guitar, but one may expect to find roughly the same numbers for the violin.

[5] Such an objective function has been defined for simpler musical structures such as a church bell and optimization techniques were successfully applied to them [13].

ations and material uncertainty may render the ultimate result significantly different from the expected outcome.

- Given the design constraints, a violin is a very optimal structure in its current form. Different successful aspects of its design consist of material selection, weight-to-stiffness ratio, cost, ergonomy, loudness, durability, repairability, and playability.[6] Accidental replication fluctuations from craftsmanship limitations with subsequent selection favoring instruments with better qualities provided the violin with an opportunity to undergo a process of natural selection over centuries [14].[7] The best instruments are maintained, improved and replicated, while the unfit are eliminated. The current inventory of violins include excellent instruments that can, more or less, satisfy any player, which of course come with huge price tags. It should also be noted that the taste of the players and the listeners, as well as the available musical repertoires, have evolved together with the design of the violin, therefore any radical change in the design will likely be perceived as undesirable, unless the instrument is being used for a new and drastically different genre of music.

Having mentioned all the challenges, there have been some major advancements in our understanding of the physics of the violin over the past few decades. The emergence of fast computers and the availability of more precise measurement systems has revolutionized our knowledge of the violin. Advanced finite element models have been made to simulate the body of a violin [8, 9, 15]. The important resonances of the violin in the low frequency range (called the "signature modes") and their relation/sensitivity to the subcomponents of the violin have been studied in great depth [10, 16]. The mid-frequency response of the violin and the origin of a broad peak at around 2 kHz (called the "bridge hill") has been identified [17, 18]; and its indeterministic high-frequency response has been treated using statistical methods [12]. CT scanning was applied to a large number of exceptionally good violins, which has made their exact geometry, plate thickness, and wood density available [19, 20]. Carefully controlled bowing machines were developed to systematically study the dependence of the bowed string vibrations to the bowing parameters [21, 22]. The playability of a violin was investigated both theoretically [23, 24] and experimentally [21, 22, 25]. And carefully-designed perceptual analysis has been applied to violins that has shed light on how musicians perceive quality(ies) of an instruments [26, 27].

We summarize this section by a quote from Jim Woodhouse [7] in an interview with

[6] For more information, the reader is referred to an interesting talk by Jim Woodhouse available at https://www.youtube.com/watch?v=wf_FfC9Uq3U.

[7] The original study is concerned with the evolution of the violin sound-hole, but it is safe to assume that other aspects of the violin design have also gone through a process of natural selection.

Joseph Curtin, a professional violin maker[8] about what science can, and cannot, do to help violin makers.

> *"It's no use coming in, and telling makers what to do. Scientific advice should come with a government health warning – may be harmful to your instrument! Science can be useful in sending you in the right direction, but if you follow some theory to the point where you start to think, 'I don't want to do this, but science says I must,' then the science is probably wrong. [...] Good violin makers make good violins. Science follows along behind."*

After pointing toward some specific contributions that science *can* make to violin making, Woodhouse responds to the question of how far science has come in understanding the violin:

> *"The image I like to use is that of a jigsaw puzzle. The edges are done, along with a few bits in the middle, but much of the picture is still blank. A jigsaw puzzle is a good image for how science generally proceeds. We do the edges first because they're easier, then we work our way in. The strong point of science is that it is cumulative. I am completely confident that more and more of the picture will appear. It will take generations more learning, and we may never know everything there is to know about the violin, but it's the attitude which is important."*

1.2 Scope and objectives

The long-term goal of this project is to make a physically-accurate model of the bowed string, capable of predicting transient behavior that agrees quantitatively with experimental measurements over a wide range of bowing gestures of musical interest. As an intermediate application, the model will be used as an experimental tool to gain a better understanding about the physics of a bowed string, and to estimate the relative significance of different physical detail in defining the final response of the instrument. Such results will not only benefit musical acousticians, but also help people in the sound synthesis domain to decide whether or not it is worthwhile to implement a specific detail in their real-time models. Even though our model itself is not optimized for sound synthesis applications, it may be used as a reference to conduct perceptual studies and to investigate how much simplification can be

[8] Pioneered by Carleen Hutchins, nowadays many fine violin makers including Joseph Curtin, George Stoppani, and Martin Schelske, perform acoustical measurements on their instruments and study musical acoustics (semi-)professionally.

made on the modeling of a particular physical detail before the change in the synthesized sound becomes noticeable to human subjects.

The model discussed in this study is adapted from an earlier model of a bowed string that was originally developed in [28], and has yielded many interesting results [29, 30, 31, 32]. That model was developed over time to include more physical details such as torsional vibrations of the string [33], bending stiffness of the string [29], effects of a close body resonance resulting in a "wolf note" [34], longitudinal bowhair compliance [35], and the effect of the bow's finite-width [35]. Our objective is to develop the next generation of that model, both by revisiting the way different physics are implemented, and by including more details into the model. We will also discuss what we think remains to make the model "complete".

We will use our model in investigating different aspects of a bowed string, most notably its playability. Unlike a plucked or a struck string, and similar to wind instruments, not all gestures applied to a bowed string lead to its singing sound. This points to a class of properties for a bowed string relevant to its ease of playing (a.k.a. playability), as opposed to the quality of its sound. Playability can be defined as "the range of bowing gestures that a player may use which results in an acceptable violin sound within a reasonably short period of time" [21]. Schelleng and Guettler diagrams will be used to investigate the playability of a bowed string, both theoretically and numerically. A Schelleng diagram indicates the limits of bow force within which the Helmholtz motion or the "speaking" sound of a bowed string is sustainable. A Guettler diagram, on the other hand, deals with the transients at the start of a bow stroke and sets the criteria for a "perfect transient," meaning no disturbing pre-Helmholtz transients at all. Toward the end of this study, we will investigate some other aspects of a bowed string that are more relevant to its sound than to its playability.

In accordance with the primary focus of this work, being the string itself, the body of the instrument is only considered from the perspective of how it affects the vibrations of the string. It should be kept in mind, however, that the body vibrations are central in defining the efficiency and directivity of sound radiation from the instrument. Moreover, understanding their detailed vibration patterns provides a guideline on how an instrument can be fine-tuned, which is of particular interest to instrument makers. This topic makes up for a large portion of the musical acoustics literature. The interested reader can check some recent reviews in [36, 37, 38].

1.3 Content and organization

The dissertation is structured as follows:

Chapter 2 describes the development of a plucked-string model, which later serves as the basis for the model of a bowed string. After a review of the relevant underlying physical theories, different methods are proposed to incorporate some of those behaviors into our particular modeling scheme. Among those details are the frequency-dependent damping of the string, its bending stiffness, its out-of-plane vibrations, its nonlinear vibrations, and its coupling to the body modes and the sympathetic strings. Finally some results are presented to evaluate the accuracy of the model and its parameters.

Chapter 3 will look into the new physical details that emerge from the interaction of the bow with the string, namely the tribology of the rosin, the torsional motion of the string, the flexibility of the bow hair ribbon in its longitudinal and transverse directions, and tension alterations of the string and the bow hair ribbon.

Chapter 4 will investigate the limits within which the Helmholtz motion is sustainable on a bowed string. After a review of the available literature on the bow force limits, experimental data will be presented that sheds light on some limitations of the underlying assumptions used in deriving earlier relations for the minimum bow force. Starting from a more robust assumption, a new relation will be derived for the minimum bow force, which will later be compared to simulation results.

Chapter 5 looks into a broader range of features of a bowed string and how they are affected by the inclusion or exclusion of a particular physical detail from the model. Those features include the minimum and the maximum bow force, the increase in the slip-to-stick ratio compared to its theoretical value, the spectral centroid, the pitch flattening, and the rate of occurrence for two special vibration regimes called the “ALF notes” and the “S-motion”. The initial transients of the bowed string will also be analyzed in the bow force versus bow acceleration plane.

Chapter 2

The ingredients of a complete plucked-string model

In this chapter, a physically-accurate time-domain model for a plucked musical string is developed. The bow and complications associated with the bowing process will be added to the model in the next chapter. The model incorporates detailed dispersion and damping behavior measured from cello strings, and a detailed description of body response measured from a cello body. The resulting model is validated against measured pizzicato notes on a cello, and good accuracy is demonstrated. The model is built on an earlier simulation of a bowed string [34] but many aspects of it are replaced with more accurate alternatives which advances the model towards much higher realism. Most of the parameters used in the model are obtained from new measurements. Longitudinal vibrations of the string, waves on the after-lengths and nonlinearity of string vibrations are not included in the current version of the model.

2.1 The development of theoretical models of a vibrating string

In 2004, Woodhouse described three methods of synthesizing guitar plucks [39]: modal synthesis, an inverse-FFT based method and a traveling-wave approach adapted from earlier simulations of bowed strings. While the two former methods were shown to give a very good match to the experimental measurements, the latter was fairly disappointing. The efficiency was not as good as the two alternatives, and the model had a tendency to become unstable, perhaps because of the way string damping and dispersion were implemented. This chapter focuses on an updated version of that model. Damping and dispersion modules are replaced with more sophisticated alternatives, and coupling to the body modes is made more accurate. Coupling to the adjacent open strings, which may or may not be tuned sympathetically with

the played string, is taken into account.

Unlike the modal and inverse-FFT based methods, which are performed in the frequency domain, the traveling-wave approach is made in the time domain, which is much better suited to simulating the transient responses, especially that of a bowed string with its strongly nonlinear frictional interaction. Time-domain simulation of a string has a long history of development, but here only a particular version is mentioned that the simulations of this study are based on (developed by McIntyre-Schumacher-Woodhouse, abbreviated as MSW throughout). The central feature of that model is to explicitly represent the motion of a string as the superposition of left- and right-going traveling wave components, and to find the incoming waves at the excitation point by convolving the history of the outgoing waves toward each end with a corresponding impulse response, called the "reflection function" (this approach is more thoroughly discussed in Sec. 2.1.2). Although the method was originally developed to simulate a bowed string, the same computational scheme can be readily adapted to other cases, such as a plucked or a struck string.

It should be emphasized that the goal here is to make the model physically accurate and to keep the link between the model and physical parameters as clear as possible. This contrasts with the priorities in the sound synthesis field, where physical details may be compromised to improve computational efficiency as long as their exclusion does not significantly worsen the quality of the synthesized sound. Having said that, the two fields have remained closely knit and have exchanged knowledge on many occasions. In fact, methods that we will use to model the damping and dispersion of a string are tailored versions of models originally developed for sound synthesis purposes.

2.1.1 The ideal vibrating string

In 1713, Taylor [40] gave the first theory of the fundamental mode of a vibrating string. He showed that the net force applied to an element of the string is proportional to its curvature, and predicted that for small-amplitude vibrations a restoring force proportional to the distance from the axis is applied to the string. He thus found the formula for the fundamental frequency of a vibrating string

$$f_0 = (1/2L)\sqrt{T_0/m_s}, \tag{2.1}$$

where L is the singing length of the string, T_0 is its tension, and m_s is its mass per unit length [41].

In 1751, Bernoulli [42] gave a theoretical justification for the superposition of modes in the case of vibrating strings. He decomposed a physical vibration as a summation of simple

harmonic oscillations based on a physical argument. The full mathematical justification of the modal superposition was later supplied by Euler. Among many other applications, this work forms the basis for what is now called "modal synthesis".

Around the same time, in 1746 d'Alembert [43] obtained the equation of motion for a vibrating string by combining Taylor's argument of the restoring force with Newton's second law. A modern statement of his formulation is the well-known equation of motion for an undamped and perfectly flexible freely vibrating string

$$m_s \frac{d^2y}{dt^2} = T_0 \frac{d^2y}{dx^2}, \tag{2.2}$$

where y is the transverse displacement of the string. D'Alembert was able to solve this differential equation, and found the general form of the solution as a superposition of two waves traveling with the speed $c_0 = \sqrt{T_0/m_s}$ in opposite directions, related via the boundary conditions. This idea formed the basis of the MSW model of a bowed string, which evolved into what has become known as "digital waveguide modeling": see for example Smith [44].

2.1.2 The McIntyre-Schumacher-Woodhouse (MSW) model

The equation of motion for an ideal string (i.e. Eq. (2.2)) is a linear second-order one. Taking into account the string's bending rigidity adds a fourth-order term, and coupling to the body introduces some complications; that said, neither of these effects introduce any form of nonlinearity. With that in mind, the current state of a vibrating string can be obtained by convolving its *past history of excitation* by its *response to a unit impulse;* the latter being the so-called Green's function (shown by g hereafter). Typically, for a bowed string the excitation is the force applied at the bowing point and the response is the velocity at the same point and in the same direction.[1]

Although simple in principle, this method cannot be efficiently applied to the problem of a vibrating string. The length of the convolution should cover hundreds of string periods to give an accurate result, something that can be readily confirmed by plucking the string and waiting for it to settle. To overcome this issue, MSW proposed to write g as the sum of a delta function (being the instantaneous velocity response of the string to the applied force) plus two traveling waves bouncing back and forth between the bridge and the finger ("finger" is used as a shorthand for finger/nut throughout), and exchanging values at the excitation point [28]. These traveling wave components are called h_1 and h_2 for the bridge and finger sides respectively. As opposed to g, the required lengths for h_1 and h_2 are of the

[1] Bear in mind that the MSW model was originally developed for a bowed string. We will soon see how to turn it into a plucked-string model.

order of one string period for a string that is rigidly terminated at both ends. This method is illustrated in Fig. 2.1. Mathematically, g can be decomposed as

$$2Z_{0T}\ g = \delta_t + h_1 + h_2 + 2h_1 * h_2 + h_1 * h_2 * h_1 + h_2 * h_1 * h_2 + \ldots, \tag{2.3}$$

where δ_t is the delta function and $*$ denotes convolution, and Z_{0T} is the characteristic impedance of the string in its transverse direction (defined as $\sqrt{T_0 m_s}$). Although the original formulation, as well as the focus of this study, was based on velocity traveling waves, the same approach can be applied to simulate displacement or acceleration waves.

Now let's consider the hypothetical case of a string that is extended infinitely on the finger side. Any outgoing wave toward the finger would never come back, hence the finger side terms (i.e. any term that includes h_2) in Eq. (2.3)) will amount to zero. For such a system, the impulse response at the plucking point consists of only two terms: A delta function followed by one reflection coming from the bridge (i.e. h_1). Assuming that the impulsively excited end of the string eventually returns to its initial position, the integral of h_1 should cancel the displacement resulting from the impulsive velocity at time zero that is equal to one. Symmetrically, the same argument applies to h_2 if the string was extended from the bridge side. This gives a mathematical constraint for h_1 and h_2 in order for them to be physically plausible

$$\int_{-\infty}^{\infty} h_1 dt = \int_{-\infty}^{\infty} h_2 dt = -1. \tag{2.4}$$

If this condition is not met the mean values of the left- and right-going traveling waves can drift, which in physical terms would correspond to the entire string shifting position; although, if the integral falls between 0 and -1 this drifting will be toward zero, hence the full-string remains stable.[2,3]

Going back to our original discussion, MSW proposed the following sequence of computations, to be repeated in every time-step:

1. The incoming velocity waves arriving at the excitation point from the finger- and bridge- sides (labeled i_1 and i_2 in Fig. 2.1) are calculated by convolving the history of the outgoing waves toward the respective direction with the reflection function for that side. These incoming waves add together to form the unperturbed velocity at the excitation point (called v_h, with subscript h standing as a reminder that v_h only depends on the past *"history"* of the string).

[2] An early model of a bowed string developed by Raman [45] as well as many of the modern day sound synthesis models fall within this category.

[3] It was shown in [24] that violation of Eq. (2.4) in the case of a bowed string results in a fundamentally different perturbation force at the bow, thus an unphysical prediction of the bow-string interaction.

2. The instantaneous response to the force acting at the excitation point is added to v_h to calculate the actual physical velocity at that point, called v (i.e. $v = v_h + \frac{F_F}{2Z_{0T}}$ where F_F is the excitation force and Z_{0T} is the string's characteristic impedance as defined earlier). In the original implementation, the excitation force was the friction force applied by the bow, but it can be any arbitrary function of time (including a constant zero).

3. The incoming waves from the finger and bridge cross the excitation point and form the new outgoing waves toward the other end (labeled o_1 and o_2 in Fig. 2.1). In the process of passing, each wave is modified by the amount $\frac{F_F}{2Z_{0T}}$.

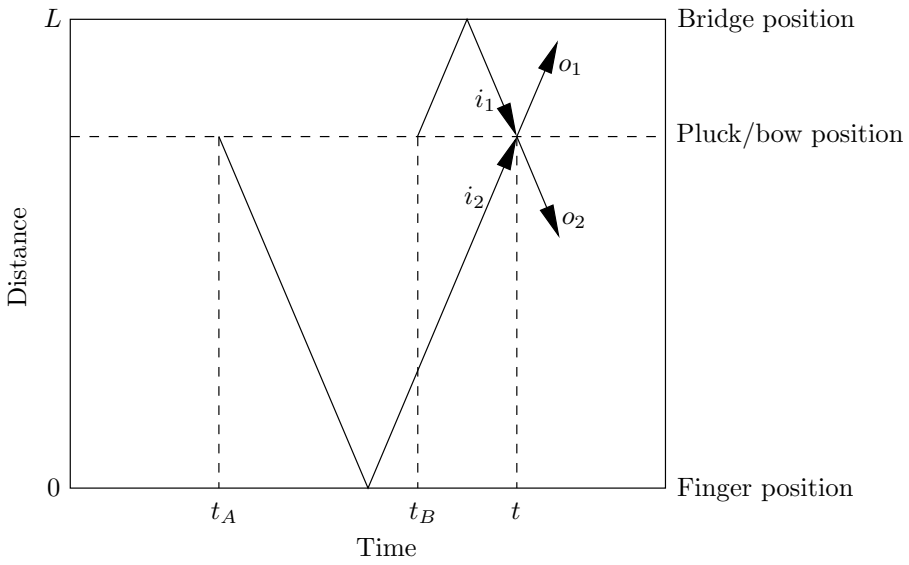

Fig. 2.1 Space-time diagram of traveling waves sent out from the plucking/bowing point towards the finger and bridge at times t_A and t_B respectively, arriving back at the plucking/bowing point at time t and forming $v_h = v_{i_1} + v_{i_2}$. The magnitudes of the new outgoing waves (denoted o_1 and o_2) are $v_{o_1} = v_{i_2} + F_F/2Z_{0T}$ and $v_{o_2} = v_{i_1} + F_F/2Z_{0T}$. (After [21])

As a side note, the MSW's proposed reflection function, in its original form, encapsulates all the processes a wave undergoes in a round trip to and from one end, consisting of delay, damping and dispersion induced by the string, as well as the coupling to the corresponding end termination (roughly a rigid boundary at the finger side, and a multi-resonance body at the bridge side). The inclusion of the body, however, requires a convolution size significantly longer than the string's period to ensure the oscillations of the body have decayed enough before the impulse response is truncated. A more efficient alternative is to include the body modes in a recursive scheme that is discussed in Sec. 2.3.5. The term "reflection function"

in the remainder of this study is only used in association to a string with rigid terminations at both ends.

2.2 The underlying physics of a plucked string

In this section, we will describe the underlying physics of different details relevant to a plucked string, including the string's dissipation and dispersion, its coupling to the body modes, the sympathetic strings, and the after-lengths of the strings. The section ends with a discussion on the nonlinear vibrations of the string. In the next section we will see how to implement some of these details into the traveling-wave scheme. Distinctions are made when necessary, but otherwise the arguments presented are applicable to the plucked strings of both guitar and any instrument of the violin family.

2.2.1 Damping of a perfectly flexible string

Assume for the moment that the string is perfectly flexible. For such a system, the reflection function has a very simple form that is a delayed inverted delta function, rounded to some extent to model the damping (see Fig. 2.2 for an example). The required delay to produce a desired fundamental frequency for the full-length string is equal to βP for the bridge side, and $(1-\beta)P$ for the finger side, where P is the string's period and $\beta = \frac{excitation\ to\ bridge\ distance}{string\ length}$ is the relative distance of the excitation point to the bridge. Adjusting the damping is a more complicated task which forms the topic of this section.

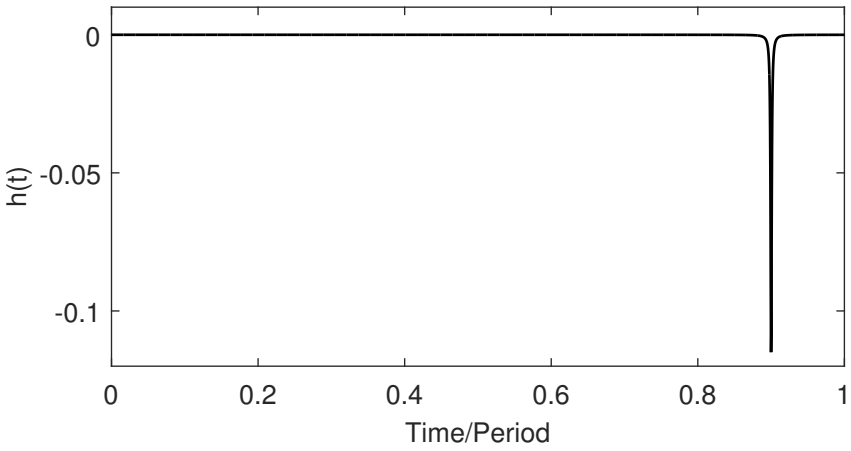

Fig. 2.2 Reflection function designed for the finger side of a damped but perfectly flexible cello C_2 string. The natural frequency of the string is 65.4 Hz, β is 0.1, the constant-Q factor is set to 500, and the sampling frequency of 2×10^5 Hz is used. Damping is modeled based on Eq. (2.8) introduced in [33].

The motion of a vibrating string may be decomposed into multiple harmonic resonators, called the string modes. The motion of each mode that is initialized with amplitude y_{0n} can be described over time as

$$y_n = y_{0n} e^{-\alpha_n t}\ e^{-i2\pi f_n t}, \tag{2.5}$$

where f_n is the natural frequency of the n^{th} string mode and α_n is the decay rate associated with that mode. Besides the decay rate (α), there are other terms to describe the damping of an oscillator, with the most common ones being: Q factor (Q), damping ratio (ς), loss factor (η), half-power bandwidth ($\triangle f$), and the amplitude ratio for two successive periods ($x_{1,2}$). Assuming that damping is small (i.e. $\frac{1}{Q_{(f)}} \ll 1$), these descriptors relate to one another in the following ways:

$$\frac{\eta}{2} \approx \varsigma = \frac{1}{2Q} = \frac{\triangle f}{2f} = \frac{\alpha}{2\pi f} \approx -\frac{ln(x_{1,2})}{2\pi}, \tag{2.6}$$

where f is the target frequency, and all descriptors are functions of frequency. Among these descriptors, Q factor is the most common to describe the decay of a vibrating string, and is defined as π times the number of periods for the amplitude to decay by the factor $1/e$. In general, these descriptors are continuous functions of frequency, although for a string of a particular length and physical properties, one can only measure their values at a discrete set of frequencies being the string's natural frequencies.

Back to the main topic and keeping in mind MSW's reflection function approach, to properly model the damping trend of a string over different frequencies, each frequency component should experience a certain amount of attenuation in a round trip to and from one end. In essence, convolving the history of the waves going towards one direction with the corresponding reflection function is equivalent to filtering the same quantity by a Finite Impulse Response (FIR) filter (called the "loop-filter"), the impulse response of which is the equivalent reflection function. Now without reducing the generality, let's focus on the bridge side of the string: there are $\beta f / f_0$ cycles of frequency component f in a round trip to and from the bridge, where f_0 is the fundamental frequency of the full-length string. Therefore, the gain of the loop filter for the bridge side (called G_1) is related to the desired Q factor in the following form:

$$G_1 = e^{-\frac{\pi \beta f}{f_0 Q}}. \tag{2.7}$$

The same expression can be used for the finger side only by replacing β with $(1 - \beta)$.

It can be shown that if the reflection functions (or equivalently the loop filters) for the bridge and finger sides are designed with a fundamental $f_0/\ \beta$ and $f_0/(1 -\ \beta)$ respectively and are designed to produce a particular trend of Q factor versus frequency (i.e. according

to Eq. (2.7)), then the whole string will have the fundamental f_0 and the same frequency-dependency for the Q factor. It is interesting to note that while G_1 depends on the length of the string (the longer the string, the more decay a particular frequency component will experience in a round trip), Q factor is independent of the string length, such that if one plots the Q factor versus frequency for different notes played on the same string, they overlay on top of each other.

As indicated in Eq. (2.4), a constraint that any physically plausible reflection function should satisfy is that its integral in the time-domain should sum up to -1. Since the delay only shifts the reflection function in the time-domain without changing the area underneath it, the damping part is the one that should satisfy that constraint. From the filter design perspective, satisfying Eq. (2.4) is equivalent to having a loop filter with a unit gain at zero frequency (i.e. at DC).

Another property that the reflection function for a perfectly flexible string should satisfy is to be non-dispersive, meaning that all frequencies should travel with the same propagation speed along the string; this is equivalent to having a linear-phase loop filter (more specifically a zero-phase filter if the delay is accounted for separately). It also implies that the reflection function should be symmetric around its peak, a necessary but not sufficient condition that a linear phase FIR filter should satisfy.[4]

Interestingly, it was noted by Crandall [46] that a linear-phase filter describing a hysteretically damped system is non-causal as its impulse response tends to, but never reaches zero on either side resulting in an impulse response with non-zero values for negative time. For practical purposes and if the system is only lightly damped, delaying the reflection function by a proper amount and then truncating it for negative times usually gives a sufficiently good approximation of the desired damping behavior that also satisfies causality [33].

Constant-Q reflection functions

A particular class of reflection functions was introduced in [33] and has been used in the following studies [21, 47, 32]. That proposed reflection function assigns the same Q factor to all string modes and is designed as a function of time and the portion of the string to be represented (β for the bridge side, and $(1-\beta)$ for the finger side).

$$h_1 = \frac{2\beta L/(2Qc_0)}{\pi\left[(t-2\beta L/c_0)^2 + (2\beta L/(2Qc_0))^2\right]}, \tag{2.8}$$

[4] Another theoretical possibility is an anti-symmetric reflection function that does not make physical sense for a string, thus is eliminated here.

where, as before, c_0 is the propagation speed of transverse waves traveling on the string. The interested reader is referred to [33] for derivation details.

An issue to be cautious about when designing a reflection function based on Eq. (2.8), or any other FIR filter for that matter, is the possibility of discretization error, which becomes problematic for short segments of lightly damped strings. As illustrated in Fig. 2.2, the reflection function of a perfectly flexible string that is also lightly damped has only a few significantly non-zero elements (a property that makes it compelling to use low-order FIR filters to model string loss for sound synthesis purposes [48]) and normalization of the area would require a large adjustment to the peak height, hence a large deviation from the desired behavior. This issue is not unexpected as the width of a constant-Q reflection function can be considered narrow for low enough frequencies, hence it fits the definition of a "narrow reflection function" as described in [33]. If a narrow reflection function satisfies Eq. (2.4), its corresponding Q factor goes as $1/n$ (n being the string mode number), hence Q tends to infinity when frequency tends to zero. The problem can be alleviated by using a larger sampling rate to the extent that the Q factor for the first string mode falls within an acceptable range of the target value; Q factors for the frequencies below that are of little practical importance. The simulation of an open D_3 cello string using this class of reflection functions is discussed in Sec. 2.4 and the results are demonstrated in Fig. 2.21.

Frequency-dependent Q factor

The constant-Q reflection function was originally proposed to model the propagation of torsional waves on a cello string, for which the Q factor is approximately constant for all modes. Later, the same method was (provisionally) applied to the transverse vibrations of the string [21, 47, 32]. As will be seen in Sec. 2.4, a constant-Q assumption is not too far wrong if the damping imposed by the coupling to the body modes is also represented by the designed reflection function and if the frequency of interest remains low enough so that damping mechanisms involving the string's bending remain negligible. However, if the reflection functions are only to capture the intrinsic damping of the strings, the constant-Q cannot be considered a good approximation at all [5]. A large portion of the string damping in low frequencies comes from its coupling to the body modes and if that extra source of damping is removed, those string modes will have significantly larger Q values.

There are different sources involved in the intrinsic damping of a stretched string, each of which is dominant in a certain range of frequencies. Valette [49] has summarized those mechanisms as the viscous effect of the surrounding air, viscoelasticity and thermoelasticity of the string material, and the internal friction representing both macroscopic rubbing (in the multi-stranded and overwound strings) and inter-molecular effects (in the monofilament

strings). The only assumed frequency-independent mechanism among the above is the internal friction, which puts a cap on the total Q value. The air viscosity effects are mainly active in low frequencies while viscoelasticity and thermoelasticity become progressively significant at higher frequencies. In this regard, for a typical string as the frequency grows the Q factor rises to a maximum and then drops until it reaches a small asymptotic value. A more thorough discussion of this topic and the design of a frequency-dependent damping filter, as well as some new experimental data is presented in Sec. 2.3.1.

On a final note, one may argue that if the damping of a string mounted on an actual instrument is dominated by its coupling to the body, then the accurate modeling of the string's intrinsic damping may not make a big difference when treating the coupled system. While that argument is valid for a plucked string, it does not necessarily apply to a bowed string particularly when studying its transient behavior. The coupling to the body only affects the wave's reflection at the bridge side, while the waves traveling between the bow and the finger are only subject to the intrinsic damping of the string. A particular example of where this difference may matter is the case for Schelleng ripples on the finger side which are essentially trapped between the bow and the finger.[5]

2.2.2 Bending stiffness of a string

In reality, all strings have some degree of bending stiffness, which in effect converts the simple second-order wave equation of an undamped and perfectly flexible string (i.e. Eq. (2.2)) to a fourth-order equation of an undamped but stiff string

$$EI\frac{\partial^4 y}{\partial x^4} - T_0\frac{\partial^2 y}{\partial x^2} + m_s\frac{\partial^2 y}{\partial t^2} = 0. \tag{2.9}$$

Assuming hinged boundaries at two ends, the stiff string's mode shapes will remain unchanged compared to ones of a perfectly flexible string (i.e. $\sin\frac{n\pi x}{L}$), but the natural frequencies will no longer be perfectly harmonic. The n^{th} natural frequency of a stiff string is given by

$$f_n = nf_0\sqrt{1+Bn^2} \approx nf_0(1+\frac{Bn^2}{2}), \tag{2.10}$$

where, as before, f_0 is the first mode frequency if the string was perfectly flexible, and B is

[5] Schelleng ripples (discussed in Sec. 4.3.1) consist of waves reflecting between the bow and the bridge or between the bow and the finger, causing a disturbance of period β/f_0 at the bowing point [50, 23].

called the inharmonicity coefficient that can be calculated from

$$B = \frac{EI\pi^2}{T_0 L^2}, \tag{2.11}$$

E being the Young's modulus, and I the second moment of area. The presence of the string's after-length results in a boundary condition somewhere between hinged and clamped [37]. A clamped boundary condition introduces a new term to the frequency of the partials (i.e. to Eq. (2.10)) and the mode shapes will be different compared to those of a perfectly flexible string. A more careful treatment of this issue falls beyond the scope of this study and is covered elsewhere [51, 49].

On a stiff string, higher frequencies travel increasingly faster than lower frequencies which results in the formation of "precursor" waves preceding the main peak in the reflection function (see Fig. 2.3 as an example). In the limit, group velocity tends to infinity as frequency tends to infinity resulting in a singularity occurring at $t = 0$ of the reflection functions. This is, however, of low practical significance in the digital domain as the highest studied frequency is always limited to the Nyquist rate (i.e. half the sampling frequency). Moreover, Eq. (2.9) becomes unphysical beyond a certain frequency as the maximum wave speed in any homogeneous material is limited to its "bulk wave speed" defined as $c_B = \sqrt{K_s/\rho}$ where K_s is the bulk modulus and ρ is the density of the material.

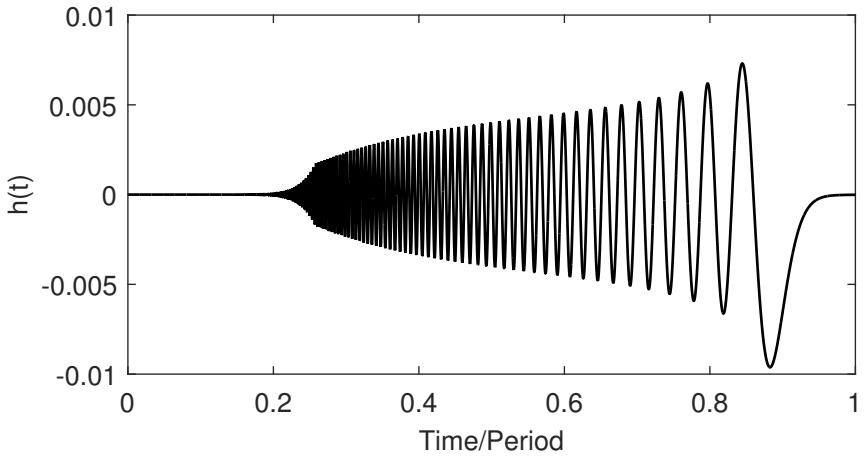

Fig. 2.3 Reflection function designed for the finger side of a damped and stiff cello C_2 string. The natural frequency of the string is 65.4 Hz, β is 0.1, the constant-Q factor is set to 500, bending stiffness is 9.1×10^{-4} Nm^2, and the sampling frequency of 2×10^5 Hz is used. Damping is modeled based on Eq. (2.8) introduced in [33], and dispersion is modeled based on a method introduced in [29].

The inharmonicity coefficient increases with reducing the length of the string (playing on higher frets of the same string, for example) but if one plots the inharmonicity of the n^{th} partial, Bn^2, with respect to the frequency (rather than the string mode number) the plots will overlay for different notes on the same string.

Another point to bear in mind regarding stiff strings is that the fourth-order equation of motion results in four solutions, only two of which are naturally included in the traveling wave approach; the other two are a pair of fast-decaying waves (a.k.a. quasi-evanescent waves). The phase velocity of those waves is almost infinite and their attenuation per unit length is high. In that regards, these waves are only important in the vicinity of the excitation point and within a short period of time after the excitation. Ducasse has estimated those limits for a piano C_2 string to be in the neighborhood of 2 cm and within 0.1 ms of the hammer excitation [52]. For thinner strings, like the ones of a cello or a violin, the spatial limit should be even smaller, but it is still of the order of the bow width and may be important in the interaction of the bow and the string [35].

The inharmonicity of normal guitar strings, both for nylon and steel strings, is above the threshold for human perception of inharmonicity [53, 5], as a consequence, the timbre of their plucked sound is affected by inharmonicity. It also results in their pitch being perceived slightly sharper than the frequency of the fundamental. Some inharmonicity may add to the naturalness of the sound, but too much of it is certainly not desirable. A practical fix that string makers use to reduce inharmonicity for low-frequency strings is to use a thin and flexible core over-wound with one or more layers of thin wire giving it the desired mass per unit length without adding too much to the bending stiffness.

In the case of a bowed string things are a bit different: if a stable Helmholtz regime (corresponding to the normal sound of a bowed string) is formed, it enforces perfectly harmonic partials due to the mode lock-in phenomenon [54], hence the perceptual arguments applicable to plucked strings do not apply there. Inharmonicity does, however, affect the formation and stability of the Helmholtz motion in the first place (which is considered an aspect of the string's playability). The operating frequency of the stick-slip for a bowed string is a compromise between the frequencies of the slightly inharmonic string resonances. This effect is similar in nature to the effect that slightly inharmonic resonances have on the playability and playing frequency of wind instruments, and is thoroughly studied in that context (see for example [55, 56], or [57] for a more recent study of the topic). We will get back to this issue in Chaps. 4 and 5, but as a general conclusion, lack of harmonic support from all string modes seems to be detrimental to stability of the Helmholtz motion on a bowed string.

2.2.3 Coupling to the body and to other strings

The resting point of the string on the bridge acts as a reflection point for the waves traveling along the string, and its vibration properties affect the vibrations of the string in that capacity. A useful measure to quantify such properties is the admittance, defined as velocity per unit force ($Y_M = V_M/F_M$), where all variables are functions of frequency. The bridge admittance is considered *"the most useful single measure of the acoustical performance of an instrument"* [12]. Typically, the bridge admittance is at least an order of magnitude smaller than the strings' admittances; as a consequence, strings are only lightly coupled to the body and the bridge can be considered a node to the first order of approximation. If it wasn't so, strong coupling to the body would perturb the strings' harmonic set of modes to the extent that the sound would not be considered musical any more. However, first-order corrections are also important, most obviously because they determine the amount of energy being transferred to the body, thus the intensity of the radiated sound, and secondly, because the coupling to the body affects the vibrations of the strings themselves [37].

The resistive loss (i.e. the real part of the admittance) at the bridge adds to the damping of the strings and the reactive component (i.e. the imaginary part) of the bridge admittance perturbs its natural frequencies [37]. This feedback to the strings is important for a plucked string mainly because it defines the decay of the partials, and for a bowed string mostly because it relates to the playability concerns. In its strong form, string-body coupling results in the notorious wolf-note phenomenon, particularly encountered by cello players.

The bridge admittance

The bridge admittance can be decomposed into the sum of multiple (in fact infinite) admittances of single-degree-of-freedom systems, each of which represents one "body mode". Assuming for the moment that the bridge only vibrates in one direction and that the modes are real (meaning the movement of the structure in that mode is such that all points along the structure simultaneously reach their maximum displacement), the bridge admittance is related to the modal properties of the body as

$$Y_M = \sum_k \frac{i\omega\ u_{Mk}^2}{\omega_k^2 + i\omega\omega_{Mk}/Q_{Mk} - \omega^2}, \tag{2.12}$$

where ω_{Mk} is the natural frequency, Q_{Mk} is the Q factor, and u_k is the "mode shape",[6] all of mode k, and i is the imaginary unit. u_{Mk}^2 represents the amplitude of the mass-normalized mode k at the bridge. To more insightfully use the mass-spring-damper equivalent, u_{Mk}^2

[6] dominant deformation at the corresponding frequency

can be replaced with $1/M_k$ where M_k is the mass of the equivalent oscillator. The value of the equivalent mass for a particular mode is of the order of the actual vibrating mass if the admittance is measured close to the anti-node of that mode, but increases with no limit as the measurement point tends to a node of that mode. This last statement highlights the importance of the relative location of each mode's nodal lines with respect to the bridge of the instrument; in fact, no energy would be transferred to a particular body mode (thus no sound radiation through that mode) if the bridge is located on a nodal line of it.

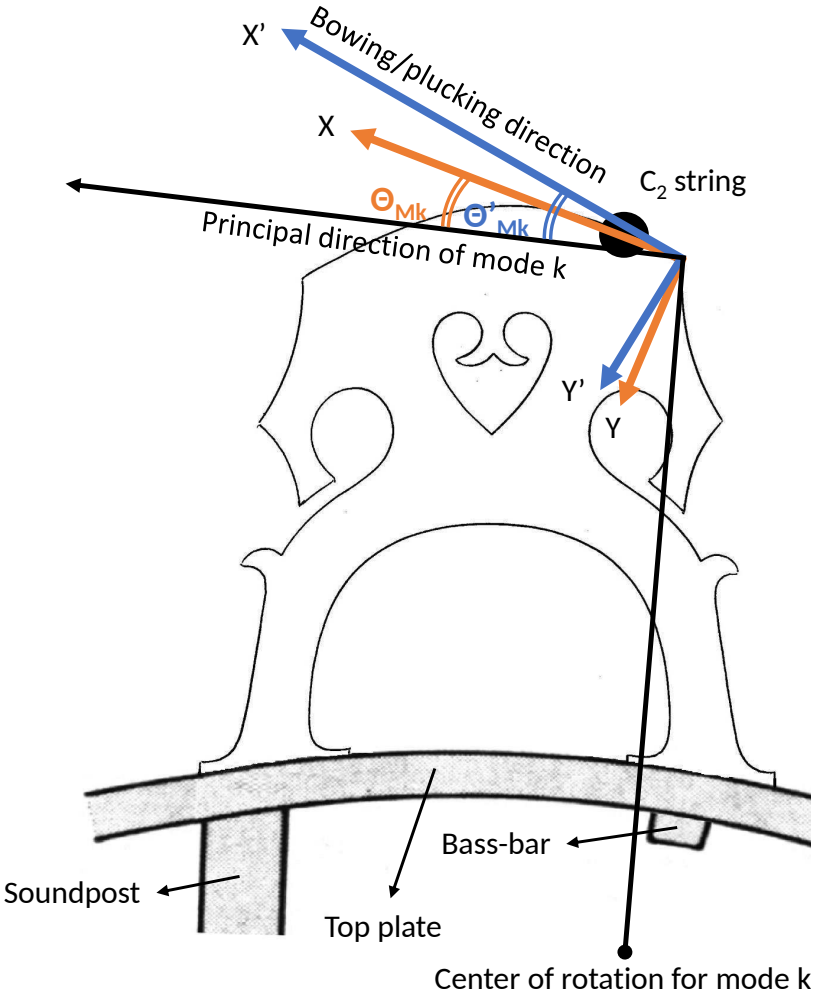

Fig. 2.4 Illustration of a cello bridge and relevant coordinate systems. The center of rotation for mode k is chosen arbitrarily. X and Y show the directions of admittance measurement, the excitation direction shown by X' and Y' may or may not be aligned with the measurement direction. The $X-Y$ coordinate system follows the curvature of the bridge-crown when defined for other strings. θ_{Mk} ranges from +90° to -90° for different modes.

As opposed to the assumption made above, the body of an instrument is a three di-

mensional structure. Each particular mode shape results in the bridge moving in a distinct direction that is not necessarily the same for all modes. The first extension to Eq. (2.12) is thus to relax the assumption of one dimensional motion. This makes the bridge admittance a 3×3 matrix whose (n,m) element represent the velocity in the m^{th} direction in response to excitation in the n^{th} direction. The admittance matrix is symmetric because of reciprocity. Measurements of this full matrix are reported in [58] and [59]; however, for the purpose of this study only a 2×2 matrix is used, which represents the vibrations of the bridge in the plane perpendicular to the string axis. The third dimension is coupled to the longitudinal vibrations of the string and is only briefly discussed in Sec. 2.2.4. The 2×2 admittance matrix is defined as

$$\begin{bmatrix} V_{M,X} \\ V_{M,Y} \end{bmatrix} = \begin{bmatrix} Y_{M,XX} & Y_{M,XY} \\ Y_{M,YX} & Y_{M,YY} \end{bmatrix} \begin{bmatrix} F_{M,X} \\ F_{M,Y} \end{bmatrix}, \tag{2.13}$$

in which the X-direction is defined as normal to the plate for the guitar, and tangent to the bridge-crown for the violin. The Y-direction is perpendicular to both the X-direction and the string axis (see Fig. 2.4). F_M and V_M are force and velocity at the bridge respectively; all the terms of Eq. (2.13) are functions of frequency.

To include the two-dimensional motion of the bridge it is necessary to consider an additional property for each mode, θ_{Mk}, that is defined as the angle of the principal direction of bridge motion in that mode with respect to the X-direction (see Fig. 2.4). Similar to the case for M_k, this spatial angle varies from one location to another. That said, it has been shown in Fig. 7 of [60] that the admittance does not vary by much when measured at the resting point of the six strings of a guitar; therefore if the exact modeling is not intended, the admittance measured for one string can be used in the model of other strings as well. The same argument applies to a violin/cello, but this time the X-direction represents the tangent-to-the-bridge-crown direction, so it varies from one string to another. This is consistent with the way that bow angle changes when different strings are bowed (see Figs. 13 and 14 of [61]). Rewriting the bridge admittance equation for the two dimensional case results in

$$\begin{aligned} Y_M &= \begin{bmatrix} Y_{M,XX} & Y_{M,XY} \\ Y_{M,YX} & Y_{M,YY} \end{bmatrix} \\ &= \sum_k \begin{bmatrix} \cos^2\theta_{Mk} & \cos\theta_{Mk}\,\sin\theta_{Mk} \\ \cos\theta_{Mk}\,\sin\theta_{Mk} & sin^2\theta_{Mk} \end{bmatrix} \frac{i\omega}{M_k(\omega_k^2+i\omega\omega_{Mk}/Q_{Mk}-\omega^2)}. \end{aligned} \tag{2.14}$$

The next logical extension regarding the bridge admittance is to relax the assumption

that the modes are real. Real modes are a physical consequence of the proportional damping assumption, meaning that the damping matrix can be written as a linear combination of the mass and stiffness matrices. In reality, however, there is no good reason to make this assumption; damping proportionality is rather a mathematical convenience. In fact, for the case of the stringed instruments, several mechanisms with vastly different natures are contributing to the total damping of the structure (namely the internal damping in parallel- and cross-grain- directions of the wood, coupling to the body of the player, and the frequency-dependent radiation damping), therefore, it should not come as a surprise to learn that the body modes are strongly complex. A more general version of Eq. (2.14) that accommodates complex mode-amplitudes is

$$Y_M = \sum_k \begin{bmatrix} \cos^2\theta_{Mk} & \cos\theta_{Mk}\,\sin\theta_{Mk} \\ \cos\theta_{Mk}\,\sin\theta_{Mk} & \sin^2\theta_{Mk} \end{bmatrix} \frac{1}{\Re e\,\{\Omega_{Mk}\}} \left(\frac{\Omega_{Mk} a_k}{i\omega - i\Omega_{Mk}} + \frac{\Omega^*_{Mk} a^*_k}{i\omega + i\Omega^*_{Mk}} \right), \tag{2.15}$$

where a_k is the equivalent of $1/M_k$ for complex modes, Ω_{Mk} is the k^{th} complex natural frequency defined as $\Omega_{Mk} = \omega_{Mk}\,(1 + i/Q_{Mk})$, and superscript * stands for complex conjugate.

In the remainder of this section the coupling of a string with the body modes is studied. The simpler problem of a single string mode coupled with a single body mode that is perfectly aligned to the former is considered first, then the more complicated case where the string and body modes are not perfectly aligned is discussed. Ultimately the vibrations of the sympathetic strings are added to the picture. The body modes are considered real within the discussion of this section, but this assumption will be relaxed in Sec. 2.3.4.

Coupling of a single string mode to a single body mode

Consider for the moment that the string only vibrates in one polarization and that the body consists of only a single mode that is lightly coupled to the string. From the string's perspective, the bridge acts like a spring below its resonant frequency, a damper at resonance, and a mass above its resonance. As a result, it moves in-phase with the exerted force below the body resonance, and out-of-phase with it above the resonance. The general effect would be increasing and decreasing the effective length of the string, respectively. When the two frequencies coincide, the main effect is to add to the effective damping of the string. The multi-resonance nature of the body can be taken into account by simply adding the effect of each individual mode to find the net perturbation to the string.

While that initial intuitive explanation is true if the string is lightly coupled to the body mode, a more general understanding of the system can be obtained by considering the combined vibrations of the string and the body as two coupled modes rather than individual

string and body modes. For instance, in the special case that neither of the systems is damped, and when the unperturbed frequency of the two systems coincides, the two coupled modes are linear combinations of the uncoupled string and body modes, vibrating either in- or out-of-phase with respect to one another.

For a more quantitative measure, consider a string of mass per unit length m_s, unperturbed n^{th} modal frequency ω_n and Q value of Q_n, vibrating in a single polarization and coupled to the k^{th} body mode with an unperturbed resonant frequency of ω_{Mk}, a Q value of Q_{Mk}, and an effective mass M_k at the point of string support. Gough [62] showed that to the first order of $1/Q_n$ and ψ^4 (defined in Eq. (2.18)), the frequencies of the two coupled normal modes can be obtained from

$$\Omega_{\pm}^2 = \omega_{+}^2 \pm \left(\omega_{-}^4 + \psi^2\right)^{1/2}, \tag{2.16}$$

where

$$\omega_{\pm}^2 = \frac{1}{2}\left[\omega_{Mk}^2 \pm \omega_n^2 + i\left(\frac{\omega_{Mk}^2}{Q_{Mk}} \pm \frac{\omega_n^2}{Q_n}\right)\right], \tag{2.17}$$

and ψ is a measure of the coupling strength calculated from

$$\psi^2 = \left(T_0 \frac{n\pi}{L}\right)\frac{2}{m_s L M_k}. \tag{2.18}$$

The real parts of Ω_+ and Ω_- represent the frequencies of the normal modes and their imaginary parts are the damping of the normal modes. If the unperturbed natural frequency of the string and the body coincide (i.e $\omega_n = \omega_{Mk}$), Eq. (2.16) reduces to

$$\Omega_{\pm}^2 = \omega_{Mk}^2 + i\frac{\omega_{Mk}^2}{2Q_+} \pm \sqrt{\psi^2 - \left(\frac{\omega_{Mk}^2}{2Q_-}\right)^2}, \tag{2.19}$$

where

$$\frac{1}{Q_\pm} = \frac{1}{Q_{Mk}} \pm \frac{1}{Q_n}. \tag{2.20}$$

Equation (2.19) implies that when the unperturbed frequencies of the string and the body modes coincide, depending on the strength of the coupling two categorically distinct cases may happen:

1. If the difference between the loss factors of the unperturbed string mode and the body mode is small compared to the coupling strength, the expression inside the square root in Eq. (2.19) will have a positive real part; as a result, the two normal modes of the system will split in frequency and will be equally damped (its value defined by the

second term in the right hand side of Eq. (2.19)). This phenomenon is called strong coupling or "veering". As typically the unperturbed body mode is much more heavily damped than the string mode, in the veering case both coupled modes will roughly have a Q factor twice the Q factor of the unperturbed body mode. This equal split of damping between the two modes is consistent with Rayleigh's calculation of modal damping [63].

2. If the difference between the loss factors of the unperturbed string mode and the body mode is large compared to the coupling strength, the expression inside the square root in Eq. (2.19) will have a negative real part; as a result, the frequencies of the two normal modes of the system almost[7] cross at the coincidence point and their damping will remain vastly different. In this case, the two modes maintain their predominantly string-like or body-like character, even in the vicinity of the crossing frequency [62]. This condition is called weak coupling or "non-veering".

A useful non-dimensional measure to define which one of the above cases happens is

$$K = 2\psi Q_- / \omega_{Mk}^2 \approx \frac{2Q_{Mk}}{n\pi}\sqrt{\frac{2m_s L}{M_k}}. \tag{2.21}$$

$K > 1$ identifies "veering", and $K < 1$ identifies "non-veering".

The typical behavior for the frequency and damping of the coupled modes for veering and non-veering cases are illustrated in Figs. 2.5a and 2.5b respectively. It was shown in [39] that for a classical guitar, veering only occurs for some string modes below 300 Hz; this implies that any realistic string model should be able to account for the non-veering case as well.

It should be noted that if the string damping is negligible compared to the body damping, the nature of the coupling is essentially defined by the damping of the body mode. Mathematically speaking, Q_- can be approximated by Q_{Mk} as is shown in Eq. (2.21). Also keep in mind the limitation of using Eq. (2.19), that is $1/Q_n$ and ψ^4 should remain small. If this assumption does not hold, it is advisable to use a more precise formula derived from transmission line theory [64, 62]. The use of transmission lines to describe the vibrations of musical strings is extensively discussed in Chap. 4.

[7] "Almost" comes from the fact that if Ω_+^2 and Ω_-^2 are different only by an imaginary amount, Ω_+ and Ω_- will be different by a complex amount. The actual crossing happens at slightly above the coincidence point.

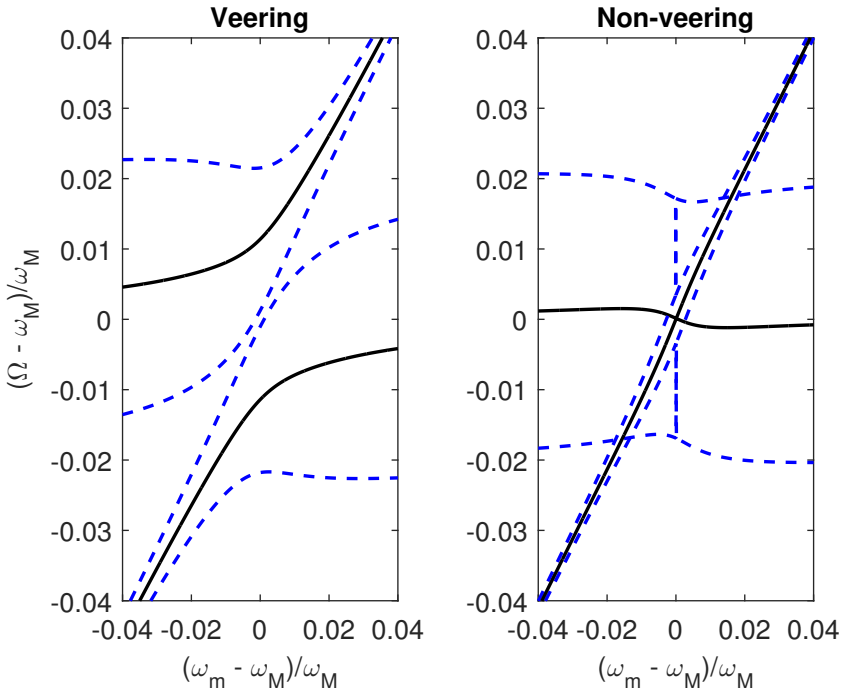

Fig. 2.5 Veering (a) and non-veering (b) behavior in a simple model of one string mode coupled to one body mode. The uncoupled body mode has a fixed frequency of 460 Hz and a Q factor of 25, while the uncoupled string mode has a Q factor of 1000 and a frequency varying over a small range. The variation of the coupled mode frequencies is plotted against the normalized difference of the two uncoupled modes. The solid lines show the frequencies of the coupled modes, and the dashed lines show plus/minus half bandwidth (recall that bandwidth is a measure of damping).

Dual-polarizations of a string

Angular dependence of the bridge admittance breaks the symmetry of the string's two transverse polarizations. The string polarization aligned with the principal direction of the body mode gets coupled, hence its frequency and Q factor are perturbed. It also efficiently transfers energy to the body and radiates relatively strongly. The uncoupled polarization, on the other hand, remains almost intact. Vibrations of the string in this uncoupled polarization may only radiate weakly through other body modes which fall close in frequency but are aligned differently from the main body resonance in question [60].

Another consequence of the angular dependence of the bridge admittance is that the excitation of the string in one polarization (labeled X' in Fig. 2.4) eventually leads to its motion in its perpendicular polarization. Off-diagonal terms of the admittance matrix, rotated by a proper amount, are the ones responsible for this effect. A proper amount of rotation for this matter can be obtained by replacing θ_{Mk} with θ'_{Mk} in Eq. (2.13). Assuming the coupling of the string to the k^{th} structural mode and looking at Eq. (2.14), it becomes immediately obvious that there will be no coupling if the angle between the initial excitation and the principal direction of mode k (i.e. θ'_{Mk}) is an integer multiple of 90°. In practice, there are always multiple body modes participating to the overall admittance in a particular frequency, hence the off-diagonal terms will have non-zero values at all frequencies. Also if the more general case of complex modes is considered, both polarizations of the string are coupled to the body, even if only weakly, regardless of the excitation direction. The reason is that for a complex mode the bridge notch sweeps an elliptical path rather than traversing back and forth along a line.

Rolling of the string at the boundaries

In some instruments, such as the violin, open strings are supported in V-shaped grooves at both ends (i.e. the bridge and the nut), therefore their torsional motion is inhibited at those boundaries. However, for the case of the guitar bridge (or the frets for stopped notes), the string is free to rotate at its boundaries. This slight rolling increases the effective length of the string for the polarization parallel to the top plate but not for the polarization normal to it. As a result, the two polarizations vibrate with slightly different natural frequencies, even in the absence of the body coupling. This effect provides another mechanism for breaking the rotational symmetry of the string.

It was shown in [60] that for a guitar, the difference of effective lengths in the two polarizations is of the same order as the diameter of the strings. It was also shown that this effect outweighs perturbations of the string frequencies due to the coupling to the body modes

in most cases. The difference in the effective length of the two polarizations is consistent across all modes of the string, therefore, the total effect would be two sets of distinct string partials. Such rolling may also act as an additional source of damping due to a partial conversion of the transverse waves to the torsional ones.

Sympathetic strings

On most stringed instruments, several strings are supported on a common bridge and are coupled to one another through that path. Although coupling happens between all such strings, the effect is much stronger if the strings are harmonically related (i.e. are unison or sympathetically tuned). This effect has been known to instrument makers for a very long time, as is evident by the existence of sympathetic -but non-played- strings in many ancient instruments such as the Norwegian Hardanger fiddle, the Indian Sarangi, or the Persian Rubab. Sympathetic strings can create a number of interesting musical effects, most notably the multi-stage decay of slightly mistuned unison piano doublets and triplets (famously discovered by Weinreich [65]). Coupling also happens between the differently but sympathetically-tuned piano strings, an effect which some modern composers have utilized in their compositions. The technique is to press a key and to push the sustaining pedal while the played key is still held down (listen for an example to the ending of Territoires de l'oubli by Tristan Murail).

Sympathetic strings are also significantly coupled in bowed instruments. The existence of such coupling can be demonstrated by a technique experienced players use to create a semi-vibrato effect when playing on an open string (particularly on the lowest string). To produce this effect, the player places his finger on the adjacent higher-pitched string, at a position corresponding to a note an octave above the bowed note (i.e. with double the frequency). As the player moves his finger backwards and forwards the intensity of the played note is modulated at twice the rocking frequency of the finger. The effect is very similar to an actual vibrato being played on a stopped string, likely because a regular vibrato also involves significant amount of amplitude modulation as well as the expected frequency modulation [66, 37]

Gough studied the theory of two strings coupled through a common end support in some detail [62]. Assuming a non-resonant bridge response, the modes of the coupled system will be the in-phase and out-of-phase movement of the two strings. For the case of identical and similarly-tuned strings, the out-of-phase mode of the strings does not involve any motion of the common support (as the force applied by one string gets canceled by the force from the other), therefore one normal mode would always occur at the unperturbed frequency of the strings, and with a Q factor corresponding to their intrinsic damping. The in-phase mode

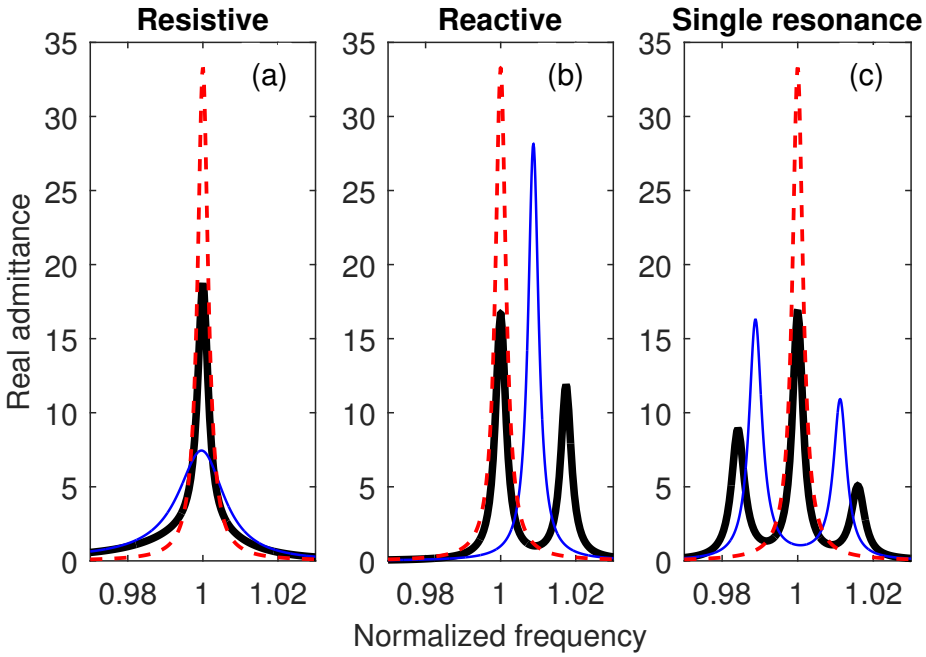

Fig. 2.6 Schematic admittance curves (real part only) of the string, $1/10^{th}$ of the string length away from the bridge. The (red) dashed curve shows the admittance for a single string with rigid terminations, the (blue) thin solid curve shows the admittance for the same string but when the end termination is flexible, and the (black) thick solid curve is the string admittance when an identical string is supported on the flexible bridge as well. Case (a) is for a purely resistive end support, case (b) is for a purely reactive end support, and case (c) is when the end support is a resonator tuned at the unperturbed natural frequency of the strings.

of the strings will involve an even larger motion at the common support (compared to the case of a single string). If the end support is purely resistive this in-phase mode happens very close to the unperturbed frequency of the strings but is damped more strongly. On the contrary, if the end-support is purely reactive the frequency of the in-phase mode would be perturbed but its Q factor remains almost intact. In reality, the body modes falling close in frequency to the string modes define the nature of coupling at the bridge, which is a combination of both resistive and reactive components. Figure 2.6 shows the real part of the admittance of a typical string, evaluated at a position $1/10^{th}$ along its length and when it shares with an identical string an end support that is (a) purely resistive, (b) purely reactive, and (c) a perfectly tuned body resonance.

Strings' after-length and the tailpiece

The after-length is the segment of a string for instruments of the violin family that extends beyond the bridge and reaches the tailpiece. The after-lengths roughly measure to $1/10^{th}$ of the open strings' length hence their first natural frequency is around 10 times higher. To the first order of approximation, after-lengths are coupled to one another and to the singing lengths of the strings through the common bridge, much the same way that the singing strings are coupled to one another. The primary effect of the after-lengths (as far as a bowed/plucked string is concerned) is to add some high-frequency sharp local resonances to the effective bridge admittance. One can also imagine some amount of energy channeling through the bridge and passing directly from the singing length to the after-length of the same string (and vice versa), making use of the stiffness and the torsion of the string (the latter being only possible if the string is allowed to roll on the bridge). After-lengths also create a path through which the resonances of the tailpiece can affect the bridge admittance. For the violin (and likely for the cello as well) the rotation of the tailpiece around the normal to the plate axis falls slightly above the wolf region and matches the bowing direction. If accurately tuned with an added mass, this resonance can interact with the body modes in that range and affect the playability of the instrument to some extent.

An after-length becomes particularly important if a wolf eliminator is installed on it, in which case the mass of the wolf eliminator lowers the fundamental of the corresponding after-length to the frequency of the wolf note. The wolf eliminator should also add to the damping of the after-length, otherwise it only moves the wolf to another frequency.

2.2.4 Nonlinear vibrations of a string

The linearity assumption made so far is only justified for small-amplitude vibrations of the string. For larger amplitudes, the transverse displacement significantly changes the effective length of the string, hence its tension. This fluctuating change in tension creates an excitation force on the bridge in the longitudinal direction of the string. Strong longitudinal vibrations of the string may also feed back into its transverse vibrations. For a normal pluck on a nylon guitar string, the longitudinal bridge force is roughly 40 times smaller than the amplitude of the transverse force. The amplitude of the longitudinal excitation grows with the square of pluck strength, hence grows faster than the transverse excitation for stronger plucks. The longitudinal excitation also depends on the Young's modulus of the string; therefore, for a steel-string guitar the longitudinal and transverse excitations are more nearly equal [67]. One would expect that for a cello string the ratio of the two falls somewhere in between.

Arguably, the most musically-relevant consequence of the string's tension alteration is the "pitch glide": a slight sharpening of the pitch for large-amplitude vibrations. Pitch glide increases with the square of the string's transverse vibration amplitude. This effect is most noticeable in the sound of a strongly plucked string for which the string starts at a higher pitch, but the difference with the nominal pitch drops almost exponentially as the amplitude of the string vibration reduces due to losses.

Getting back to the general problem of the nonlinear string vibrations and ignoring the losses, dispersion, and the coupling to the body for the moment, the equation of motion for the longitudinal displacement of the string (shown by ξ) becomes

$$m_s \frac{\partial^2 \xi}{\partial t^2} = ES \frac{\partial^2 \xi}{\partial x^2} + \frac{1}{2} \frac{\partial \left(\frac{\partial y}{\partial x}\right)^2}{\partial x}, \tag{2.22}$$

and the equation of motion for the single-polarization transverse vibrations of the string takes the form

$$m_s \frac{d^2 y}{dt^2} = T_0 \frac{d^2 y}{dx^2} + ES \frac{\partial \left\{ \frac{\partial y}{\partial x} \left[\frac{\partial \xi}{\partial x} + \frac{1}{2} \left(\frac{\partial y}{\partial x}\right)^2 \right] \right\}}{\partial x}. \tag{2.23}$$

The last term in both equations is the nonlinear coupling term [68], and S is the cross-sectional area of the string. Note that in general these coupling terms are functions of both time and position. The tension of the string is also a function of both variables and it can be found from $T = T_0 + ES \left[\frac{\partial \xi}{\partial x} + \frac{1}{2} \left(\frac{\partial y}{\partial x}\right)^2 \right]$. However, if the inertial term (i.e. the left hand side) of Eq. (2.22) becomes negligible, a special case occurs for which the tension can be considered uniform along the string. This approximation is justified as long as the frequency

of the first longitudinal mode of the string is much higher than the frequency of the first transverse mode, and/or if the transverse vibrations of the string do not contain significant components that when doubled fall close, or above the first longitudinal mode. It has been shown in the appendix of [68] that if the spatially uniform tension approximation applies, the longitudinal excitation force at the bridge (i.e. $(T - T_0)$ at the bridge) will only contain components with double the frequency of the transverse vibrations (resulting from each n^{th} transverse mode acting on itself and exciting the $2n^{th}$ longitudinal mode). This can be intuitively explained by the fact that the string's elongation due to a particular sinusoidal transverse mode is indifferent for two consecutive half-periods of the transverse vibration. Care should be taken not to confuse the spatially uniform tension approximation with zero longitudinal displacement of the string elements. Indeed, for the spatially uniform tension approximation to hold, the string must vibrate in the longitudinal direction, precisely in a fashion (corresponding to its $2n^{th}$ longitudinal mode) that compensates for the spatially varying stretch that the transverse vibrations puts the string through. That is also why the inertia of the string for longitudinal vibrations should remain negligible for the spatially uniform tension approximation to hold, otherwise such vibrations would require a net force acting on each element of the string along its length, thus a gradient of tension along the string.

For a perfectly flexible string, whose partials are perfectly harmonic, these double-frequency terms fall on top of the main transverse partials hence they cannot be distinguished, nor can they have noticeable auditory consequences because of the masking effect. However, as was shown in Sec. 2.2.2, real strings have some degree of bending stiffness, and a consequent inharmonicity. As the inharmonicity grows with the partial number, the double-frequency terms will create a shadow set of partials with one-fourth the inharmonicity of the main partials and can be distinguished (one-fourth comes from the fact that inharmonicity grows with the *square* of the partial number).

If the spatially uniform tension approximation does not apply, the longitudinal string modes are going to be excited by many more terms. More precisely, the l^{th} longitudinal mode is excited by the interactions of transverse modes n and $l - n$ as well as n and $l + n$ in their sum and difference frequencies (a result of a second-order nonlinearity) with n and l being natural numbers. The longitudinal mode l responds most strongly to the mixing terms that have frequencies close to its natural frequency, which gives a measure to identify the nonlinear terms that tend to dominate. For instance, most of the strong odd nonlinearly-excited partials originate from adjacent parents (e.g. from the interaction of f_5 and f_6 rather than f_4 and f_7) as those parents couple through the first longitudinal string mode that has a lower frequency and has a better chance to fall close to the frequency of the mixing term

(around f_{11} in this example).

Because of the inharmonicity and based on the same argument mentioned for the double-frequency terms, the frequency of the components originating from n and $n+l$ parents fall slightly above f_l and f_{l+2n} (for the difference and sum respectively), and the frequency of the components originating from n and $l-n$ parents fall slightly below f_l and $f_{|2n-l|}$. This creates a cluster of peaks around the original transverse modes that sometimes makes them hard to identify or analyze in measured data (an example can be found in the extraction of a string's frequency-dependent damping in [60]).

A further complicating factor is that, as was shown in Sec. 2.2.3, the modal frequencies for the n^{th} transverse modes for the two polarizations are slightly different (say $f_{n,1}$ and $f_{n,2}$) so their interactions with $f_{m,1}$ and $f_{m,2}$ (two polarizations of the m^{th} transverse mode) creates four sets of combinations rather than one. This form of cross-coupling requires some amount of coupling between the two polarizations, which does exist (at least for the reasons mentioned in Secs. 2.2.3 and 2.2.3), and their presence results in a further smearing of the side-bands around the original transverse peaks.

For the purpose of modeling, Bank and Sujbert classified the nonlinear vibrations of a string into five different regimes based on the norm of the string's slope at the bridge ($\|\partial y/\partial x\|$, representing the strength of the excitation), and the ratio of the longitudinal fundamental frequency to the transversal fundamental frequency in the linear case (f_0'/f_0 equal to $\sqrt{\frac{ES}{T_0}}$). Figure 2.7 shows the boundaries of these regimes, the term "significant" used in the following discussion is defined as falling within 10% of the maximum value.

- **"Linear"**, in which the amplitude of excitation is so small that the transverse and longitudinal vibrations of the string can be considered independent. In this case, essentially the string nonlinearity does not need to be taken into account.

- **"Even phantoms"**, in which tension variation is significant compared to the transverse bridge force but is still small compared to the initial tension of the string. The former implies that the sound produced by the longitudinal excitation at the bridge may make a perceptible contribution to the total radiated sound of the instrument, while the latter implies that longitudinal waves converting back to transverse waves may not noticeably affect the transverse vibration of the string. It also means that there will be no significant pitch glide present in the sound of the instrument. As for the modeling, one possible approach is to calculate the string's elongation in each time step and use the calculated tension alteration to excite the bridge in the string's longitudinal direction. This force contributes to the excitation of the body modes, assuming the full 3×3 bridge admittance is included in the model.

- **"Tension modulation"**, that is similar to the "even phantoms" regime in that the tension variation can still be considered spatially uniform, but is different in that the tension variations is no longer negligible compared to the static tension of the string, thus affects the transverse vibration as well. The result is a significant pitch glide; non-planar motion of the string giving rise to its whirling (or orbital) motion [69, 70], as well as the eventual appearance of the partials that were originally absent from the vibrations of the string (e.g. the third partial for a string plucked at $1/3^{rd}$ along its length) [71], although this latter requires some degree of flexibility at a termination point to happen. Variable length delay lines were proposed [72] to include this effect into the traveling wave scheme although energy conservation consideration should be taken into account to avoid instability and to maintain the link to physical reality.

- **"Longitudinal modes"**, in which the transverse vibrations contain frequencies that when doubled, fall close, or above the frequency of a longitudinal mode. The dynamic change of tension can excite the longitudinal modes close to their resonances, therefore the tension will no longer be spatially uniform along the string [73]. As a consequence, the bridge force will have more components than the double-frequency terms. Similar to the case for the "even phantoms" regime, in this regime the tension variation is significant compared to the transverse force at the bridge, but is small compared to the static tension of the string. Therefore, the longitudinal excitation at the bridge is significant but the back-coupling to the transverse vibrations is not so. Again, similar to the "even phantoms" regime, a computationally efficient and physically valid way to deal with this situation is to solve the transverse string vibrations in the linear regime and then excite the bridge in the longitudinal direction by a proper amount computed in each time step. Although for this vibration regime the dynamics of the longitudinal modes should be taken into account, extra elements would be needed to model the longitudinal modes and it would not be as straight forward to find the net excitation on each of those.

- **"Bi-directional coupling"** is the final case, in which the transverse and longitudinal vibrations become fully coupled and the tension variation becomes significant compared to the string's static tension. An approach to model this regime is proposed in [74], in which they first solve the model assuming a spatially uniform tension (same as "tension modulation" regime) and then make corrections to the tension by adding the effect of the significantly contributing longitudinal modes, for which they used a modal model.

Bank and Sujbert's definition of *significant* leads to the transition from spatially-varying to spatially-uniform tension distribution occurring when the ratio of the first longitudinal

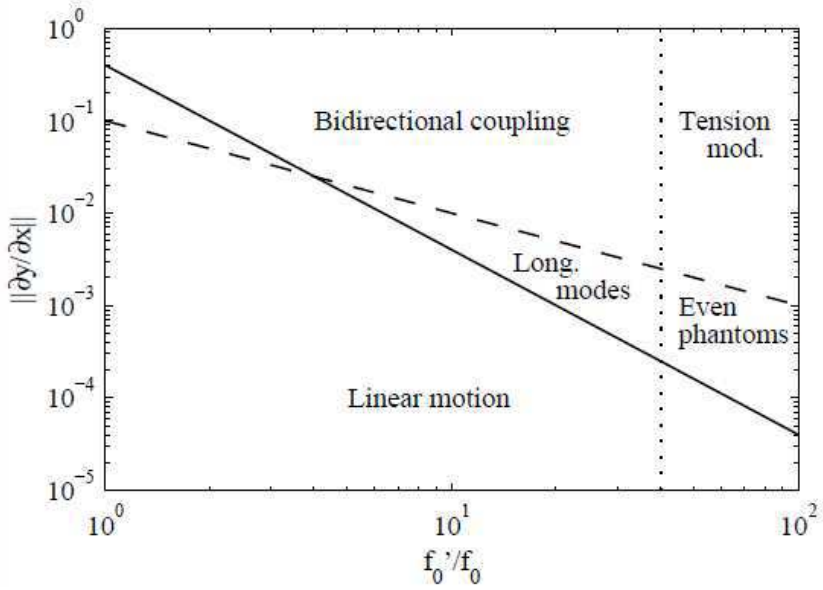

Fig. 2.7 Map of nonlinearity classes, where different nonlinear regimes are outlined as a function of the slope at the bridge and as a function of the ratio of the (linear) longitudinal and transverse fundamental frequencies. (From [74])

mode frequency to the first transverse mode frequency becomes 40 (the exact number may vary based on the nature of the excitation as well as the limit set to define "significant"). Such a high limit is hardly reached by real musical strings unless their tension is intentionally lowered from its nominal value. This ratio is about 3 to 5 for a nylon guitar string and ranges from 10 to 20 for metal strings [74]; as a result, "tension modulation" and "even phantoms" regimes discussed above would realistically not be the case. In this regards, modeling techniques developed to deal with these regimes are only useful for qualitative studies or to give the listener a flavor of their auditory consequences. For the purpose of making a physically accurate model, however, it makes more physical sense to choose a scheme that can deal with "longitudinal modes" and/or "bidirectional coupling" regimes; otherwise, one would end up keeping some terms and neglecting the others which are of the same order of magnitude. If the accurate modeling of the nonlinear string vibrations is intended it might make more sense –both physically and computationally– to use alternative schemes such as modal synthesis or finite difference, in place of the traveling-wave approach.

The arguments in this section were based on the assumption that the string is terminated at rigid boundaries. If that is not the case, the string mode shapes may vary in a sense that the bridge no longer falls on their nodes (as was discussed in Sec. 2.2.3). This creates a path to couple the string modes, which were otherwise orthogonal and non-interacting [71]. The strength of such coupling is proportional to the ratio of the string's characteristic impedance

to the imaginary part of the bridge impedance in the corresponding transverse direction. It has been confirmed for piano strings that the nonlinear terms generated by the above mechanism are negligible in comparison to the components that can also be produced by a rigid bridge approximation [68]; however, it is conceivable that the nonlinear terms generated by the flexible bridge play a more significant role in the case of a guitar or a cello.

Another source of nonlinear force acting on the bridge, ignored so far, is the inclined after-length of the strings. The fluctuating component of the string tension passes through the bridge to the after-length (either by sliding through the bridge notch or by slightly moving the bridge), it then applies a force in the direction normal to the plate and with a magnitude equal to the fluctuating part of the tension projected normal to the plate. As opposed to the nonlinearities mentioned before, which were in the third order of the initial excitation amplitude, this new nonlinearity behaves in the second order of the initial excitation amplitude [71].

Aside from the nonlinear mechanisms, a flexible bridge can result in a linear coupling of the longitudinal and transverse string modes through the off-diagonal terms of the 3×3 bridge admittance matrix. Such linear coupling may also happen through the nut and tailpiece, if a body mode shape involves those two points moving apart from one another in the string's axis (e.g. think of the whole instrument bending longitudinally). Finally, the longitudinal vibrations of the string can be linearly excited directly by the player if the excitation force is not perfectly perpendicular to the string (e.g. produced by skewed bowing). To simulate the longitudinal motion of the string excited by any of these linear mechanisms it can be simply treated by the traveling-wave approach, the same way that the transverse vibrations were treated.

2.3 Modeling of a plucked string

Different physical details involved in the vibrations of a plucked string were discussed in the previous section. In this section, implementation of some of those details into the simulations and the extraction of relevant parameters are discussed. In accordance with the primary focus of this study, the parameters are measured for the cello, however some parameters are measured for the guitar as well. Longitudinal vibrations of the string, after-lengths, and the string's nonlinear vibrations are not included in the current version of the model. As for the dispersion, a hinged boundary condition is assumed for all strings and the quasi-evanescent waves are also ignored.

2.3.1 Measuring the string properties

Valette's frequency-dependent model, earlier discussed in Sec. 2.2.1, is used to simulate the string's damping. Recall that Valette's model considers the net effect of the viscous damping of the surrounding air, viscoelasticity and thermoelasticity of the string material, and the internal friction. Viscoelasticity and thermoelasticity both manifest themselves by creating a complex Young's modulus, which comes into the equation of motion through the bending stiffness term, whose significance increases with the square of the frequency. Aerodynamic loss and internal friction can be cascaded in the form of a complex tension. Putting those considerations into mathematical form, the Q factor of the string's n^{th} mode can be calculated from

$$Q_n = \frac{T_0 \; + \; EI(n\pi/L)^2}{T_0\left(\eta_F + \frac{\eta_A}{\omega_n}\right) + EI\eta_B(n\pi/L)^2}, \tag{2.24}$$

where η_F, η_A ,and η_B are the coefficients determining "friction", "air" and "bending" damping respectively [5]. The common way to estimate these three coefficients is to treat them as variable parameters to fit Eq. (2.24) to the measured Q factors for a particular set of string resonances. Alternatively, a crude theoretical approximation for the air damping can be found in Sec. 2.13.1 of [67], in which the air flow is assumed non-turbulent and the dissipation is assumed purely viscous. η_B may also be estimated from the complexity of the Young's modulus for the string's material, which is a more general property and independent of the string's geometry. However, there is no easy way to apply the latter to over-wound strings, and even for a mono-filament string, the complexity of the Young's modulus may itself be a function of frequency and the string's tension. Once the parameters are identified, the required gain of the loop filters for either side of the string and at each frequency can be calculated based on Eq. (2.7) and filter design methods can be applied to design a pair of loop filters.

In this regard, the Q factors of the first 30 modes were measured for 7 sets of nominally-identical "D'Addario Kaplan Solutions" cello strings (model KS510 4/4M). The measured Q factors for each string mode were later averaged to minimize the effect of manufacturing variations in addition to the noises present both in data collection and in damping extraction (the set of Q factors was provided by Fan Tao of D'addario). The measurements were made on a rigid granite base so that the results only correspond to the intrinsic damping of the strings. The unknown parameters of Eq. (2.24) were then estimated by manually fitting that equation to the averaged set of measured Q factors. As any deviation of the boundaries from being perfectly rigid results in an added damping, the fit is made to the ceiling of the

measured Q factors. Both measured and fitted data are illustrated in Fig. 2.8; the plus/minus one standard deviation is also included, which indicates the variability of measurements and the Q factors are plotted in logarithmic scale to make the details visible over all frequencies. The parameters used to make the fits in Fig. 2.8 as well as other string properties are summarized in Table 2.1.

Table 2.1 Measured and estimated properties for a set of D'Addario Kaplan Solutions cello strings. All parameters are relevant to the transverse vibrations, and the effective length of the open strings is assumed to be 690 mm.

Tuning			A_3	D_3	G_2	C_2
Frequency	f_0	Hz	220	146.8	98	65.4
Tension	T_0	N	171	135.9	135.5	131.5
Mass/unit length	m_s	g/m	1.85	3.31	7.40	16.14
Bending stiffness	EI	$10^{-4}N/m^2$	3.26	2.48	1.88	6.20
Inharmonicity	B	10^{-6}	39.5	37.9	28.7	97.8
Characteristic impedance	Z_{0T}	Kg/s	0.56	0.67	1.00	1.46
Loss coefficients	η_F	10^{-5}	22	23	20	12
	η_B	10^{-2}	11.4	12.5	13	4.7
	η_A	1/s	0.12	0.11	0.04	0.07

The general trend and value of Q factors looks almost identical across the four cello strings, when plotted against the string mode number (as opposed to the string mode frequency). As is evident in Fig. 2.8, Valette's proposed relation gave a relatively better fit to the Q factor trend of the C_2 and G_2 strings rather than the D_3 and A_3 strings. For the D_3 and A_3 strings the drop of the Q factors beyond their peak value is steeper than it is predicted by the Valette's relation. Across all strings, the highest Q factor occurs at the second or the third mode, with the maximum values ranging from 1200 to 3000 (C_2 string was the least damped). This observed trend of Q factors for cello strings is significantly at odds with the ones earlier reported for guitar strings [60, 5]: for guitar strings (both nylon and steel) the highest Q value normally occurs at around the 10^{th} mode, whereas for a cello string the maximum Q is typically observed at the second or the third mode. In those earlier studies the strings were not mounted on a rigid base, rather, their inherent loss factors were calculated by making a fit to the floor level of the loss factors for all string modes when a full octave was played on the same string mounted on an actual guitar.

To further investigate this observation, a full set of steel guitar strings as well as three treble nylon guitar strings (i.e. G_3, B_3, E_4) were mounted on a rigid base shown in Fig. 2.9.

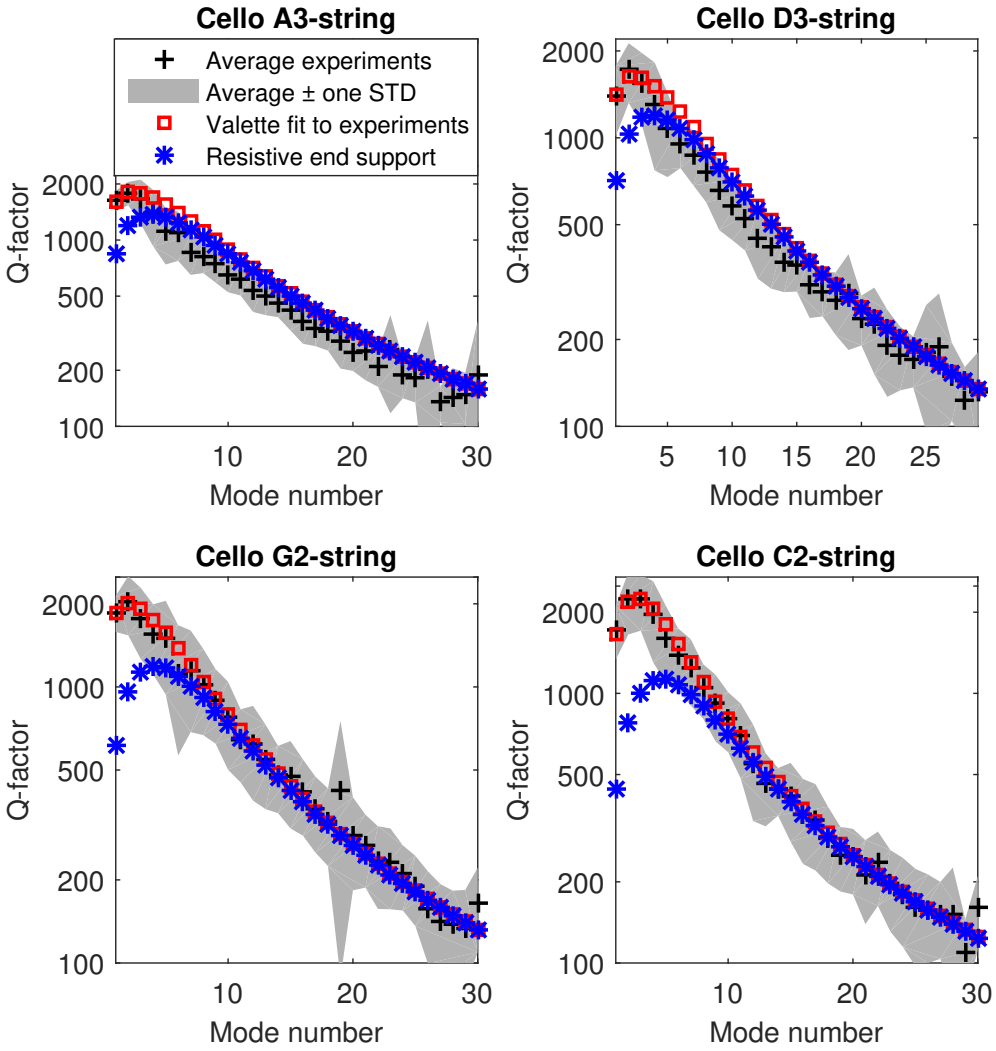

Fig. 2.8 Average Q factor (plus signs) plus/minus one standard deviation (grey shade) for D'Addario Kaplan Solutions cello strings. The red squares show the fitted curve to the measured data, and the stars show what happens to the squares if the strings' rigid end termination at the bridge was turned into a purely resistive end support with an impedance equal to 500 Ns/m that is roughly the maximum impedance for a cello bridge admittance in the parallel-to-the-bridge-crown direction (the stars are discussed within the text in Sec. 2.4).

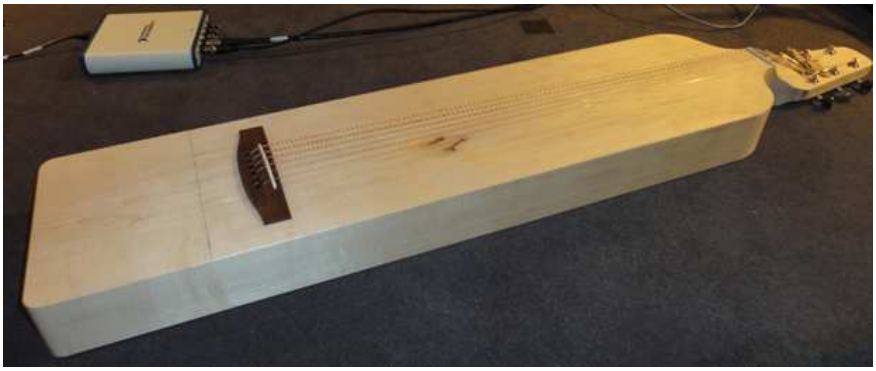

Fig. 2.9 The rigid base used to measure the Q factor of the guitar strings.

The base was a one-piece maple wood weighing around 25 kg (different from the one that cello strings were measured on). The Q factors were subsequently extracted for the first 30 modes of each open string. The steel strings were of model "Cleartone 12-53 Phosphor Bronze", and the nylon strings were of model "Pro-Arté hard tension (EJ46)", both in new condition. A Valette fit to the measured data for the steel D_3 and nylon E_4 strings is shown in Fig. 2.10 (the plus signs). The method used to estimate the frequency of the string modes and their Q factors was first introduced in [75]. The method calculates the short-time Fourier transform of the signal and fits an exponential decay to the height of each harmonic in successive time frames.

The measured physical properties for the steel guitar strings are summarized in Table 2.2. The results in Fig. 2.10 (and the results for all other guitar strings not produced here) show that the trend for the steel guitar strings is, in fact, genuinely different from the trend for the cello strings (assuming both granite and wooden bases have provided adequately rigid terminations). The extracted values for the bending stiffness of all guitar strings are in agreement with earlier measurements reported in [5]; the minor differences in the case of the steel strings can be associated to the fact that different models of steel strings are used in the two studies. The Q factors for the three treble nylon strings are also in fair agreement with the earlier results (the results for the B_3 and G_3 strings are not reproduced here). The most striking difference with the earlier measurements is concerning the range of Q factors for the steel strings: for the recent measurements done on a rigid base the maximum Q values easily reach up to 12,000 and stay well above 5,000 within the range of analyzed string modes, whereas in the earlier measurements the maximum Q was limited to no more than 3000 across all six strings.

The first candidate to explain this discrepancy is the assumption made in the earlier study that the floor level of all string modes represents the intrinsic loss factor of the string

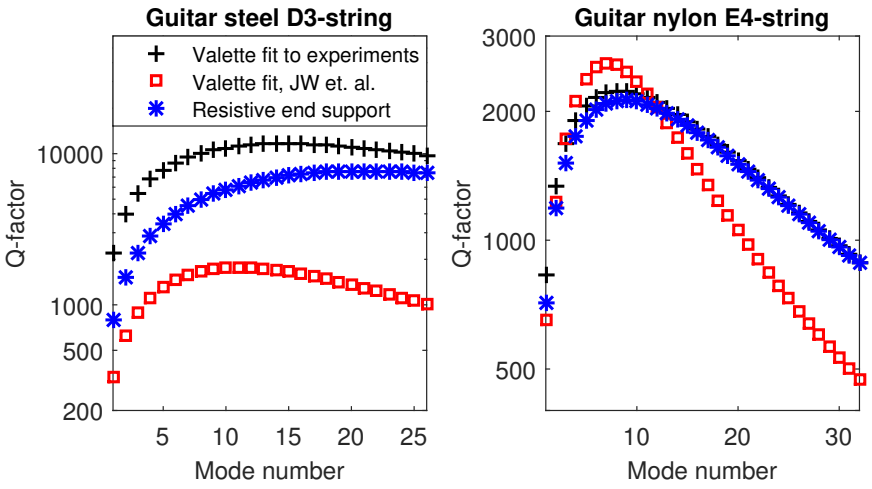

Fig. 2.10 Frequency dependency of the Q factor for open D_3 steel (left), and E_4 nylon (right) guitar strings. Plus signs show the Valette fit to the measured data and the squares are reproduced from [5] showing the Valette fit to the ceiling of all string partials when a full octave was played on the strings mounted on an actual guitar. The stars show what happens to the plus signs if the strings' rigid end termination at the bridge was turned into a purely resistive end support with an impedance equal to 550 Ns/m that is roughly the maximum impedance for a guitar bridge admittance in the normal-to-the-plate direction.

and that the damping introduced by the body coupling is negligible in the vicinity of the body anti-resonances. To investigate this hypothesis, the measured Q factors (shown by plus signs in Fig. 2.10) are modified to include the impact that a purely resistive end support corresponding to the impedance of the guitar bridge in the vicinity of the deepest anti-resonance (roughly of 550 Ns/m magnitude) would have on the Q factors of the string modes.[8] Those re-calculated Q factors are shown by the star signs in Fig. 2.10. As expected the effect is very small for the nylon E_4 string both because a nylon E_4 is only weakly coupled to the body due to its relatively small characteristic impedance, and because its intrinsic loss factor is already relatively large, which makes the share of the body-induced damping almost negligible. The effect for the steel D_3 string is much more pronounced: coupling to the body can account for a large portion of the discrepancy at the first few harmonics, although it certainly may not alone justify such a large gap at the higher frequency range (note that the damping introduced by the end termination is inversely proportional to the string mode number so is less significant for higher string modes). For the lack of a better explanation,

[8] The coupled Q factors are calculated from $\frac{1}{Q_n^*} = \frac{1}{Q_n} + \frac{2Z_{0T}}{n\pi R}$, where Q_n is the Q factor of the n^{th} string mode with rigid terminations, and Q_n^* is its modified value when the same string is terminated at a purely resistive end termination with an impedance R.

the discrepancy can be associated to the differences in the method used to extract the Q factor of the string modes, or the way that the string was stopped at the frets in the earlier measurements.

Table 2.2 Extracted properties for a set of steel guitar strings.

Tuning			E_4	B_3	G_3	D_3	A_2	E_2
Frequency	f_0	Hz	329.6	246.9	196.0	146.8	110.0	82.4
Tension	T_0	N	104.0	103.7	133.7	133.2	128.7	111.0
Mass/unit length	m_s	g/m	0.56	1.00	2.06	3.65	6.29	9.67
Radius	r	$10^{-2}mm$	15.2	20.3	31.7	41.9	54.6	67.3
Bending stiffness	EI	$10^{-6}N/m^2$	86	266	164	280	424	728
Inharmonicity	B	10^{-6}	19.3	59.9	28.6	49.1	76.9	153.2
Characteristic impedance	Z_{0T}	Kg/s	0.24	0.32	0.52	0.69	0.90	1.03
Loss coefficients	η_F	10^{-5}	3	3.5	2.8	2.2	4	4.4
	η_B	10^{-4}	1	1	4	7	3	3.8
	η_A	1/s	0.37	0.22	0.18	0.19	0.12	0.06

One last note on the frequency-dependent Q factor is the case for finger-stopped strings. Even though changing the length of the string (by playing different notes on it) should not change the loss factor versus frequency trend, stopping the string at one end by the finger will introduce a significant amount of damping. This effect is particularly strong for the instruments that do not have frets, such as the instruments of the violin family. The impedance at the termination point of a finger-stopped string is almost purely resistive, so it is not expected to change the effective length of the string by a significant amount. In [76], the damping of a finger-stopped string was compared to one of an open string. Looking at those results one can find that tripling η_F and keeping η_A and η_B unchanged (all with respect to the measured parameters for an open string) provides a practical fit to the damping of the finger-stopped strings; keeping in mind that there is no physical reason that the damping added by finger should match one –or a combination– of the three damping mechanisms considered for an open string. On the bright side, however, any more sophisticated model would still be ad-hoc at best, given the variations of the geometry and physics of the players' fingers, as well as the variation of their left hand techniques.

Using the parameters reported in Table 2.1, the desired gain factor over the full range of frequencies and for each note was calculated by combining Eqs. (2.24) and (2.7). The DC gain was always enforced to be 1 to comply with Eq. (2.4), and for the finger-stopped notes, η_F was tripled. Equation (2.24) naturally limits the Q factor at high frequencies (to

the value of $1/\eta_B$ that would be around 20 for a cello string); however, for practical reasons concerning the filter design procedure, the Q factor was fudged to be no less than 150. This limit was never reached before the 25^{th} mode of the strings; moreover, it will be seen later that the fractional delay filter used for the accurate tuning of the strings adds some damping to the high-frequency range, which compensates, to some extent, for the underestimation of damping in that range.

2.3.2 Adding the damping to the model

After finding the desired gain as a function of frequency for the loop filters, the next logical step is to find a technique to design such filters. The method used here is similar to the one described in [44]: Matlab's *invfreqz* routine is used to design a filter based on the desired amplitude response. Similar to any other phase-sensitive filter design method, *invfreqz* gives its best result in designing a minimum-phase filter; for that reason, a minimum-phase version of the desired amplitude response is made first. This was achieved using the non-parametric method of folding the cepstrum to reflect non-minimum-phase zeros inside the unit circle [44]. The weight function for *invfreqz* is set to $1/f$, and the filter is designed with 1 zero and 300 poles by default. If the initial number of poles results in an unstable filter, the number is changed iteratively until a stable filter is achieved (this method led to stable filters for the first octave on C_2 and D_3 cello strings). 300 poles may seem excessive, but a high-order filter is necessary to ensure a good fit at the first few string modes, particularly for the C_2 string (this issue is further discussed in Sec. 2.4). Admittedly, an FIR scheme was a more physically-appropriate choice to model the damping of a one-sided string, specifically if the body modes are excluded. The concept of IIR filters is based on the closed-loop scheme and an oscillatory behavior of the system to be modeled. That is not the case for a single round trip along a rigidly terminated string. In that regard, several attempts were made to design a proper FIR filter both by truncating the inverse FFT of the desired frequency response and by using matlab's filter design toolbox. Both methods proved to be problematic particularly for the shorter segment of the string, and the fit was never as good as the one obtained by *invfreqz*. It is not claimed here that one cannot design an equally suitable FIR filter for this application.

Subsequently, the designed damping filter was phase-equalized using Matlab's *iirgrpdelay* routine (a 16-order filter is used here). The minimum-phase damping filter and the phase-equalizing filter were then cascaded into an almost-linear-phase damping filter with the desired amplitude response. The phase-equalization may not have been fully successful in making the filter linear-phase, but the matter ceases to be practically important once the dispersion filter is added, which totally outweighs these slight phase deviations.

Tuning was implemented at last, using a combination of an integer-sample delay and an order 6 Farrow fractional delay [77] for each side of the string (totaling βP for the bridge side, and $(1-\beta)P$ for the finger side). If a stiff string is to be modeled, tuning would be postponed until after the design of the dispersion filter. In summary, the order of the filters for each segment of the string is as follows: damping filter, phase-equalizing filter, dispersion filter (if a stiff string is being modeled), integer delay filter, and fractional delay filter.

2.3.3 Adding the dispersion to the model

Inharmonicity was accounted for using an all-pass filter with a unit gain at all frequencies, which only delays the signal in a frequency-dependent manner. The method used to design such a filter was based on a technique introduced by Abel and Smith in [78], which makes a dispersion filter in the form of cascaded first-order all-pass filters. This method was later applied to the particular problem of a stiff string in [79].

In summary, in this method the frequency-dependent part of the group delay (total delay of a stiff string minus the linear-phase term corresponding to a pure delay) is broken down into segments of 2π area. Associated with each segment is a first-order all-pass filter with a pole placed at the center of the corresponding frequency band. The pole radius sets the bandwidth of the group delay peak for each band, and in that way determines the trade-off between the smoothness of the final filter and its ability to track sudden changes in the desired group delay. The radius of each section is set in a way that within each band the minimum group delay (happening at the edges of the band) is equal to 0.85 times the maximum group delay (happening at the center of the band). Ultimately the designed first-order sections are paired up with their complex conjugates to produce real second-order all-pass filters. These second-order filters are implemented in cascaded second-order sections and are directly implemented into the loop filter without being converted to the transfer function form. The reason for this is to avoid round-off errors resulting in an unstable filter, a common problem for all-pass filters [80].

The original implementation proposed in [79] uses a first-order Newton's approximation to find the solution to the equation that gives the frequency of the poles (Eq. (8) in [79]); but here the exact solution to that equation has been calculated. The first-order approximation gives a convincingly close approximation to the desired behavior for the longer segment of the string (although, not surprisingly, never as good as the closed-form solution), but it proved to be problematic in designing the dispersion filter for the shorter segment of the string, at least for the way it was originally implemented in [79]. Figures 2.11a and 2.11b show the desired group delay behaviors against the results obtained from the exact solution and the first-order approximation, respectively for the short and long segments of the open

C_2 string (β is here chosen to be 0.10).

A filter designed based on the abovementioned method gives an almost constant group delay to all frequencies above the target frequency (marked by a star on the horizontal axis of Figs. 2.11a and 2.11b), which results in a spike-like behavior in the equivalent reflection functions. Time-domain details of this kind may be insignificant in producing audible effects as human ears are not too sensitive to phase, but they may affect the playability of a simulated bowed string by creating an unphysical disturbance at the bowing point. This can significantly compromise the accuracy of the model in predicting the playability of a bowed string. In this regard, a relatively high order (order 20) dispersion filter is used for each side of the string. The order is reduced whenever an order 20 filter resulted in a design frequency range passing the Nyquist rate (common for the bridge side and for a small bow-bridge distance). The order of the dispersion filter for the C_2 and D_3 cello strings as a function of β is illustrated in Fig. 2.11c. Perhaps coincidentally, these plots for the C_2 and D_3 strings overlay. The dispersion filter was excluded whenever the filter order would become less than 2, which is the case for β smaller than 0.028. The equivalent reflection function for the finger side of the open cello C_2 string is shown in Fig. 2.12, both for a perfectly flexible and for a stiff string. Damping parameters for both plots are based on the data in Table 2.1, and β is again set at 0.10. Even with an order 20 dispersion filter, some evidence of the spike-like behavior can be seen at non-dimensionalized time 0.4 for the stiff string case.

It is noteworthy that the inharmonicity of the n^{th} partial of the full string is jointly defined by the inharmonicity of the n^{th} partials for the two segments of the string. Having that in mind, for the cases where the bow/pluck is extremely close to the bridge the Nyquist rate may only cover the first few partials leaving the higher partials of the full string with an effective inharmonicity which is less than the target value. As a practical fix for those cases, an inflated inharmonicity is given to the finger side of the string to compensate.

An alternative to the abovementioned technique to model the dispersion is a method proposed by Woodhouse [29] which was used in calculating the reflection function shown earlier in Fig. 2.3. Like the constant-Q reflection function, this model was extensively used in earlier studies [21, 47, 32], hence deserves a critical review based on its merits and limitations. Results from the original implementation of the Woodhouse model and the new implementation based on Abel and Smith's method are presented in Sec. 2.4.

2.3.4 Measuring the properties of a cello body

The first step to implement a realistic body model is to extract the vibrational properties of an actual instrument; namely the mode frequencies, Q factors, modal masses, and their spatial angle. In this regard, calibrated measurements were carried out on the bass-side

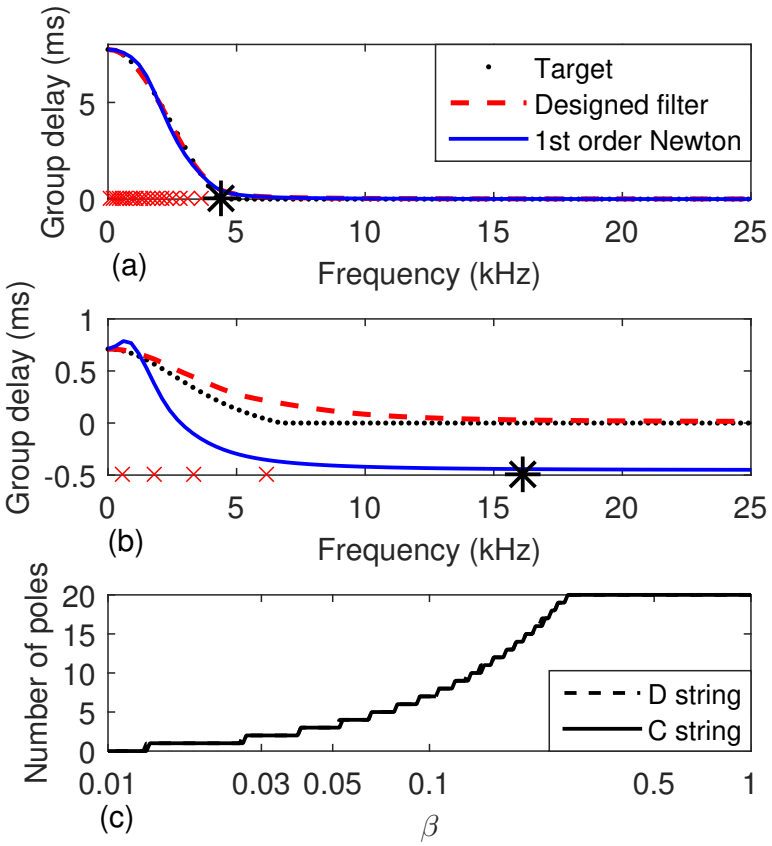

Fig. 2.11 Group delay of the designed filter (dashed line) for the finger side (a), and the bridge side (b) of the open cello C_2 string compared to the desired response (dotted line), and a filter designed with first-order Newton's approximation (solid line). The crosses show the position of the poles used in the designed filter and the star shows the upper limit of the design frequency. A constant group delay is assigned for the frequencies beyond that range. (c) shows the order of the dispersion filter for the C_2 and D_3 strings as a function of β.

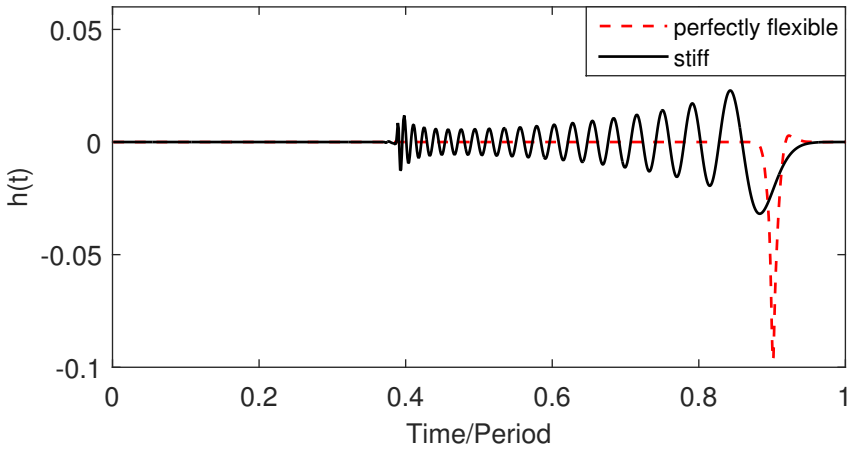

Fig. 2.12 Equivalent reflection function (impulse response of the loop filter) designed for the finger side of a damped cello C_2 string, perfectly flexible (red dashed line) and stiff (black solid line). The natural frequency of the string is 65.4 Hz, βP of 0.1, frequency-dependent Q factor based on the data in Table 2.1, bending stiffness of $9.1\text{x}10^{-4}$ Nm^2, sampling frequency $6\text{x}10^4$ Hz. Note the spike-like behavior in the stiff string's reflection function at non-dimensionalized time 0.4 which represents all frequencies above the design frequency for the dispersion filter.

corner of a mid-quality cello. A miniature hammer (PCB Model 086E80) and LDV (Polytec LDV-100) were used to measure the 2×2 admittance matrix in the coordinate system explained in Sec. 2.2.3. The strings were brought to the proper tension, but later both their singing- and after-lengths were damped using small pieces of foam. The instrument was supported on top by a chemistry stand holding it around the pegs, and it was sitting on its pin at the bottom. The direction of the impact was precisely controlled using a custom-made pendulum system. Note that the X-direction is chosen such that for most of the modes θ_{Mk} falls somewhere close to zero. More precisely, for a cello at frequencies below 700 Hz, a cello bridge rotates around its foot at the soundpost side, but this center of rotation moves towards the bass-bar side as the frequency increases. It should be recognized that this image is very simplistic and there is a strong mode-by-mode variation even in the low frequency range. As we enter the high frequency range, the principal direction of the modes becomes more of a random property.

Strictly speaking, one should account for the energy loss into the damped strings before doing modal extraction on the bridge admittance. A way to do this is described in [12] and [60]. The strings can be assumed perfectly damped elements whose impedance adds to the impedance of the body to form the measured impedance at the bridge. The assumption of perfect damping for a string means that the energy of any outgoing wave is fully absorbed

and there is no reflected wave. In practice, even damped strings are not perfectly damped and this method will result in over-compensation of the admittances, sometimes resulting in modes with negative damping. More importantly, this source of energy extraction from the vibrating body modes is present as long as the instrument is strung (regardless of the strings being damped or not). Therefore, it was decided to consider the damped strings as an extension of the body and to directly use the measured admittances for mode fitting.

Mode fitting was performed using an analysis method described in [12]. This method uses the Matlab function *invfreqs* allowing rational fraction polynomial approximation. It first involves modal extraction through pole-residue fitting, followed by an optimization procedure allowing selection of the best sets of complex and real residues by minimizing the mean of the modulus-squared deviation between measurement and reconstruction. This method was performed on Y_{XX} and Y_{YY} separately, and then the modes deemed to be the same for the two fittings (i.e. modes with similar frequencies and Q factors) were merged. This resulted in the final set of frequencies and Q factors. Modal masses and spatial angles were later optimized to give the best fit to all admittances (see Eq. (2.14)). Note that there is some redundancy in defining two properties (mass and angle) to fit three sets of data (Y_{XX} and Y_{YY} and $Y_{XY} \approx Y_{YX}$). The top priority for the best fit was given to Y_{XX} as direction X is chosen to be more closely aligned to the principal direction of coupling to the body, later to Y_{XY} as it defines the coupling of the two polarizations, and lastly to Y_{YY}.

In theory, the abovementioned technique can be generalized to fit complex modes to the data, using Eq. (2.15). However, the process of extracting complex modes from experimental results becomes increasingly ill-conditioned as the frequency grows [81], therefore a mode fitting using complex amplitudes does not necessarily result in a more realistic fit compared to one obtained by real amplitudes. In this regard, the real-mode assumption is imposed here. Using the described method, 67 modes were fitted from 90 Hz to 2 kHz.

To maintain the quality of fit, the frequency range of 0-90 Hz was included first, but the modes falling within that range were later removed from the simulations as any relative bridge-corpus motion is unlikely over those low frequencies, thus those were deemed to be fixture modes in which the cello moves as a solid body. Beyond 2 kHz, where modal overlap increases and the fitting process becomes increasingly difficult and ambiguous. A statistical fit is used, which assigned 166 extra modes to the frequency range 2 kHz to 7 kHz. A complete discussion of the statistical fit can be found in [39]. In short, a random number generator created modal frequencies with a correct density and spacing statistics, as well as damping factors, and modal masses with approximately correct statistical distribution. The resulting fit is compared to the measured admittances and some statistics of the fitted parameters are shown in Figs. 2.13 and 2.14 respectively.

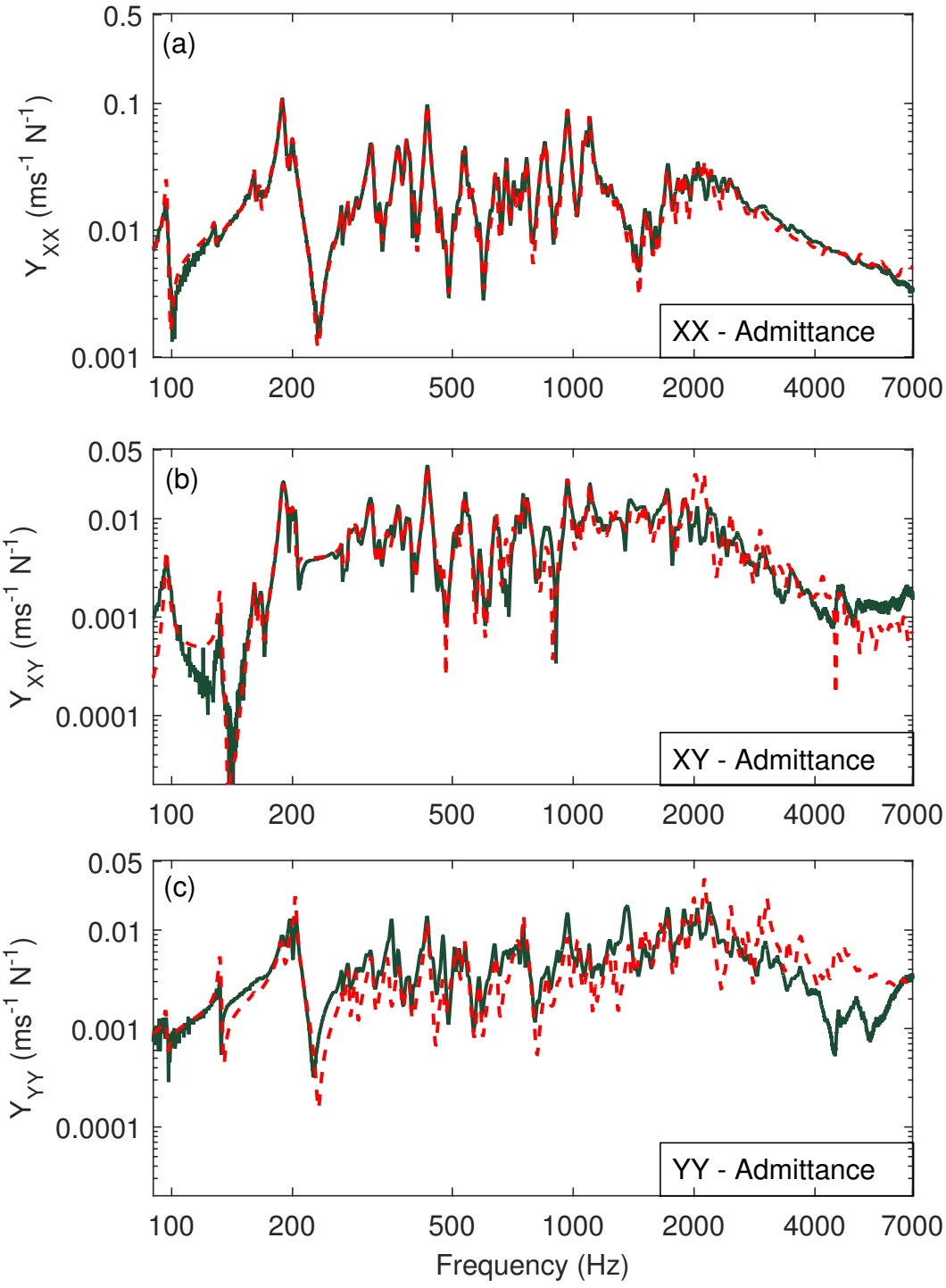

Fig. 2.13 Measured admittances in the perpendicular to string axis plane (green solid curve) and the fitted admittances to them (red dashed curve) for (a) XX admittance (b) XY admittance and (c) YY admittance. Note that the vertical scales are different in (a) and (b)-(c).

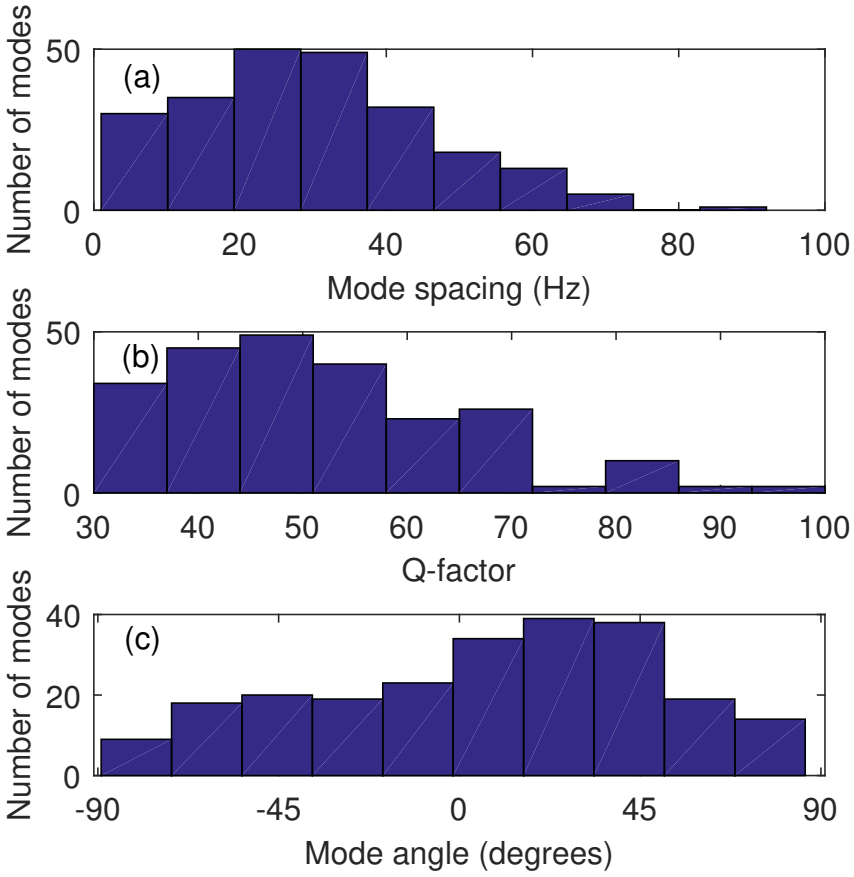

Fig. 2.14 Statistical distribution of mode spacing (a), Q factor (b), and spatial mode angles (c) for the fitted modes to the bridge admittances.

2.3.5 Adding the body and the sympathetic strings to the model

Each body mode is simulated as an independent resonator that gets excited by the exerted force of the string at the bridge. It was possible to include the body modes inside the IIR loop filter of the bridge side, but for the benefit of having direct access to the physical velocity of the bridge, it was decided to implement them separately. This also gives a simple and efficient recipe to synthesize the radiated sound from the instrument.[9] The complex amplitude of the k^{th} mode at sample $i+1$ can be calculated from its amplitude at sample i as

$$A_{k,i+1} = A_{k,i} e^{h(i\omega_{Mk} - \omega_{Mk}/2Q_{Mk})} + F_{Mk}.h/M_k, \tag{2.25}$$

where h is the time-step and F_{Mk} is the instantaneous force applied by the string(s), projected in the principal direction of mode k. It corresponds to the reaction force at the bridge when the incoming waves from the string (in both transverse polarizations) get reflected which involves their phase reversal. That is where the factor of 2 comes from.

$$F_{Mk} = -2.Z_{0T}.\left(v_{o1X'}.cos\theta'_{Mk} + v_{o1Y'}.sin\theta'_{Mk}\right). \tag{2.26}$$

$v_{o1X'}$ and $v_{o1Y'}$ are velocity waves sent from the excitation point towards the bridge in the X' and Y' polarizations β/f_0 seconds before the current time-step. As was mentioned earlier the physical reaction force at the bridge has extra terms corresponding to the resistive response of the semi-infinite (or perfectly damped) strings attached to the bridge (six in the case of the guitar and 2×4 in the case of the cello considering the string segments on both sides of the bridge). This resistive reaction force, which is independent of the traveling waves along the string, has already been accounted for as an extension of the body so it is not included in Eq. (2.26). The physical velocity of the bridge projected in the X' and Y' directions ($V_{M,X'}$ and $V_{M,Y'}$) can be obtained by adding the contribution of all body modes in the following form:

$$V_{M,X'} = \mathfrak{Re}\left\{\sum_k A_k cos(\theta'_{Mk})\right\}, \tag{2.27}$$

[9] The radiated sound in that case would be a summation of the mode amplitudes weighted according to their radiation efficiency. Radiation efficiency here is defined as the transfer function from the bridge-notch velocity to the radiated sound at an arbitrary point in the surrounding medium, and the vector of its values for individual modes is a set of amplitudes required to reconstruct the radiation efficiency plot by the same modal frequencies and Q factors used to reconstruct the bridge admittance.

and

$$V_{M,Y'} = \mathfrak{Re}\left\{\sum_k A_k sin(\theta'_{Mk})\right\}. \tag{2.28}$$

These projected velocities consequently add to the history of $v_{o1X'}$ and $v_{o1Y'}$, filtered once by the bridge-side loop filter to give the actual velocity waves arriving at the bowing/plucking point from the bridge side. For the finger side, as the finger/nut is assumed rigid, the incoming waves can be simply calculated by filtering the history of the outgoing waves toward the finger by the finger-side loop filter. If a single-polarization simulation of the string is intended, the terms in the Y'-direction are simply removed.

As already discussed, several strings are coupled through a common support; as such, excitation of one string results in the vibration of the others. Those strings are called the sympathetic strings throughout acknowledging the fact that they may, or may not, be tuned sympathetically to the played string. This can be straightforwardly embedded into the simulations by adding the reaction force of the sympathetic strings to Eq. (2.26), which turns it into

$$F_{Mk} = \sum_{j=C,G,D,A} -2.Z_{0T,j}.\left(v_{o1X',j}.cos\theta'_{Mk} + v_{o_{1Y'},j}.sin\theta'_{Mk}\right). \tag{2.29}$$

Similar to the case for a single string, the contribution of the moving bridge adds to the reflected waves at the bridge, this time for all strings. Since the only excitation acting on the sympathetic strings is the moving bridge and there is no external force acting on those strings in a round trip from the bridge to the finger and back, the sympathetic strings are modeled with a single loop-filter (as opposed to the finger-side and bridge-side loop filters for the played string).

In principle, the vibrations of the after-lengths could be added to the model using the same method, except the after-lengths are terminated at a fairly flexible floating tailpiece rather than a rigid termination at the nut. The relevant natural frequencies and mode shapes of a cello tailpiece can be found in [82] and they can be put into our modeling scheme, the exact same way that the body modes were included. A computationally-cheaper alternative is to measure the bridge admittance with the after-lengths undamped, and to include them implicitly into the model of the body.

2.3.6 Summary of the plucked-string model

In summary, each polarization of the plucked string is modeled using a pair of traveling waves, one going toward the bridge and the other toward the finger. These two traveling waves exchange values at the plucking point. To find the value of the incoming wave from

each side, the past values are filtered by an IIR damping filter (order 300), a cascaded set of second-order sections representing dispersion (order 20), delay-equalization filter (order 16), a fixed delay, as well as a fractional delay filter (order 6). The two polarizations of the string are coupled to one another through a common multi-resonator support (being the bridge) with 233 modes. The model of the body can accommodate complex modes, although real mode parameters are used here. Each polarization of the sympathetic strings is added using a single loop-filter designed with the same order of sections mentioned for the plucked string. Rolling of the string on the bridge or the fret may result in the two polarizations having slightly different pitches; the ability to account for this detail is embedded into the model by giving the two polarizations slightly different delay lengths (equal delays are used for the two polarizations of a cello string as its rolling is inhibited by the v-shaped bridge notch). A 60 kHz sampling frequency is used for all simulations. The schematic of the model for a single polarization of a plucked string is illustrated in Fig. 2.15.

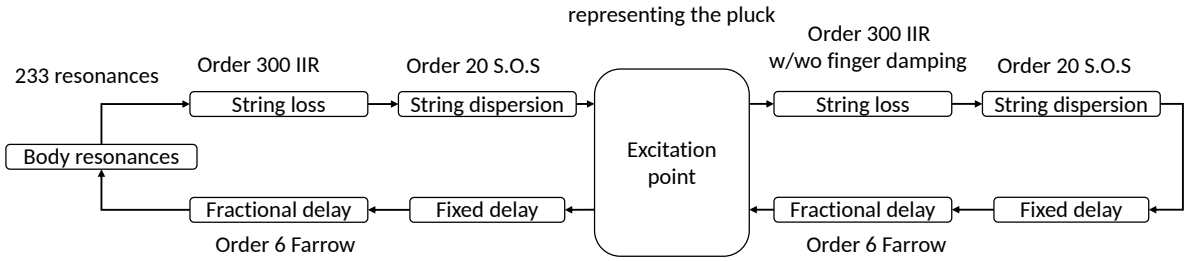

Fig. 2.15 Schematic of the plucked-string model.

The magnitude and the group delay of the loop filter (i.e. the combination of the fixed delay, fractional delay, and the string loss for the perfectly flexible string, plus the string dispersion for the stiff string) is plotted in Fig. 2.16 for both sides of the open cello D_3 string. Recall that for practical reasons, the Q factor at each frequency is constrained to be no less than 150 (represented by the straight segments of the "target" curve in magnitude plots), and the group delay remains constant above the design frequency of the dispersion filter. As expected the group delay of the perfectly flexible string remains constant to a good accuracy. The slight deviation of the magnitude from the target (in Figs. 2.16a and 2.16b) is caused by the fractional delay filter. In any case, that effect only becomes significant at high frequencies, for which the target is fudged to $Q = 150$.

2.3.7 Simulating the pluck

Physically speaking, the initial condition of a plucked string is zero velocity, and non-zero acceleration (and displacement). In principle, it is possible to initialize the waveguides to

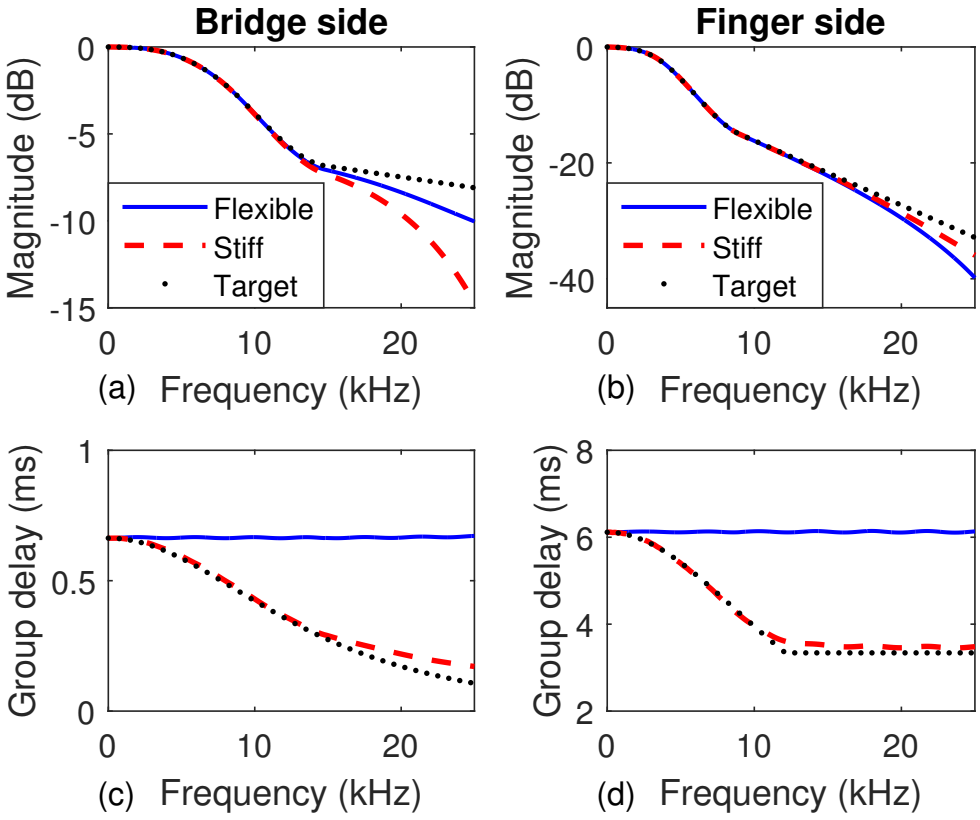

Fig. 2.16 Magnitude (a) and group delay (c) of the loop filter for the bridge side of the open D_3 cello string minus the contribution of the body modes. (b) and (d) are showing the same quantities for the finger side. Target value is shown by dotted line, the designed filter for the perfectly flexible string is shown by the solid line and the designed filter for the stiff string is shown by the dashed line. β is chosen at 0.10 and all relevant parameters are according to data presented in Table 2.1. The slight fluctuations of the group delay for the flexible C_2 and D_3 strings is caused by the limitation of the phase-equalizing filter.

produce arbitrary initial conditions; the values of two traveling waves add to form the physical velocity at each point, hence there are two degrees of freedom to set the initial velocity and acceleration [44]. While that possibility was available, an alternative approach is used here.

An ideal pluck can be defined as one that is produced by pulling a single point of the string sideways and then suddenly releasing it with no initial velocity: the force for such a pluck has a constant non-zero value, say F_P, at $t < 0$ which suddenly turns into zero starting at $t = 0$. One can offset this force by value $-F_P$, and only cause an offset in the displacement of the string, which does not matter as long as one deals with velocity waves. What it means in implementation is that both traveling velocity waves can be initialized with zero value, and at time zero, a constant force is applied at the plucking point, which persists over the time of simulation (essentially a delta function in space and a step function in time). The direction of this step force (also known as the angle of release) can be varied to set the initially-excited polarization of the string. The angle of release is one of the main parameters that guitar players use in order to control the tone color and the decay rate of the sound produced by the instrument (a comprehensive discussion of the topic can be found in [83]).

An ideal pluck is hard to achieve in reality: the closest one can get to that is by looping a thin wire around the string at the plucking point and gently pulling the wire until it suddenly breaks (first proposed by Reinecke [84]). Using the fingernail or a plectrum of finite size in place of a thin wire results in a further rounding at the plucking point. The detailed interaction of the plectrum/fingernail with the string and the exact way the pluck is executed have a significant effect on the final sound of the instrument and it has been covered in some detail in [85, 86]. In general, it would have been more straightforward to implement the detailed interaction of the string with any spatially distributed object if the traveling displacement waves are modeled in place of the velocity waves that are used here [87]. A physical way to take spatially distributed force into account when dealing with velocity waves is to use buffers in the initialization of the traveling wave components. For the present model, it was decided to use the step function with no filtering, which makes the synthesized results more comparable with the experimental results obtained by wire-breaking.

On a final note, in actual playing conditions, plucking (and particularly strumming) produces a combination of initial velocity and initial displacement, which are also known to be correlated to one another. This also leads to the possibility of non-planar (i.e. elliptical) initial excitation of the string that is shown to have a significant auditory consequence, at least for a plucked harp string [88].

Sound examples for a simulated open D_3 string excited by the above method is available

at this link,[10] when different features were being progressively added to the model. Cases include a perfectly flexible string terminated at rigid ends, a stiff string terminated at rigid ends, a stiff string terminated at a realistic bridge and vibrating in a single polarization, a stiff string terminated at a realistic bridge and vibrating in both polarizations, and finally the last case in addition to the sympathetic strings. The response is the traveling velocity wave within the string and going towards the bridge, which is proportional to the string force acting on the bridge. The signal that is converted to a sound file is a low-pass filtered version of that traveling wave. The low-pass filtering is to simulate the radiation from the instrument's body in its simplest form, that is considering the instrument body as a pulsating sphere of roughly the right diameter (see Eq. (6) of [5]).

2.4 Evaluating the accuracy of the plucked-string model

The techniques described in Sec. 2.3 were applied to simulate 10 seconds of plucked sound for the first 12 notes on the C_2 and D_3 cello strings. The results were later analyzed to extract the frequency and Q factor of, at least, the first 15 string modes using the same method discussed in Sec. 2.3.1. The damping added by the finger of the player is included for all finger-stopped strings throughout, and not for the open strings.

Figure 2.17 shows the extracted Q factors and inharmonicities (equal to Bn^2 in Eq. (2.10) and calculated from $\left[(f_n/nf_0)^2 - 1\right]$ for each string mode) for both synthesized open C_2 and open D_3 strings, when the stiffness option is turned on and off. For the moment, the end termination of the strings is assumed rigid (i.e. the contribution of the flexible body is turned off in the model) to solely focus on the vibratory behavior of the strings. The open string case is chosen here to magnify possible flaws in the modeling of damping. Figure 2.17 is plotted for 20 different β values (i.e. for different pluck-bridge distances). Ideally, both Q factor and inharmonicity should be independent of the plucking point, hence plots for different β values should overlay. This clearly is the case except for the first few string modes of the C_2 string, showing a slight variation. This variation vanishes almost entirely as soon as the bridge is turned from a rigid termination to a realistic flexible one. The desired trends for Q factor and inharmonicity (earlier shown in Fig. 2.8 and calculated from parameters in Table 2.1) are also overlaid for both strings. The demonstrated precise tracking of the desired Q factor could only be achieved by using a very high order damping filter; lowering the number of poles from 300 to 100 significantly degraded the final result. Inharmonicity of both perfectly flexible C_2 and D_3 strings displays a bit of variation from being constantly zero, caused by the limitation of the phase-equalization procedure, but the range of variation

[10] http://mt.music.mcgill.ca/~hosseinm/research/mus_acc/thesis_mat/

is almost negligible compared to the inharmonicity by the strings' stiffness. Note that the desired Q factor and inharmonicity trends are genuinely different for the C_2 and D_3 strings, so the plot for each stiff string should be only compared to its corresponding flexible one. It is satisfactory to see that the Q factors for both strings are not affected by the dispersion filter.

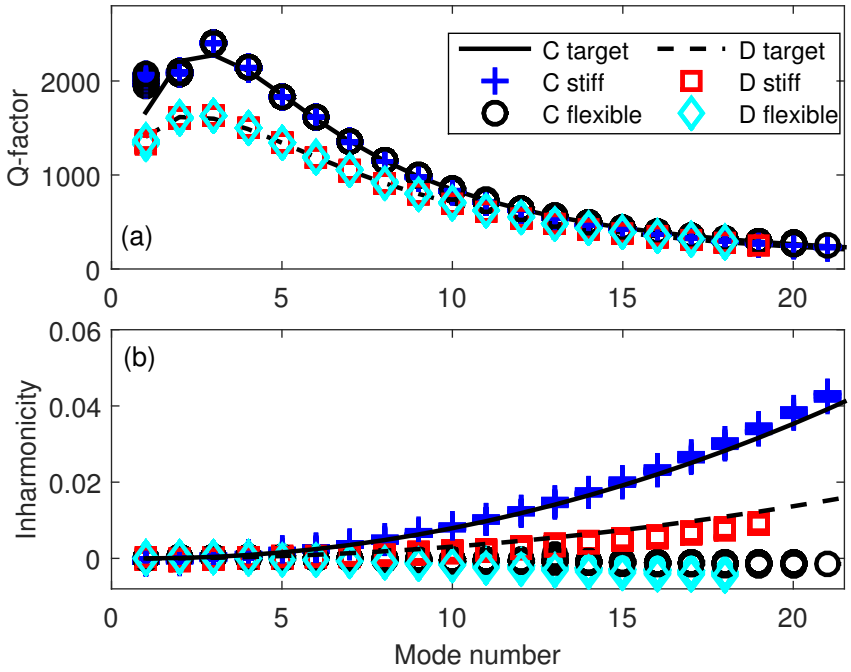

Fig. 2.17 Trend of the Q factor and inharmonicity (*i.e.* $\left[(f_n/nf_0)^2-1\right]$) versus the string mode number for the stiff and flexible open C_2 and D_3 cello string. All strings were terminated at rigid boundaries and the results are extracted from 10 seconds of simulated plucked response. β is varied in 20 steps and the results are overlaid.

Figure 2.18 shows what happens to the simulated results when the body contribution is added to the model. Since it is already demonstrated that the response of the string is not a function of the plucking point, the plots are only drawn for the smallest β value (equal to 0.02) to excite the largest number of modes before the first missing harmonic appears (the $1/\beta^{th}$ harmonic); instead, the plot is made from the first finger-stopped semitone to the 12^{th} one on each string. The equivalent results for the case of rigidly terminated strings is also included for comparison; the strings' stiffness is included in both sets of simulations. Q values are no longer comparable to the ones of open strings due to the additional damping considered to simulate the lossy termination at the player's finger contact point. The Q factors and inharmonicities are both plotted against the string mode frequency and are overlaid for

different notes played on the same string (note the different scaling of the horizontal axes in Figs. 2.17 and 2.18).

As expected, once the body is included in the model, the Q factors drop significantly and in a frequency-dependent manner. It is also encouraging to see that the frequencies of the string modes are perturbed when compared to their counterparts obtained by the rigid termination assumption. This perturbation is more severe for the C_2 string and in the low frequency range, where veering is more likely to occur (note the difference in the plotting range for the inharmonicities of the C_2 and D_3 strings). An interesting observation, which is in accordance with the earlier findings in Sec. 2.3.1 (compare stars with the plus signs in Fig. 2.8), is that a fit to the ceiling level of the Q factors for the modes of a string mounted on an actual cello does not quite reach the Q factor of the same string with rigid end terminations. For instance the highest Q factor among all partials of the first 11 semi-tones played on the C_2 string barely reaches 600 which compares to 1200 achieved for the rigid end terminations case. Note that the numbers are much lower than the numbers in Fig. 2.8 as the finger damping is added for both cases demonstrated in Fig. 2.18. The difference is expected to get worse with increasing Q factor of the string and with decreasing impedance mismatch of the string and the body at the bridge.

The next logical step is to see how the simulated coupled string-body model compares to its experimental counterpart. Figure 2.19 shows such comparison, in which the simulated Q factors for the open C_2 and D_3 cello strings (terminated both at rigid ends and ones corresponding to an actual instrument) are overlaid on the experimental data. The experimental data was obtained from the same cello whose bridge admittance was used to fit the modal properties of the body. The C_2 and D_3 strings used for the measured data were also "D'Addario Kaplan Solutions" cello strings (model KS510 4/4M).

The results are in very good agreement with the numerical predictions, showing only very modest discrepancies. In any case, the exact values of the measured Q factors should not be over-interpreted: they will be sensitive to string excitation angle and exact tuning, as well as to the usual uncertainties in measuring vibration damping.

As another sanity check for the simulation of the string-body interaction, one can treat the model as an actual instrument with strings undamped and simulate the standard measurement of the bridge admittance (by exciting the bridge with an impulse and measuring its velocity). Figure 2.20 shows the result of such assessment. Both polarizations of all four strings were included in the model, but there was no external excitation acting on any of those. Instead, the bridge was excited by an impulse in the X direction at the beginning of the simulation and let go for 10 seconds. The simulated bridge admittance in the X-direction is compared to the measured one, when all strings were free to vibrate. The plots are all

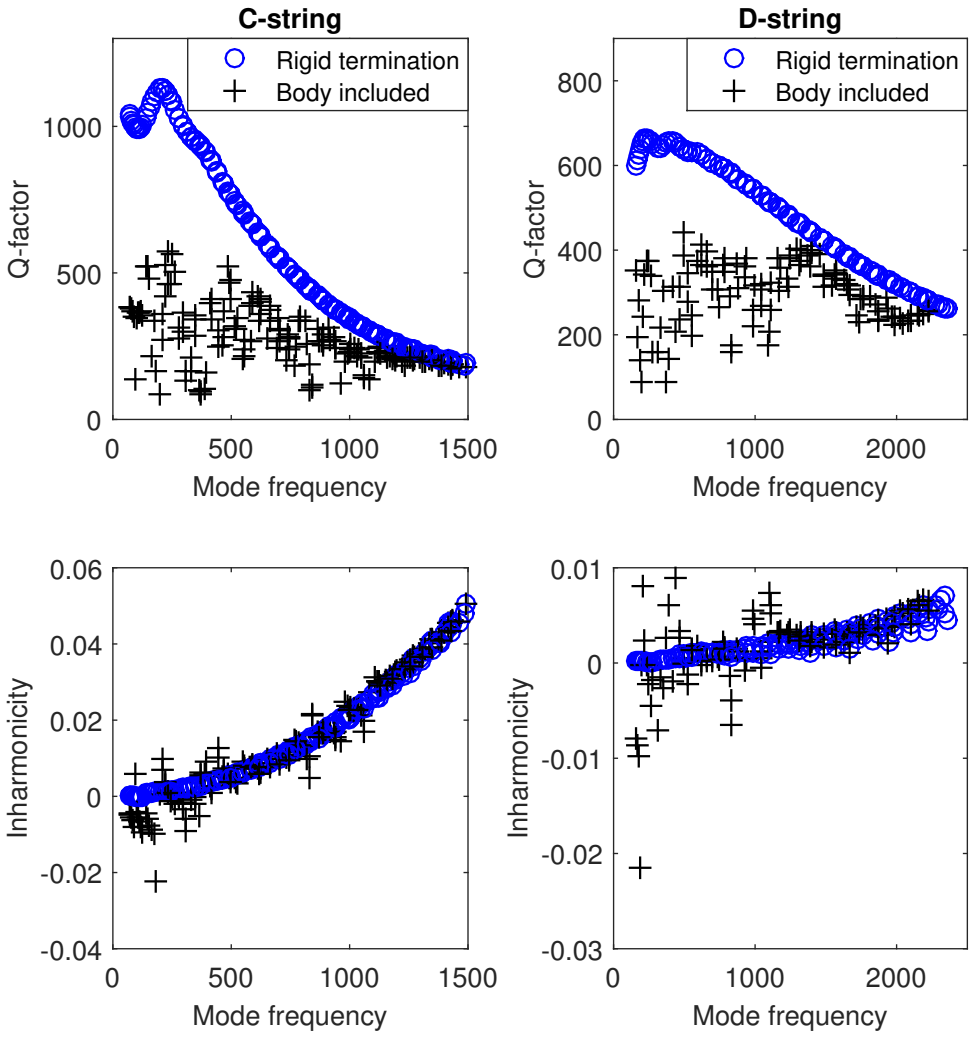

Fig. 2.18 Trend of Q factor (upper plots) and inharmonicity (lower plots) versus the string mode frequencies for the stiff C_2 (left plots) and the stiff D_3 (right plots) cello strings. Circles show the case when the strings are terminated at rigid boundaries and plus signs show the case when the flexible body is included in the simulations. The first 11 semitones are played on each string and the results are extracted from 10 seconds of a simulated plucked response.

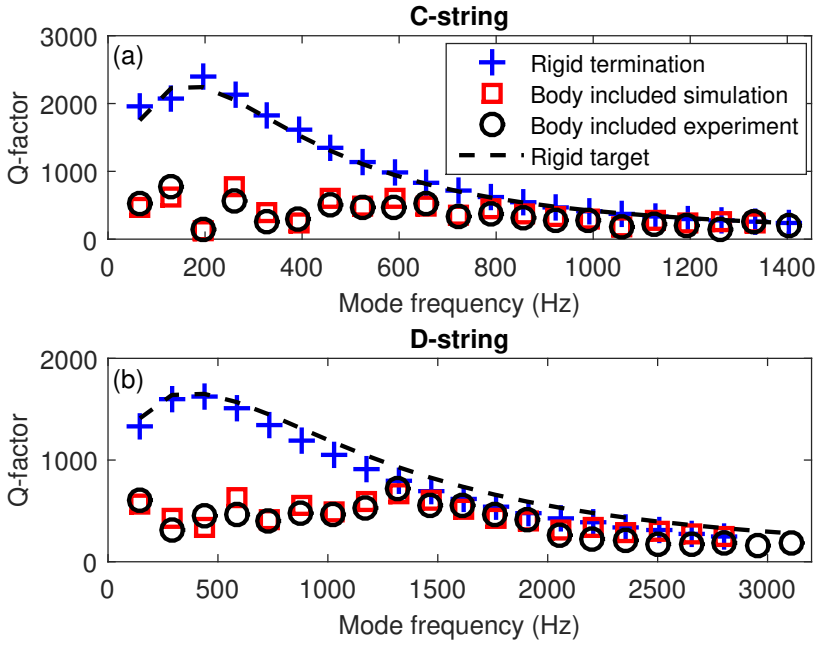

Fig. 2.19 Q factor versus fundamental frequency for the open C_2 (top) and open D_3 (bottom) cello strings. Plus signs show the Q factor of the synthesized pluck with rigid terminations, squares show the same quantity when the coupling to the body modes are included and the circles are the equivalents of the squares but for the data measured on an actual instrument. The body modes were fitted to the bridge impedance of the same instrument but the strings properties in the simulations do not necessarily match the properties of the strings mounted on the cello.

in-scale and no modification is made to match the two.

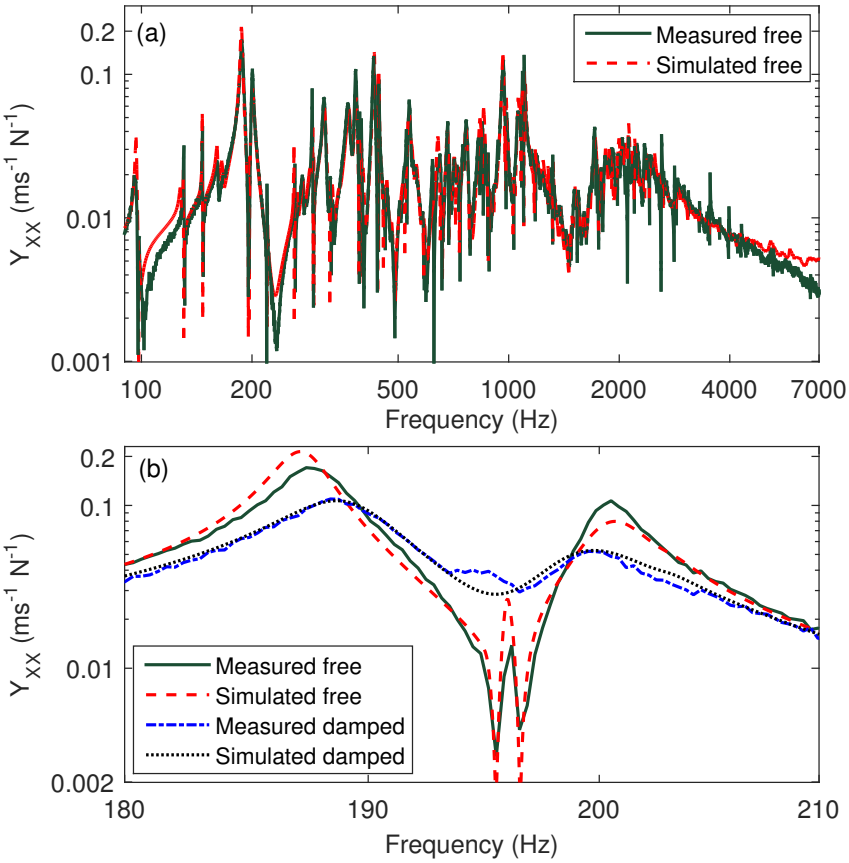

Fig. 2.20 Simulated versus measured bridge admittance in the X direction when all four strings are free to vibrate (a), and a zoomed version of that plot covering only the "wolf-note" area (b). Both measured and simulated data for the strings-damped case are also included in the lower plot for comparison.

As one would expect, the general trend of the admittance for the strings-undamped case is similar to the strings-damped cases (earlier shown in Fig. 2.13a) with the only significant difference being sharp string resonances added for the strings-undamped version. Figure 2.20b is a zoomed version of, perhaps, the most important frequency range of Fig. 2.20a: the wolf note area. Aside from the fact that the strongest body effect is around the wolf frequency, it was interesting to see how the sympathetic strings are interacting with the body modes present in that frequency range. The 2^{nd} harmonic of the G_2 string and the 3^{rd} harmonic of the C_2 string both fall in that region. The two would coincide if the strings were perfectly flexible but are slightly mistuned due to different inharmonicities. Both the experimental bridge admittance and the simulated one for the strings-undamped case are added to the plot, for comparison. It can be seen that the two strong body modes falling on the two sides of the string resonances are repelled by the reactive components of the string modes. These

effects have been very well captured by the model.

Finally, Fig. 2.21 shows the equivalent of Fig. 2.17 but using the old implementation of the dispersion (discussed in the end of Sec. 2.3.3) and a constant-Q damping model (discussed in Sec. 2.2.1). This particular combination was used in many earlier studies such as [21, 47, 32] to model a cello string and in [39] to model a guitar string. Figure 2.21 shows the Q factor and inharmonicity of the open D_3 string (C_2 string is excluded for clarity), with and without dispersion and for 20 different β values. Note that the older implementation uses a constant-Q damping model (set to 1800 here) and for that reason is not directly comparable to the results presented in Fig. 2.17. The sampling rate to obtain the results of Fig. 2.21 is set to 200 kHz (compared to 60 kHz used for this newer implementation), which was the standard throughout earlier studies.

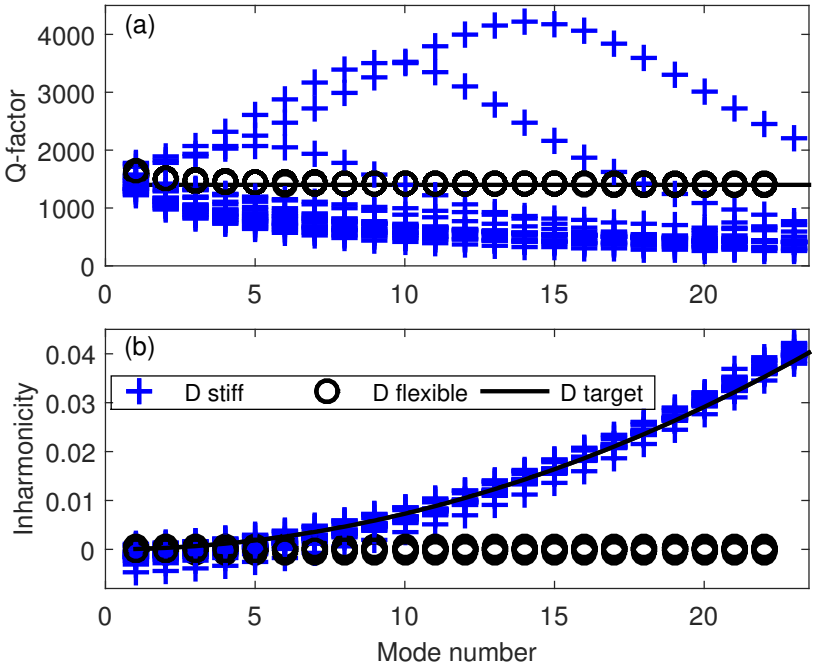

Fig. 2.21 Trend of Q factor and inharmonicity (*i.e.* $\left[(f_n/nf_0)^2-1\right]$ versus the string mode number for stiff and flexible open D_3 cello string, based on the old implementation. The strings had rigid terminations and the results are extracted from 10 seconds of simulated plucked response. β is varied in 20 steps and the results are overlaid.

It can be seen that the Q factor of a perfectly flexible D_3 string follows the intended constant value of 1800 fairly accurately. For the same simulation made on the C_2 string or with a lower sampling rate on the D_3 string (neither reproduced here), the Q factors of the first few string modes were slightly above the desired value. As was discussed in Sec. 2.2.1 this effect is an artifact of discretization error and the final normalization in the process of

designing the filter. Gratifyingly, the inharmonicity of the perfectly flexible case stays very close to zero, more accurately than the case for the newer implementation presented earlier. The resulting tuning, however, is slightly poorer than the new implementation, which could have been improved if a fractional delay was used in the old implementation. In any case, the difference is very small and can only become alarming if one tries to study effects such as pitch flattening (discussed in Chap.5). Once the dispersion is included, the results are much less satisfying. Although the inharmonicity of the simulated plucks well matches the desired trend, it drastically affects the Q factor of the partials, and it has also made the Q factor a sensitive function of β. Instability was also observed in some cases which echoes earlier difficulties reported to synthesize a guitar pluck using this technique [39]. It should be noted that the observed instability (and more generally Q factors higher than the target value) are not inherent in the way the string stiffness is modeled; rather they should be related to the way the stiffness module is implemented. A more careful implementation using the same theoretical approach should be able to address this issue. Including the body into the model alleviates the situation to a large extent, but not enough to justify unconditional use of that model.

2.5 Summary of findings

In this chapter, we discussed the development of a refined model of a plucked string. Various details and their underlying physics were explained comprehensively, and some methods were suggested to include them into the model of a plucked string. Among those details were the frequency-dependent damping of the string, an accurate implementations of dispersion, and the interaction of the string vibrating in two polarizations with a realistic bridge as well as the sympathetic strings supported on the same bridge. Parameters used for the damping of the strings were extracted from real measurements of cello and guitar strings, and as such, those numbers can be used safely in other studies, regardless of the approach taken to do the modeling. The quasi-evanescent waves and the nonlinear vibrations of the string are still the missing components of our plucked-string model.

Using some sample results, it has been demonstrated that the model of the string precisely follows the target trend for the Q factors and dispersion. More importantly, the fully coupled model of the plucked string was compared to the plucked sounds of an actual instrument, which demonstrated the ability of the model to produce a response with similar Q factors to the experiments. The simulations were made for the open C_2 and D_3 cello strings and the most significant inconsistency was observed for the D_3 string, for which the damping was slightly underestimated over the full range of frequencies. This observation was associated

to the fact that the string used in the experiments was of a different model than the string whose parameters were used in the simulations. Another simulated data checked against the experiments was the bridge admittance when all strings were either damped, or free to vibrate. It has been shown that the measured and the simulated bridge admittances are almost indistinguishable for the strings-damped case. More importantly, it has been verified that the effect of the sympathetic strings and their interaction with the body modes is very well captured by the model.

Chapter 3

The ingredients of a complete bowed-string model

The development of a highly-refined model of a plucked string was discussed in the previous chapter. In this chapter, we will add the bow to the model. The chapter starts with a background on the vibrations of a bowed string as well as a review on the development of the earlier models concerning a bowed string. We will then move to the complications that the bowing process add to the picture, namely the tribology of the rosin, torsional waves on the string, transverse and longitudinal vibrations of the bow hair, a resonant bow stick and quasi-static changes in the tension of the string and bow hair due to the bow force. Features missing in the model are the finite width of the bow hair (the model assumes a single-point bow contact), and the dynamic changes of bow impedance in both the transverse and longitudinal directions as it moves on the string. The main unresolved issue in regards to the modeling of a bowed string remains the detailed friction behavior of the rosin.

3.1 The development of theoretical models of a bowed string

3.1.1 Helmholtz observations of a bowed string

Looking at a bowed string with the naked eye gives the impression that the string moves back and forth between two curved boundaries. Helmholtz was the first to note that this is an optical illusion and in reality the vibration of a bowed string is formed by a V-shaped corner (or multiple corners) traveling back and forth between the bridge and the finger. At each instant, the singing length of the string is divided by the corner(s) into two or more sections of straight lines. On the other hand, according to the d'Alembert (or traveling waves) argument conveyed in Chap. 2, the corners must travel with a wave propagation speed $c_0 = \sqrt{T_0/m_s}$ along the string. Assuming a constant tension along the string, the net

force acting on each element of a straight section is zero; therefore that element is either at rest, or has a constant transverse speed. Only when a corner passes through the spatial location of that particular element can it have an acceleration, which is in fact, a delta function for a perfectly sharp corner. The Helmholtz traveling corner solutions can describe the motion of a bowed, plucked, or stuck string very intuitively [37].

Returning to the problem of a bowed string, for the simplest case –where there is only one corner traveling back and forth between the bridge and the nut– every time that the corner passes through the bow it either triggers a stick or a slip. During the time that the corner is on the finger-side of the contact point, the bow and the element of the string beneath it move together which is called sticking; when the corner reaches the bow it triggers a slip which carries on until the corner reflects at the bridge and arrives back at the bow and causes sticking to resume. Ingeniously, Helmholtz confirmed these deductions by studying Lissajous patterns observed by a vibrating microscope looking at a spot of luminous paint applied to the string [2]. This vibration regime (called the Helmholtz motion) is distinctive in that it is the only motion that creates the "speaking" sound of the violin, and it is the goal of the vast majority of bow strokes.

3.1.2 Raman's model of a bowed string and the Friedlander-Keller graphical friction-curve method

The first systematic analysis of bowed string dynamics was made by Raman in the early part of the twentieth century [45]. In his hand calculations, Raman assumed a perfectly flexible string terminated at both ends by terminations with real reflection coefficients of less than unity (physically speaking, a dashpot). He also assumed that the string is being excited by a velocity-dependent friction force applied at a single point dividing the string in a rational fraction. Although lack of computer-aided simulations at the time made him make many simplifying assumptions, he was remarkably successful in predicting the possible regimes of vibration for a bowed string. Raman was also the first to point out the existence of minimum bow force [89] as well as the geometrical incompatibility of the ideal Helmholtz motion with a uniform velocity across a finite-width bow [45], both of which were confirmed later.

Using Raman's simplified dynamical model, Friedlander [90] and Keller [91] published two independent, but very similar studies. They proposed a graphical construction for relating the friction force at the bowing point (F_F) to the velocity of the string there (v). The friction force at the bowing point should satisfy two equations simultaneously: the equation of string wave impedance and the constitutive law, governing the friction force.

$$F_F = 2Z_{0T}.(v - v_h) \tag{3.1}$$

$$F_F = F_{F(v-v_b)} \tag{3.2}$$

The solution to the velocity and the force can be found as the intersection of these two equations when plotted on the same graph (as shown in Fig. 3.1). v_h in Eq. (3.1) is the unperturbed velocity at the bowing point. Equation (3.1) suggests that the friction force is proportional to the difference between the actual velocity of the string at the bowing point and the velocity it would have had if the bow was suddenly removed. The proportionality constant is twice the transverse characteristic impedance of the string ($Z_{0T} = \sqrt{T_0 m}$). v_b in Eq. (3.2) is the bow speed, and $F_{F(v-v_b)}$ represents the functional dependency of friction force on the relative sliding speed (a.k.a. "friction-curve"). The friction-curve consists of two positive-sloping curves separated by a vertical line at $v = v_b$. The magnitude of the friction can vary up to some limit if the string is sticking to the bow (represented by the vertical portion of the friction-curve), but it is progressively less as the relative sliding speed increases (shown by the curved portions).

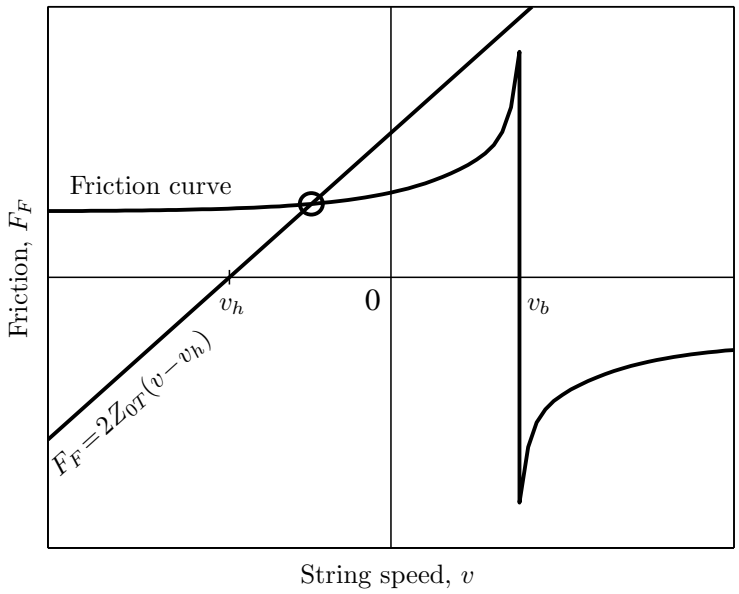

Fig. 3.1 Friedlander's graphical construction for the calculation of F_F and v. The solution to Eqs. (3.1) and (3.2) is given by the intersection of the two, as shown here with a circle. (From [3])

Friedlander noticed that for sufficiently large bow force there can be three intersection points. To circumvent this ambiguity, he suggested considering the effect of the finite-width of the bow, which he thought of as similar to that of adding a particle at the bowing point. In 1979, McIntyre and Woodhouse resolved this ambiguity by showing that out of the three solutions, the middle one is always unstable, and by introducing a hysteresis rule to choose

the right one from the remaining two (if the string is sticking it continues to do so and vice versa). They could also give an explanation for the pitch flattening effect (a small flattening of pitch as the bow force increases) using this hysteresis rule and the asymmetric pattern of stick and slip arising from it [34].

Both Fridlander's and Keller's results indicated that if dissipation is not taken into account, all periodic motions are unstable, including the Helmholtz motion. As identified later in [92, 93, 94] any small perturbation to the Helmholtz motion produces subharmonic modulation of the Helmholtz motion, which results in such instability. In reality, because of the energy losses in the system (provided by the string, the terminations and conversion of energy to torsional waves) that instability is usually suppressed, but under certain circumstances these subharmonics can be heard, or seen in measurements of bowed-string motion [92].

3.1.3 Cremer's rounded-corner model

The next major development in modeling the bowed string dynamics was introduced by Cremer and Lazarus in 1968. Acknowledging the fact that on any real bowed string the sharp corners (resulted from Raman type damping) are unlikely to occur due to dissipation and dispersion, they proposed a modification of the Helmholtz motion by "rounding" the traveling corner [95]. Cremer further exploited the corner-rounding idea and developed a model of periodic Helmholtz-like motion on a perfectly flexible string with spring-dashpot at the bridge side, and a rigid termination at the finger side. His observations revealed that when the normal force exerted by the bow on the string is small, the corners tends to round, whereas sharp corners result when increasing the bow force [96, 50, 51]. *"A sharper Helmholtz corner implies more high-frequency content in the sound, so this gave a first indication of how the player can exercise some control over the sound spectrum of the note: ideal Helmholtz motion is completely independent of the player's actions, except that its amplitude is determined by the bow speed and position" [3].*

3.1.4 MSW's model of a bowed string

In 1979, McIntyre and Woodhouse presented a complete theoretical model of the bowed string [34], which can be regarded as the precursor to digital waveguide modeling later developed by Julius Smith [97]. The MSW model extended Cremer's corner-rounding concept to include transient motion of the string, and refined the Friedlander-Keller graphical solution technique for the ideal case that the bow has zero width, and the friction force depends only on relative bow-string velocity. The most critical aspect of their proposed computational architecture

however, was to explicitly represent the motion of a string as the superposition of two left- and right-going traveling components. A complete explanation of MSW's model was conveyed in Chap. 2, so we do not repeat it here.

The MSW model was remarkably successful in describing the general behavior of a bowed string, as well as some minor details of it including pitch flattening, secondary waves (or the Schelleng ripples), and the wolf note phenomenon. As was seen in Chap. 2, this model is applicable to plucked strings by eliminating the bow; as well, it can be generalized to wind instruments [28]. All simulations of this study are carried out using an updated version of that scheme.

3.2 The underlying physics of a bowed string

In Chap. 2, we discussed the physical details involved in the vibrations of the string and its interaction with the instrument's body to the point that was essential to understand the vibrations of a plucked string. In this section, we present the new physical details that emerge from the interaction of the bow with the string.

3.2.1 Torsional motion of a bowed string

The friction force from the bow is applied tangentially on the surface of the string; therefore, it applies torque and excites the torsional vibration of the string as well. Torsional waves are not effectively coupled to the body of the instrument (reflecting at the bridge, they pose a torque rather than a net transverse force); therefore, they are not likely to be responsible for a significant portion of the radiated sound except for the rare case of "whistling" violin E_5 string [98]. Torsional waves are, however, coupled to the transverse waves at the bowing point and can affect the sound and the playability of the instrument in that capacity. Torsional waves on a normal over-wound string are much more heavily damped than the transverse waves, therefore their coupling to the transverse waves introduces significant amount of damping, to the extent that they have been identified as the first candidate to stop the already discussed Friedlander instability from happening [92, 93, 94].

Once the torsion is taken into account, the effective characteristic impedance of the string seen by the bow should be modified from Z_{0T} to Z_{tot} defined as

$$\frac{1}{Z_{tot}} = \frac{1}{Z_{0T}} + \frac{1}{Z_{0R}}, \tag{3.3}$$

where Z_{0R} is the characteristic impedance of the string in the torsional direction. The bow is virtually transparent to the transverse waves in the slipping phase; therefore, most of the

transverse-to-torsional conversion happens in the sticking phase. In other words, during the sticking phase rolling of the string on the bow creates a passage for the otherwise-trapped waves on either side of the bow to pass to the other side. In this regard, the inclusion of the torsional motion is expected to affect details such as the "Schelleng ripples" more than the Helmholtz motion itself. Using the same argument, torsional motion is believed to be more influential during transients and when a high bow force is employed [37]. Torsional motion is not normally excited in the case of a plucked or struck string unless the string has a discontinuity (such as a dent or a bend), or it is allowed to roll on the termination points, which breaks its rotational symmetry.

The equation of motion for undamped torsional motion of the string is

$$K_R \frac{\partial^2 \phi}{\partial x^2} - I_R \frac{\partial^2 \phi}{\partial t^2} = r f(x,t), \tag{3.4}$$

where ϕ is the angular displacement, K_R is the torsional stiffness, r is the string radius, and I_R is the polar moment of inertia per unit length of the string [35]. I_R can be calculated from $I_R = m_s \kappa^2$ where, as before, m_s is mass per unit length of the string and κ is the radius of gyration. For the case of a solid (or a monofilament) string, Eq. (3.4) reduces to $G\frac{\partial^2 \varphi}{\partial x^2} - m\frac{\partial^2 \varphi}{\partial t^2} = r f(x,t)$ where G is the shear modulus of the string. For the wound strings the distribution of the stiffness and mass is more complicated than that (see [33] or [99] for example). Solving Eq. (3.4) results is a torsional wave speed of $C_R = \sqrt{K_R / I_R}$ and a characteristic torsional impedance of $Z_{0R} = K_R C_R / r^2$. This suggests that, unlike the case for the transverse waves, torsional waves are non-dispersive; as well, their propagation speed (hence their natural frequencies on a finite-length string) is not a function of the string's tension. Nonetheless, Loach and Woodhouse found in their experiments that the natural frequencies of the torsional waves reduce to some extent, by increasing the tension [33].

Schumacher studied a wide range of violin E_5 and D_4 strings and concluded that torsional waves travel 2 to 8 times faster than the transverse waves. For the same set of strings he found that the ratio of torsional characteristic impedance to transverse characteristic impedance lies between 1.4 and 3.44 [99]. More recently, Loach and Woodhouse investigated the same parameters for nylon, gut, and steel, cello D_3 strings and found 5.14, 4.7 and 3.94 for C_R/C_T, and 3.27, 2.39 and 2.07 for Z_{0R}/Z_{0T}, respectively [33]. The ratio Z_{0R}/Z_{0T} is a good measure for the amount of energy exchange between the transverse and torsional waves when either of those impinges on a barrier.[1] Woodhouse and Loach also measured the Q factor for the first few torsional modes of selected cello strings. The Q factors remained almost constant over different modes and were averaged to 45, 20, and 34 for nylon-, gut-, and steel-cored strings respectively. Those Q factors dropped with an exaggerated reduction of the tension,

[1] The amount of exchange is equal for the two cases due to reciprocity.

but were almost unchanged for any tension above half the nominal tension. As expected, the torsional waves had little or no dispersion.

Serafin et al. performed a study to investigate the effect of the string's torsional motion on its playability [100]. They used a bowed-string model to produce the Schelleng diagram (i.e. the playability map in the bow force versus β space) when torsional motion of the string was included or excluded. Their simulated data suggested that the torsional motion has a negligible effect on the playability. However, this result may be in need of revisiting as the string model used in their simulations was the same old implementation, shown in Sec. 2.4 to produce unreliable results. Also, their model did not account for the coupling to the flexible bridge, which is an important factor in defining the limits of playability. We will get back to this issue in coming chapters.

3.2.2 The flexible bow

So far in our discussions, we have ignored any flexibility or width for the bow, as would be the case if the string is bowed with a rigid rod that has a single-point contact with it. A real bow, however, is both flexible and has a finite width. The flexibility of the bow is discussed here and its finite width is left for the next section.

When a string is bowed, the time-varying friction force drives the string in the bowing direction, but it also excites the bow hair ribbon in its longitudinal direction (see Fig. 3.2 for the definition). Vibrations of the bow hairs, in turn, add up to the nominal speed of the bow and form the "effective" bow speed at the bowing point.

The bow hair ribbon also has some degree of flexibility in the direction perpendicular to it (called the bow hair's transverse direction and displayed in Fig. 3.2). As was discussed in Sec. 2.2.3, misalignment between the bowing direction and the principle directions of the body modes, couples the polarizations of the string in the bowing- and perpendicular-to-bow directions. Vibrations of the string and the bow hair in their transverse directions add a fluctuating component to the bow force and can affect the playability of the string in that capacity.

A typical cello bow hair ribbon consists of around 290 hair strands, of which, around 50 are in immediate contact with the string (less than that if the bow is tilted). The diameter of each hair strand is in the range 0.16 mm to 0.25 mm [35] and the typical length of the bow hair bundle is around 59 cm. As reported in [35], Young's modulus and density of the hair material are roughly 7 GPa, and 1100 kg/m^3 respectively. Assuming 50 active hair strands, the characteristic impedance of the bow hair ribbon in the longitudinal direction becomes approximately 7.9 kg/s, 10 kg/s, 28 kg/s for the violin, cello, and double-bass bows, respectively [35]. Wave speed in the longitudinal direction of the bow is approximated at 2300

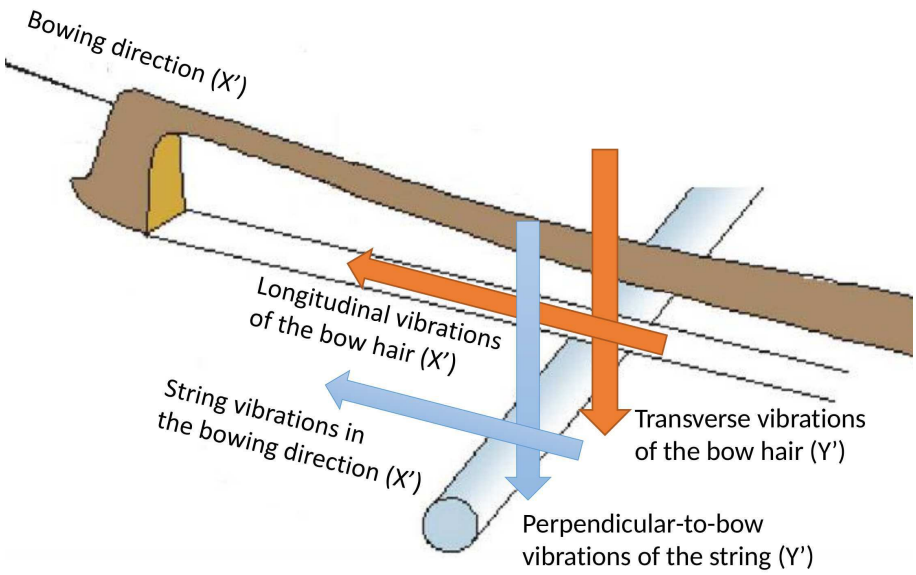

Fig. 3.2 The geometry of the bow and string illustrating different polarization directions of the string and the bow hair ribbon (after [101]). For ergonomic reasons the bowing direction, X' is approximately aligned with the X direction defined in Sec. 2.2.3, but the two can be misaligned if the player uses inclined bowing. (After [21])

m/s [102], which results in the first bow hair longitudinal mode happening at 1950 Hz. A typical bow hair ribbon is pre-tensioned to 70 N, which results in a first natural frequency of 75 Hz, and a characteristic impedance of 0.79 kg/s both in its transverse direction (assuming all bow hair strands are moving together in this direction). Gough estimated the Q factor of bow hair vibrations in transverse and longitudinal directions at 20 and 10, respectively [101]. In reality damping of the bow hair ribbon in both directions is dominated by the dry friction between individual strands, hence is most likely amplitude dependent.

Note that the characteristic impedance of the cello strings in their transverse direction ranges from 0.4 kg/s to 1.1 kg/s which is a relatively close match to the characteristic impedance of the bow hair in its transverse direction, and is around an order of magnitude smaller than the characteristic impedance of the bow hair in its longitudinal direction. This gives a guideline for the strength of the coupling that can potentially happen between the two systems. The strength of coupling in each particular frequency also depends on where the frequency of interest falls with respect to the resonances of both systems and where the contact point falls with respect to the node or antinode of the closest bow hair mode shapes.

The bow-stick (i.e. the wooden part of the bow) also has some degree of flexibility, and is commonly regarded by players as having a profound effect on the sound and playability of a bowed string. Some players went as far as claiming that they can identify which bow is

used to play, just by listening to the piece. Little evidence was found to support this claim in an experiment comparing the sounds produced by bows ranging from excellent to very poor qualities [103]. On theoretical grounds, too, it is hard to draw a direct link between the bow-stick properties and the string vibrations, given the weak coupling between the stick and the bow hair, and then from the bow hair to the string. This point was reinforced in a study done by Gough [101], in which he did a thorough analysis on the modal properties of a bow-stick and its coupling to the bow hairs.

Based on the evidence at hand, it seems safe to conclude that the definition of a good bow is mostly the matter of its ergonomic features, affecting player's ability to properly execute the intended bow gesture, rather than its vibrational properties affecting the timbre. Weight, balance point, and camber are important factors for that matter; more significantly, when the player aims to execute bouncing bow techniques such as spiccato, sautille, or ricochet [104]. In fact, among the cases that Gough studied the only situation in which the vibrational properties of the bow-stick could play a role was when the player plays bouncing bow techniques on the upper half of the bow (i.e. closer to the tip) [101].

The proper execution of bouncing bow techniques also depend on another property of the bow: its rigid body bouncing mode. The bow is almost pivoted at the frog by the hand of the player and is sitting on the string at some point along its length. The flexibility of the bow hair and the angular moment of the bow make up for a single-degree-of-freedom system that can vibrate at low frequencies. Depending on the position of the contact point with respect to the frog, the bouncing frequency of the bow can vary in the range 6 Hz to 40 Hz [105]. This frequency can be altered, to some extent, by adjusting the firmness of player's hand, and by tilting the bow. Experienced players make use of this vibration mode by adjusting its mode frequency to their intended bouncing frequency.

3.2.3 The finite-width bow

The practical importance of the bow's finite width was first noted by Raman who pointed out the kinematic incompatibility of the perfect Helmholtz motion with a finite-width bow [45]. Assuming a perfect sticking, the portion of the string in contact with the hair ribbon only transposes and maintains its angle with respect to the bow, while the segments of the string on the two sides of the bow will incline and form sharp bends on the two edges of the hair ribbon (see Fig. 3.3). Adding together the bending stiffness of the string, this results in a tendency to slip. This eventually leads to partial mini-slips during the nominal sticking phase, before the main Helmholtz slip happens. The longitudinal compliance of bow hairs ease the situation to some extent, but does not eliminate it. The slips at the bridge side demonstrate themselves as spikes added to the bridge force. In general, the spikes are

irregular and are perceived as added fuzzy noise [92], but under special circumstances they may form a periodic structure [47].

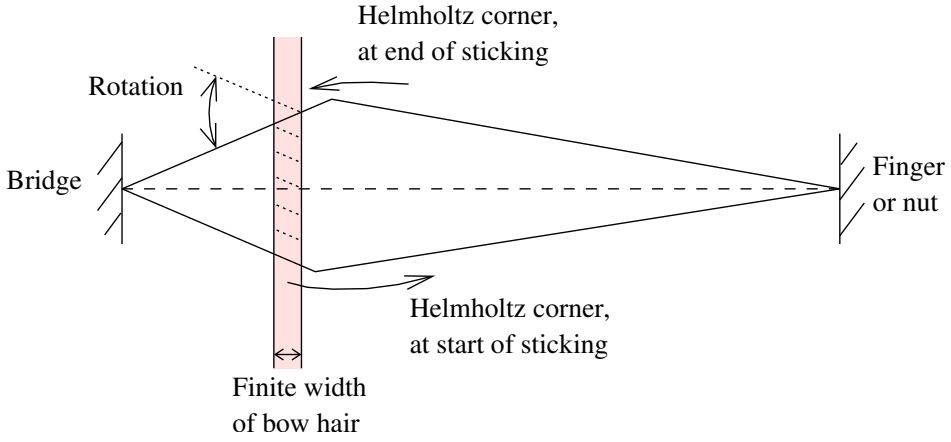

Fig. 3.3 The geometrical incompatibility of the perfect Helmholtz motion with a finite-width bow. The dashed lines show the angle that the portion of string underneath the finite-width bow would have had if the string was perfectly stuck to the bow hair ribbon. The solid line shows the actual shape that a stiff string will take to avoid sharp bends on the two edges of the bow hair ribbon. The amount of rotation marked in the figure is made possible by partial mini-slips during the nominal sticking phase. (After [101])

Another effect of the bow's finite-width is to filter out the frequencies with wavelengths shorter than the width from the sharpening process of the Helmholtz corner[2] [106]. Also, as was shown in [35], the width of the bow can influence transformation of the transverse waves to torsional waves when the former impinge on either side of the bow during the sticking phase. All the effects relating to the finite-width are expected to be scaled down by tilting the bow, hence changing its effective width.

Efforts to include the finite-width into the model of the bowed string were made, first by modeling a two-point-contact bow [92], and later by modeling a bow with multiple hair strands [47]. The latter study used a finite difference scheme to solve the forth-order differential equation of the portion of the stiff string in contact with the bow. Outside the contact region the familiar traveling wave approach was applied, which also gave the boundary conditions of the finite difference region on the edges of the bow. That study used the Friedlander's friction-curve to describe the frictional behavior at the contact region and simulated bow hair compliance in the longitudinal direction with a spring-dashpot for each hair strand. The results of the finite-width model and the single-point contact model were shown to be consistent in the sense that the two converge when the contact width becomes very

[2]This can be thought of as the effect that a finite-size fingernail/plectrum has on a plucked string.

small.

More recently, Maestre et al. [107] made a model of a bowed string that takes into account bow hair compliance in both directions and the finite-width of the bow hair ribbon. Although computationally efficient, their model was developed primarily for sound synthesis purposes and involves some simplifying assumptions. The torsional motion of the string was excluded, some of the parameters used to fit the bridge admittance and the coupling of the two string polarizations were not always physically accurate, the string's damping was adjusted for the best sound quality with no direct link to the underlying physics of damping, the model of the bowhair was very simplistic, and a thermally-inspired model of friction (as will be discussed in Sec. 3.2.5) was used but in a simplified form and with manually adjusted parameters. Given the different scope of that work, it will not be further discussed in this study.

3.2.4 Time-varying bowing parameters and gestural inputs from the player

There are at least three major input parameters involved in the bowing process: bow speed (v_b), bow-bridge distance (β), and bow force (F_N). Not only controlling these parameters simultaneously and precisely (according to a defined trajectory) is out of the capability of a human player, but also a bowing machine can introduce some noise. A slight variation in input parameters may lead to significantly different final result given the chaotic nature of a bowed string. This was clearly the case for the recent experiments carried out by Galluzzo who used a bowing machine to create nominally-identical bowing gestures, which in some instances ended up creating fundamentally different vibration regimes on the bowed string. He also observed a "patchy region" in the large-β range of his Schelleng diagram, which he attributed to the noise of the input parameters by the bowing machine.

Additional less significant parameters to consider are tilt, inclination (bow angle with respect to the top plate), and skewness (bow angle with respect to the string axis). Tilting the bow essentially changes the number of the hairs in direct contact with the string and the effective width of the bow, therefore its effect is not hard to guess based on our discussion in the previous section. The effect of inclination is also straightforward: bow inclination by a certain amount is equivalent to rotating the body admittance matrix in the opposite direction and by the same amount. Bow skewness is perhaps the most complicated of the three to understand. When the bow deviates from being perfectly perpendicular to the string, the contact point of the bow with the string moves by a little bit along the string during each slip cycle. Experienced players constantly use this technique to smoothly drive the bow toward or away from the bridge [108]. A skewed bowing may also excite the longitudinal vibrations of the string.

In recent years, motion capture techniques have been widely used to extract gestural inputs of professional players when playing an actual repertoire [109, 110, 111, 112]. This has provided a large body of data that is interesting both for sound synthesis purposes [109] and for music pedagogy. These results provide a combination of parameters that a professional player uses to achieve a desired tone color and dynamic range, while also taking into account future actions of the player. More relevant to our study, availability of such data gives enough motivation to include some of those parameters into the numerical model, and to compare the results against experiments.

3.2.5 Friction models

The behavior of a bowed string largely depends on the constitutive law governing the friction between the bow and the string, and in this regard, while making physically accurate models of the string and the bow remains an essential component of a realistic model, it may not produce accurate results without a reliable model of friction. The friction behavior involved in the bowing process is dominated by the tribology of the rosin, more so than it depends on the surface condition of the string and the hair strands. In fact, it is much easier to bow a string with a rosin coated rod (preferably made out of a thermally non-conductive material like wood) than it is to bow it with a professional bow that is not coated by rosin.

Rosin is commonly made by boiling the extract of softwood timbres (mostly conifers), and mainly consists of abietic acid. It is an amorphous material, and as such, does not melt at a well-defined temperature. There are variants of rosin, but a common one is a brittle solid at room temperature, becomes relatively soft and formable at $60°C$, turns to a rubber-like sticky material and undergoes a glass transition at $75°C$, and finally becomes fully melted at around $93°C$ [113].

The "Friction-curve" model

As discussed in Sec. 3.1.2, traditionally the friction coefficient between the bow and the string was thought of as a sole function of the relative sliding velocity. This assumption was perhaps reinforced over time by the significant success that the models based on this assumption had in describing the detailed behavior of a bowed string, at least qualitatively. Namely, the friction-curve model could successfully predict Helmholtz motion and other regimes on a bowed string, Schelleng ripples, pitch flattening, and the wolf note. It is known now that any friction model involving a counter-clockwise hysteresis loop can be sufficiently tuned to produce those effects.

The numerical values for the velocity dependency of the friction coefficient was first

measured by Lazarus [114] and later by Smith and Woodhouse [113]. In both studies two rosin coated surfaces were forced to rub against one another with a constant speed, and the friction coefficient was measured as a function of the imposed sliding velocity. Those two studies found fairly similar numbers, although they used different base-functions to find the best fit to the data. The fitted function that Smith and Woodhouse found is

$$\mu = 0.4e^{(v-v_b)/0.01} + 0.45e^{(v-v_b)/0.1} + 0.35, \tag{3.5}$$

where μ is the velocity-dependent friction coefficient. It should be noted that the consistency of the two abovementioned studies does *not* necessarily suggest that the friction coefficient is a function of the sliding velocity; rather it might be a function of one or more internal variables (such as the temperature), which themselves have a functionality of the relative velocity among other variables. If that is true, the constant slipping experiments done by Lazarus and Smith-Woodhouse become a special case of a more general phenomenon, thus their results do not apply to the friction of a bowed string with its quick changes in relative velocity.

As an alternative to the constant slipping data, but still assuming a velocity dependent behavior, Galluzzo measured the drop in the friction coefficient as a function of the velocity jump within a single flyback of a string bowed by a rosin coated rod. He measured force drop at the bridge for several values of normal forces. He then calculated velocity jump and friction coefficient variation based on that.[3] The best fit to his results (what he called the "reconstructed" friction-curve) became

$$\mu = 0.4e^{(v-v_b)/0.7} + 0.35 \tag{3.6}$$

If plotted against one another, the reconstructed friction-curve is much flatter on top when compared to the friction-curve obtained from constant slipping experiments. He also found that the steady response of a bowed string modeled using this new friction law gives a better match to the experimental results obtained by a bowing machine; however, it makes a very poor prediction of the initial transients of a bowed string. The discrepancy between the two measured friction-curves, together with the fact that neither of those were successful in predicting the transients of a bowed string pointed to the fact that the velocity-dependent friction coefficient was a wrong approximation in the first place.

[3] As was pointed out in [92], both variables are linearly related to the force jump.

The thermal friction model

The first body of evidence to raise suspicion on the velocity-dependency assumption was reported in [115] and [113], in which Smith and Woodhouse measured the friction and relative sliding speed between a rosin-coated rod and a wedge, mounted on a vibrating cantilever beam over a wide range of sliding speeds and normal forces. They found that the hysteresis loop, plotted in the friction-velocity plane, was considerably at odds with the result of the simpler steady sliding measurements. They found that the temperature of the rosin plays a central role in the friction force exerted by the bow on the string; indeed, they noted, rosin is already close to its glass transition point at room temperature so partial melting of rosin is possible under normal playing condition.

Using a different approach, Woodhouse et al. deduced the friction and velocity of a bowed string at the bowing point by monitoring the forces exerted by the string on the two terminations and working backwards from a knowledge of the impulse response of that string [116]. They too found hysteresis loops similar to the ones observed in the former study [113], and different with what could be expected from a velocity-dependent model. They also provided more evidence for the partial melting of the rosin by looking at a bowed-on rosin-coated rod under scanning electron microscope [116]. The surface of the rosin layer, on which the string slipped only once, showed trails of melted and re-solidified material.

Assuming a temperature dependent friction model, Smith and Woodhouse [116] proposed the following sequence of events: the tangential force at the contact reaches the limiting static friction force and slipping starts; rubbing of the two surfaces against one another creates heat, softens the rosin and reduces the friction coefficient; once the Helmholtz corner has passed from beneath the contact point, the disturbance force reduces and sticking recommences; heat loss through conduction results in reduction of contact temperature and consequently the increase of limiting friction coefficient again. This self-buffering behavior (earlier studied for skis on ice [117]) produces a time lag in the temperature increase of the rosin layer in response to the change in the sliding speed, hence creates the hysteresis loop observed in earlier studies.

Mathematically speaking, they argued that the heat generated through friction is counterbalanced by convection, absorption and conduction, according to the following law:

$$F_F.\,(v_b - v) = \dot{m}_{out} c_{vr} \Theta_{out} - \dot{m}_{in} c_{vr} \Theta_{in} + \rho_r V_r c_{vr} \frac{d\Theta}{dt} + \int_{-\infty}^{t} g_{\Theta(t-\tau)} \Theta_{(\tau)} d\tau, \tag{3.7}$$

where $\dot{m}_{in}$ and $\dot{m}_{out}$ are the mass flow rates of rosin in and out of the contact patch, c_{vr} is the effective specific heat capacity of rosin (assumed constant), Θ is the temperature

of the rosin, ρ is the density of rosin, V_r is the volume of the contact patch, and g_Θ is a suitable Green's function for the heat diffusion problem. The left-hand term of Eq. (3.7) is the rate of heat generation given by the product of the frictional force and the sliding velocity, and the right-hand terms are, respectively, convection as the cold material flows into the contact region while heated material flows out (the first and the second terms), absorption as the temperature of the material within the contact patch changes (the third term) and conduction into the two neighboring solids (the last term). This formulation can be implemented in time-stepping simulations to calculate the temperature of the rosin at the contact and in each time-step of the bowed string simulation [3].

Once the temperature is known, two types of general behavior can be imagined to find the friction force as a function of the temperature: viscoelastic, and perfectly plastic. If the rosin is melted and the layer of melted rosin is thick enough, it would behave like a viscous liquid, whose viscosity varies by temperature. In that case, the friction force would be linearly related to the relative velocity of the two surfaces

$$F_F = A\gamma_{(\Theta)}\frac{(v_b - v)}{\delta_r}, \tag{3.8}$$

where δ_r is the thickness of the contact patch between bow and string, A is the real area of contact, and γ is the viscosity of the rosin. Conversely, if the rosin is sufficiently solid or if the layer of rosin is very thin, it behaves like a plastic solid, which only deforms once the shear stress reaches the shear yield strength (k_y) of rosin. In this case, k_y is assumed to be temperature-dependent.

$$F_F = Ak_y sgn(v_b - v), \tag{3.9}$$

where $sgn(v_b - v)$ represents the sign of $(v_b - v)$. The corresponding versions of Friedlander's graphical construction of friction-curve for the two abovementioned thermal models are illustrated in Fig. 3.4.

Smith and Woodhouse found that among the two models, the thermal plastic model gives a better match to the stick slip vibrations of the cantilever beam in their experiment; also, it is able to produce hysteresis loops very similar to those obtained in their experiments.

Woodhouse applied this thermal friction model to simulate the bowed string, and compared the results to those of the friction-curve model [32]. For steady bowing, he found the thermal friction model, at least with the set of parameters he used, is more "benign" in that the desired Helmholtz motion was established more rigorously and faster than with the old friction-curve. His results were further extended by Galluzzo, in which he compared the results from both the friction-curve model and the thermal model to the results obtained

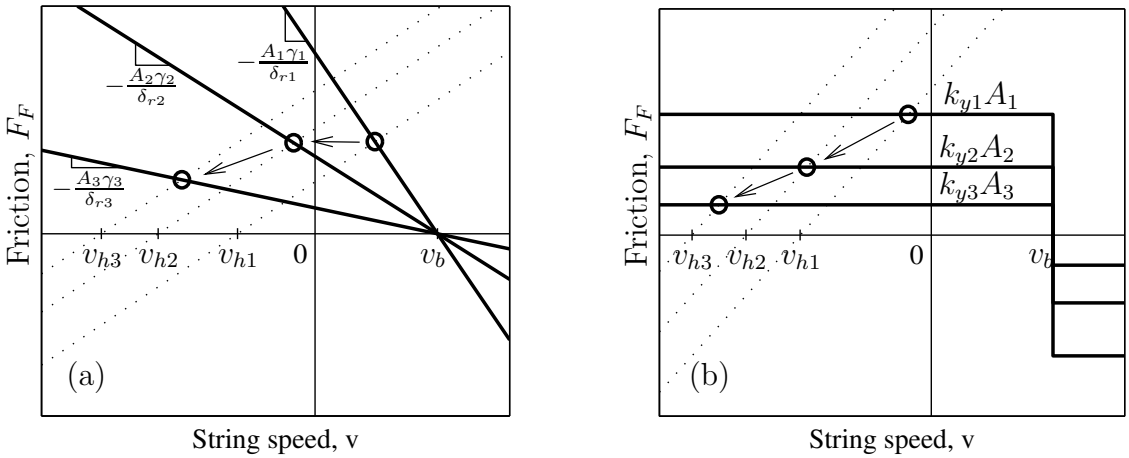

Fig. 3.4 Equivalents of the Friedlander's graphical construction of friction-curve for (a) the "thermal viscous model", and (b) the "thermal plastic model" of rosin friction. Note that as opposed to the case for the classic velocity dependent model, for both thermal models the friction-curve may change between time steps. To illustrate the use of Friedlander's construction, three successive operating points are indicated by circles corresponding to the three load lines indicated by dotted lines. (After [21])

experimentally and using a bowing machine [21]. Galluzzo concluded that although the playability limits predicted by the thermal model better match the experiments (off only by a factor of two), the thermal model clearly fails to predict the transition of Helmholtz motion to double slipping at low bow forces; predicting instead, that Helmholtz motion degenerates almost directly into constant slipping. He also observed an overheating problem with the thermal model where in high bow force and high bow speed, Helmholtz waveforms became progressively more rounded with the slipping phase becoming elongated. Both these observations were in contrast with the experimental results. Another discrepancy that Galluzzo reported was regarding the first slip, when both the bow and the string start from the rest. As the experiments suggest, the friction force is supposed to suddenly jump from a maximum value to a much smaller value, however, the thermal model shows a more gradual decline as it needs the slipping to persist over some time before the rosin heats up, softens, and allows the friction force to drop to a lower value.

Given the above discussion, it is safe to conclude that if one -and only one- state is to be chosen to describe the tribology of the rosin, it would be the temperature. However, some concerns about the model need to be addressed before it can be used reliably to predict the detailed behavior of a bowed string. Research on this matter is currently under way, but below is a list of some challenges and possible improvements:

- As opposed to the viscosity, which can be experimentally measured in a rheometer,

there is no direct way of measuring the yield stress as a function of temperature. To deal with this situation, Smith and Woodhouse defined the relation between the two in a way that fits their constant slipping results (i.e. Eq. (3.5)), when the effective contact area and the effective thickness of the rosin layer were set by guesswork. Those two parameters were defined so that the transition from high yield stress to an almost constant low yield stress happens in a sensible range of temperatures, but any uncertainty in those parameters would propagate to the final results.

- Equation (3.7) is relatively solid in terms of considering all relevant paths of heat transfer; however, some assumptions are involved in the way it is implemented, which may be in need of revision. For instance, the specific heat capacity of the rosin is assumed constant over different temperatures, which also includes the heat needed for the phase change. This assumption may introduce a large approximation as the heat needed for phase change affects the higher range of the temperature more than the lower range (in that case c_{vr} itself becomes a function of the temperature). g_Θ (the Green's function for heat diffusion) is solved assuming one-dimensional heat transfer, and the torsional motion of the string, which involves a larger area in the heat transfer problem, is ignored.

- As the contact temperature rises, it is possible that the viscous thermal model (or a combination of the two models) becomes more relevant in describing the tribology of the rosin. This, together with the above argument, may address the overheating issue observed by Galluzzo. After all, the friction model of Smith-Woodhouse was validated for a limited range of temperatures and there is no good reason to trust it beyond that.

- Both the hysteresis loop and the bridge force signal obtained by bowing machine have shown a significant amount of creeping in the nominal sticking phase. It is relatively easy to include such creeping into the model of the bowed string by simply tilting the vertical portion of the friction velocity relation in either the friction-curve or the thermal model.[4]

- Galluzzo suggested two possible reasons to explain the unphysical gradual drop of the friction force in the first flyback: the "junction growth", and the "rosin build up".

  - Junction growth: If a plastic model is to be believed, the friction force required to induce slipping becomes equal to $k_y A$. Keeping the contact patch under shear force results in a gradual deformation of asperities, which in turn, increases the

[4] More generally, by making it not vertical in any other sensible way.

effective contact area. Different models are suggested to explain this behavior (see for example [118])

  - Rosin build up: As a side effect of the creeping, mentioned earlier, patches of rosin are being gathered in front of the string during the sticking phase. The triggering of the slipping requires that patch to break up, hence an increase in the limiting static friction coefficient, followed by a sudden drop once the slipping has started.

- For small values of normal force and for a relatively large area of contact, the friction force is proportional to the normal force with the constant of proportionality being the friction coefficient (called the Amonton's law). In the microscopic level, the real area of contact is much smaller than the apparent area of contact. The real area of contact grows proportionally with the normal force and as the yield stress of the two surfaces in contact is constant, the friction force becomes proportional to the normal force. However, when the apparent contact area is small (like the contact of two perpendicular cylinders, or the contact of a sphere with a flat surface), it is possible under large normal forces that the real contact area reaches the apparent contact area (called a Hetrzian contact [119]). At that point, for a cylinder-on-cylinder contact, the real area grows with $F_N^{2/3}$ rather than F_N, hence the friction coefficient drops (with $F_N^{-1/3}$) instead of remaining constant. In any case, reaching a Hetrzian contact seems to be the case only for bowing with a rigid rod, whereas with a real bow other parameters such as the hair ribbon bottoming up on the stick or practical playability limits stop the player to reach such high bow forces.

- The idea of junction growth together with the Hertzian contact considerations were put together in a finite difference scheme and were applied to find the limiting static friction coefficient as a function of normal force and the value of constant bow acceleration [21]. Although that method was relatively successful in finding the correct friction coefficient before the first slip (not surprisingly, as it fits a function with three variables to a 2-D grid), it has a tendency to become unstable after the first slip.

3.3 Modeling of a bowed string

Following the approach taken in Chap. 2, after giving an overview on the relevant physical details, we propose ways to implement some of them into our particular modeling scheme. In doing so, it is assumed that the bow never gets detached from the string (i.e. never bounces), the bow is only in contact with one string at a time (excluding double or triple stops), and the bow is in contact with the string at a single point (ignoring the finite-width of the bow).

As the thermal model is not yet up to the task, we will provisionally use the friction-curve model (according to Eq. (3.5)), but will be cautious about that when evaluating the results.

3.3.1 Adding the torsional waves to the model

To implement the torsional waves into our model, they are treated in the same way as we treated the single-polarization transverse vibrations of a non-dispersive string. Two traveling waves were assigned, which get filtered in each round trip to the finger or the bridge. There is no coupling to the body modes, and the values of torsional waves are modified by the amount $\frac{F_F}{2Z_{0R}}$ when passing to the other side of the bow. For friction calculation purposes, Z_{0T} is replaced by Z_{tot} defined in Eq. (3.3), and v_h becomes the sum of four incoming wave terms, instead of two. Aside from the friction calculation part, Z_{0T} remains in effect in the modeling of the transverse vibrations. A constant-Q of 34 is assigned to all torsional modes, 758 Hz and 300 Hz to the fundamental frequency, and 1.8 kg/s and 2.6 kg/s to the characteristic impedance of the torsional waves for open D_3 and C_2 strings, respectively.

3.3.2 Adding bow's flexibility to the model

Perpendicular-to-bow vibrations of the string are coupled to the transverse vibrations of the bow hair, hence to model the former properly, the latter should be taken into account. We assumed that all individual hairs are active in the transverse vibrations of the ribbon. The β_{bow} (distance from the contact point to the frog divided by the full length of the hair ribbon) is considered constant (typically at 0.31) within the short period of simulation. If a time-varying β_{bow} was intended, the loop filters should have been redesigned at every time-step, or less costly, at every several time-steps.

Table 3.1 Summary of cello bow properties used in simulations

Hair strands	T_{0b}	m_b	f_{0bL}	Z_{b0L}	Q_{bL}	f_{0bT}	Z_{b0T}	Q_{bT}
290	70 N	0.0089 kg/m	1950 Hz	10 kg/s	10	75 Hz	0.79 kg/s	20

Transverse vibrations of the bow hair and the bowed string are coupled at the contact point. The constraint at the contact point is that they share a common velocity and apply the same amount of force to one another in opposite directions (assuming they never get detached). To find the unknown common velocity and the mutual force, the unperturbed velocity of the string and the bow are first calculated in the absence of one another (called $v_{hY'}$ and v_{bhT} respectively). With simple math it can be shown that the matched velocity (v_{match}) is equal to

$$v_{match} = \frac{v_{hY'}.Z_{0T} + v_{bhT}.Z_{b0T}}{Z_{0T} + Z_{b0T}}, \tag{3.10}$$

where Z_{b0T} is the characteristic impedance of the bow hair ribbon in its transverse direction. The resulting fluctuating force in the contact region (F_{Nfluc}) will then become

$$F_{Nfluc} = 2Z_{0T}.(v_{match} - v_{hY'}). \tag{3.11}$$

This force is used to modify the relevant incoming waves before they are passed to the other side of the bowing point. It is also added to the nominal value of the bow force, supplied by the player, to give the effective bow force, as in Eq. (3.12). Since the bow force is being dynamically updated for each time-step, the friction-curve should be re-scaled, accordingly.

$$F_{Neff} = F_{Nnom} + F_{Nfluc}. \tag{3.12}$$

Longitudinal vibrations of the bow hair can also be modeled using the traveling-waves approach, and with the framework already established for the transverse vibrations of the string. In the presence of bow hair longitudinal vibrations, the effective bow velocity will have a fluctuating component caused by the velocity of the contact point on the bow hair relative to the bow-stick. This relative velocity can be found from

$$v_{bFluc} = v_{b\ 1in\ L} + v_{b\ 2in\ L} + \frac{F_F}{2Z_{b0L}}, \tag{3.13}$$

and the effective bow speed can be calculated from

$$v_{bEff} = v_b - v_{bFluc}, \tag{3.14}$$

where, as before, F_F is the instantaneous friction force between the bow and the string, v_b is the nominal bow speed provided by the player, and $v_{b\ 1in\ L}$ and $v_{b\ 2in\ L}$ are the incoming longitudinal velocity waves, from the tip and the frog respectively, arriving at the contact point. It is noteworthy that since the friction-curve is a function of bow speed, it should be recalculated with v_{bEff} instead of v_b at each time-step.

In a similar fashion as discussed for the modeling of the body, the stick modes are taken into account using a set of independent resonators. Fourteen modes are considered in this case whose frequencies, modal masses, and mode angles were all extracted from [101]. The flexibility of the bow-stick was lumped at the tip side as the frog was assumed much more heavily damped by the grip of the player's hand or the bowing machine. Stick modes are coupled to both transverse and longitudinal vibrations of the hair ribbon. The excitation of the stick modes can be calculated from

$$F_{b,k} = Z_{b0L}.2.v_{b\ 1in\ L}.cos\theta_{bk} + Z_{b0T}.2.v_{b\ 1in\ T}.sin\theta_{bk}\ , \tag{3.15}$$

where θ_{bk} is the spatial angles of the k^{th} stick mode with respect to the bowing direction (longitudinal direction of the bow), and $v_{b\ 1in\ L}$ and $v_{b\ 1in\ T}$ are the incoming longitudinal and transverse velocity waves coming from the tip respectively.

As was pointed out in Sec. 3.2.4, the hand of a player, as well as any realistic bowing machine will add some noise to the bowing parameters, most significantly on the bow force and the bow speed. It is interesting to examine the sensitivity of the bowed-string model to such noises in the input parameters. In this regard, we included the capability of adding a brown noise[5] to the bow force and the bow speed (i.e. to Eqs. (3.12) or (3.14)) whose range was a known percentage of the nominal value of the corresponding parameter.

3.3.3 Static alterations of tension for the bow and the string

The tension of both bow hair ribbon and the bowed string are statically increased in response to the transverse force applied at the bowing point (called F_T). This effect is different from the pitch glide that was discussed earlier in Sec. 2.2.4. The increase in the tension of a string can be obtained by the following equation:

$$\delta_T = ES\left(\sqrt{\left(\frac{F_T\beta(1-\beta)}{T_0+\delta_T}\right)^2+\beta^2}+\sqrt{\left(\frac{F_T\beta(1-\beta)}{T_0+\delta_T}\right)^2+(1-\beta)^2}-1\right) \tag{3.16}$$

Equation 3.16 can be also applied for the increase in the tension of the bow hair if β, L, ES, and T_0 are replaced by their equivalents for the bow hair ribbon.

The results of a tensile test (data provided by Fan Tao from D'Addario) is used to calculate ES for a C_2 "Thomastik Spirocore" cello string, which was estimated at 8270 N (virtually the same value was obtained for a G_2 Spirocore string as well). We had no measured data for the D_3 string, but the steel core of a D_3 "Kaplan solutions" string has a diameter of 0.015 inches, which results in an ES of approximately 23350 N (the windings make a small contribution to the longitudinal stiffness of a string). The lateral force applied to a string is the triangular sum of the normal bow force and the floor level of the friction force (summing to $\sqrt{1^2+0.35^2}F_N \approx 1.06F_N$). However for the bow hair, only the normal bow force acts in its transverse direction, while the floor of the friction force results in an increase of the tension on one side of the contact point and an equal reduction on the other

[5] Brown noise is a random noise whose power density is proportional to $1/f^2$.

side. Assuming all strands of bow hair are deflecting together in the transverse direction, ES of the hair bundle becomes 43960 N.

Figure 3.5 shows the percentage variation in the frequency of the first mode as a function of the normal bow force and the relative placement of the bow and the string. The plots are shown for open C_2 and D_3 strings, as well as the bow hair when placed on those strings. As reported in [21], an experimental fit to the maximum bow force for a D_3 string, beyond which the Helmholtz regime is not sustainable, is approximately $0.13/\beta$ (for a bow speed of 0.05 m/s). Scaling that value for the C_2 string results in a maximum bow force of $0.28/\beta$. Those limits are shown by the solid white lines in Figs. 3.5a and 3.5b. The limits of the color axes are also set to only cover the range of values in the playable range, anything beyond that is shown by the same dark-red color. There is no such criteria for the bow hair, but for practical reasons the player always plays close to the frog when he/she wants to apply a large bow force. The first reason is that the bow hair will bottom out on the bow-stick if a large bow force is applied around the middle of the bow length, and the second reason is that applying a large force away from the frog requires a large torque to be provided by the players wrist.

As shown in Fig. 3.5, the maximum increase in the frequency of the C_2 and D_3 strings is respectively 0.8% and 0.4% of their nominal value. To put that in perspective, the threshold of human perception for a shift in frequency is roughly 0.2% of its nominal value [120]. If the string's tension would change profoundly depending on bow force (across the typical range of bow force used by a player), violin playing in the manner we know it today would hardly be possible. A further discussion of the pitch flattening/sharpening is provided in Chap. 5. The alteration of the frequency and tension for the bow hair is much larger than that of the strings and it seems to be a significant factor in defining the vibrations of the bow hair.

As the contact point of the bow with the string does not change dynamically in our model, the tension of the bow hair and the bowed string is adjusted once before each simulation begins and stays the same for the duration of that simulation.

3.3.4 Initialization of the model with the Helmholtz regime

Among the endless possibilities, two kinds of simulations will be carried out within this study: The Guettler diagram and the Schelleng diagram. The Guettler diagram looks at the initial transients when the bow force stays constant and the bow accelerates monotonically from rest. As a result both the string and the bow are at rest in the beginning of the simulation.

On the contrary, the Schelleng diagram looks at the ability of a bowed string to sustain the Helmholtz motion when the bow force and the bow speed are kept constant. In accordance with Schelleng's assumption, the Helmholtz motion should be properly initialized at the

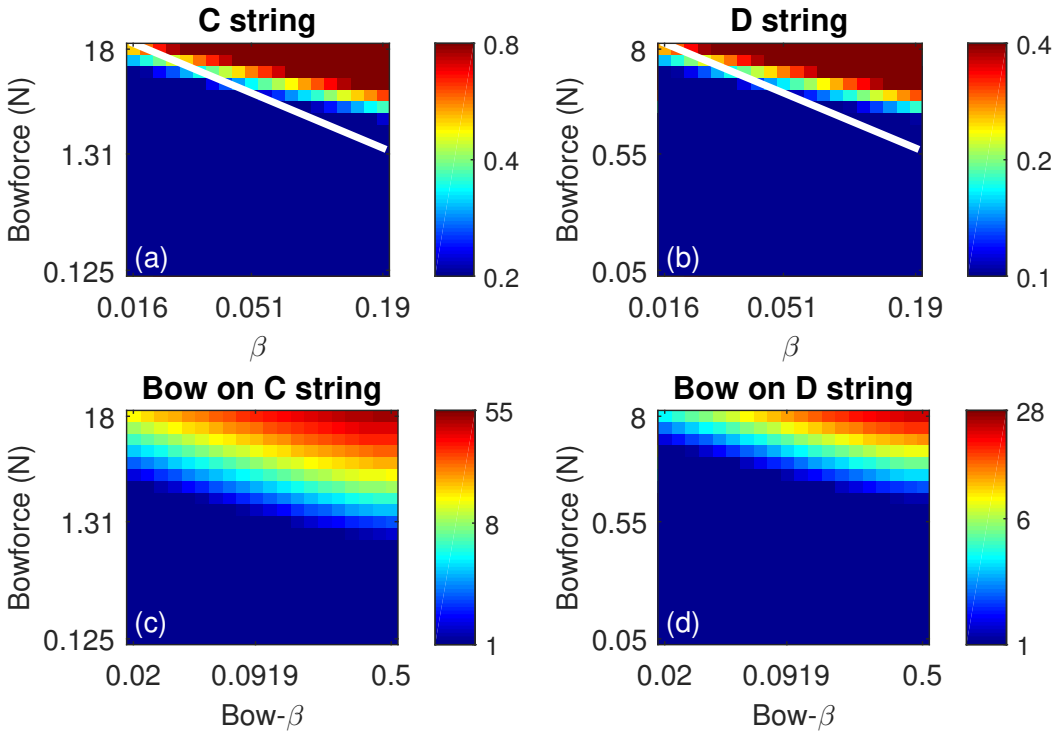

Fig. 3.5 Percentage variation in the frequency of the first mode as a function of the normal bow force and the relative placement of the bow and the string. (a) and (b) show the frequency deviation for open C_2 and D_3 strings, while (c) and (d) show the frequency variation of the bow hair ribbon. Note the difference in their horizontal axes. The solid white lines in (a) and (b) show the approximate maximum bow force within which a Helmholtz motion is stable, for a bow speed of 0.05 m/s.

beginning of the simulation. In order to do that, the traveling waves corresponding to the transverse vibrations of the string in the bowing direction were initialized by the expected sawtooth waves of proper magnitude and phase. There were multiple recursive (i.e. IIR) filters used in our model, which should be initialized properly. Otherwise, the "inertia" of those filters puts a drag on any vibrations of the string at the beginning of the simulations. To overcome this issue, the Helmholtz regime was imposed on all filters for a few cycles before the actual simulation starts, so that they get "warmed up" in a sense.

The detailed vibrations of the bowed string will be different from the ideal Helmholtz motion due to effects such as pitch sharpening/flattening, Schelleng ripples, dispersion, and extended slip phase. This inconsistency results in some extra disturbance within the first few periods of simulation, which may degenerate an otherwise-stable Helmholtz motion. Another source for such unintended disturbances is that the body modes and other traveling waves in the model, aside from the two associated with the vibrations of the string in the bowing direction, start from zero in our current initialization of the model.

3.4 Waveform identification

3.4.1 Bridge force signature waveforms

Before describing the waveform identification algorithm, it is helpful to review different regime types that can be formed on a bowed string[6]:

- **Helmholtz motion** is characterized by one stick and one slip per cycle and is the goal for the vast majority of bowing gestures. This vibration regime involves only a single stick and slip per period and is formed by a single Helmholtz corner traveling along the string and triggering stick or slip any time it passes underneath the bow.
- **Double/multiple slip** which corresponds to multiple Helmholtz corners traveling along the string. This motion is typically caused if the normal bow force is too small, thus one or more untimely slips occur. It can be characterized by the "whistling" sound of a bowed string.
- **Raucous motion** is typically caused when the normal bow force is too large, and as a result the Helmholtz corner cannot trigger a slip when it arrives at the bow from the finger side. This regime can be characterized by a "crunching" sound.
- An **ALF note** is a musical tone with a frequency much lower than that of the first string mode. If the bow force is too large to form a Helmholtz regime, vibrations of a

[6]Not all of these vibrations regimes will be identified by our algorithm.

bowed string would usually become non-periodic and irregular leading to the raucous regime. However with a precise control of the bowing parameters those vibrations may become periodic, in a sense that the Helmholtz corner repeatedly reflects once, or multiple times, between the bow and the finger before it gains enough strength to trigger slipping[7] [122].

- A **decaying (or constant slipping)** regime occurs when the sticking phase never persists for a significant amount of time. This is the case if a very small bow force is used.

- **S-motion** is similar to the Helmholtz motion in that there is a single stick and slip per nominal period, but the s-motion involves large ripples superposed on the expected sawtooth bridge force. S-motion is formed if a large bow force is applied and when the bow is placed near, but not on top of, a nodal point of one of the first few modes of the string (i.e. when $1/\beta$ is close to an integer).

- **Helmholtz crumples** regime is a subcategory of Helmholtz motion that is created when the bow is placed exactly on a nodal point of a string mode. In that situation, the bow may not feed energy into that mode and its integer multiples and as a result those modes are absent from the spectrum of the otherwise sawtooth-shaped bridge force. In the time-domain, the upward slope of the bridge force is a staircase rather than a straight line. Because of the finite-width of the bow and the flexibility of the bridge, Helmholtz crumples are rare in practice. A particularly interesting musical effect that can be created by Helmholtz crumples is to place the bow at exactly half-way from the finger to the bridge, in which case all the even harmonics will be missing from the spectrum and as such the produced sound would be similar to that of a clarinet.

- **Double/multiple flyback motion** is formed by an odd number of closely spaced and equally strong Helmholtz corners traveling along the string. The sign of the adjacent corners is always opposite to one another, therefore their sequence causes a number of stick-slip alternations. The result is an unpleasant "shrieky" sound that players attempt to avoid. Figure 3.6 shows the time-space diagram of a double flyback, for which the Helmholtz corners are spaced apart by $\beta P/2$ and can be thought of as the string deforming in a "W" shape rather than a "V" of the Helmholtz motion. Double/multiple flyback motion is initiated if the player applies an incorrect gesture at the beginning of the note, and it is particularly hard to get rid of as its region of stability largely overlaps with that of the Helmholtz motion [123]. It means that there

[7] Guettler pointed out that the slipping phase may also be triggered by reflected torsional waves [121].

is no adjustment that the player can make to initiate a transition to the Helmholtz regime, except for stopping the note and starting over.[8] On the bright side, the player can rest assured that there will be no switching to double flyback once the Helmholtz regime is established, and for the same reason we do not expect to see any instances of double flyback in our simulations which are initialized with a Helmholtz regime. Despite the musical significance of the double flyback regime, it has received very little attention in the literature with the exception being a rather old study by McIntyre and Woodhouse [123].

Figure 3.7 shows typical examples of different vibration regimes discussed above. The data is measured experimentally by Galluzzo and the figure is reproduced from [21]. The figure does not contain any example of ALF note and Helmholtz crumples.

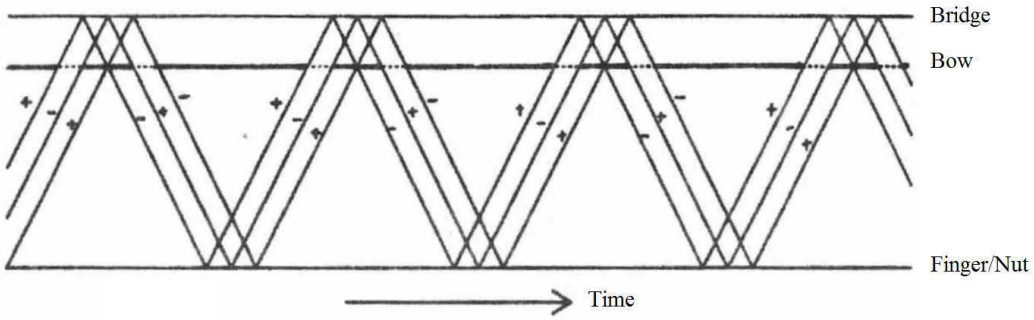

Fig. 3.6 Space-time diagram illustrating the kinematics of the double flyback regime. The states of sticking or slipping are shown on the figure with the line in the position of the bow, where a thick solid line represents sticking and a thin dashed line represents slipping. (From [123])

3.4.2 Waveform identification algorithm

The waveform identification routine used in this study is a revised version of the algorithm introduced by Woodhouse [32] and further expanded by Galluzzo [21]. The major distinction of the current version is that it also makes use of the stick-slip state of the bowed string, in addition to the bridge force that was used by the earlier versions. The stick-slip state signal is transformed to a corresponding ideal bridge force (i.e. the force increases linearly as sticking persists, and drops suddenly when slipping is triggered) and analyzed in the same way as the actual bridge force. The algorithm primarily looks at the transformed stick-slip signal for classification but the bridge force signal is still used to identify cases

[8] This contrasts with the case for double slip or raucous regimes for which the player can increase or decrease the amount of normal bow force to make a transition to the Helmholtz motion.

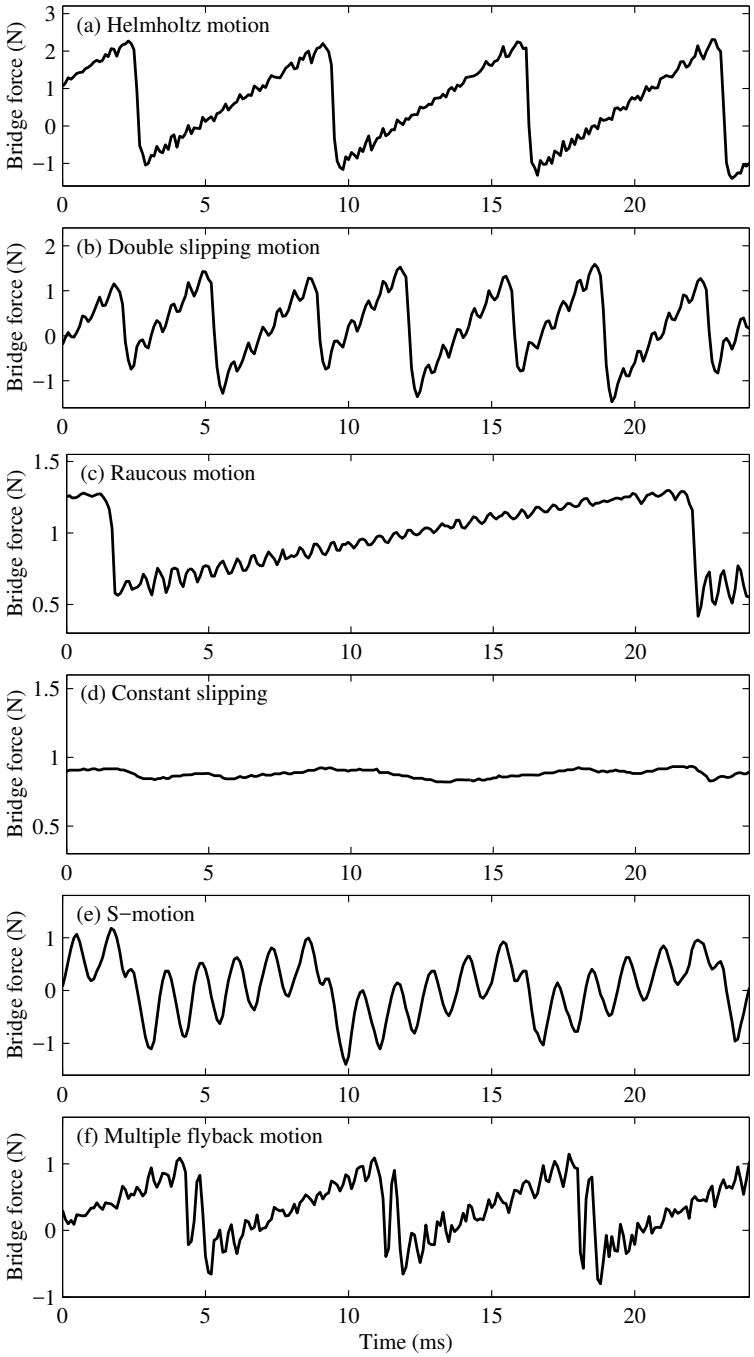

Fig. 3.7 Typical examples of the six most common types of motion on a bowed string. (a) Helmholtz motion manifests itself as a saw-tooth wave; (b) double slipping motion as a double saw-tooth wave; (c) raucous motion as a prolonged or irregular saw-tooth wave; (d) constant slipping as a generally flat and featureless signal; e) S-motion as very large ripples superimposed on a saw-tooth wave; and (f) multiple flyback motion as a saw-tooth wave with two (or sometimes more) flybacks. The horizontal scales of the above plots are the same, although the vertical scales are not. (From [21])

such as the S-motion. The algorithm is primarily developed to classify a waveform produced by a constant bow speed, but it can deal with the result of an accelerating bow as well if the signal is first normalized to the instantaneous bow speed. Such re-scaling is not needed if we are looking at the stick-slip history rather than the bridge force. The routine goes over individual episodes of stick and slip one by one, therefore it can be used to calculate the pre-Helmholtz duration at the beginning of a note as well. The steps taken to classify each waveform, described below, largely overlap with their original description in [21]. The interested reader is referred to the original reference for more details and examples.

The sawtooth shaped signal is first processed by subtracting the expected upward slope. The result is a staircase wave whose horizontal sections represent sticking episodes, and its (almost-) vertical portions represent slipping episodes. The ripples (either caused by the secondary waves or by the S-motion) are later removed from the staircase using a rectangular averaging filter with a duration of βP, which is the theoretical period of the ripples. A histogram is then calculated from the smoothed version of the staircase, the peaks within which identify the significant episodes of sticking. A sample of the processed bridge force and its histogram are shown in Fig. 3.8.

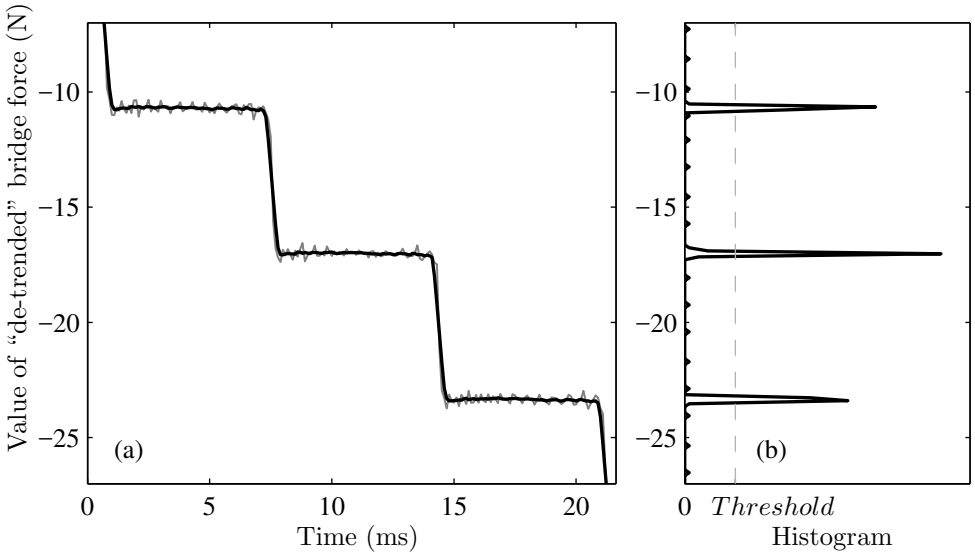

Fig. 3.8 Typical output from the string vibration waveform identification algorithm. (a) shows a normalized and "de-trended" sample of measured bridge force waveform; the gray and black lines show the result before and after being filtered, respectively. (b) shows the histogram of the data, with the same vertical scale; the three peaks in the histogram correspond to the three "steps of the staircase" in (a). The dashed gray line in (b) indicates the threshold set to identify significant sticking episodes. The data in this figure corresponds to a Helmholtz motion. (From [21])

The constant slipping (or decaying) cases are identified if the histogram contains no signif-

icant peaks. The theoretical spacing between the peaks for a Helmholtz motion is $2v_b Z_{0T}/\beta$. An untimely slip is identified if the spacing between two consecutive peaks is significantly shorter than the expected value. If that spacing is much larger than the theoretical value, particularly if that is accompanied by very large peaks, it indicates a raucous motion. If the spacing between the peaks is close to the expected value, the motion is deemed to be of the Helmholtz regime except when the difference between the filtered and unfiltered versions of the staircase is too large, which is an indicator of the S-motion. ALF notes can be identified within the samples initially classified as raucous motion by their strong periodicity and a dominant frequency much smaller than that of the first string mode. The distinction between multiple slip and the decaying regimes, between Helmholtz motion and S-motion, and between Helmholtz motion and double slip at large β values is not always obvious and the outcome depends very much on the parameters of the classification routine. In fact, there are many cases where a human listening to the sound files cannot distinguish those regimes either. This uncertainty should be kept in mind before drawing strict conclusions based on the classified results of the model.

3.5 Summary of findings

The development of a detailed model of a bowed string was described in this chapter. In the next two chapters, we will see the application of this model in studying some aspects of a bowed string. There is no easy way to examine the accuracy of a bowed-string model, comparable to the way that the plucked-string model was evaluated in Chap. 2. Indeed, it has been demonstrated in [21] that it is well possible for a particular model to make a better prediction of the steady state response of the bowed string, while another model is more successful in predicting its transients. Given the accurate modeling of the string and the body, as well as the number of physical details considered for the bow, it is expected that the model can predict the correct trend of change and its significance in response to a change in one of the input parameters. The most dubious part of the model is the friction, and we will remain cautious about that, when evaluating the results.

Chapter 4

Probing the minimum bow force using time-domain simulations

The development of a highly-refined model of a bowed string was discussed in the two earlier chapters. In this chapter, that model is used to study the lower limit of bow force in steady-state bowing. The basis for this evaluation is the concept of "playability" of an instrument brought forward by Woodhouse in the 1990s [24]. The minimum bow force is a particularly important property of a bowed string as it directly relates to the vibrational properties of the instrument (the admittance of the body at the string termination at the bridge). A modification of the classical theory for the minimum bow force is derived and implemented. The new model is used to explore the effect of a bridge termination with a single and several resonances. The influence of coupling to sympathetic strings and the second polarization direction of the main string motion are studied separately. Following, the influence of the torsion, string stiffness and body resonances on the all-important perturbation force at the bowing point is analyzed, one parameter at a time. Following, a thorough exploration of the lower limit of bow force is performed, including an analysis of a property of the string motion ("sawtoothness") within the playable area above the minimum bow force limit. This is done for different bridge terminations (single resonance at different frequencies and modal mass, multi-resonant cello-like). These simulations give new insights into the reduction of the allowed range in bow force close to a strong body resonance (a.k.a. the "wolf note").

4.1 Theoretical developments of the bow force limits

When a player plucks a guitar string, almost regardless of the strength and the position of the pluck, it will lead to a "musical" guitar sound with a pitch very close to the first mode frequency of the string. By contrast, not all gestures applied to a bowed string lead

to the desired "singing" sound: a bowed string is a nonlinear oscillator, capable of a richer repertoire of vibration regimes than a plucked string. This motivates the investigation of factors influencing the ease of playing, or "playability", which can be somewhat independent of questions relating directly to sound quality. Two famous examples of playability factors are the minimum and maximum bow forces.

Recall that the Helmholtz motion, which results in the singing sound of a bowed string, is formed by a single corner, traveling back and forth along the string and triggering slip and stick when passing underneath the bow. If the player does not apply enough normal bow force, the friction may be too weak to hold the string until the corner arrives, thus an untimely slip occurs during the nominal sticking phase. This results in more than one slip per cycle and a consequent "surface" sound. On the contrary, if the bowhair's grip on the string is too strong, the disturbance force caused by the arriving corner may be insufficient to trigger the slip. This results in a chaotic motion of the string that leads to a "raucous" or "crunchy" sound. The boundary between the range of bow forces, within which the Helmholtz regime is sustainable, and those two cases mentioned above are called the minimum bow force and the maximum bow force, respectively.

Distinctions should be made between the minimum bow force and the more familiar phenomenon of the wolf note. For the wolf note to occur the bow force should be smaller than the minimum bow force for that particular set of β and bow speed, but not all instances of bow force below the minimum bow force lead to a warbling sound. In order for that to happen, the bow force should also surpass a maximum limit above which the double/multiple slip is not sustainable either, so that the result becomes an alternation between the Helmholtz motion and double/multiple slip [24].

Early work by Raman [89], later built upon by Schelleng [23], led to simple approximate formulae for the minimum and maximum bow forces. Of the two, the former makes a better candidate to account for differences between the playability of different instruments, or for the note-by-note variations on a given instrument. A string that is terminated at rigid boundaries has a minimum bow force very close to zero, which binds this property very closely to the bridge admittance. On the contrary, the maximum bow force is almost independent of the properties of the body; also, it is most likely the case that the maximum bow force available to the player is limited by two other factors before it reaches the maximum bow force: excessive pitch flattening and too much noise because of the partial slips.

In the remainder of this section Schelleng's work on the minimum bow force is reviewed, together with an extension of his argument by Woodhouse [24]. In the following section, the analysis is extended to a more general form involving less restrictive assumptions. The revised model predicts some significant differences of behavior compared to the earlier work,

and these predictions are verified using time-domain simulations. Finally, some particular physical details are discussed to show how they may affect the minimum bow force: torsional motion of the string, the presence of sympathetic strings, and out-of-plane vibrations of the string.

4.1.1 Schelleng's argument on bow force limits

Schelleng's argument of minimum bow force [23] runs as follows: The bridge gets excited by the sawtooth-shaped force applied by the string; the resulting displacement amplitude of the bridge is calculated assuming it acts like a dashpot; and the portion of the string between the bridge and the bow is treated quasi-statically to calculate the perturbation force at the bowing point according to the static tension of the string and its angle with respect to the bow at the bowing point. If the calculated perturbation force for a particular combination of bow force and bow-bridge distance exceeds the limiting static friction force at the bowing point, the Helmholtz motion becomes self-contradictory, thus the string motion would involve two or more slips per string period. Note that this criteria does not make any claims about the formation of the Helmholtz motion in the first place. In general, the formation of the Helmholtz motion is much harder than maintaining it, as is demonstrated numerically in [30].

Mathematically speaking for an ideal Helmholtz motion, the bridge force is a sawtooth waveform with the ramp slope of $T_0 v_b/\beta L$, interrupted by sudden jumps of magnitude $T_0 v_b/\beta L f_0$. It is worth clarifying that for an ideal Helmholtz motion the force at the bridge is a perfect sawtooth with vertical drop as opposed to the displacement at the bowing point, which is an asymmetrical sawtooth with an upward slope associated with the sticking phase and covering $(1-\beta)^{th}$ of the period, followed by a downward slope associated with the slipping phase that covers the remaining β^{th} of the period. If the bridge reacts as a resistive end-support with resistance R, its velocity would be proportional to the applied force. This results in a quadratic-form displacement within each cycle that can be formulated as

$$D_{Bridge}=\frac{T_0 v_b t^2}{2R\beta L}+D_0, \qquad -\frac{1}{2f_0}< t <\frac{1}{2f_0}. \tag{4.1}$$

The origin of time here is chosen at half way through the cycle and D_0 is the integration constant.

Treating the short segment of the string between the bow and the bridge quasi-statically, such displacement at the bridge would result in a perturbation force at the bowing point that can be calculated from

$$F_{pert} = \frac{{T_0}^2 v_b t^2}{2R\beta^2 L^2} + K_0, \quad -\frac{1}{2f_0} < t < \frac{1}{2f_0} \ . \tag{4.2}$$

The constant K_0 can acquire a non-zero value, making use of indeterminacy of the friction force at the sticking phase. This non-zero value includes the effect of the displacement offset at the bridge and at the bowing point. The value of K_0 can be found by enforcing the condition that the perturbation force at the bowing point is zero during the slipping phase, a result of the fact that the force should be solely defined by constitutive law governing the friction force. Imposing that condition, the constant K_0 becomes

$$K_0 = -\frac{v_b Z_{0T}^2}{2R\beta^2}. \tag{4.3}$$

Replacing K_0 into Eq. (4.2) gives a parabolic shaped perturbation force with the peak value $-K_0$ at time zero (i.e. half way through the Helmholtz cycle). Keeping in mind that the floor level of the friction force is ignored so far, the perturbation force should not exceed $F_N(\mu_s - \mu_d)$ for the Helmholtz motion to be self-consistent. μ_d is the friction coefficient at the maximum sliding speed within the cycle, and is responsible for pulling the bowing point sideways toward the bowing direction. Keeping the above argument in mind, the normal bow force should be greater than a minimum level, called F_{min}, so that the static limiting friction force becomes greater than the perturbation force at the bowing point added to the floor level of the dynamic friction force; or

$$F_{min} = \frac{v_b Z_{0T}^2}{2R\beta^2(\mu_s - \mu_d)}. \tag{4.4}$$

The primary focus of this study is on the minimum bow force, but for future references it is worthwhile to mention Schelleng's maximum bow force [23] as well:

$$F_{max} = \frac{2 v_b Z_{0T}}{\beta(\mu_s - \mu_d)}. \tag{4.5}$$

By combining Eqs. (4.4) and (4.5) Schelleng drew his now-famous diagram that maps the playable range in the bow force versus bow-bridge distance plane in log-log scale. A schematic of the Schelleng diagram is shown in Fig. 4.1. On the log-log scale, the maximum bow force line has a slope of -1, while the minimum bow force has a slope of -2, which means the playable range becomes narrower as the bow gets closer to the bridge. The two limits will cross at some point creating a wedge like shape in the playability plane. This simple model predicts that the string is not playable if the bow is placed closer to the bridge than the limit set by the apex of this wedge. Schoonderwaldt et al. [22] have argued that the playable range would indeed become wider in linear scale as the bow moves toward the bridge, except

when it gets very close to the tip of the wedge. Whether or not the player feels more control playing closer to the bridge depends on the answer to the question of whether the human perception of force is on a linear or logarithmic scale; in either case, there is no doubt that the player should work literally harder to play close to the bridge as he/she is required to use a larger bow force.

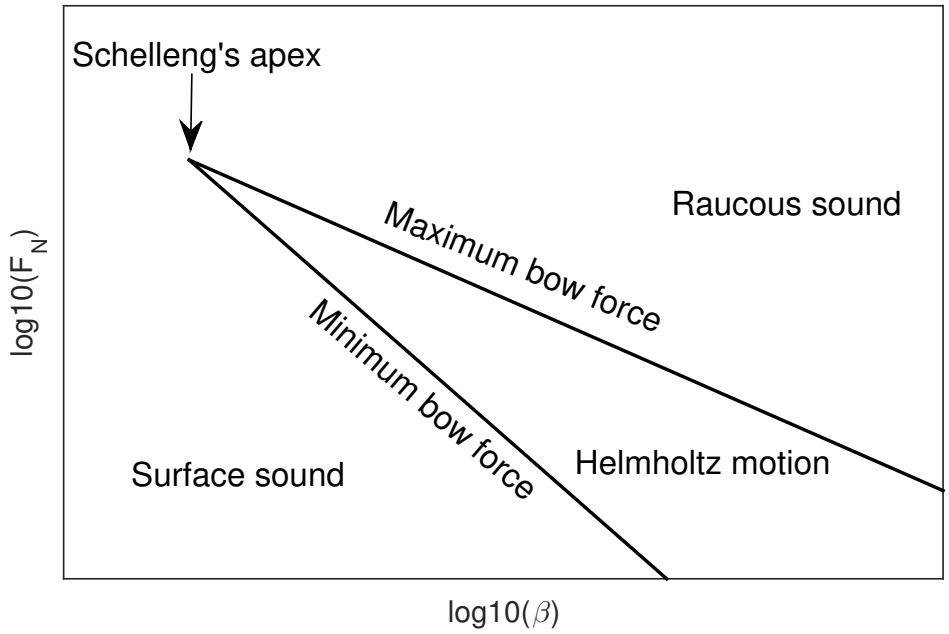

Fig. 4.1 The "Schelleng diagram", the plot of the playable range in log-log scale. The horizontal axis represents the normalized bow-bridge distance and the vertical axis represents the normal bow force applied by the player. The playable range falls below the maximum bow force according to Eq. (4.5), and the minimum bow force according to Eq. (4.4).

Schelleng himself, proposed two particular corrections to Eqs. (4.4) and (4.5). The first correction is concerning μ_d (i.e. the friction coefficient at the maximum sliding speed). Following the maximum sliding speed, that is equal to $\frac{v_b(1-\beta)}{\beta}$ for an ideal Helmholtz motion, μ_d becomes a function of the parameters β and v_b, depending upon the shape of the friction curve. Schelleng [23] assumed a hyperbolic friction curve with asymptotic value $\mu_d^{'}$ and a velocity offset v_0, and from that he found a more general form of Eq. (4.5) as

$$F_{min}=\frac{Z_{0T}^2}{2R(\mu_s-\mu_d^{'})} \cdot \frac{v_b+\beta v_0}{\beta^2} \tag{4.6}$$

The term βv_0 , in particular, results in the minimum bow force limit to be a curved line, even in the log-log scale [22]. In the same line of study, Schumacher found a modification

to the maximum bow force limit for a more general class of friction-curve models [99]. The correction to both minimum and maximum bow forces become less important when the player uses a larger bow speed.[1] In any case, the velocity-dependent friction coefficient is now known to be wrong in some respects [113, 32], so the details of this correction are subject to debate. That said, the hysteresis loop in the F_F-v plane will still have an almost perfectly vertical portion, whose maximum value can be regarded as μ_s, and the friction force drops to its minimum value at the maximum sliding speed, which can be called μ_d. As a result, switching to a more realistic friction model should not change the results in a drastic manner.

Another modification that Schelleng proposed for the bow force limits is to take into account the torsional motion of the string. As was argued in Chap. 3, the friction force from the bow is applied to the surface of the string, away from its center-line, and causes twisting in the string when pulling it aside. In that regard, the effective characteristic impedance of the string from the bow's perspective would be $Z_{tot}=Z_{0T}Z_{0R}/(Z_{0T}+Z_{0R})$ where Z_{0R} is the characteristic torsional impedance of the string. In order to take that effect into account, Z_{0T}^2 in the numerator of the minimum bow force should be replaced with $Z_{0T}Z_{tot}$, and Z_{0T} in the numerator of the maximum bow force should be replaced with Z_{tot}. The expected effect is a reduction in the minimum and maximum bow force by the same factor. We will further investigate this issue throughout this chapter.

4.1.2 Incorporating measured body behavior

There were three restrictive assumptions involved in Schelleng's argument: (a) The excitation force at the bridge can be approximated by the force resulted from a perfect Helmholtz motion; (b) the short segment of the string, between the bow and the bridge, can be approximated as a straight line, thus be treated quasi-statically; (c) the bridge acts as a resistive support with no resonating component.

Woodhouse argues that the least robust of the three is the last of the above [24]. The first problem with the resistive-bridge assumption is that there is no straightforward way to calculate the effective resistance for different instruments, or for different notes played on the same instrument. Schoonderwaldt et al., in the appendix of [22], proposed a way to calculate the equivalent bridge resistance from a known set of decay rates for coupled string-body modes. The Q factor of the string modes vary based on the played note and are not known apriori, although they can be calculated with some effort if the properties of the string and the bridge admittance are known. The second, and a more fundamental issue with Schelleng's argument, is that it ignores the relative phase of the bridge motion with

[1] In that situation the sliding speed becomes so large that μ_d becomes almost equal to its asymptotic value for all combinations of bow force-β.

respect to the string vibrations. Based on the resistive-bridge assumption, the second slip may only occur at the middle of the sticking phase; whereas if that restrictive assumption is relaxed, the second slip may occur anywhere within the sticking phase.

In responding to these concerns, Woodhouse introduced a way to consider a more realistic multi-resonance bridge case. His model can be regarded as the first to relate the minimum bow force to the measured properties of the instrument. The general argument is the same as Schelleng's, with the difference being that Woodhouse applies the sawtooth excitation force to the measured bridge admittance. His method also searches for the maximum bridge displacement within the whole sticking phase. To start with, Woodhouse's method breaks down the sawtooth excitation into its harmonic components by expressing it in terms of Fourier series. Force at each harmonic is then multiplied by the measured bridge admittance at the corresponding frequency, which in general is a complex quantity. The real part of the summation over all harmonics gives the physical velocity of the bridge notch. By integration, using a proper scaling factor (again by treating the short segment of the string quasi-statically), and finding the integration constant by imposing $F_{pert}\left(\pm 1/2 f_0\right) = 0$, the minimum bow force takes the form

$$F_{min} = \frac{2 v_b Z_{0T}^2}{\pi^2 \beta^2 (\mu_s - \mu_d)} \cdot \left[\max_t \left\{ \mathcal{R}e \sum_{n=1}^{\infty} \frac{(-1)^{n+1}}{n^2} Y_M(2n\pi f_0) e^{2n\pi i f_0 t} \right\} + \mathcal{R}e \sum_{n=1}^{\infty} \frac{Y_M(2n\pi f_0)}{n^2} \right], \tag{4.7}$$

in which Y_M is the measured admittance at the bridge notch. In theory, the summations should be taken over an infinite number of harmonics, but the significance of the harmonics drop with $1/n^2$, so it would practically suffice to find the summation over the first few harmonics. Z_{0T}^2 in Eq. (4.7) should be replaced by $Z_{0T} Z_{tot}$ to capture the effect of the string's torsion in the way proposed by Schelleng.

It should be noted that the minimum bow force limit obtained in this fashion gives an underestimation of the actual minimum bow force. The Helmholtz motion is not possible for a bow force below that limit but there is no guarantee that the Helmholtz motion would be sustainable above it. Other effects, most of which working toward destabilizing the Helmholtz motion, should be taken into account to make a more realistic prediction of the minimum bow force.

4.2 Minimum bow force revisited

An earlier version of our bowed string simulation model [124] predicted multiple occurrences of Helmholtz motion below the minimum bow force set by Eq. (4.7), particularly when the string's fundamental frequency fell on, or slightly below, a strong body resonance. Looking more closely, it was seen that the simulated excitation force acting on the bridge was largely skewed from being a perfect sawtooth. If proven correct, this phenomenon could invalidate the first assumptions made in deriving the minimum bow force relation, both by Schelleng and by Woodhouse.

To investigate this observation in a qualitative manner, we bowed the C_2 string of a cello with a prominent wolf note close to the frequency of the strongest body mode, while monitoring the bridge force using a pickup system.[2] The pickup system was made out of two small pieces of piezoelectric crystal mounted beneath the C_2 string notch on the bridge in a V-shaped configuration (first proposed in [84]). The crystals produce outputs that can be combined to give a signal proportional to the transverse force at the string notch in the bowing direction.

The force signal obtained from the sensors is plotted in Fig. 4.2. Based on a few slowly upward moving glissando played on that instrument, the hardest frequency range to play was identified to fall in the range of 171 Hz to 173 Hz (called the "wolf region"), although the instrument could more easily be made to warble a bit lower at around 169 Hz. The bow-bridge distance was not accurately controlled, but the bow was placed at around $\beta = 0.1$ (this can be confirmed by the spacing of the "Schelleng ripples" [50, 23] in the force signal). The upper trace in Fig. 4.2 shows the familiar sawtooth that is obtained at a fundamental of 190.6 Hz, well above the wolf region. The middle and the lower traces show, respectively, the bridge forces when the fundamental falls slightly above (at 174.9 Hz), and slightly below (at 169.2 Hz) the wolf region. It can be seen clearly that the upward slope of the sawtooth is skewed in both cases. If the frequency content of the bridge force is calculated, the fundamental is systematically weaker compared to an ideal sawtooth wave, when the played note falls below the wolf region, and it is stronger when the played note falls above that range.

In order to investigate this observation theoretically, and to find a more general version of the minimum bow force, we took one step back, and assumed a perfect stick-slip at the bow in place of a perfect sawtooth bridge excitation force.[3] In doing so, it is mathematically convenient to describe the vibrations of a string in the form of a lossy transmission line, common in electrical engineering domain [125]. The analogy can be formulated in different

[2] The measurements were made in Cambridge University with the aid of Jim Woodhouse.
[3] This approach was kindly suggested by Jim Woodhouse in personal communications.

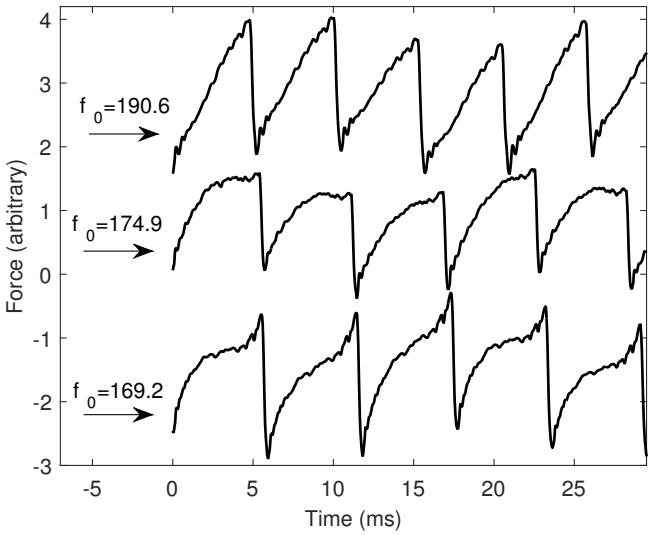

Fig. 4.2 The bridge force measured experimentally using two small pieces of piezoelectric crystal mounted beneath the C_2 string notch on the bridge in a V-shaped configuration. The upper trace is for $f_0 = 190.6$ Hz, far away from the wolf region. The middle trace is for $f_0 = 174.9$ Hz, slightly above the wolf region, and the lower trace is for $f_0 = 169.2$ Hz slightly below the wolf region.

ways, but for our purpose, force would be considered as the equivalent to the voltage, and velocity would be equivalent to the current. This makes the definition of the impedance (the ratio of the "effort" to the "flow") compatible for the two systems. The use of the electrical circuit analogy for vibrating musical strings was pioneered by Kock [126], applied to the violin acoustics by Schelleng [127], and was used in some other studies following that [64, 128, 62].

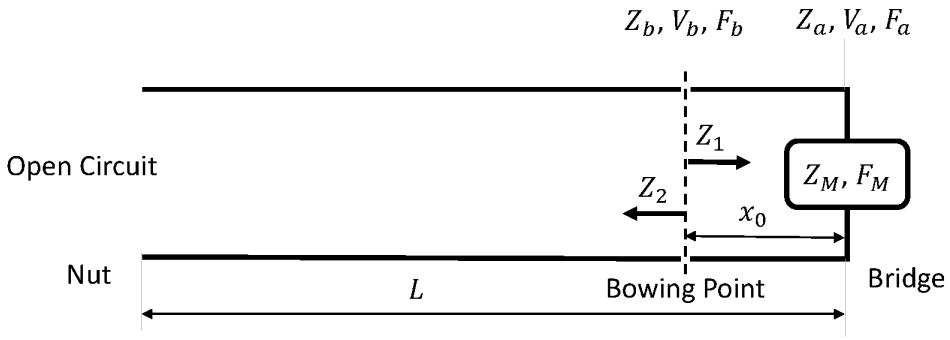

Fig. 4.3 Schematic for the transmission line analogy of a bowed string.

A schematic view of the transmission line analogy is shown in Fig. 4.3. The string is

assumed to be terminated rigidly (equivalent to an open circuit) at the nut/finger, and at a multi-resonance system with impedance Z_M at the bridge. The bridge admittance can be conveniently measured using a combination of an impulse hammer and a laser doppler vibrometer, or can be synthesized from a known set of body mode frequencies (ω_{Mk}), Q factors (Q_{Mk}), modal masses (M_k), and mode spatial angles (θ_{Mk})

$$\frac{1}{Z_M}=\sum_k \frac{i\omega.\cos^2\theta_{Mk}}{M_k\left(\omega_k^2+i\omega\omega_{Mk}/Q_{Mk}-\omega^2\right)}. \tag{4.8}$$

As far as the bow force limits are concerned, we are primarily interested in the impedance at the bowing point (i.e. Z_b in Fig. 4.3). Z_b is the sum of the impedances on the two sides of the bowing point, called Z_1 for the bridge side, and Z_2 for the finger side. Those impedances can be calculated from

$$Z_1=Z_{0T}.\frac{Z_M+Z_{0T}\tanh\left(ikx_0\right)}{Z_{0T}+Z_M\tanh\left(ikx_0\right)}, \tag{4.9}$$

$$Z_2=Z_{0T}\coth\left(ik\left(L-x_0\right)\right)\ , \tag{4.10}$$

$$Z_b=Z_1+Z_2, \tag{4.11}$$

where L is the total singing length of the bowed string, x_0 is the distance from the bowing point to the bridge, and Z_{0T} is the characteristic impedance of the string in its transverse direction. For an undamped and perfectly flexible string, k is the wave number defined as ω/c_0, where ω is the excitation angular frequency, and c_0 is the wave propagation speed through the perfectly flexible string. However, for the more general case of a stiff string with frequency-dependent damping, k can be calculated from

$$k=\left(\omega/c\right)\left(1-i/Q_s\right)^{1/2}. \tag{4.12}$$

Q_s is the unperturbed Q factor of a string mode with frequency ω, and c is the frequency-dependent wave propagation speed through a stiff string with inharmonicity factor B and an unperturbed fundamental frequency ω_0, if it was perfectly flexible. This frequency-dependent propagation speed can be calculated from

$$c=c_0\sqrt{1+B(\omega/\omega_0)^2}. \tag{4.13}$$

Similar to Eq. (2.10), Eq. (4.13) points to the fact that for a stiff string, higher frequencies travel increasingly faster than the lower frequencies. The frequency-dependent damping of

the string and its relevant parameters have already been discussed in Sec. 2.3.1. It was possible to relate k to more general properties of the string such as its tension and bending stiffness; however, here we have opted for inharmonicity and Q factor as those are more straightforward to measure from the response of a plucked string.

If the velocity at the bowing point is known, it can be convolved by the inverse Fourier transform of the impedance at the bowing point to find the perturbation force acting on the bow in the time-domain. It is theoretically possible then to find the perturbation force at the bowing point and to compare that with the limiting static friction to figure out whether or not the Helmholtz motion is self-compatible. While that is an interesting approach (further discussed in Sec. 4.4), it will involve some complications regarding the exact shape of the imposed velocity at the bowing point. Before going into those details, it is encouraging to look at the excitation force at the bridge that can be obtained using this model, assuming an ideal square-wave velocity at the bowing point.[4] The bridge force obtained from such assumption can be used to excite the bridge and to find a modified relation for the minimum bow force, in a similar way that it was done to derive Eq. (4.7).

To calculate the bridge excitation force, one also requires the transfer function between the velocity of the string at the bowing point (V_b) to its velocity at the bridge (V_a), assuming the bow is removed at the moment. Considering a fixed boundary condition at the finger side, this transfer function will take the form

$$\frac{V_b}{V_a}=\frac{\sin k(L-x_0)}{\sin kL}. \tag{4.14}$$

As before, k is the wave number for a damped and stiff string, and can be calculated from Eq. (4.12). Now the transfer function between the bridge force (F_M) and the imposed velocity at the bowing point (V_b) becomes

$$\frac{F_M}{V_b}=\frac{V_a.Z_M}{F_b/Z_b}=Z_bZ_M\frac{V_a}{F_b}\xleftrightarrow{\text{reciprocity}}Z_bZ_M\frac{V_b}{F_a}=Z_bZ_M\frac{V_b}{V_a}.\frac{V_a}{F_a}=\frac{Z_bZ_M}{Z_a}\frac{V_b}{V_a}. \tag{4.15}$$

And by replacing the relevant parameters

$$F_M=V_b.\frac{Z_MZ_{0T}\left[\frac{Z_M+Z_{0T}\tanh(ikx_0)}{Z_{0T}+Z_M\tanh(ikx_0)}+\coth\left(ik\left(L-x_0\right)\right)\right]}{Z_M+Z_{0T}\coth\left(ikL\right)}.\frac{\sin k(L-x_0)}{\sin kL}. \tag{4.16}$$

The derivation of Eq. (4.15) is straightforward except from the third to the fourth equality, which is due to reciprocity: velocity at point 'a' in response to force at point 'b' is equal to

[4] If the string vibrates in the perfect Helmholtz regime, its contact point with the bow will have the exact same velocity as the bow (i.e. v_b) in the sticking phase, which covers $(1-\beta)$ of the full period. The sticking phase suddenly switches to the slipping phase, during which the string has a constant velocity of $v_b\frac{1-\beta}{\beta}$.

the velocity at point 'b' in response to force at point 'a'. Note that Z_M is different from Z_a in that the former is the bridge impedance if the string was removed, but the latter is the impedance at the bridge in the presence of the string; the same applies to F_M versus F_a. If $Z_M \to \infty$ (equivalent to a rigid termination at the bridge), Eq. (4.16) transforms the square shaped imposed velocity at the bowing point to a perfect sawtooth excitation force at the rigid bridge, thus the original assumption made in deriving Eq. (4.7).

$$\lim_{Z_M \to \infty} F_M = V_b . Z_{0T} [\coth(ikx_0) + \coth(ik(L - x_0))] . \frac{\sin k(L - x_0)}{\sin kL}. \tag{4.17}$$

By dividing F_M obtained from Eq. (4.16) by its special case from Eq. (4.17), we can find the frequency-dependent parameter ζ that shows the deviation of the modified excitation force from being a perfect sawtooth.

$$\zeta = \frac{Z_M \left[\frac{Z_M + Z_{0T} \tanh(ikx_0)}{Z_{0T} + Z_M \tanh(ikx_0)} + \coth(ik(L - x_0)) \right]}{[Z_M + Z_{0T} \coth(ikL)] . [\coth(ikx_0) + \coth(ik(L - x_0))]}. \tag{4.18}$$

Figure 4.4 shows the simulated bridge force from numerical evaluation of Eq. (4.16); this figure is directly comparable to Fig. 4.2. The parameters used for the evaluation are for a bowed C_2 cello string (see Table 2.1), stopped at positions corresponding to the fundamental frequencies of 169.2 Hz, 174.9 Hz, and 190.6 Hz. The bow was positioned at $\beta = 1/9.21$ and had a constant speed of $v_b = 5$ cm/s. The body is assumed to have a single strong resonance at 172 Hz aligned with the bowing direction, with a Q factor of 40 and an effective mass of 120 g. A Gaussian low-pass filter with a cut-off frequency of 795 Hz is applied to the imposed velocity at the bowing point, both to avoid numerical instabilities and to crudely simulate the corner rounding effect, leading to an extended slipping phase (see for example Fig. 5 of [24]). The Schelleng ripples observed in Fig. 4.2 could be made visible in the waveforms shown in Fig. 4.4 as well, if the imposed velocity had a further prolonged slip phase. Aside from that, the similarity between the two plots is satisfying, at least at the qualitative level.

As the next logical step, the minimum bow force as a function of the played note is plotted for a single-resonance body with properties mentioned above ($F_M = 172$ Hz, $M = 120$ g), as well as for a realistic bridge admittance measured for an actual cello (the same parameters reported in Chap. 2). Aside from the excitation force at the bridge, which is now a modified sawtooth wave, the remainder of the implementation is exactly the same as what was done in [24]. Note that, similar to the bridge admittance, parameter ζ is a complex value, so the relative phase of the excitation force and the response are taken into account in the minimum

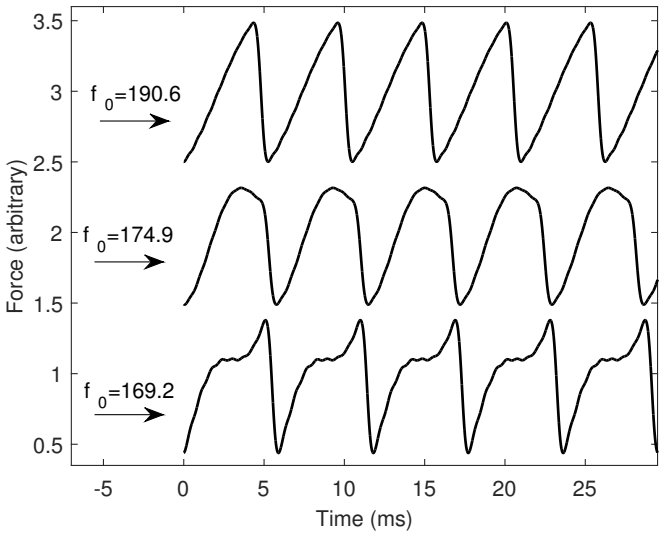

Fig. 4.4 Simulated bridge forces, directly comparable to ones shown in Fig. 4.2. The upper trace is for $f_0 = 190.6$ Hz, far away from the wolf region. The middle trace is for $f_0 = 174.9$ Hz, slightly above the wolf region, and the lower trace is for $f_0 = 169.2$ Hz slightly below the wolf region.

bow force calculated using this approach.[5]

Figure 4.5 shows the comparison of the minimum bow force prediction by Eq. (4.7), and its corrected version using parameter ζ defined in Eq. (4.18). It can be seen that for both cases of single- and multi-resonance body properties the frequency of the hardest note to play (the peak in the minimum bow force plot) is slightly shifted upward. This frequency has shifted from 172 Hz to 174.6 Hz for the single-resonance case and from 189 Hz to 190 Hz for the multi-resonance case. The smaller peak at around 86 Hz in Fig. 4.5a represents the note that has its 2^{nd} harmonic close to the body resonance frequency. The upward shift of the peak frequencies compared to the ideal sawtooth case should not come as a surprise as the lower-than-expected magnitude of the bridge excitation at the fundamental frequency results in a smaller minimum bow force at the frequency of the body resonance, while the peak of the minimum bow force happens at a higher frequency where the fundamental is stronger-than-expected. To further investigate this issue, the frequency of the peak for the single-resonance case is plotted against β (see Fig. 4.6). Recall that Fig. 4.5 was plotted for a single value of $\beta = 1/9.21$.

[5]By imposing the motion of the string at the bowing point, the length of string on the finger side is effectively isolated from any influence on the bridge force velocity. Considering that, Eq. (4.18) takes a much simpler form:

$$\zeta = \frac{Z_M \sin k\beta L}{Z_M \sin k\beta L - iZ_{0T} \cos k\beta L}. \tag{4.19}$$

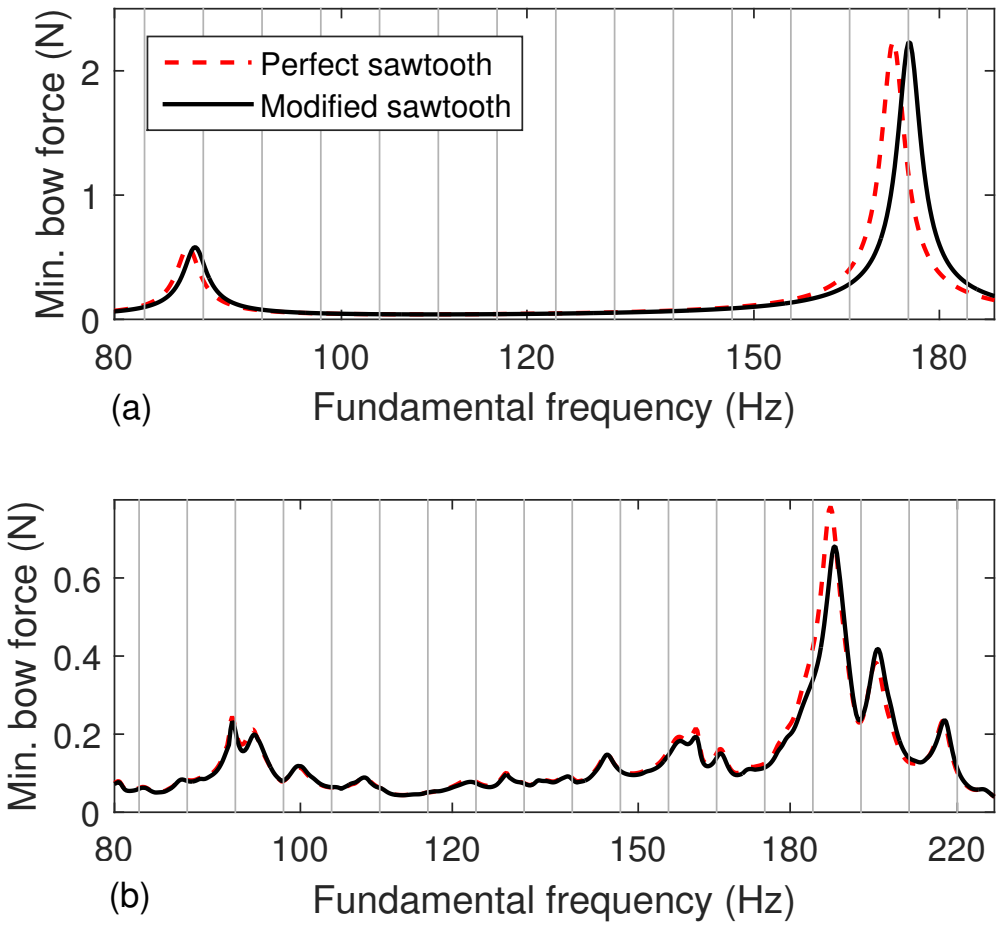

Fig. 4.5 Calculated minimum bow force for a single-resonance body with the resonance frequency of 172 Hz (a) and the same quantity for the body properties measured on an actual cello (b). The red-dashed line shows the calculated minimum bow force predicted by Eq. (4.7) and the black-solid line shows the same quantity corrected by parameter ζ, defined in Eq. (4.18) . The vertical lines indicate musical scale spaced by a semitone.

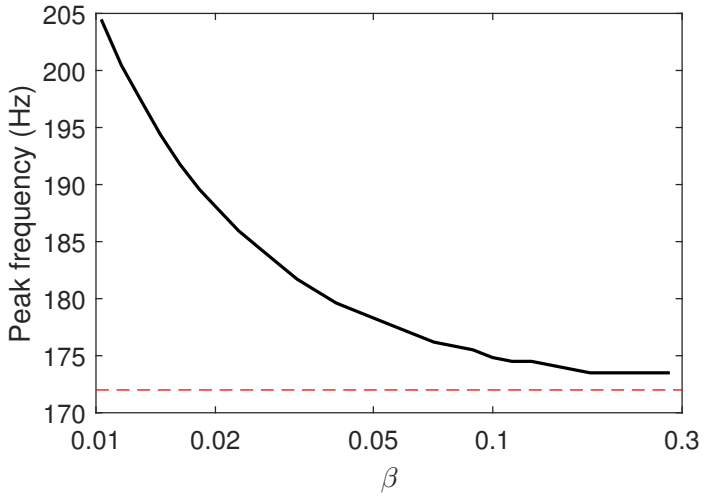

Fig. 4.6 Peak frequency in the minimum bow force plot calculated for the single-resonance case, plotted as a function of the relative bow bridge distance. The red-dashed line shows the resonance frequency of the body mode at 172 Hz.

The frequency of the peak at larger β values starts at only slightly above the frequency of the body resonance (at 172 Hz), but increases to around 205 Hz at $\beta = 0.01$. This is a fundamentally different prediction from what was made by Eq. (4.7); the latter would predict the peak frequency at 172 Hz, regardless of the bow-bridge distance. Figure 4.7 shows a similar result for the more realistic body properties (the same body properties that were used to obtain the results of Fig. 4.5b). Since each β value leads to more than one peak in the minimum bow force plot, the plots are shown for all 30 logarithmically-spaced values of β. The dominant modal frequencies of the body in the range of interest were at 189 Hz and 199 Hz. The body also had a strong mode at 433 Hz which is appeared in the minimum bow force plot at half of its frequency. Those three particular frequencies are marked in Fig. 4.7 by dashed vertical lines. The general trend is the same as what was observed in Fig. 4.6: the frequency of the peaks in the minimum bow force plots are systematically shifting upward as the bow gets closer to the bridge.

The dependency of the peak frequency upon the β value has an interesting consequence for the Schelleng diagram: The minimum bow force line becomes curved even if the variations of μ_d are not taken into account. Figures 4.8 and 4.9 show the modified Schelleng limits for the same single- and multi-resonance body properties. In each figure the top plot is showing the Schelleng diagram when the played note falls below the body resonance, while the lower plot shows what happens when the note falls above the body resonance. In particular, an

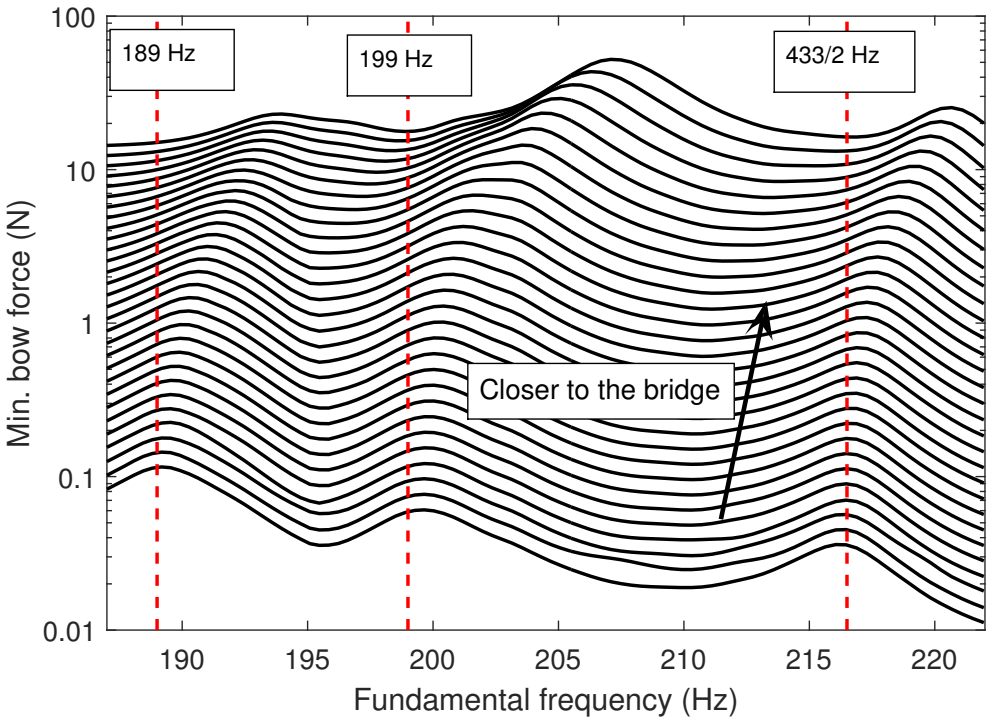

Fig. 4.7 Minimum bow force for a realistic multi-resonance body, plotted for 30 values of beta logarithmically-spaced from 0.01 to 0.3. The arrow shows the direction of decreasing β. The vertical lines show the frequency of body resonances located at 189 Hz and 199 Hz, with another mode at 433 Hz appeared at half of its frequency.

interesting case is demonstrated in Fig. 4.8b, in which the peak in the minimum bow force plot passes through the played frequency (180 Hz in here) as the bow gets closer and closer to the bridge, resulting in a bump in the minimum bow force limit that splits the playable range into two non-connected regions. A bump like that did not appear when more realistic body properties are considered (see Fig. 4.9). The general effect is, however, consistent over the two plots: for the most part of the practical β values, the minimum bow force limit is curved downward below the body resonance, and is curved upward above that. It is, therefore, safe to assume that at frequencies close –but less than– the body resonance, it is relatively easier to play closer to the bridge (relative to the -2 slope in log-log scale that the player may expect from experience), while at frequencies higher than the wolf region, it makes more sense for the player to use a larger bow-bridge distance.[6] We will see many more samples of modified Schelleng diagrams in Sec. 4.3.

4.2.1 Effect of the sympathetic strings on the minimum bow force

The bowed instruments usually have four strings, among which usually only one is bowed on at any time. The other three non-played but freely-vibrating strings are coupled to the bowed string as well as other freely-vibrating strings through the common bridge that supports them. Those three strings are called the "sympathetic strings" throughout, even though they may, or may not, be tuned sympathetically to the bowed string (see Sec. 2.2.3 for a more extensive discussion). As far as the bowed string is concerned, any effect from the sympathetic strings should come into play by modifying the bridge admittance as seen by the bowed string. The effective bridge impedance (Z_{Meff}) is the sum of the bridge impedance in the absence of the sympathetic string(s), with the impedance of the sympathetic string(s) at the bridge

$$Z_{Meff}=Z_M+Z_{0sym}\coth\left(ik_{sym}L_{sym}\right), \tag{4.20}$$

where the subscript "sym" represents the corresponding parameter for the sympathetic string(s). Equation (4.20) is for a single sympathetic string, but the summation can be taken over all sympathetic strings, if desired. Replacing Z_M by Z_{Meff} in all earlier equations gives their equivalents if the sympathetic strings are taken into account.

Figure 4.10a shows the real part of the effective bridge admittance (i.e. the inverse of Z_{Meff}) when a single G_2 sympathetic string is also supported on the same bridge. It can

[6] A common approach that the players use to play around the wolf note is to squeeze the instrument between their knees which adds to the damping of the body modes and makes the wolf note slightly more playable. Based on the findings of this section, an alternative approach to play "through" the wolf note may be to use an small bow-bridge distance for notes below the body mode and to use a large bow-bridge distance for the notes above it.

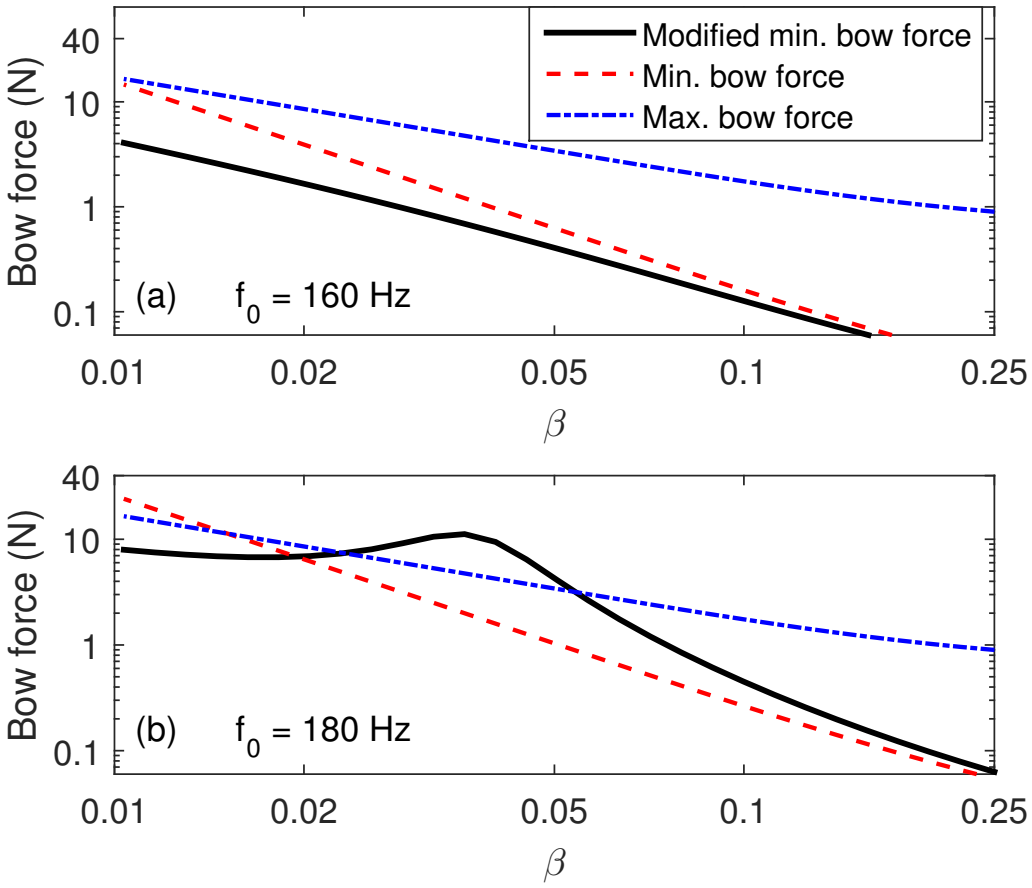

Fig. 4.8 The Schelleng diagram plotted for a single-resonance body at 172 Hz and plotted for a string's fundamental frequency at 160 Hz (a) and 180 Hz (b). The blue dashed-dotted line shows the maximum bow force calculated from Eq. (4.5), the red-dashed line shows the minimum bow force calculated from Eq. (4.7), and the black-solid line is the same quantity corrected by parameter ζ, defined in Eq. (4.18). The variations of the dynamic friction coefficient (μ_d) as a function of β is taken into account.

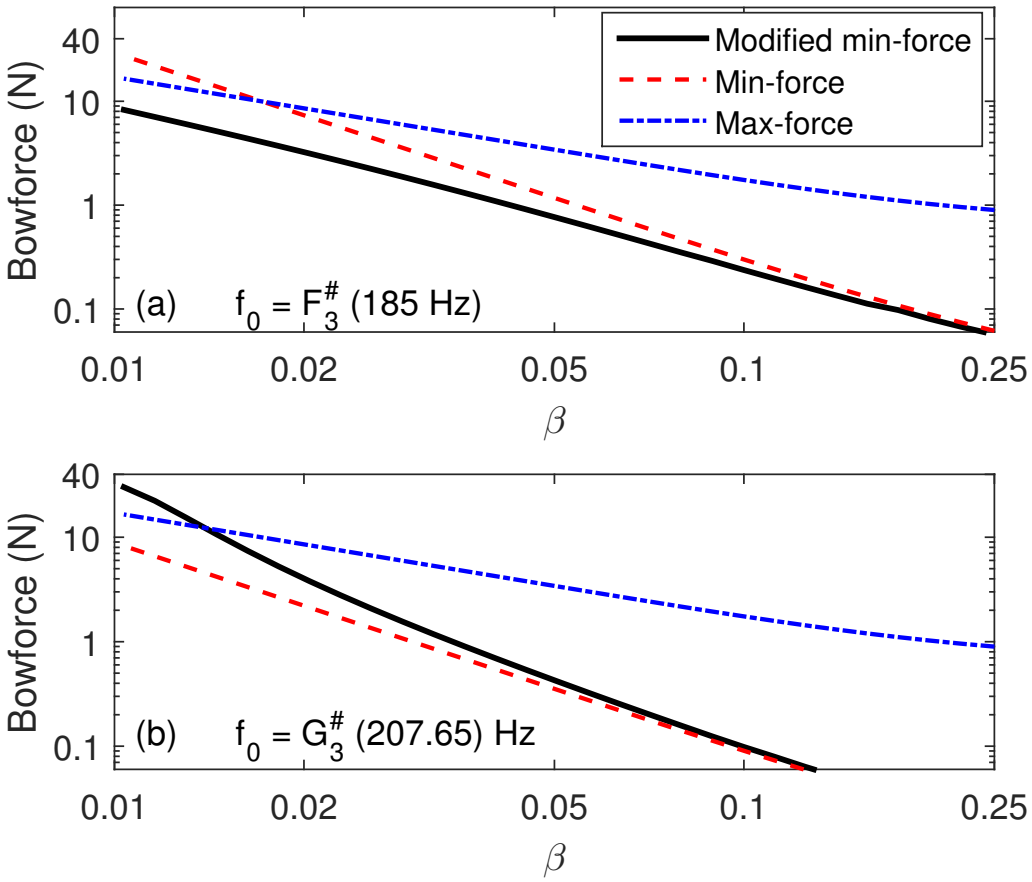

Fig. 4.9 The Schelleng diagram plotted for a multi-resonance body with strong resonances at 189 Hz and 199 Hz. The top plot is for a string's fundamental frequency at 185 Hz and the bottom plot is for a string's fundamental frequency at 207.65 Hz. The blue dashed-dotted line shows the maximum bow force calculated from Eq. (4.5), the red-dashed line shows the minimum bow force calculated from Eq. (4.7), and the black-solid line is the same quantity corrected by parameter ζ, defined in Eq. (4.18). The variation of the dynamic friction coefficient (μ_d) as a function of β is taken into account.

be seen that the general effect in the plotted range is to add two sharp local resonance structures at around 98 Hz and 196 Hz. The admittances with and without the sympathetic string look very similar away from those frequencies. There can be some interaction between the sympathetic strings and the body resonance if they fall very close in frequency; that interaction will result in some repulsion of the two peaks, a sample of which was presented in Fig. 2.20. Figure 4.10b shows the minimum bow force plot, equivalent to what was shown earlier in Fig. 4.5a, but calculated from this modified admittance. Not surprisingly, the minimum bow force is most affected at 98 Hz, its almost-integer multiples, and the subharmonics of all of those multiples. Two examples of those subharmonics, visible in the range plotted here, are a 65.4 Hz peak that has its 3^{rd} harmonic coincident with the 2^{nd} mode of the sympathetic string, and a small spike at 146.83 Hz, which is half the 3^{rd} mode frequency of the sympathetic string.

Looking more closely at the modified admittance, it becomes clear that there is always a dip at the exact frequency of the sympathetic string modes, accompanied by a closely spaced peak.[7] For the particular case of a single-resonance body, the peak always happens before the dip at frequencies below the body resonance, and after the dip at frequencies above the body resonance. This trend is necessary so that the combined set of resonances, including the sympathetic strings, obey Foster's theorem: in a driving-point response, resonances and anti-resonances will always alternate [129]. Translating this into the minimum bow force plot creates an interesting shape at 98 Hz. There is a dip exactly at 98 Hz which has a peak below, reflecting what happens in the admittance at around 98 Hz; as well as another small peak slightly above 98 Hz that is the consequence of the peak at slightly above 196 Hz in the admittance curve (look at the magnified box in Fig. 4.10b). Care should be taken not to misattribute this double peak structure to the coupling of the bowed and the sympathetic strings, and the consequent peak splitting. Evidently, this double peak situation does not apply to the minimum bow force plot at around 196 Hz as the fundamental and all of its harmonics have their peaks at slightly above the pure multiple of 196 Hz in the admittance.

Figure 4.11 shows the equivalent to Fig. 4.10 but with multi-resonance realistic body modes. All sympathetic strings are also included in this case (the G_2, D_3, and A_3 strings, for the minimum bow force plotted for the open C_2 string). It can be seen in the top plot that the changes occurred to the admittance plot at the frequencies of the G_2 and D_3 strings (at 98 Hz and 146.83 Hz, respectively) fits the general expectation when the sympathetic string's frequency falls below that of the dominant body resonance. However, the 2^{nd} mode of the G_2 string and the 1^{st} mode of the A_3 string show little sign of any peak around them and are

[7] A very similar effect may be expected when a wolf suppressor is installed on a string's after-length, thus lowering its frequency to the range of the wolf note, although the higher modes of an after-length with wolf suppressor are not necessarily harmonically related.

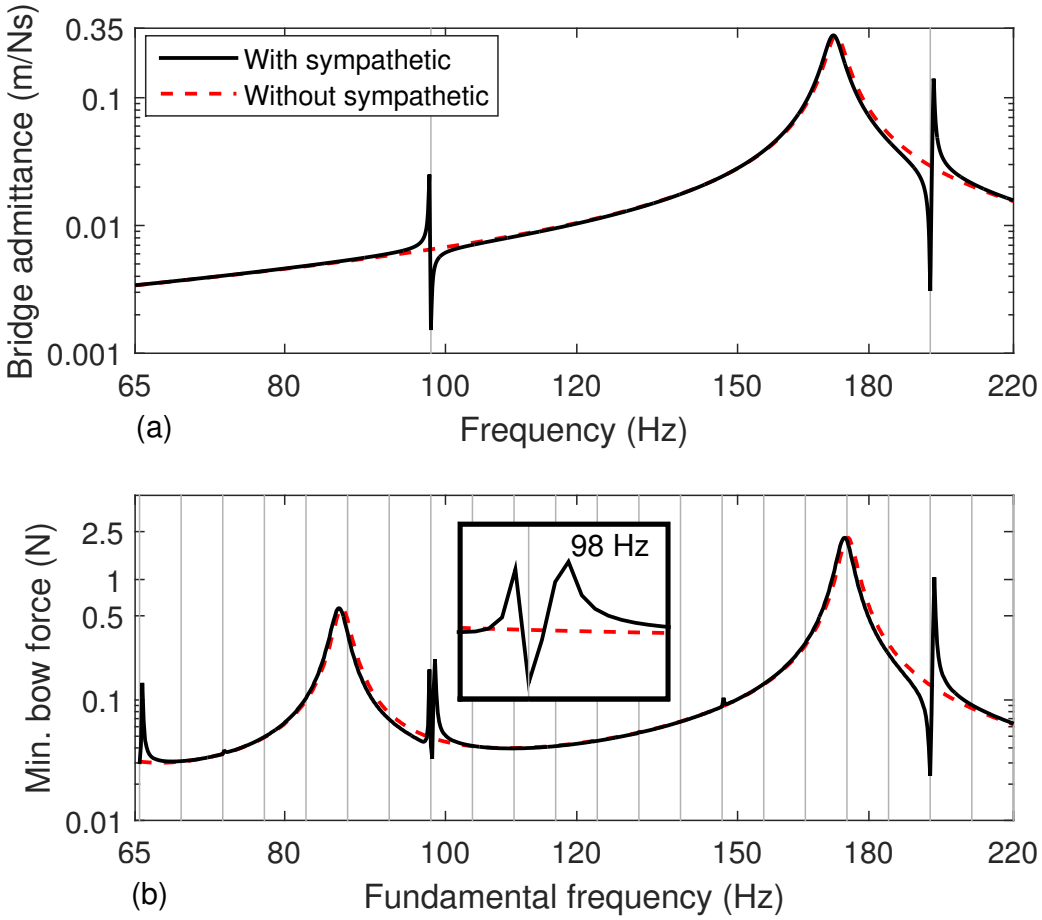

Fig. 4.10 The bridge admittance (a) and the minimum bow force calculated from it (b) for a single-resonance body mode located at 172 (Hz). The calculation of the minimum bow force is made from Eq. (4.7) corrected by parameter ζ, defined in Eq. (4.18). The black-solid curve is for the case where an open G_2 string tuned at 98 Hz is supported on the same bridge, and the red-dashed line shows the case without the sympathetic string. The grey vertical lines in the top plot show the frequency of the sympathetic string and its 2^{nd} harmonic, and in the bottom plot they show the musical scale spaced by a semitone. The box in the bottom plot is a zoomed version of the same plot at around 98 Hz.

mostly manifested by a dip at their exact frequency. Looking at the minimum bow force plot calculated from this modified admittance, the dip can be consistently found at the frequency of the fundamental and all harmonics of the sympathetic string modes. With the exception of a peak slightly below 146.83 Hz, the other dips did not have a peak around them. The reason behind that is a more random distribution of the phase for the realistic-body case.

Leaving aside those details, both Figs. 4.10 and 4.11 suggest that the sympathetic strings strongly affect the minimum bow force at around the notes that are harmonically related to them, and as such, it may well be worth including their effect in the minimum bow force calculation. Regardless of the formulation used to calculate the minimum bow force, one can take the effect of the sympathetic strings into account by replacing the measured bridge impedance with the effective bridge impedance, calculated from Eq. (4.20). The qualitative effect of each sympathetic string and the magnitude of the effect depends on the properties of the bridge admittance in that frequency range, and may vary from one instrument to another. As an example, distinction should be made between a cello that has its body resonance at around G_3 with one that has it at around $F_3{}^{\#}$. Even if those modes are equally strong, the mode at G_3 is more likely to be suppressed by the presence of the harmonically related open strings.

Two other factors that should be kept in mind when studying the detailed effect of the sympathetic strings are their exact tuning, and their inharmonicity. Although these factors are small in absolute terms, their effect may become significant given the fact that open strings have large Q factors and slight deviations in frequency can largely affect their interactions with other strings or with the body modes.

4.2.2 Effect of the out-of-plane vibrations of the string on the the minimum bow force

As was pointed out in Sec. 2.2.3, a string is generally free to vibrate in two perpendicular transverse polarizations. In the presence of a single body mode with the same frequency as the unperturbed string mode, the string polarization aligned with the body mode will be effectively coupled, while the other string polarization remains uncoupled, hence unperturbed.[8] Such two-dimensional coupling creates a tendency for out-of-plane vibrations of the string if the excitation acting on it is not perfectly aligned with either of those two perpendicular polarizations.

Back to the main topic of admittance at the bowing point, the presence of the two coupled

[8] If the unperturbed frequency of the string and the body do not exactly coincide the coupled modes of the string and body maintain their string-like and body-like properties, but the fact that they are interacting holds regardless.

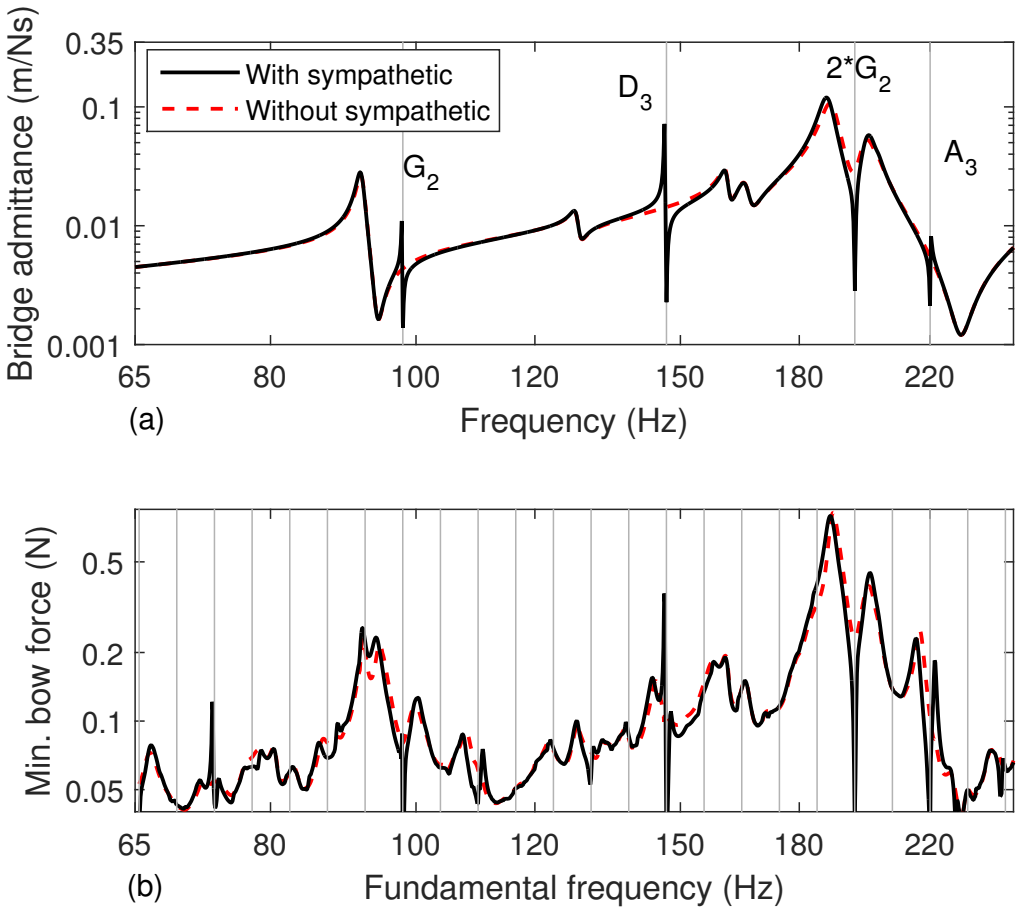

Fig. 4.11 The bridge admittance (a) and the minimum bow force calculated from it (b) for a multi-resonance realistic body. The calculation of the minimum bow force is made from Eq. (4.7) corrected by parameter ζ, defined in Eq. (4.18). The black-solid curve is for the case where three open G_2, D_3, and A_3 strings tuned respectively at 98 Hz, 146.83 Hz, and 220 Hz are supported on the same bridge, and the red-dashed line shows the case without the sympathetic string. The grey vertical lines in the top plot show the frequency of the sympathetic strings and their relevant harmonics, and in the bottom plot they show the musical scale spaced by a semitone.

string-body modes in addition to an uncoupled string mode translates into the admittance curve in the form of three peaks around the coupling point. The peak that corresponds to the uncoupled vibrations of the string is rather sharp and occurs at the unperturbed string frequency, and the two others are more heavily damped and perturbed in frequency. Gough [128] argues that the existence of the uncoupled string mode aids the formation and stability of the Helmholtz motion. He also suggests that it has implications for the occurrence of the wolf phenomenon through changing the number of zero crossings for the imaginary part of the admittance.[9] Given the relevance of the input admittance to our discussion of the minimum bow force, we will investigate this matter in some more details, and evaluate which one of the single- or dual-polarization impedances (if any) should be used in our formulation.

Consider first the single-polarization vibration of a finger-stopped C_2 string with a constant Q factor of 500, and an unperturbed first mode frequency of 172 Hz, coupled to a body mode with the same unperturbed frequency, a modal mass of 120 g, a Q factor of 40, and perfectly aligned with the bowing (i.e. admittance evaluation) direction. The red-dashed line in Fig. 4.12a shows the admittance evaluated at $\beta = 1/13.3$ according to Eq. (4.11). As expected, there are two split and heavily-damped coupled modes, representing the in-phase and out-of-phase motions of the string and the bridge.

Now consider the dual-polarization case: to give a "worst case", suppose the body mode is inclined by $\theta'_M = 45°$ with respect to the admittance evaluation direction. To make the two cases compatible, the mass of the body mode is reduced to $M = 120\ \cos^2\theta'_M = 60$ g, so that the bridge admittance in the bowing direction would remain the same in the absence of string coupling. To find the coupled admittance, the applied force must be resolved into the coupled and uncoupled polarization directions of the string, and the resulting velocities projected back into the evaluation direction.

$$Z_1 = Z_{0T} \cdot \frac{Z_M + Z_{0T}\tanh(ikx_0)}{Z_{0T} + Z_M\tanh(ikx_0)}, \tag{4.21}$$

$$\acute{Z}_1 = Z_{0T}\coth(ikx_0)\ , \tag{4.22}$$

$$Z_2 = Z_{0T}\coth(ik(L - x_0))\ , \tag{4.23}$$

$$\frac{1}{Z_b} = \frac{(\cos\theta'_M)^2}{Z_1 + Z_2} + \frac{(\sin\theta'_M)^2}{\acute{Z}_1 + Z_2}. \tag{4.24}$$

[9] See Schelleng's original argument regarding the number of the unstable poles in [127] and Gough's response to that in [62] and [128].

The admittance calculated based on Eq. (4.24) is shown by the black-solid line in Fig. 4.12a. Exactly as argued by Gough [128], a sharp third peak appears at the unperturbed frequency of the string. Furthermore, the coupled modes are repelled more widely than before because the effective body mass is smaller, resulting in a stronger coupling of the string and the body mode.

A point that was neglected in Gough's argument is that in order for such a sharp peak to appear in the admittance, the string needs to be free to vibrate in the out-of-plane direction, as was the case in Gough's experiments performed using electromagnetic excitation of the string in the bowing direction. However, this is not the case when a bow is in contact with the string: it will significantly limit motion in the perpendicular-to-bow direction, and add damping. A more relevant bowing-direction admittance would take into account a frictionless bow remaining in contact with the string at the bowing point. That is, of course, not practical to measure, but it can be evaluated theoretically. The bowhair may be regarded as another transmission line coupled to the string at the bowing point and terminated rigidly at both boundaries (i.e. at the frog and the tip). The fully-coupled impedance of the string at the bowing point then becomes

$$\frac{1}{Z_b}=\frac{\left(\cos\theta'_M\right)^2}{Z_1+Z_2+Z_{bow}\left(\sin\theta'_M\right)^2}+\frac{\left(\sin\theta'_M\right)^2}{\acute{Z}_1+Z_2+Z_{bow}\left(\cos\theta'_M\right)^2}, \tag{4.25}$$

where Z_{bow} is the transverse impedance of the bowhair at its contact point to the string, which can be calculated from:

$$Z_{bow}=Z_{0b}\left(\coth\left(ik_b x_{0b}\right)+\coth\left(ik_b\left(L_b-x_{0b}\right)\right)\right), \tag{4.26}$$

in which Z_{0b} is the characteristic impedance of the bowhair in its transverse direction, k_b is the wave number of the bowhair, L_b is the full length of the bowhair and x_{0b} is the distance of the contact point to the frog. Note that Eq. (4.26) will be reduced to Eq. (4.24) (meaning no coupling to the bowhair) if the bowing direction is aligned with, or normal to the principle direction of the bridge motion. This is satisfying as the string would not have any tendency to vibrate in the perpendicular-to-bow direction if either of those are the case.

The blue dash-dotted line in Fig. 4.12a shows the numerical evaluation of Eq. (4.25). The parameters used for the bow are extracted from Table 3.1. The distance between the contact point and the frog is chosen to be 0.2015 m. It can be seen that the sharp uncoupled resonance has been moderately affected by the coupling to the bow-hair: its normalized frequency has been reduced from 1 to around 0.99, probably due to the added mass from the bow-hair, and it is more heavily damped as well. To put this extreme case in perspective a comparable plot is shown in Fig. 4.12b in which a finger-stopped D_3 string with an unperturbed first

mode frequency of 172 Hz is coupled to a body mode with the same unperturbed frequency, but this time with a modal mass of 300 g: a more realistic value than the earlier case with mass 120 g. The body mode is inclined by $\theta'_M = 20°$ and the total mass is reduced to $M = 300 \cos^2 \theta'_M = 264.9$ g when both polarizations are considered. It can be seen that the unperturbed string resonance visible in the black solid line is heavily suppressed by the coupling to the bow-hair ribbon (see the blue dashed-dotted line) and is merged with the in-phase split mode at normalized frequency of around 0.98.

As a crosscheck, the results presented in Fig. 4.12 were compared to similar results obtained from the time-domain simulation of the bowed string when the friction is turned to zero, and they agreed very well to one another (the time-domain simulation results are not reproduced here).

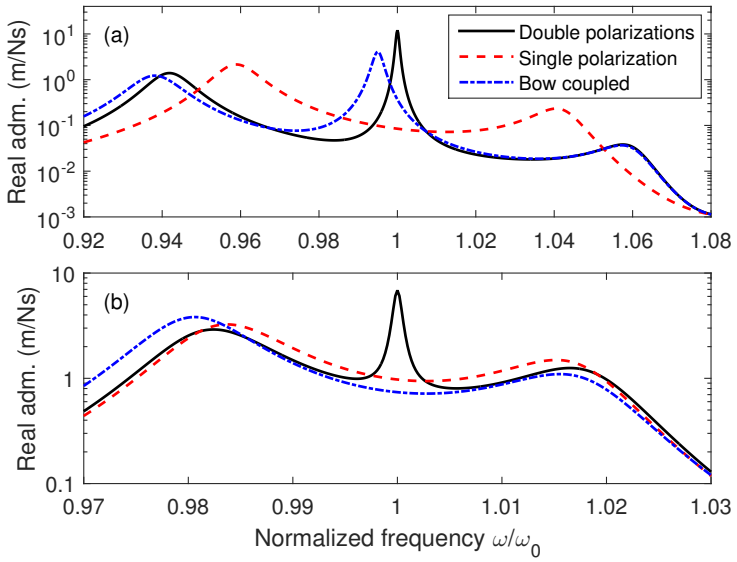

Fig. 4.12 The real part of the input admittance at the bowing point, evaluated at $1/13.3^{th}$ of the string length away from the bridge. Red-dashed line shows the case for the single-polarization vibration of the string, black-solid line shows the case for dual-polarization, and the blue dashed-dotted line is the same as the dual-polarization case except that a frictionless bow is kept in contact with the string. Both unperturbed string and body resonances are located at the normalized frequency of 1. (a) is for a C_2 cello string coupled to a body mode with an effective mass of 60 g and a spatial angle of $\theta'_M = 45°$, and (b) is for a D_3 cello string coupled to a body mode with an effective mass of 264.9 g and a spatial angle of $\theta'_M = 20°$. Note the different scaling of the two plots.

The detailed shape of the coupled impedance at the bowing point depends on many parameters, such as the mode frequencies of the bow hair, the distance of the contact point from the frog, and the static alteration of the bow-hair tension. Therefore, the particular set

of parameters chosen here is not claimed to represent the exact effect that the coupling to the bow hair has on the admittance of the string. However, having examined many similar computed cases, the coupled response seems to remain more similar to the single-polarization case than to the dual-polarization case when typical body properties are considered. That is because any large deviation of the coupled case from the single-polarization case would require a significant out-of-plane motion of the string which comes with a premium of a large amount of energy loss into the heavily damped ribbon of bow-hair.

The above discussion showed that the second polarization of the string has a small effect on the admittance at the bowing point, but it does not mean that it can be ignored altogether. There is a second mechanism for influence via fluctuations in the bow force. The limited flexibility of the bowhair allows for some perpendicular-to-bow vibrations of the string, which may modulate the normal bow force by an appreciable amount and affect the nonlinear interactions of the string and the bow in that capacity [62, 130, 28]. Indeed, it will be seen in Sec. 5.1.4 that the normal bow force fluctuates by as much as 10% of its nominal value for a bowed typical D_3 open string. Our qualitative observations of a bowed string using a high-speed camera also confirmed a significant amount of perpendicular-to-bow vibrations of the string.

4.3 Validation with time-domain simulation results

After a theoretical discussion of the bow force limits, we will use the time-domain model of the bowed string, developed in the earlier chapters, to investigate the validity of our findings. An alternative was to make measurements on an actual instrument which is not pursued here; firstly, due to the lack of proper facilities (e.g. a bowing machine), and secondly, because of the flexibility and reliability that the simulations can offer.

4.3.1 The anatomy of the perturbation force at the bow

As has been discussed in Sec. 4.1.1, the perturbation force at the bowing point, assuming a perfect Helmholtz motion and a resistive end support, is a downward hyperbola with its maximum value in the middle of the sticking phase. This pattern repeats every cycle and in between those hyperbola are sections of slipping represented by a constant friction force equal to $\mu_d F_N$. The actual waveform of friction force, however, is much more complex than that, and even its overall appearance varies significantly by the input parameters. With the aim of getting some understanding of that complex picture, we will go through the different components added to form it. Time-domain simulations of the bowed string will be used to demonstrate cases which signify the importance of each individual component.

The first notable structure in the perturbation force is the pattern of Schelleng ripples, which are a consequence of rounding of the Helmholtz corner. When the corner arrives at the bow from the finger side, it begins to interact with the bow before slipping is triggered; similarly, on the bridge side the tail of the corner continues to interact with the bow after recapture has been triggered. Those interactions occur in the sticking phase, during which the bow acts as a barrier and reflects the waves that arrive at it. That reflection requires an increase in the perturbation force at the bow, giving rise to the so-called "rabbit ears" appearing in the friction force just before and after the slipping phase [23]. These reflected waves at the bow get trapped between the bow and their corresponding termination point, and together with their counterparts from the cycles before and after, form a structure of ripples with period βP [50, 23]. The formation of the Schelleng ripples and their spacing is demonstrated in Fig. 4.13 using the time-space diagram.

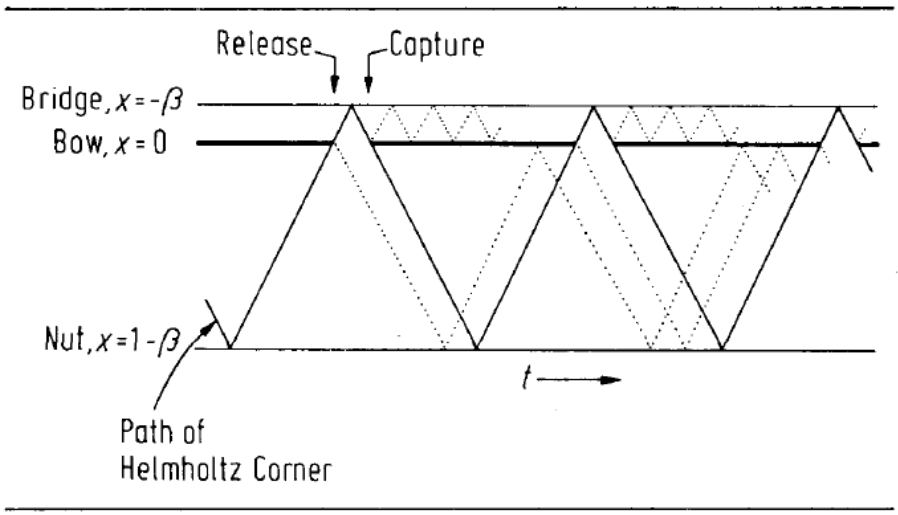

Fig. 4.13 Space-time diagram of traveling wave, illustrating the creation of the Schelleng ripples. The two solid lines at $x = -\beta$ and $x = 1 - \beta$ represent the bridge and the nut/finger respectively. The bow is placed at $x = 0$. The solid lines at the bowing point show the sticking phases during which the bow acts as a barrier to the waves arriving from its both sides, while the gaps in between represent the slipping phases during which the bow becomes virtually transparent. The solid zigzag path is the main Helmholtz corner and the dotted paths are the Schelleng ripples. (From [92])

A consequence of the friction-curve model is that the ripples on the finger side tend to be larger than the ones on the bridge side, because they are produced by the large jump of the friction force before triggering of the slip, while the ones on the bridge side are created from the smaller jump before recapture. Also note that the ripples are a side-product of the rounded corners, and as such, would not exist on an undamped and perfectly flexible bowed

string that is terminated at rigid supports.

The Schelleng ripples are demonstrated in Fig. 4.14a, which is the normalized simulated friction force at the bowing point (F_F/F_N) for a damped but perfectly flexible C_2 string terminated at rigid supports. The red-dashed line shows the value 1.2 that is the limit set for the static friction coefficient in our model. The velocity of the string at the bowing point is also plotted, to indicate the timing of transitions between sticking and slipping. The only source of dissipation in this system is the damping of the string, which is very low; so the general trend of the friction force is flat, apart from the prominent Schelleng ripples. The arrows with numbers '1' and '2' point to the "rabbit ears". β was chosen at around 1/13, and as such, there are 13 Schelleng ripples in each string period. The "rabbit ears" do not have implications for minimum bow force as they happen at the boundaries of the slipping phase. The more important ripples for that matter are the ones that are only reflected once at each boundary, and therefore, are less worn off. Those two ripples are shown by arrows number '3' and '4' for the bridge and finger sides, respectively.

The next influence on the friction force at the bowing point is torsional motion of the string. As was pointed out in Sec. 4.1.1, the primary effect of the torsional motion is expected to be a modification in the effective characteristic impedance of the string as seen by the bow. The secondary effect of the string's torsional motion is to create a trap-door which allows the Schelleng ripples (or any other disturbances) arriving at the bowing point during the sticking phase to be transformed from transverse to torsional, and vice versa, and to pass through the bow causing a smaller perturbation force. This effect is demonstrated in Fig. 4.14b which is the same as Fig. 4.14a except that the torsional motion of the string is added to the model. The ripples are much weaker in comparison to the ripples in Fig. 4.14a. There is also a mild hill-like structure in the friction coefficient that is likely caused by the added damping of the torsional motion.

Bending stiffness of the string is another source for spatial spread of the otherwise sharp Helmholtz corner. In a nutshell, the higher frequency waves travel along the string faster than the low frequency waves; as a result, the high-frequency content of the corner arrives at the bowing point some time before the main peak arrives, forming what is called "precursor waves".[10] Since those precursor waves hit the bow in the nominal sticking phase, they have to be reflected, in the process of which there will be an increased perturbation force at the bowing point. After a few periods, the reflected precursor waves from different cycles merge and it will be hard to backtrack the origin of each one of those individually. The overall effect is then, a non-structured series of disturbances hitting the bow in the sticking phase.

[10]To get a sense of the precursor waves, compare the black-solid line in Fig. 2.12 with the red-dashed line. What is shown in that figure is an impulse traveled a round trip from the excitation point to the nut, but a very similar effect would happen if instead of an impulse, a corner is sent toward the nut.

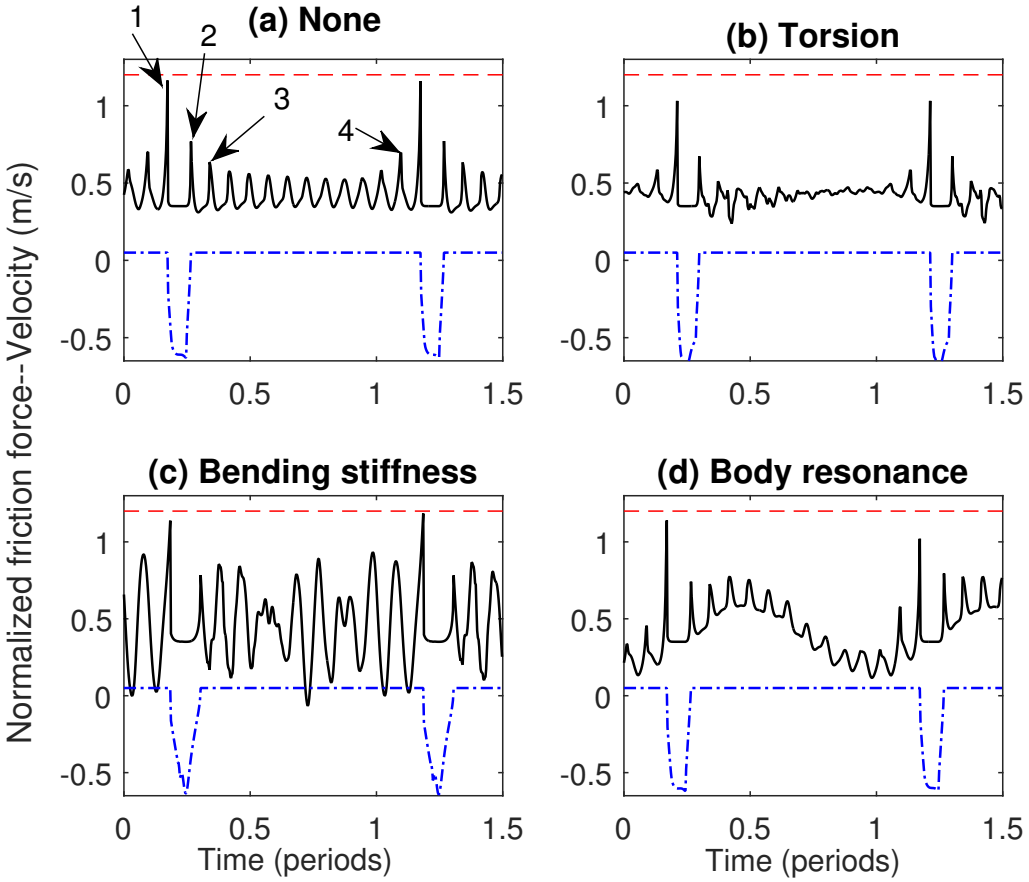

Fig. 4.14 Samples of simulated friction force at the bowing point, non-dimensionalized by the normal bow force (black-solid line), overlaid on the synchronized string velocity at the same point (blue dashed-dotted line). (a) is for a rigidly terminated, damped, but perfectly flexible string, and (b) to (d) are the same as (a), except in (b) the torsional motion of the string is included, in (c) the string's bending rigidity is included and in (d) the bridge is a single resonator with mode frequency of 172 Hz (the features are added individually). The simulations are made on the C_2 string played at 164.23 Hz with a normal bow force of 0.746 N and $\beta = 0.0764$. The red-dashed line shows the constant value of 1.2, which is the maximum value considered for the static friction coefficient.

Figure 4.14c demonstrates a sample of such disturbances. All the parameters of the model were the same as the ones used for Fig. 4.14a, except the bending stiffness of the string is added now.

There is an alternative frequency-domain explanation for the above effect. The bending rigidity of the strings results in inharmonicity, meaning the string's mode frequencies will no longer be perfectly harmonic, the frequency of the higher modes are rather skewed toward higher frequencies. Once the Helmholtz regime is formed, the stick-slip mechanism and the mode lock-in phenomenon [54] enforces a perfectly harmonic motion. Boutillon argues that the stick-slip frequency of the string adjusts itself to balance the reactive powers of all string modes so that the partials that are driven below their natural frequency would compensate for the ones that are driven above their natural frequency [131]. Pushing each string mode to vibrate in a frequency slightly different from the frequency it would have chosen freely requires an extra effort by the bow that is demonstrated in the form of the jaggedy behavior in the perturbation force.

Potentially the most significant contribution to the perturbation force at the bow is the one already discussed: the motion of the bridge. Figure 4.14d shows an example of how a non-rigid bridge affects the friction force at the bow, all other parameters being the same as for Fig. 4.14a. For simplicity, a single-resonance body has been considered with a resonance frequency slightly above the played frequency of the string. The effect is a sinusoidal contribution to the friction force. For a more realistic multi-resonance case the body-induced perturbation would be a superposition of such sine waves, which is usually dominated by the strongest body resonance falling close to the string's fundamental, or one of its harmonics.

A combination of the four abovementioned structures is more or less present in all samples of friction force at the bow. There are two less-obvious structures which may, or may not, be significant depending on the input parameters: the torsional reflected spike, and the sub-harmonics.

The already discussed "rabbit ear"-shaped fluctuation in the friction force sends a pair of waves with the same shape toward the two ends of the string, not only in the transverse direction, but also in the torsional direction. Similar to the case for the transverse waves, the torsional waves get reflected at both boundaries and arrive back at the bow creating a disturbance. The main difference is that the torsional waves are much more heavily damped as compared to the transverse waves (typical Q factor of 45 versus hundreds for the transverse waves), therefore the waves that have been reflected multiple times are of little practical importance. The torsional waves also travel at a speed of roughly 5 times faster than the transverse waves (4.59 times for the particular C_2 string that we have modeled). The

torsional fluctuation reflected once at the bridge always arrives back to the bowing point during the nominal slipping phase, in which time, the bow is virtually transparent to the string; therefore, the reflected wave can easily pass through the bow.[11] However, the reflected torsional wave at the finger-side arrives at the bowing point during the nominal sticking phase and creates a fluctuation in the friction force. A sample of such disturbance force is shown in Fig. 4.15, for which $\beta = 0.0182$ and the bow force is 6.98 N (a large bow force and a small β value leads to a large spike). For clarity, all other options except for the string's damping and torsional motion are excluded from the model. It can be seen clearly that the torsional disturbance follows the shape of the friction force at the times around the triggering of the stick and the recapture. The time delay is exactly $(1-\beta)$ times the ratio of the transverse to torsional wave propagation speed. The biggest disturbance happens due to the reflection of the stick to slip transition, however, the direction of that disturbance is toward the bowing direction. So, if anything, such a spike would create a tendency for forward slipping, which is unlikely to occur because of the positive offset of the friction force.

The last notable structure in the perturbation force at the bow is the subharmonics. McIntyre et al. have noticed, for the first time, the existence of a subharmonic structure in the sound of a bowed string [92]. The time-space illustration of the effect is shown in Fig. 4.16. In summary, any disturbance at the bowing point sends a pair of waves toward the two ends, which after $1/\beta$ reflections between the bow and the corresponding end, reach the bow during the slipping phase and pass to the other side. The precise timing of this path relative to the path that the main Helmholtz corner is traversing, gives rise to a subharmonic structure with the frequency βf_0. Care should be taken not to confuse the subharmonics with the Anomalous Low Frequencies (ALF) which occur above the maximum bow force and are often called subharmonics by musicians [122]. For more detailed explanation of the subharmonics and their relation to the so-called Friedlander's instability the interested reader is referred to [92]. The origin of the initial disturbance can be anything in reality, but in our simulations there is always an unintended disturbance at the bow and within the first few periods because of the imperfect initialization of the Helmholtz motion (see Sec. 3.3.4 for more details). Among the $1/\beta$ times that the subharmonic disturbance should be reflected at the bow, it may coincide with a perturbation of a different nature and cause the total perturbation at the bowing point to exceed the limiting static friction, thus triggering an untimely slip. Due to the nonlinear nature of the bowed string, once that second slip

[11] The sign of this reflected wave is in the bowing direction, hence if it is strong enough, it can terminate the slipping phase prematurely an create a stick-slip alternation. Galluzzo observed such phenomenon in his simulated results which were obtained with the "reconstructed friction-curve" (see Fig. 6.5 of [21]). He did not find any experimental evidence for this phenomenon, therefore it likely does not happen if a more realistic friction model is used.

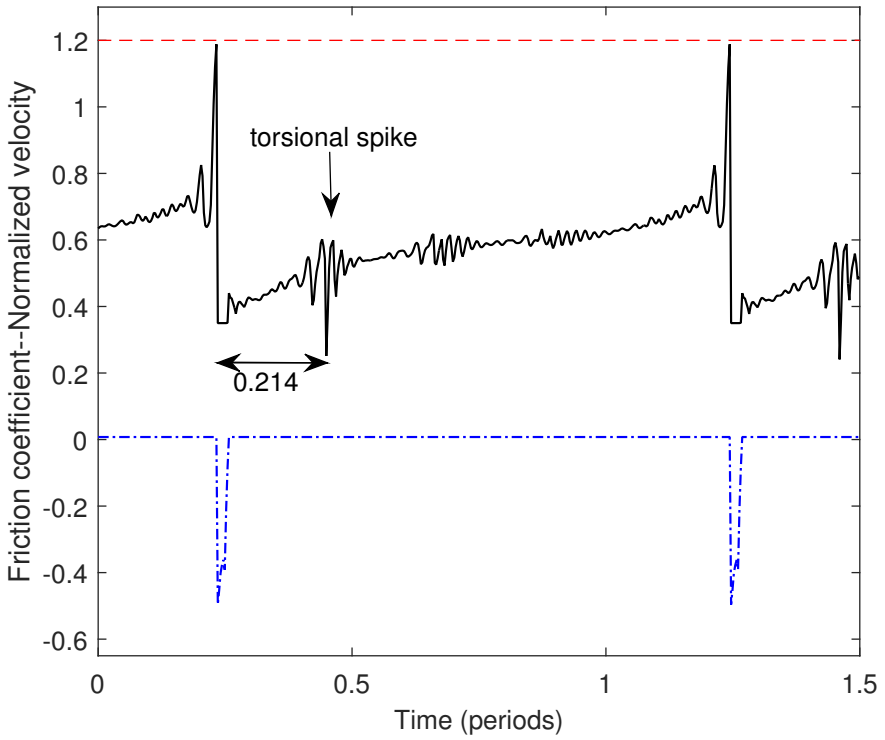

Fig. 4.15 Simulated perturbation force at the bowing point overlaid on the synchronized string velocity at the same point for a rigidly terminated, damped, but perfectly flexible string whose torsional motion is also considered. The red-dashed line shows the constant value of 1.2, which is the maximum value considered for the static friction coefficient. The torsional spike indicated by the arrow is the finger-side reflection of the disturbance force at the bowing point, occurred 0.214 periods earlier.

has occurred, the bowed string may never switch to the Helmholtz regime again. In real playing conditions, the bowing parameters, as well as the played note, vary relatively quickly; therefore it is not likely that the subharmonics will be manifested so often.

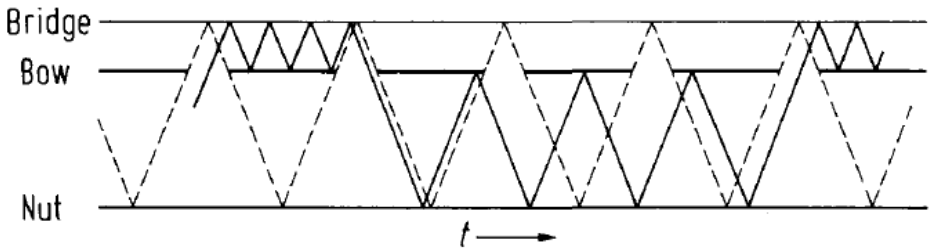

Fig. 4.16 Space-time diagram of traveling wave, illustrating the path of a subharmonic. In this particular example the bow is placed $1/4^{th}$ of the string length away from the bridge. The initiated disturbance reflects 4 times on each side of the bow until it reaches the bow in the slipping phase and passes to the other side. The precise timing of the Helmholtz motion makes the string look like 4 times longer to the subharmonic. (From [92])

A sample of such subharmonics in our simulated results in illustrated in Fig. 4.17. Note that the main Helmholtz corner should travel back and forth the full length of the string whereas the disturbance at the finger side only traverses $(1-\beta)$ of the full length, therefore, it catches the main corner from behind. The high frequency content of those initial disturbances normally get attenuated after a short period of time and the disturbance responsible for the subharmonic structure is a "force build-up" formed by the merging of the low frequency content of those initial disturbances. So essentially the subharmonic structure shown in Fig. 4.17 is generated by the beating of the maxima in the perturbation force caused by the body resonance, with the force build-up that changes its relative timing due to its slightly different frequency. For the parameters used in our simulations, the magnitude of the subharmonic decays to a smaller asymptotic value if the simulations are continued for an extended period of time.

Figure 4.18 shows the spatial distribution of a example simulated *velocity* wave traveling along a damped stiff string terminated at a flexible bridge. The abovementioned force build-up is following the main Helmholtz corner, and the precursor waves are exceeding it.

4.3.2 The playable range and sawtoothness

After a look into the details of the perturbation force at the bow, it is time to compare the results of the time-domain simulation model with the predictions of the minimum bow force corrected by parameter ζ, defined in Eq. (4.18). Note that among the four general

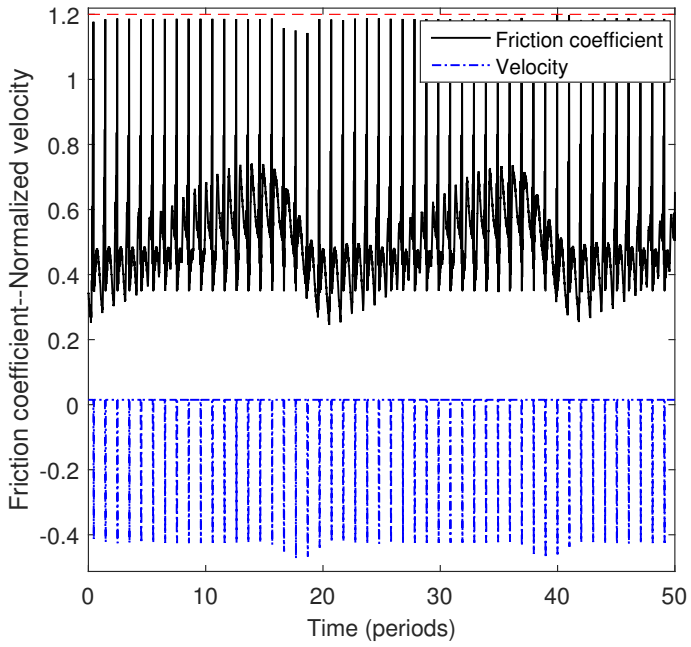

Fig. 4.17 A demonstration of the subharmonic effect on the perturbation force at the bow (black-solid line) and the velocity at the same point (blue dashed-dotted line). The red-dashed line shows the constant value of 1.2, which is the maximum value considered for the static friction coefficient.

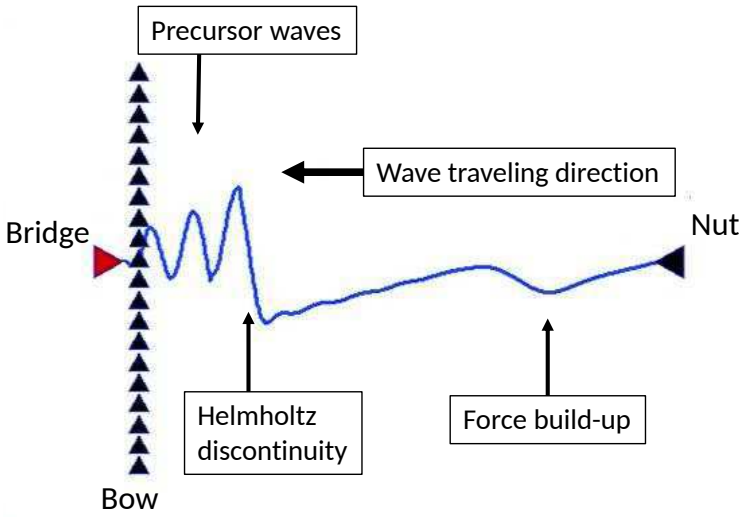

Fig. 4.18 The spatial distribution of a sample simulated *velocity* wave traveling along a damped stiff string terminated at a flexible bridge. As the force build-up only travels between the bow and the nut, it gets closer to the main Helmholtz corner, until it caches the corner from behind and causes a consequent relatively large flyback of the string.

and two particular mechanisms of disturbance at the bow, both original and revised versions of Eq. (4.7) only look at the flexible bridge effect, demonstrated in Fig. 4.14d. All other mechanisms except the trapdoor effect of the torsional waves demonstrated in Fig. 4.14b are detrimental to the stability of the Helmholtz motion; therefore, both original and revised predictions of minimum bow force are expected to underestimate the minimum bow force to some extent. Clearly, a better analytical relation is one that can get closer to the actual minimum bow force. As discussed earlier, the results of the time-domain model of the bowed string are taken as the reference here and the analytical predictions are all compared against that. In accordance with Schelleng's original argument, for each combination of β-F_N, the string is initialized with Helmholtz motion and it is monitored to see whether or not it can sustain that vibration regime. For the matter of classification, any motion of the string that involves only one stick and slip per string period, including the S-motion [132], is classified as Helmholtz motion.

Figures 4.19 and 4.20 demonstrate the comparison of the Schelleng diagrams calculated from simulated data on C_2 and D_3 strings respectively, overlaid on the theoretical maximum bow force relation from Eq. (4.5) (blue dashed-dotted line), minimum bow force from Eq. (4.7) (red-dashed line), and its revised version by parameter ζ, defined in Eq. (4.18) (black-solid line). The variations of the dynamic friction coefficient as a function of the sliding speed is also considered in the calculation of those theoretical limits. For more clarity only a single body resonance is considered. In accordance with the results presented in Sec. 4.2, the frequency of the body resonance is 172 Hz, its effective mass is 120 g, and its Q factor is 40. Only a single polarization of the string is considered and the body mode is perfectly aligned with the bowing direction. The string damping parameters are based on Valette's relation and are representing a finger-stopped string (see Sec. 2.2.1 for more details). The stiffness of the string and its torsional motion are initially excluded from the model to make the comparison more meaningful, but their effect will be considered later. The simulations are made on 24 values of string fundamental frequencies starting from 162.35 Hz and increasing by 20-cent steps. The frequencies shown on top of different subplots are the relative frequencies of their fundamental to the frequency of the body mode at 172 Hz, indicated by the word "Body Mode". The string was bowed with a constant bow speed of 5 cm/s. The data points in each subplot are spaced logarithmically on the β axis from 0.016 to 0.19 in 20 steps, and on the bow force axis in 30 steps. The limits of bow force for each string frequency and β value are carefully chosen so that they give maximum resolution while still covering the full playable range at that particular combination.

The color scheme used in Figs. 4.19 to 4.27 is the amount of deviation of the calculated bridge force from being a perfect sawtooth wave. The criteria used to quantify that property

(named "sawtoothness", for the lack of a better word) is the relative strength of the fundamental frequency component to the second harmonic at twice its frequency, divided by 2 that is the expected relative strength for a perfect sawtooth wave. In that regard, a sawtoothness of 1 represents a perfect sawtooth, any value smaller than that is a weaker-than-expected fundamental, and any value larger than that represents a stronger-than-expected fundamental. Although the criteria is relatively simple, it reveals a clear and consistent systematic deviation from a perfect sawtooth.

It is immediately striking how well the revised version of the minimum bow force relation predicts the boundary between the Helmholtz motion and double/multiple slips. For the reasons already conveyed, both equations are slightly underestimating the minimum bow force however, the revised equation makes a much better prediction of the trend. Of particular interest are the relative frequencies of -9.65 Hz to +4.02 Hz in Fig. 4.19, and -3.92 Hz to +1.99 Hz in Fig. 4.20 where there are frequent occurrences of Helmholtz motion below the level set by Eq. (4.7). The revised minimum bow force limit is curved in a manner that avoids this situation most of the time, missing only 4 instances of Helmholtz occurrences across all simulated cases. The frequencies most affected by the body resonance are limited to a narrower range for the D_3 string as compared to the C_2 string. Also it is encouraging to see that the β value of the "bump" in the minimum bow force limit depends on the fundamental frequency of the string that is simulated, as was qualitatively predicted in Fig. 4.6. This is obviously absent from Eq. (4.7) as it predicts the minimum bow force to be a straight line, except the almost-invisible curvature at larger β values due to the β-dependency of the dynamic friction coefficient. Another very encouraging result is the split of the playable range by a local maxima in the minimum bow force limit that is consistent between the simulated data and the predicted minimum bow force limit (see, for instance, the relative frequency of +6.06 Hz in Fig. 4.19). The maximum bow force limit set by Eq. (4.5) makes a very good prediction of the boundary between the areas with Helmholtz motion and with raucous regime, lending credence to the original argument made by Schelleng. The few exceptions for which the Helmholtz motion was achieved above that boundary were checked manually and were identified as S-motion [132]. The S-motion samples are, indeed, expected to appear in the Schelleng diagram as vertical columns with β values close, but not equal to integer fractions, penetrating in the otherwise raucous territory. As for the sawtoothness, and again as expected, the general rule is that at frequencies lower than the body resonance the share of the fundamental is weaker-than-expected, while it becomes stronger-than-expected at frequencies above the body resonance. There is some β-dependency as well, and the best illustration of that can be seen in Fig. 4.19, the relative frequency of +6.06 Hz, where the fundamental is weaker-than-expected for small β values and it becomes stronger-than-expected at larger

β values. There seems to be no particular bow force dependency for the sawtoothness that results in the equi-sawtoothness lines being vertical in each subplot.

The effective body mass used to simulate the data presented in Figs. 4.19 and 4.20 is chosen to be smaller than the typical value for a cello, to make the trends more visible. Figures 4.21 and 4.22 present the same results when the body mass is turned to a more realistic value of 300 g, all the other parameters were the same as the ones used for Figs. 4.19 and 4.20, respectively. It can be seen that all effects are relatively less significant; nonetheless, the general picture remains the same. The prediction of the minimum bow force from Eq. (4.7) still passes through the playable range in Fig. 4.21 from the relative frequency of -3.92 Hz to +1.99 Hz, while the revised prediction just barely misses a few samples.

After verifying that the predicted minimum bow force, corrected by Eq. (4.18), gives a close estimation of the minimum bow force predicted by the simulations, it is encouraging to see how the prediction of sawtoothness from Eq. (4.18) compares to the simulations. Figure 4.23 contains comparable information, presented in a different form, to the results shown in Figs. 4.19 to 4.22. Equation (4.18) makes no distinction between samples that only differ by their bow force values, which has made it possible to condense the equivalent to all subplots illustrated in each of Figs. 4.19 to 4.22 into a single subplot. The color map for Fig. 4.23 is set to logarithmic for better clarity. The range of sawtoothness predicted in Fig. 4.23 is wider than the range we have seen in simulated results. This discrepancy is probably caused by the fact that many of β–frequency combinations shown in Fig. 4.23 do not lead to a Helmholtz regime with any chosen bow force, hence are not represented in the simulated results. Other than the range of variation, results in Fig. 4.23 compare very well with ones obtained from simulations.

As an extra step toward making the simulations more realistic, the single-resonance body is replaced by the multi-resonance body which was earlier used in Sec. 4.2. The instrument has two dominant modes in the range of frequencies plotted here which are at frequencies 189 Hz and 199 Hz, and with effective masses in the bowing direction of 314 g and 1170 g respectively. Figs. 4.24 and 4.25 show the results for such simulations for the C_2 and D_3 string. The number at the top of each subplot shows the fundamental frequency of the simulated string in absolute terms. As there are more than one mode contributing in the plotted frequency range, the transition through the body resonances is not as clear as it was for the single-resonance cases. That said, there is a clear tendency for the Helmholtz region to extend toward lower β values in Fig. 4.24, for the frequencies 186.48 Hz to 190.84 Hz, while the Helmholtz region is reduced in the small-β range, for the frequencies above 202.19 Hz.

An interesting feature to look at in Figs. 4.24 and 4.25, as well as in Figs. 4.19 to 4.22, is

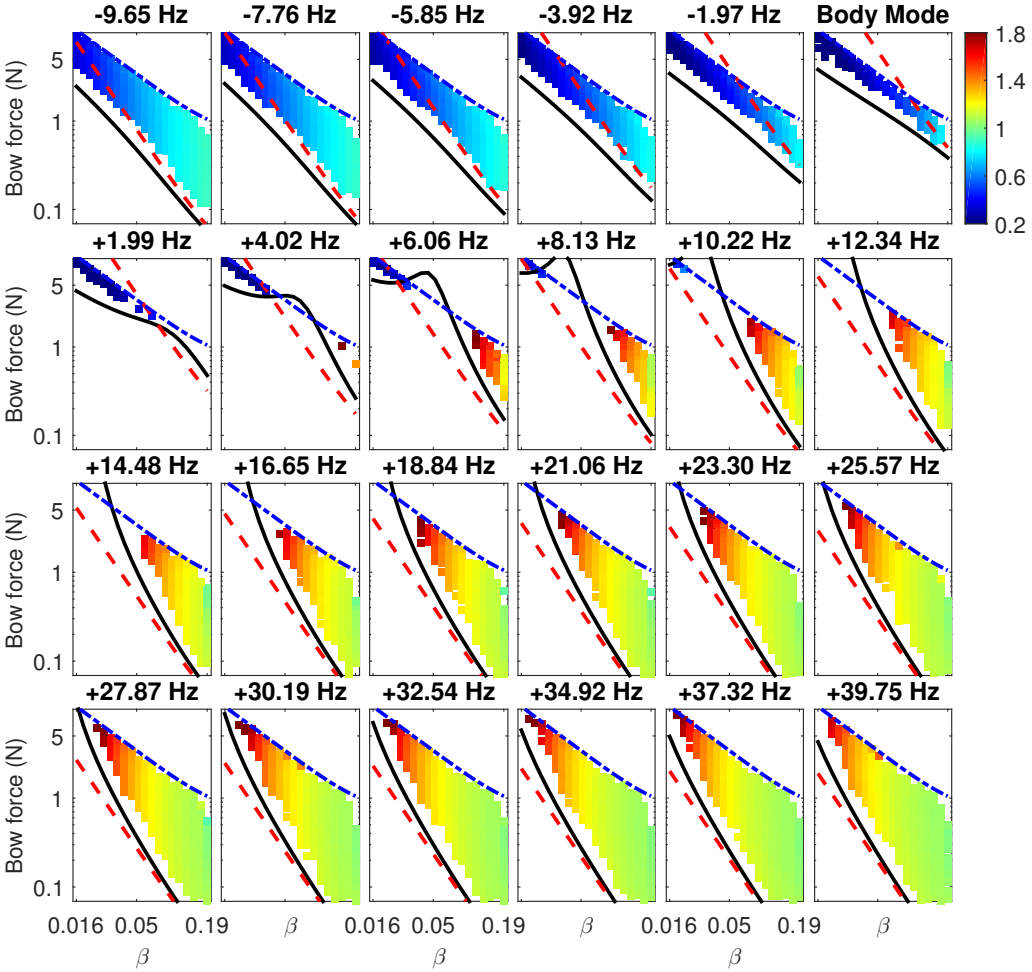

Fig. 4.19 The Schelleng map of the playable range for a simulated damped but perfectly flexible C_2 cello string terminated at a single-resonance body at 172 Hz and with an effective mass of 120 g. The torsional vibrations of the string were excluded from the simulations. The number on top of each subplot shows the relative frequency of the played note with respect to the body resonance. The color of the simulated sample points represents their sawtoothness, defined in the text and according to the scale shown on the color bar. The overlaid blue dashed-dotted line shows the maximum bow force limit calculated from Eq. (4.5), the red-dashed line shows the minimum bow force calculated from Eq. (4.7), and the black-solid line is the same quantity corrected by parameter ζ, defined in Eq. (4.18).

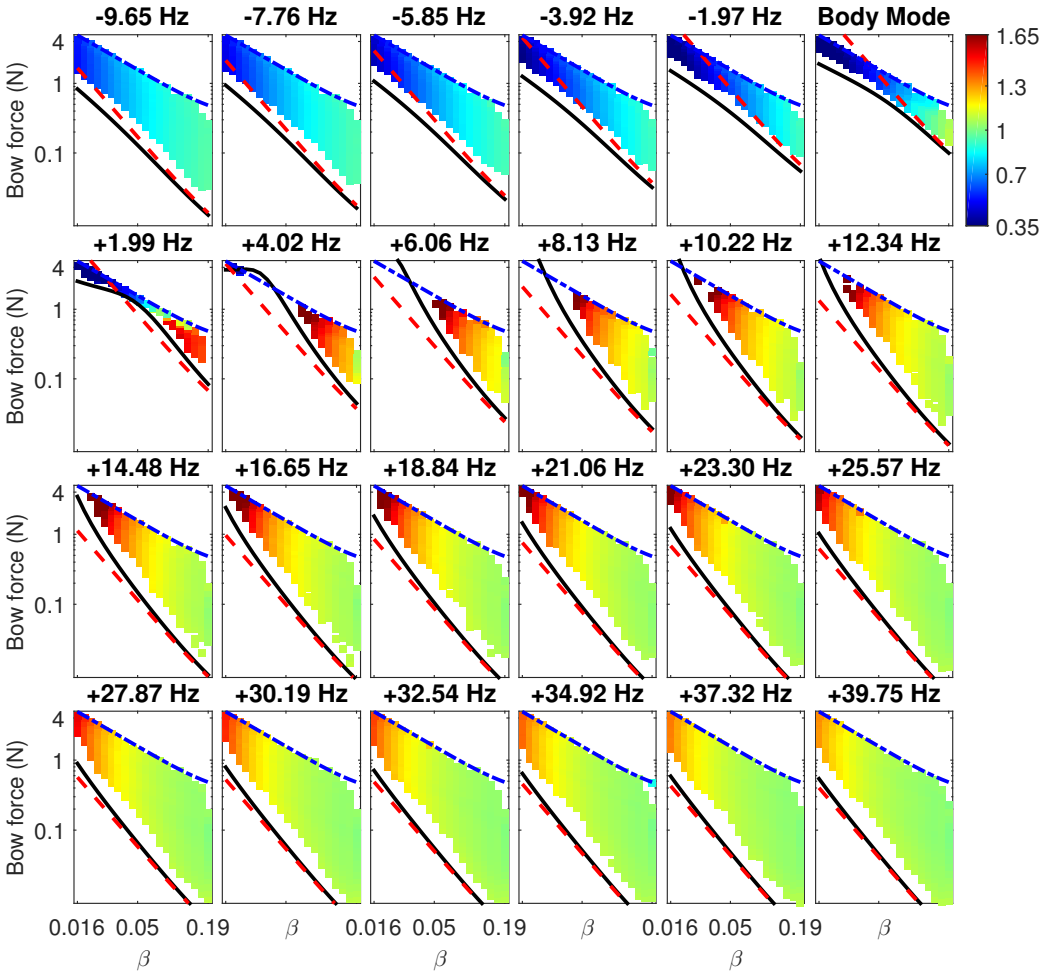

Fig. 4.20 The Schelleng map of the playable range for a simulated damped but perfectly flexible D_3 cello string terminated at a single-resonance body at 172 Hz and with an effective mass of 120 g. The torsional vibrations of the string were excluded from the simulations. The number on top of each subplot shows the relative frequency of the played note with respect to the body resonance. The color of the simulated sample points represents their sawtoothness, defined in the text and according to the scale shown on the color bar. The overlaid blue dashed-dotted line shows the maximum bow force limit calculated from Eq. (4.5), the red-dashed line shows the minimum bow force calculated from Eq. (4.7), and the black-solid line is the same quantity corrected by parameter ζ, defined in Eq. (4.18).

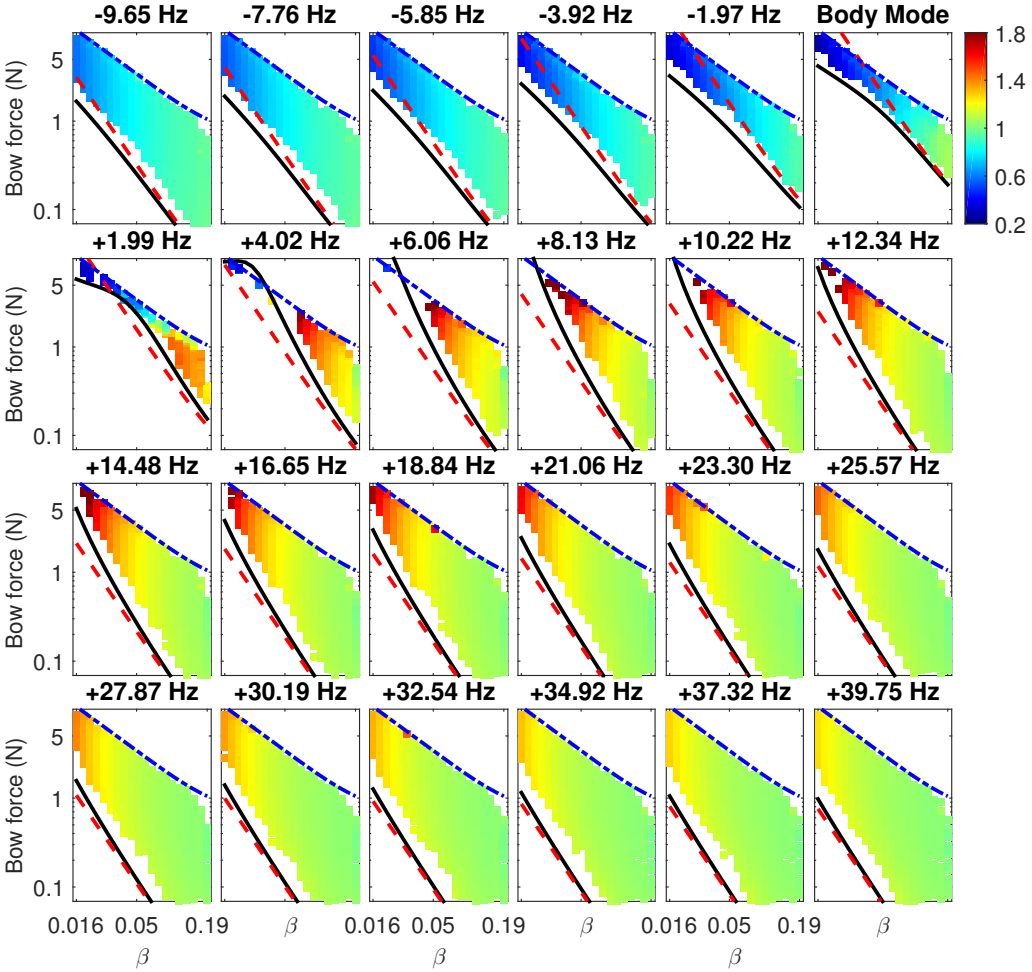

Fig. 4.21 The Schelleng map of the playable range for a simulated damped but perfectly flexible C_2 cello string terminated at a single-resonance body at 172 Hz and with an effective mass of 300 g. The torsional vibrations of the string were excluded from the simulations. The number on top of each subplot shows the relative frequency of the played note with respect to the body resonance. The color of the simulated sample points represents their sawtoothness, defined in the text and according to the scale shown on the color bar. The overlaid blue dashed-dotted line shows the maximum bow force limit calculated from Eq. (4.5), the red-dashed line shows the minimum bow force calculated from Eq. (4.7), and the black-solid line is the same quantity corrected by parameter ζ, defined in Eq. (4.18).

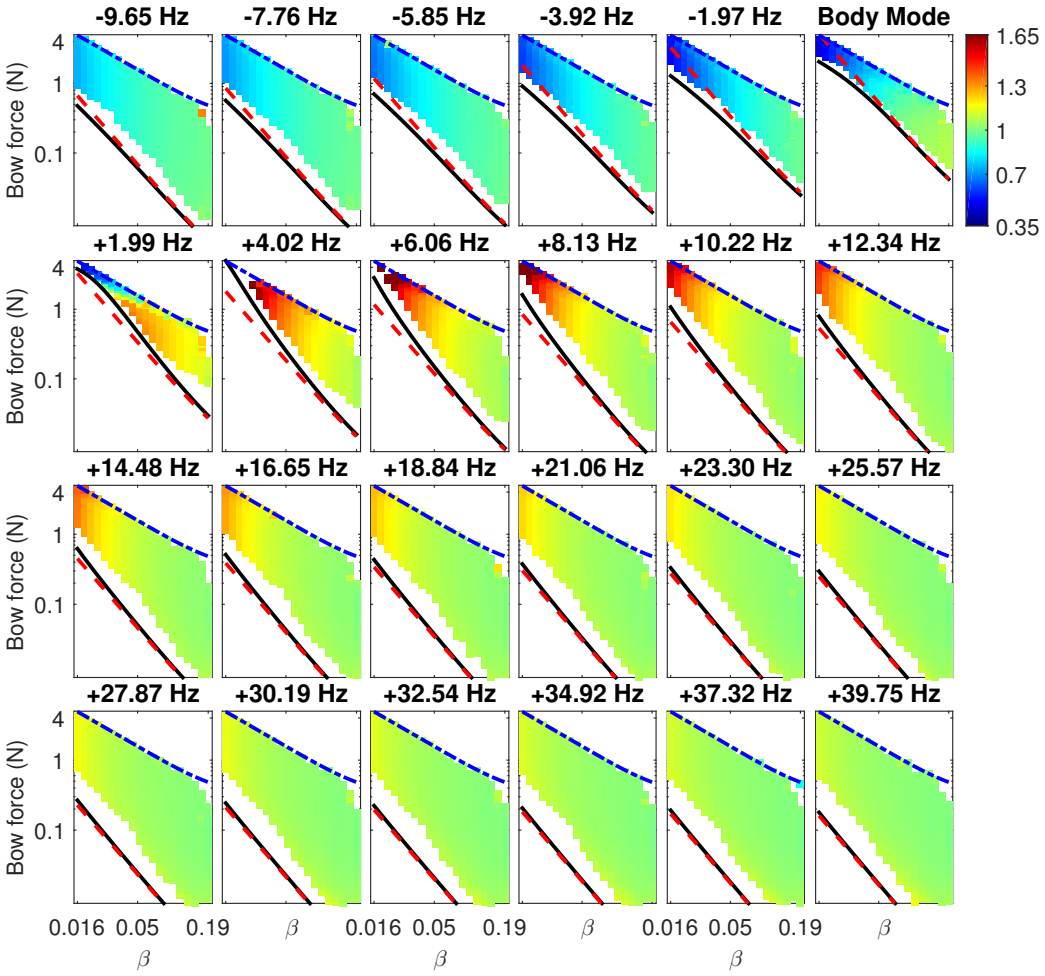

Fig. 4.22 The Schelleng map of the playable range for a simulated damped but perfectly flexible D_3 cello string terminated at a single-resonance body at 172 Hz and with an effective mass of 300 g. The torsional vibrations of the string were excluded from the simulations. The number on top of each subplot shows the relative frequency of the played note with respect to the body resonance. The color of the simulated sample points represents their sawtoothness, defined in the text and according to the scale shown on the color bar. The overlaid blue dashed-dotted line shows the maximum bow force limit calculated from Eq. (4.5), the red-dashed line shows the minimum bow force calculated from Eq. (4.7), and the black-solid line is the same quantity corrected by parameter ζ, defined in Eq. (4.18).

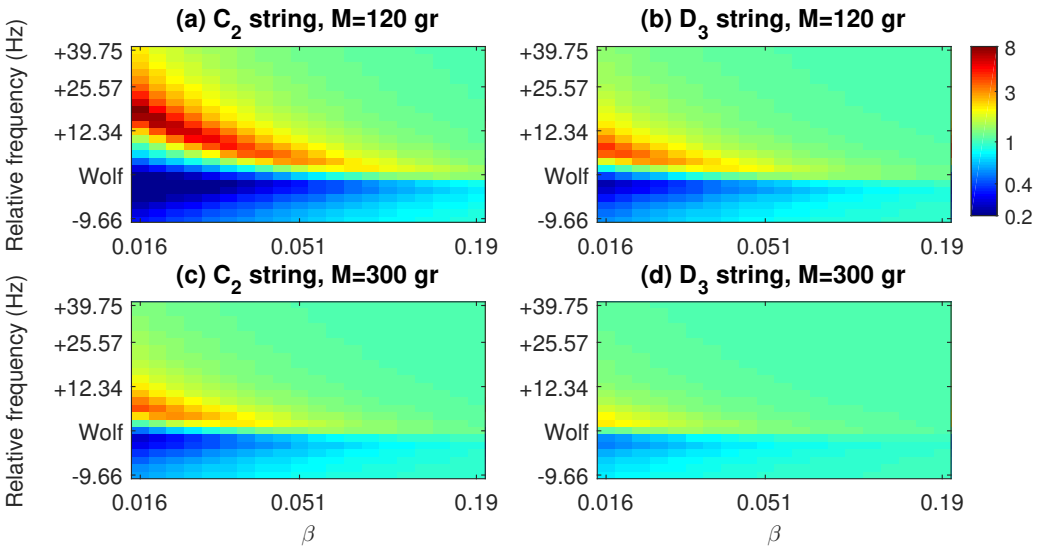

Fig. 4.23 Sawtoothness predicted by Eq. (4.18) as a function of the played frequency and the bow-bridge distance. In all cases, a damped but perfectly flexible string is coupled to a single body resonance at 172 Hz. The simulated string (either C_2 or D_3) as well as the effective mass of the body resonance are shown on top of each subplot. The color of each data point shows the value of sawtoothness criteria (defined in the text and comparable to Figs. 4.19 to 4.22) according to the color bar shown on the top right side.

the gap between the prediction of the minimum bow force and its value based on simulated results. The gap becomes narrower closer to the body resonance where the movement of the bridge is the major contributor to the perturbation at the bow. Away from the wolf region, other effects – not accounted for in the theoretical relations – gain significance and widen the gap. Other than the bridge movement, the other contributors to that gap discussed so far are the Schelleng ripples and the intrinsic damping of the string. Another contributor, which is an artifact in the simulated results, is the imperfect initialization of the Helmholtz motion. A possible way to eliminate the latter is to start the simulation at the intended β value, using the bow force which certainly leads to a Helmholtz regime, and then continuously, and very slowly, decreasing the normal bow force until the Helmholtz motion breaks into a double slip motion. No effort has been made here to perform a study of that kind.

The torsional vibrations of the string and its bending stiffness have thus far been omitted from the predictions and simulations. In an effort to see their relative significance, those two effects are added to the simulations and are compared to the predictions. The results presented in Fig. 4.22 (the damped but flexible D_3 string terminated at a single body resonance with 300 g of effective mass) are taken as the base case. Figure 4.26 shows the results of a similar simulation when the torsional vibrations of the string are taken into account.

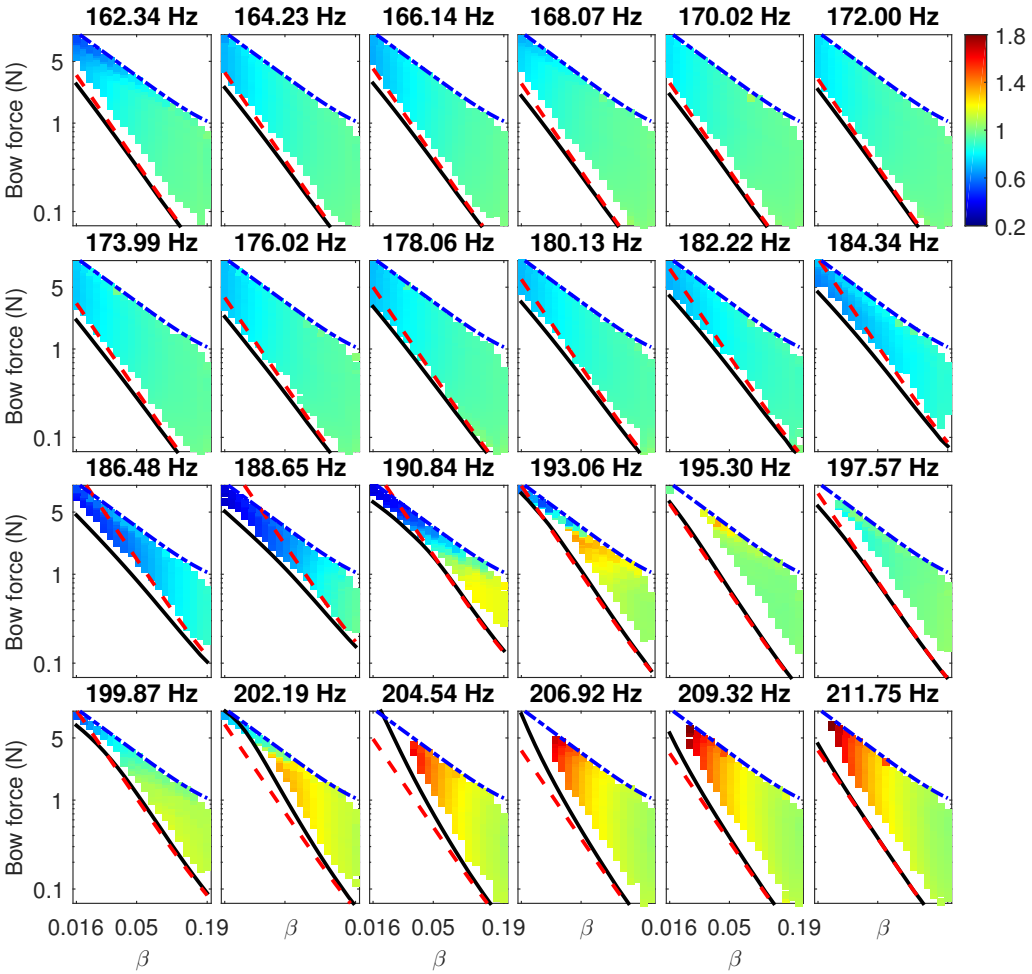

Fig. 4.24 The Schelleng map of the playable range for a simulated damped but perfectly flexible C_2 cello string terminated at a multi-resonance body with two dominant resonances at 189 Hz and 199 Hz. The torsional vibrations of the string were excluded from the simulations. The number on top of each subplot shows the relative frequency of the played note with respect to the body resonance. The color of the simulated sample points represents their sawtoothness, defined in the text and according to the scale shown on the color bar. The overlaid blue dashed-dotted line shows the maximum bow force limit calculated from Eq. (4.5), the red-dashed line shows the minimum bow force calculated from Eq. (4.7), and the black-solid line is the same quantity corrected by parameter ζ, defined in Eq. (4.18).

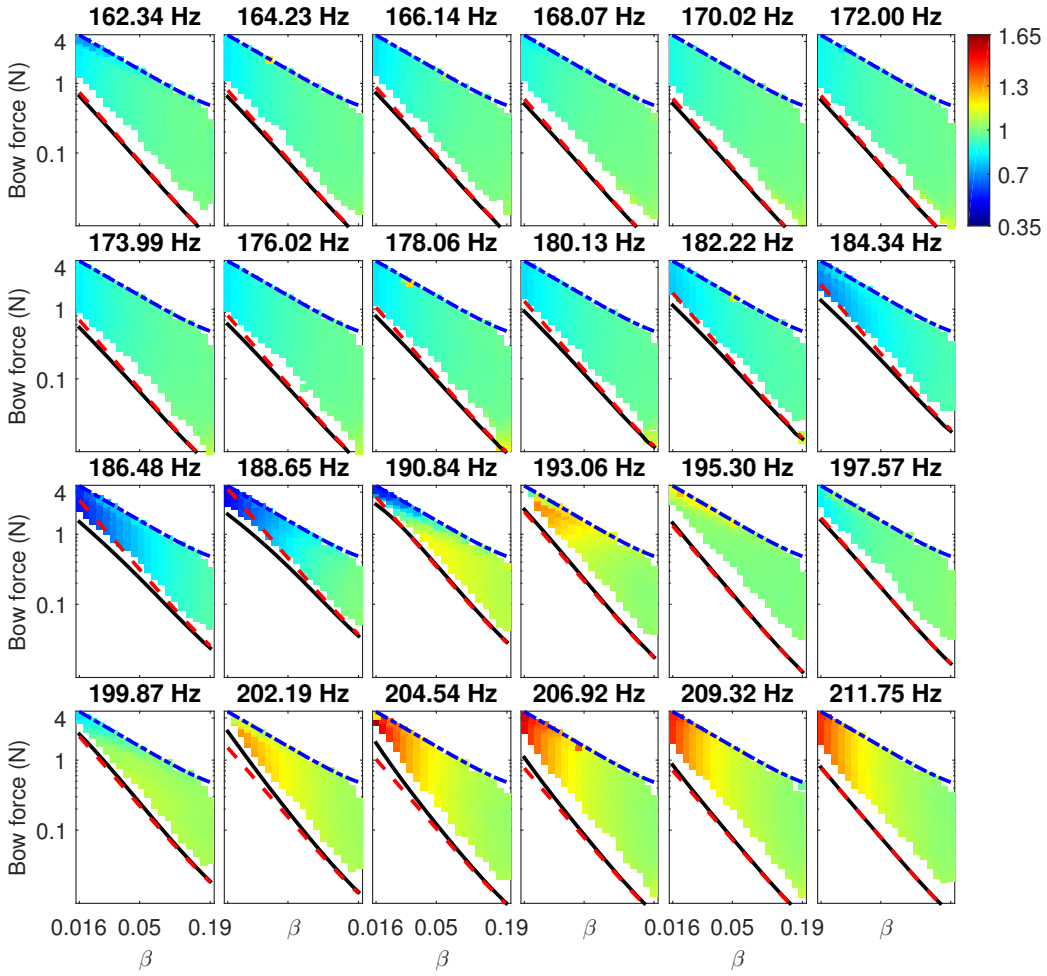

Fig. 4.25 The Schelleng map of the playable range for a simulated damped but perfectly flexible D_3 cello string terminated at a multi-resonance body with two dominant resonances at 189 Hz and 199 Hz. The torsional vibrations of the string were excluded from the simulations. The number on top of each subplot shows the relative frequency of the played note with respect to the body resonance. The color of the simulated sample points represents their sawtoothness, defined in the text and according to the scale shown on the color bar. The overlaid blue dashed-dotted line shows the maximum bow force limit calculated from Eq. (4.5), the red-dashed line shows the minimum bow force calculated from Eq. (4.7), and the black-solid line is the same quantity corrected by parameter ζ, defined in Eq. (4.18).

Overlaid on the simulated results are the predictions of the maximum and minimum bow forces (shown by the dashed-dotted blue and black-solid lines) and calculated from Eqs. (4.5) and (4.7), corrected by parameter ζ, defined in Eq. (4.18). The black-dotted and red-dashed lines are the same quantities calculated by replacing the characteristic impedance of the string (i.e. Z_{0T}) by the effective characteristic impedance, Z_{tot}, defined in Sec. 4.1.1. Curiously, the predictions made using Z_{0T} are much closer matches to the simulations than the ones made using Z_{tot}. We will get back to this observation and its possible reason in the next section.

Aside from predictions and only looking at the simulated results, the difference between Figs. 4.22 and 4.26 is almost negligible. Inclusion of the torsional waves in the model introduced some samples of double slip into the range where all simulations were expected to lead to the Helmholtz regime. Such sparsity of Helmholtz samples was more severe in small β values and for frequencies below the body resonance. For those frequencies, the maximum perturbation from the moving bridge happens in the first half of the nominal sticking phase, which is where the disturbance from the reflected torsional wave occurs as well. For most of the samples, these two effects were not significant enough to make the transition to double slip. The transition happened when just enough periods were passed from the beginning of the simulation for the disturbance generated due to imperfect initialization of the Helmholtz motion to coincide with the reflected torsional wave that evidently created enough perturbation force to trigger an untimely slip.

Finally, Fig. 4.27 shows the results of the same simulations as Fig. 4.26, when the bending stiffness of the string is also included. The inclusion of the bending stiffness has resulted in a reduction of the Helmholtz region by a little bit from both high-force and low-force sides, in an almost frequency-independent manner. The reason behind the higher required normal bow force for a stiff string was discussed earlier in Sec. 4.3.1. As for the shrinkage of the playable range from the high-force side, one may note that the bending stiffness of the string spreads the high-frequency and low-frequency components of the main Helmholtz corner, as a result when the main peak arrives at the bowing point it creates a smaller jump in the velocity compared to what it would have created if the string was perfectly flexible, hence a lesser chance of triggering the timely slip. Satisfyingly, we can see that the total effect of the torsional vibrations of the string and its bending stiffness is relatively small and the calculated limits overlaid on Fig. 4.27 are still making a fairly close prediction of the playable range close to a strong body resonance which is where the bow force limits matter most.

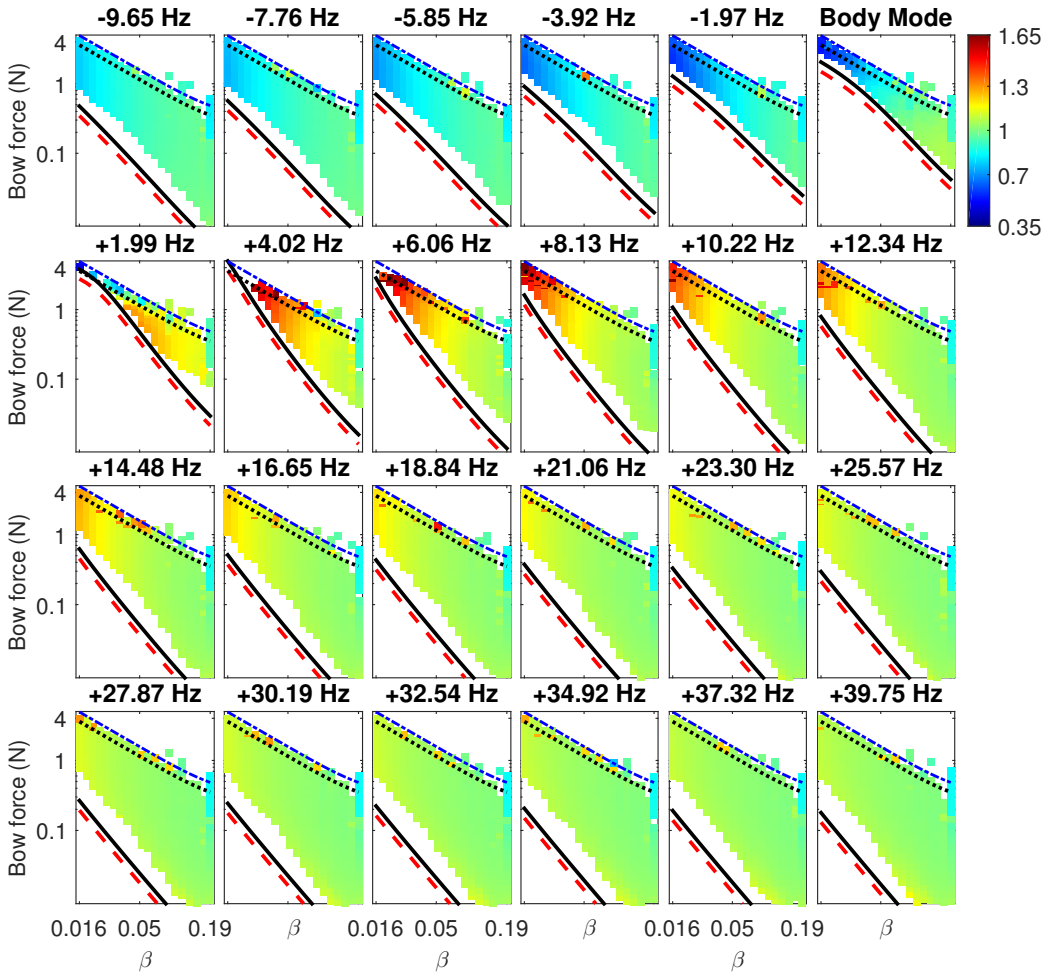

Fig. 4.26 Same as Fig. 4.22, but the torsional vibrations of the string is added. As before, the blue dashed-dotted line shows the maximum bow force limit calculated from Eq. (4.5), the black-solid line shows the minimum bow force calculated from Eq. (4.7) and corrected by parameter ζ, defined in Eq. (4.18). The red-dashed line and the black-dotted lines are the minimum and maximum bow forces calculated by replacing the characteristic impedance of the string (i.e. Z_{0T}) by the effective characteristic impedance, Z_{tot} defined in Sec. 4.1.1.

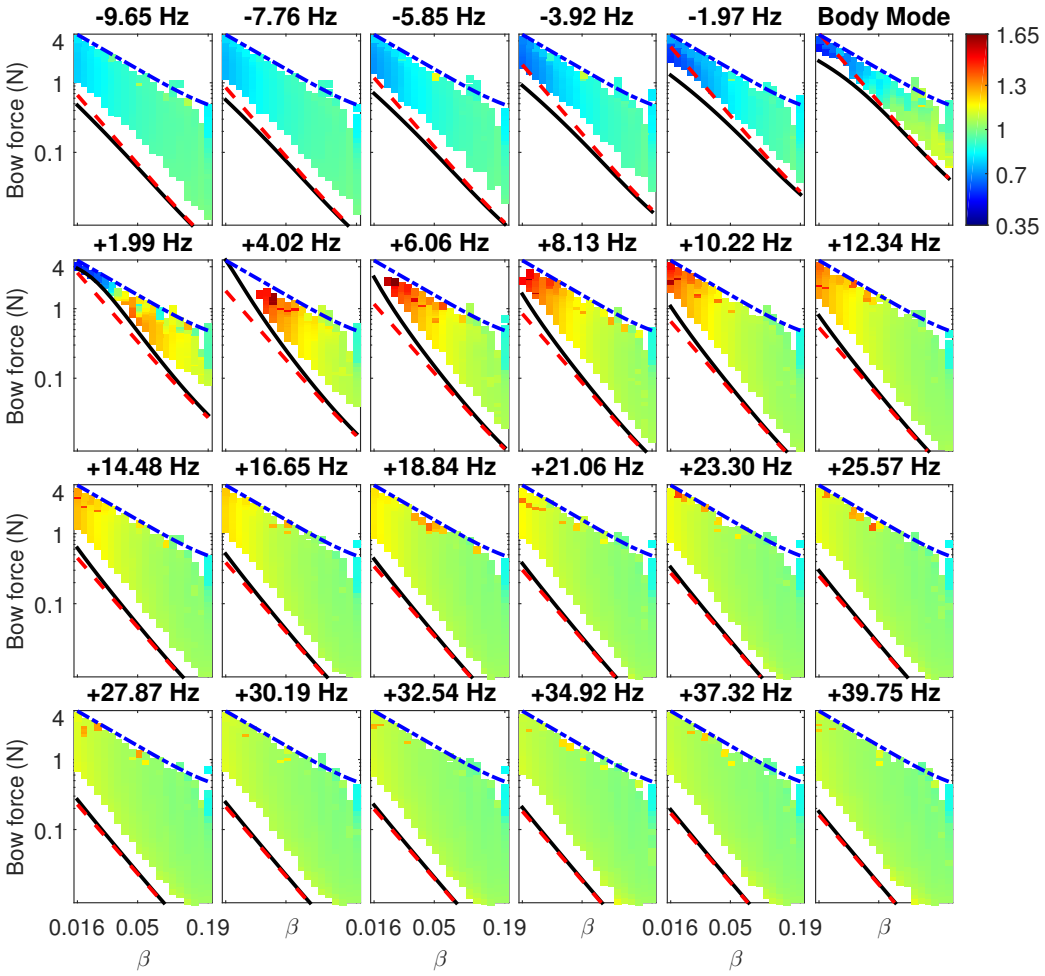

Fig. 4.27 Same as Fig. 4.22, but the bending stiffness of the string and its torsional vibrations are added.

4.3.3 Does the Schelleng apex really exist?

This brings us to the question of whether or not the Schelleng wedge-shaped apex really exists. The answer is most likely yes, but with some reservations. For a real instrument and far from the wolf note, the distribution of the phase for the bridge admittance becomes a random variable, and given the fact that all harmonics play a role (even if not equally weighted) in defining the minimum bow force, the Schelleng assumption of a purely resistive bridge admittance may not be too far wrong. Indeed, in the two experiments done on the topic [21, 22], the slope of -1 and -2 for the minimum and maximum bow forces plotted in the logarithmic scale have been empirically confirmed within relatively good approximations. When the played note (or one of its first few harmonics) falls close to a strong body resonance, things become different. For the frequencies below the body resonance, the minimum bow force limit would be curved downward and extends playable range to β values smaller than predicted by Schelleng's relation; the result is a not-so-sharp apex at the smallest playable β. On the contrary, if the played note falls above the body resonance, the minimum bow force would be curved upward and reduced the wedge shaped playable range before it reaches the ideal apex at a smaller β. It becomes particularly hard to call the playable range "wedge shaped" for the extreme case that the bump in the minimum bow force limit splits it into two non-connected regions. Such situation does not occur for the cases with realistic body modes, presented in Figs. 4.24 and 4.25.

4.4 Direct use of bowing-point impedance in finding the minimum bow force

Going back to our discussion of the derivation of the minimum bow force relation, an alternative and easier-in-principle approach to find the perturbation force at the bowing point would have been to directly convolve the impedance with the imposed velocity at that point, rather than using Eq. (4.18) to find the revised excitation force at the bridge. As a bonus, the Schelleng ripples will be automatically included in the perturbation force calculated from Eq. (4.11), and there would be a straightforward way to add the effect of the torsional waves as well. We will see here how far we can go with this alternative approach and what are the pitfalls involved with it.

Figure 4.28 illustrates the evaluation of Eq. (4.11) to generate results comparable with Fig. 4.14d. The blue dashed-dotted line shows the imposed velocity at the bowing point chosen at $\beta = 0.0764$. The played frequency is 164.23 Hz and the string is coupled to a body with a single-resonance at 172 Hz aligned with the bowing direction, with a Q factor of 40 and an effective mass of 300 g. The imposed velocity is rounded using a Gaussian low-pass

filter with a cut-off frequency of 795 Hz. The black-solid line shows the perturbation force at the bowing point according to Eq. (4.11) and the red-dashed lines are the maximum values of the perturbation force used to derive Eq. (4.7) and corrected using Eq. (4.18). The string was perfectly flexible and its torsional vibrations were excluded. It can be seen that the two predictions are in close agreement meaning that the steps taken to derive Eq. (4.18) from Eq. (4.11) are self-consistent. Taking the perturbation shown in Fig. 4.14d as the reference, Fig. 4.28 shows much weaker presence of the Schelleng ripples in the perturbation force. The inconsistency should not come as a surprise as the Schelleng ripples are the joint product of the corner rounding and the deviation of the velocity at the bowing point from being a square wave. In that regard, unless the imposed velocity at the bowing point is exactly what it would have been if the string was actually being bowed, there should be no expectation for realistic modeling of the Schelleng ripples, regardless of how well the corner rounding (i.e. impedance at the bowing point) is modeled. In particular, for a realistic velocity at the bowing point, both downward and upward portions of the slipping phase advance into the nominal sticking phase but in an asymmetrical manner (see Fig. 5 of [24] for instance). Increasing the slipping phase in Fig. 4.28 (even in a symmetric manner) by 20%, which was roughly the number seen in Fig. 4.14d, did create ripples of comparable size and spacing. In reality, the disturbances on each side of the bow can easily pass to the other side if they arrive at the bowing point sometime within the slipping phase. This possibility is excluding by our approach of imposing velocity at the bowing point, therefore, we are effectively decoupling the portions of the string on the two sides of the bow.

Equation (4.11) results in a much worse prediction of the perturbation force if the driving frequency does not perfectly match the stick-slip frequency that the string would have chosen freely, if bowed on. In that case, the hysteresis loop in the F_F-v plane becomes a sensitive function of the driving frequency and takes shapes not resembling any plausible friction model. In explaining the situation, the exact stick-slip frequency of a bowed string is unknown and different from the frequency of its first mode when we take into account effects such as the string's bending stiffness, pitch flattening, and proximity to a strong body mode. Pitch flattening only gains significance when a large bow force is applied, therefore can usually be ignored for the analysis of the minimum bow force. The operational frequency would then be a compromise among the slightly inharmonic string modes. A potential way to find that operational frequency was proposed by [131] based on balancing reactive powers created by each string mode being driven away from its natural frequency. That makes a good topic for future studies but has not been pursued here. Given the above discussion, there is no motivation to directly use Eq. (4.11) in place of what we have done in Sec. 4.2. Even though the former method captures a flavor of the Schelleng ripples and disturbances

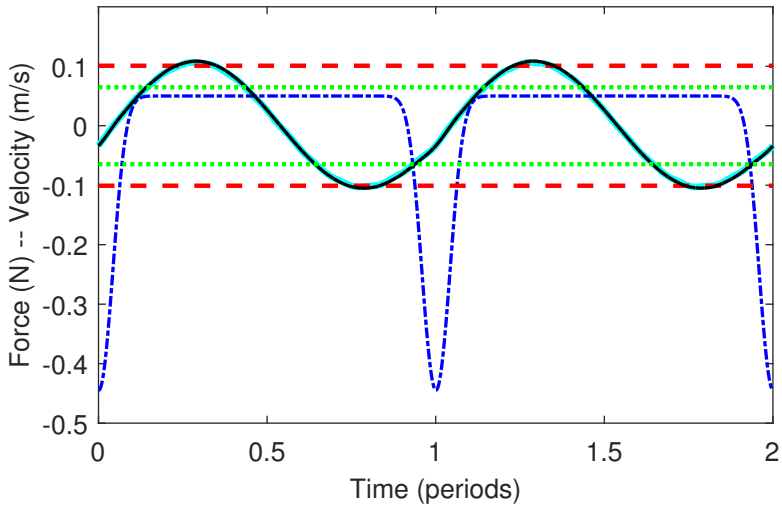

Fig. 4.28 The perturbation force at the bowing point (black-solid line) calculated using Eq. (4.11) overlaid on the imposed string velocity at the same point (dashed-dotted blue line). The evaluation is made for a C_2 string played at 164.23 Hz with the normal bow force of 0.746 N, and β is equal to 0.0764. The bridge is a single resonator with mode frequency of 172 Hz. The red-dashed lines show the plus/minus maximum perturbation force used to derive Eq. (4.7) and corrected using Eq. (4.18). The cyan-solid line fully covered by the black-solid line is the perturbation force at the bowing point calculated using Eq. (4.27) and the green-dotted line shows the equivalent to the red-dashed line when Z_{0T} is replaced with Z_{tot}.

caused by the string's bending stiffness, it does it in an unpredictable biased way and leads to unreliable results.

It should be noted that the unphysical disturbances caused by enforcing the bowed point to move in a slightly different fashion is mostly contained on the finger side, and as such, does not affect the correction made to the bridge excitation based on Eq. (4.18). Indeed, that is easy to try by convolving the velocity at the bowing point by the bridge-side impedance only. This experiment was done and the amplitude of perturbation force was very close to the prediction of Eq. (4.11).

Lastly, we get back to the surprising observation in Fig. 4.26 that adding the torsional vibrations of the string does not shift the playability limits in a way consistent with replacing Z_{0T} with Z_{tot}. The use of transmission lines can reveal the underlying physics leading to this phenomenon. In order to take into account the torsional vibrations of the string, Z_b defined in Eq. (4.11) should be replaced with

$$Z_b = \frac{(Z_1+Z_2)Z_R}{(Z_1+Z_2)+Z_R}, \tag{4.27}$$

where Z_R is the impedance at the bowing point if only the torsional motion was allowed, and can be calculated from

$$Z_R = Z_{0R}\left(\coth\left(ik_R x_0\right) + \coth\left(ik_R\left(L-x_0\right)\right)\right), \tag{4.28}$$

in which k_R is the wave number of the torsional waves along the string. The cyan-dotted line in Fig. 4.28 shows the resulting perturbation force at the bowing point if Eq. (4.28) is used in place of Eq. (4.11) and the same velocity is imposed at the bowing point. The calculated perturbation force is only slightly different from one that was calculated without the inclusion of the torsional vibration. This is consistent with the results of the time-domain simulations and very different from what could be obtained by replacing Z_{0T} with Z_{tot} in Eq. (4.7). That result is also shown as a green-dotted line for comparison.

The key to this discrepancy is that the first torsional mode of the string has its first mode frequency at almost 5 times greater than the first transverse mode of the string which is also very close to the frequency of the stick-slip when the string is bowed. As a result for the frequencies below the 5^{th} harmonic of the bowed string the numerical value of Z_R remains very large, and subsequently, the bowing-point impedance at the bowing point evaluated from Eq. (4.28) remains very close to what Eq. (4.11) suggests. The magnitude of the admittances (inverse of the impedances) obtained from Eqs. (4.11) and (4.28) are compared to one another in Fig. 4.29. To his credit, Schumacher left the door open to this possibility noting that replacing Z_{0T} by Z_{tot} ignores "*the normal-modes structure of*

the rotational modes, thus in effect treating the string as if it were unbounded for rotational waves." [99].

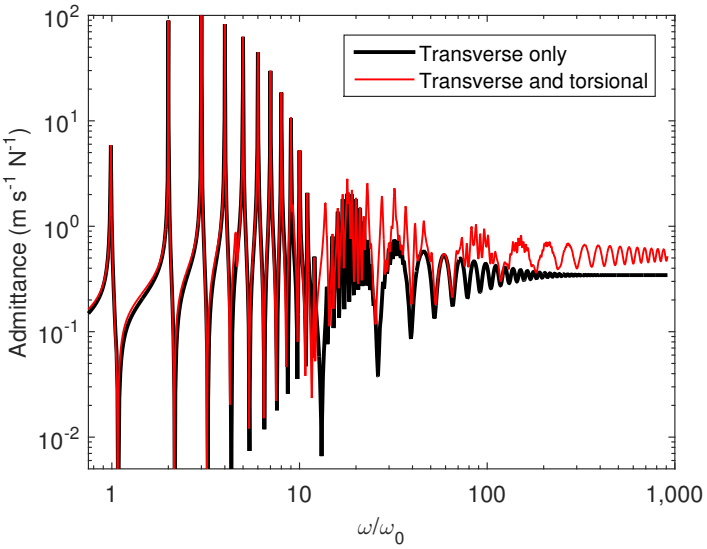

Fig. 4.29 The magnitude of the bowing point admittance (inverse of the impedance) plotted against the normalized frequency. The results excluding the torsional motion and obtained from Eq. (4.11) are shown by the thick black line and the results including the string's torsion and obtained from Eq. (4.28) are shown by the thin red line.

4.5 Summary of findings

In this chapter, we reviewed the state of the art in formalizing the minimum bow force needed to sustain the Helmholtz regime on a bowed string. In a step toward generalizing the argument by Woodhouse, we went one step back and assumed a perfect stick and slip at the bow rather than a perfect sawtooth force excitation. The time-domain simulation of a bowed string, introduced in the earlier chapters, was used to evaluate the accuracy of the predictions. The revised version of the minimum bow force is demonstrated to make a much better prediction than the original version close to a strong body resonance. In the next chapter, we will further use time-domain simulations to study the steady and transient responses of a bowed string.

Chapter 5

Dependence of bowed string's macro-behavior on the model parameters

In the previous chapter, we demonstrated a particular application of our time-domain model in validating a revised relation for the minimum bow force. In this chapter, we will look into some other details of a bowed string's vibrations as well as their dependence on different parameters of the model. Given the broad range of topics that could be covered, we inevitably limit our scope to a single case of an open D_3 cello string, acknowledging the fact that some metrics may not strongly demonstrate their effect for this particular case. Based on the limitations of the friction model used in our simulations, we do not expect a close quantitative match to the experiments. Having said that, it seems reasonable to expect the right trend of outcome by including (or excluding) different physical details in the model. To that end, the influence of a number of factors on the upper and lower limits of bow force and some perceptually important metrics are studied as functions of bow-bridge distance and bow force. These factors include noise in the bowing parameters (representing fluctuations in the player's bow control), finger stopping of string, bow hair vibrations in transverse and longitudinal directions, flexible bow stick, string polarizations, torsion, stiffness and string terminations. The perceptually relevant parameters include spectral centroid and in particular, pitch flattening. This extensive comparative study is done by starting from a base case representing a realistic cello and switching factors on and off, one by one. The fluctuations of bow force and bow hair velocity at the contact point with the string is highlighted and surprisingly large deviations from the nominal values are observed. According to the classic (and the revised) theory both minimum and maximum bow force limits scale with bow speed. This effect was studied as well and compared with experimental results from previous

studies. The transient behavior is studied by means of Guettler diagrams where the bow is accelerating from rest with a constant bow force. Also here a base case is used to allow comparisons of the influence of finger stopping, rigid terminations torsion and stiffness on the successful formation of Helmholtz motion and the duration of the pre-Helmholtz transient. A quantitative analysis of a bowed string is a very challenging task due to the wealth of input parameters affecting its vibrations. This task is made possible to pursue thanks to our versatile model of a bowed string.

5.1 The steady-state vibrations of an open cello string

The steady-state vibrations of an open D_3 string is studied using a 100×100 grid of simulated data points in the β-F_N plane (i.e. the Schelleng diagram). The output of each simulated data point is 1 second worth of force signal applied by a bowed string to the bridge. The string is initialized with the Helmholtz motion at the beginning of each simulation. The data points are spaced logarithmically on the β axis from 0.016 to 0.19, and on the bow force axis from $1.28 \times 10^{-4}/\beta^2$ N to 5 N. In this way, a triangle of double-slip and decaying samples is removed from the analyzed range, giving increased resolution around the more important Helmholtz region. It should be noted that an actual player cannot control, and thus utilize, a constant bow force below around 0.1 N [111], therefore the simulated data with bow forces below this limit are mainly of research interest. The simulated data is processed by the waveform identification routine presented in Sec. 3.4.2 that classifies each sample into one of the decaying, double-slip, Helmholtz, S-motion, raucous, or ALF regimes. In addition to that, three other metrics are calculated from the last 0.5 s of each data point:

1. The increase in the slip-to-stick ratio as a percentage of its theoretical value.
2. The spectral centroid relative to the fundamental frequency.
3. The amount of pitch flattening as a percentage of the fundamental frequency.

The second and third metrics are directly relevant to the experience of the listener; the first metric does not have a direct musical consequence, but sheds light on the underlying mechanics of the string motion (a particular application was seen in Sec. 4.4).

5.1.1 The base case

As the base case, we chose an open damped and stiff D_3 cello string which is only allowed to vibrate in a single transverse polarization and is being bowed with a constant bow speed of 5 cm/s. The torsional motion of the string is also included in the simulations. The string is

terminated at a realistic multi-resonance bridge whose properties were discussed in Chap. 2. The base case represents a real cello string, bowed by a rosin-coated rod.

Figure 5.1a shows the Schelleng diagram calculated for the base case. Instances of Helmholtz motion are shown in black, instances of S-motion are shown in cyan, and instances of ALF regime are shown in green. Instances of decaying and double-slip regimes occur in the empty area below the Helmholtz regime, and instances of raucous regime occur in the empty area above it. Those samples are eliminated from the plot for clarity. As expected, the S-motion occurrences appear as columns in large β values extending into the raucous territory. For all β values there are at least 10 simulated samples of double-slip/decaying below the first instance of Helmholtz motion. This margin was considered to make sure that the predicted minimum bow force is not affected by the selected range for simulations.

Figure 5.1b shows how the Schelleng diagram differs from the one of the base case when a brown noise with a range of 5% of their nominal values is added to the nominal bow force and bow speed (see Sec. 3.3.2). As in Fig. 5.1a, the Helmholtz occurrences are shown in black, the S-motion is shown in cyan, and the samples with ALF regime are shown in green. In addition to that, the samples which were of Helmholtz regime for the base case but are otherwise when the noise is added are shown in red, and conversely, the samples which were not of Helmholtz regime in the base case but have become such when the noise is added are shown in blue. Generally, there are more red squares in Fig. 5.1b than there are blue squares, meaning that added noise has made the occurrence of the Helmholtz samples less frequent. In particular, the red samples are more dense in the bottom-right side of the Helmholtz region creating a "patchy" region. It is encouraging to see that the model can produce such a region as appeared in the experimental results reported in [21] as well. It is noteworthy that in the experimental results the patchy region appeared in the same β-range but for bow forces about ten times higher.

Figure 5.2 shows the three metrics, defined on page 148, for the base case. The values are only shown for the data points identified as being of Helmholtz motion. An important trend to look for in the plot of each metric is the path of the points with the same values of that metric.

The lines with the same extended slipping phase are almost parallel to the minimum bow force limit (slope of -2 in the log-log scale) with a slight tendency of more extension of slipping phase for smaller β values making the slope steeper than -2. The range of variations is relatively broad, starting from the theoretical value of βP for the top-right side of the Helmholtz region, extending to as long as three times the theoretical value in the lower-left side of the Helmholtz region. The slipping phase is slightly shorter than the ideal case for

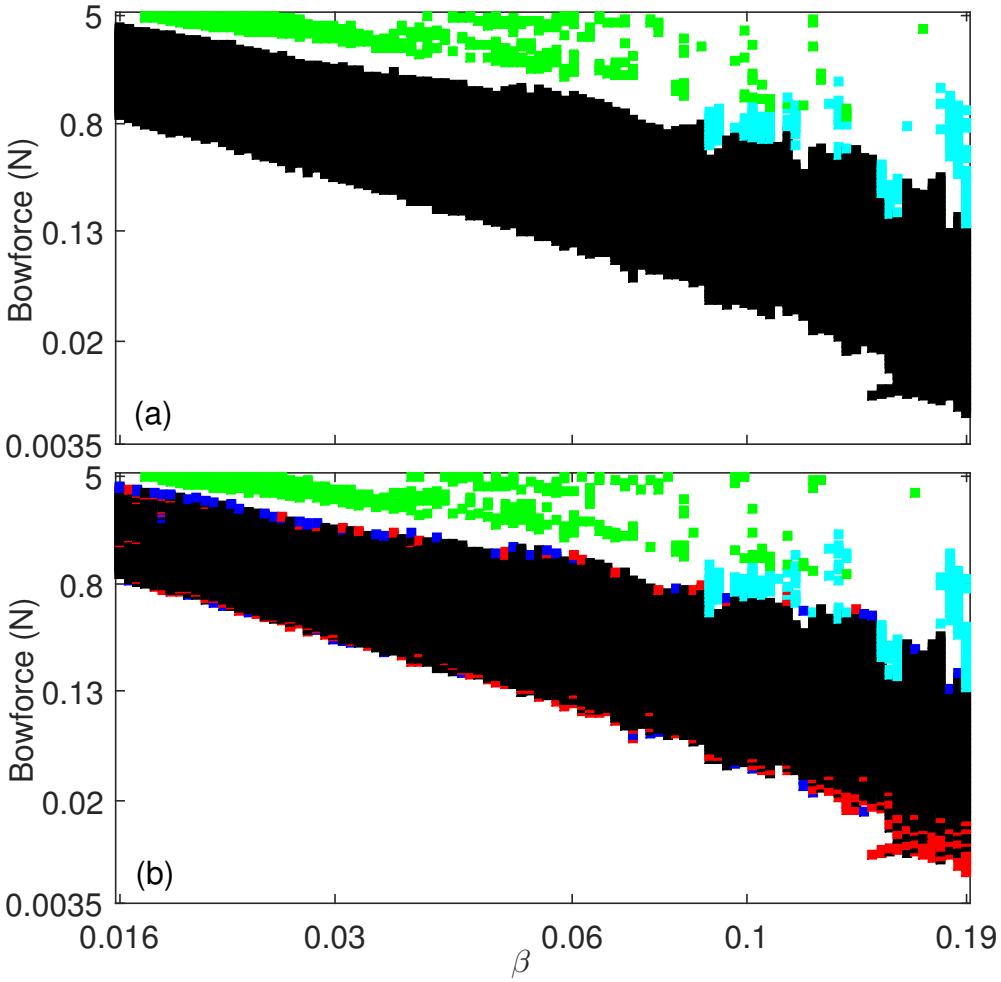

Fig. 5.1 Schelleng diagram calculated for the base case (a), and when a brown noise with a range of 5% of their nominal values is added to the nominally-steady bow speed and bow force (b). The Helmholtz occurrences are shown in black, the S-motion is shown in cyan, and the samples with ALF regime are shown in green. The red squares in (b) show the samples which were identified as Helmholtz motion in (a) but have become otherwise in (b), and conversely, the blue squares are the samples which were not Helmholtz motion in (a) but have become one in (b). A bow speed of 5 cm/s is used for all cases.

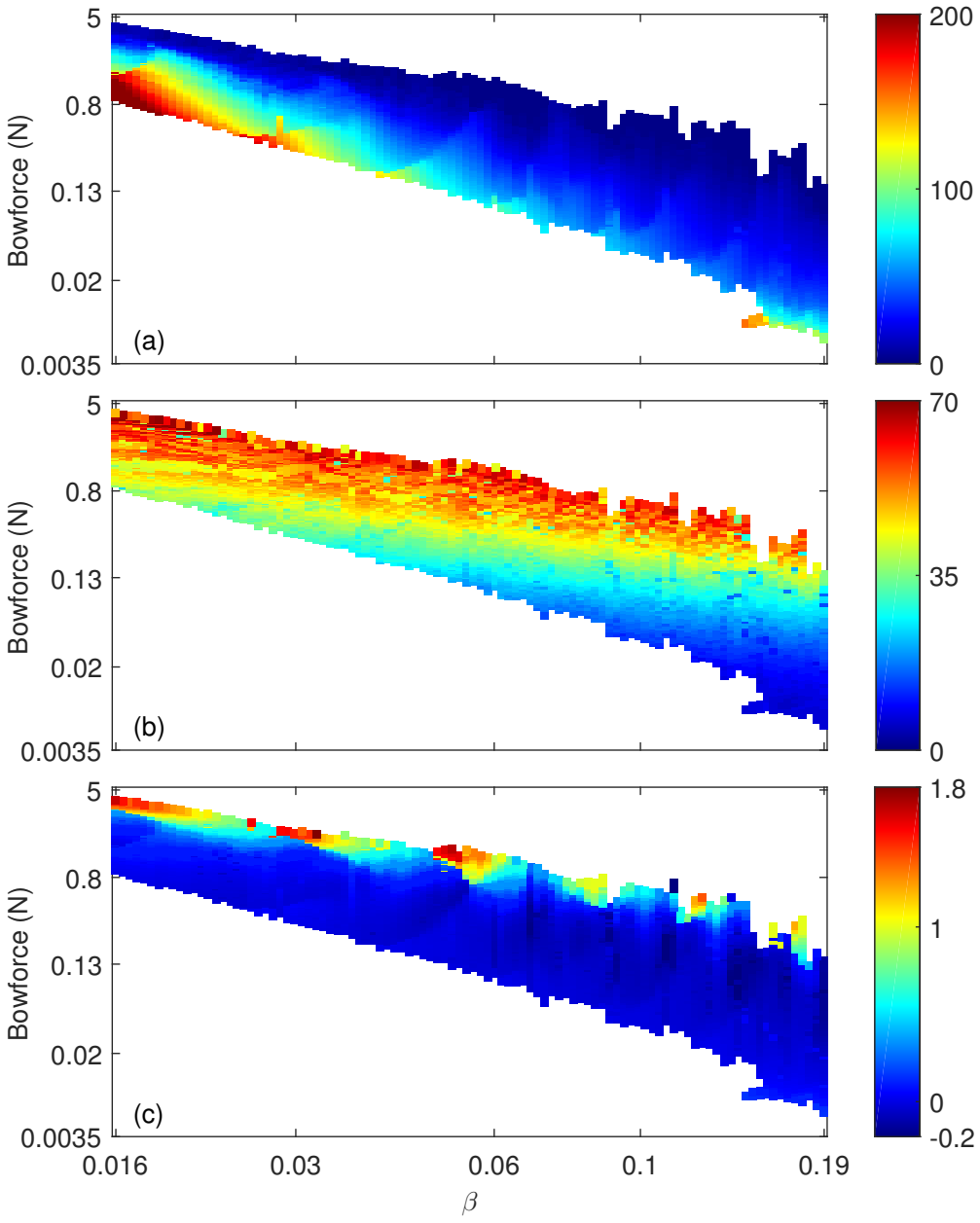

Fig. 5.2 Different metrics of the base case in the β-bow force plane. (a) The increase in the slip-to-stick ratio as a percentage of its theoretical value, (b) the spectral centroid relative to the fundamental frequency, and (c) the pitch flattening as a percentage of the fundamental frequency.

only a few samples, which were identified as Helmholtz motion with large ripples.[1]

The spectral centroid relative to the fundamental frequency is plotted in Fig. 5.2b. The samples with the same relative spectral centroid are laid out almost horizontally, and the values roughly range from 6 on the bottom side of the plot, to 70 on its top side. The overall appearance is more speckly than the two other plots, which might be an artifact of the post-processing routine. The strong dependence of the spectral centroid on the bow force is in accordance with experimental findings reported in [133].

The last plotted metric is the percentage of pitch flattening. The lines with the same amount of flattening are almost parallel to the maximum bow force limit (slope of -1 in log-log scale). This is in accordance with the experimental results reported in [133] and interestingly, they also observed the maximum amount of flattening at some intermediate value of β. The static alteration of tension is also taken into account to calculate the values shown in Fig. 5.2c. If the static alteration of tension is not taken into account, the samples on the top-left corner of the Helmholtz region would have an even larger amount of flattening (see Fig. 3.4 for a quantitative measure of the static alteration of tension).

A notable structure observed consistently in Figs. 5.2a and 5.2c is a set of ripples, equally spaced on the β axis by around 0.015 (note that the axis is plotted in the logarithmic scale). A similar structure is reported in experimental results of [133] (see their Fig. 8). Interestingly, the ripples disappear if either, or both, the torsional motion of the string or its stiffness are excluded from the model. This is demonstrated in Figs. 5.3a and 5.3b, directly comparable to Figs. 5.2a and 5.2c, for which the torsional motion of the string is excluded. Given that the two sets of simulations use the exact same loop-filters for the bridge and finger sides, it seems safe to assume that the ripples are not a numerical artifact of the routine used to model the string.

The fact that the ripples need both torsional motion of the string and its stiffness to appear leads one to hypothesize that they are created by the excitation of the torsional string modes by the oscillatory behavior of the precursor waves, a consequence of the string's bending stiffness. It is not clear, however, what has caused the short spacing of the ripples. The 0.015 spacing on the β axis corresponds to the 66^{th} torsional mode of the string. This is particularly unexpected because the precursor waves sweep down from very high frequencies (theoretically infinite) to somewhere around the fundamental frequency of the bowed string at which point the slipping triggers, which makes one wonder why this force should excite a particular torsional mode of the string. Given that those ripples have not made an appreciable impact on the boundaries of the Helmholtz region, they can be ignored for the analysis

[1] The waveform classification routine does not make a clear distinction between Helmholtz motion and S-motion. For the S-motion samples the theoretical length of the slipping phase is a fraction of βP depending on the number of corners that travel along the string.

of the minimum and maximum bow forces regardless of them being genuine or an artifact.

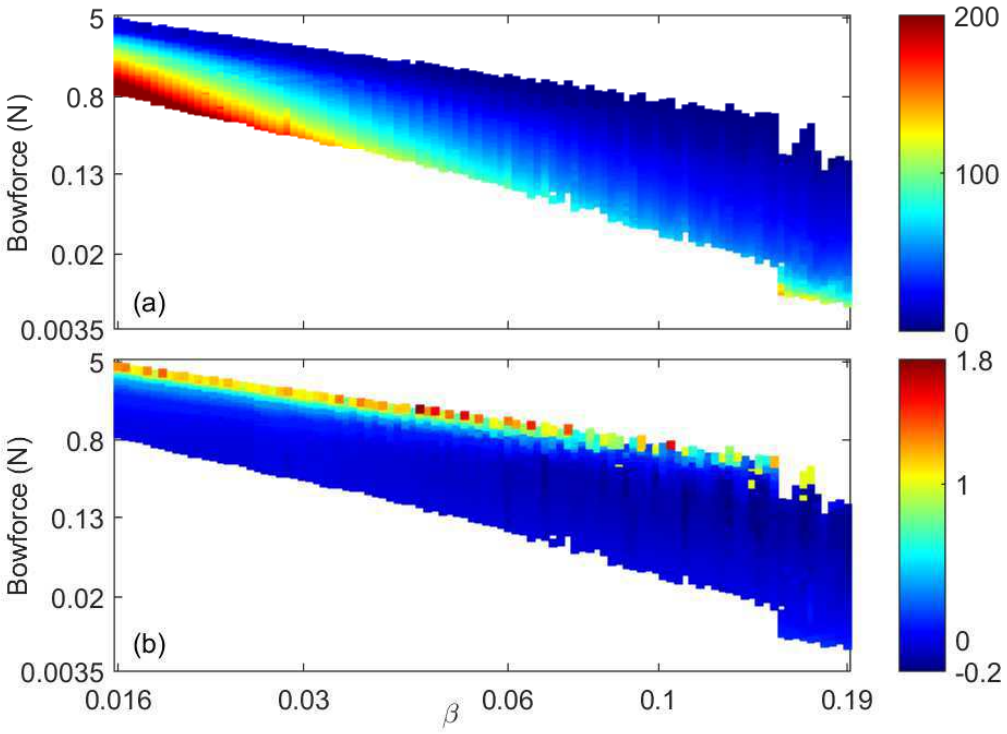

Fig. 5.3 The increase in the slip-to-stick ratio as a percentage of its theoretical value (a) and the pitch flattening as a percentage of the fundamental frequency (b), plotted in the β-bow force plane. The model is the same as the base case, except the torsional motion of the string is excluded.

5.1.2 General effects of model variations

After a look at the general appearance of the plot for different metrics, it is time to see how each physical detail of the model affects those metrics. Eight particular variations of the model are considered for this investigation:

- **"Finger-stopped"** is the same as the base case, except the intrinsic damping of the string is increased to reflect the added damping by the finger of the player (see Sec. 2.3.1 for the damping of a finger-stopped string). This situation may not be possible in reality, but one may think of it as removing the nut and stopping the string by the finger of the player at the same physical location.

- **"Hair long. vib."** is the same as the base case, but the vibrations of the bow hair in its longitudinal direction are also included. The bow-stick is considered rigid for this case and the β_{bow} is chosen at 0.31.

- **"Flexible bow-stick"** is the same as the base case, but the vibrations of the bow hair in its longitudinal direction coupled to a flexible bow-stick are also included.
- **"Dual-polarizations"** is the same as the base case, but the perpendicular-to-bow vibrations of the string, coupled to the vibrations of the bow hair in its transverse direction are also included. The bow-stick is considered rigid for this case and the β_{bow} is chosen at 0.31.
- **"No torsion"** is the same as the base case, but the torsional motion of the string is excluded.
- **"No stiffness"** is the same as the base case, but the bending stiffness of the string is excluded. One may think of it as having a perfectly flexible string.
- **"No torsion/stiffness"** is the same as the base case, but both the torsional motion of the string and its bending stiffness are excluded.
- **"Rigid terminations"** is the same as the base case, but both termination points of the string at the bridge and the nut are considered rigid.

Figure 5.4 shows a chart that compares the three metrics mentioned in the previous section, as well as the minimum and maximum bow forces, for the eight variations of the model, relative to their value for the base case.

The maximum and minimum bow forces are, respectively, quantified as the number of Helmholtz occurrences in the upper and lower halves of the simulated grid (i.e. bow force steps 1-50 and 51-100). Keep in mind that the bow force ranges from $1.28 \times 10^{-4}/\beta^2$ N to 5 N at each β value. The samples are only counted up to $\beta = 0.08$ (i.e. $\beta - step = 65$) for that purpose. For larger β values, distinction between the Helmholtz and decaying regimes, as well as between the Helmholtz and S-motion regimes, becomes highly sensitive to the parameters of the waveform identification routine, thus ambiguous. A positive number in Fig. 5.4a means more Helmholtz occurrences in the upper half compared to the base case, equivalent to a larger maximum bow force. On the contrary, a positive number in Fig. 5.4b means less Helmholtz occurrences in the lower half compared to the base case, equivalent to a larger minimum bow force. The two plots are arranged so that looking at both of them makes it apparent how the Helmholtz region is shifted or expanded/contracted. The minimum bow force could not be evaluated for the "Rigid terminations" case (marked by N/A) as its actual value is very small, much smaller than the limit considered for our simulated grid of data points.

Each bar in Figs. 5.4c to 5.4e represents the average change in the value of that metric for the corresponding case, to its value for the base case. The average is only calculated over the β-bow force combinations that led to Helmholtz motion in both cases. In this way, we do not allow the variations in the size and position of the Helmholtz region to bias the calculated trend.[2] Admittedly, averaging over the full Helmholtz region obscures the variations across that region. For that reason, the individual plots of the pairwise differences are carefully reviewed to make sure that the reported trend is consistent over the broad range. The only observed anomaly of that kind is reported in Fig. 5.7 and will be discussed in Sec. 5.1.3.

It is useful to look at how the playable range of different cases compare to that of the base case. Adding to the damping of the string makes a minimal effect on the maximum bow force, but it significantly increases the minimum bow force. It seems that adding to the intrinsic damping of the string acts similar to adding a resistive loss to the bridge. Although this makes sense from the energy balance point of view,[3] it is not clear how the damping of the string affects the perturbation force at the bowing point (see Schelleng's argument in Sec. 4.1.1). Adding the longitudinal vibrations of the bow hair reduces both the minimum and maximum bow forces by a small amount. It is consistent with the expected reduction in the effective characteristic impedance of the string. The compliance of the bow hair is arranged in parallel to the impedance of the string, the same way that the torsional motion of the string is organized. Adding the bow-stick strengthens the effect of the compliant bow hair by a small amount, but it does not make a fundamentally different effect. Adding the second polarization of the string significantly reduces the minimum bow force accompanied by a minimal increase of the maximum bow force. A more detailed discussion on the effect of the second polarization is conveyed in Sec. 5.1.4. In accordance with our findings in Chap. 4, removing the torsional motion of the string moves the Helmholtz region upward, and removing the bending stiffness expands it from both top and bottom sides. Surprisingly, the maximum bow force is affected more strongly by the torsional motion than the minimum bow force is.

Looking at Fig. 5.4c, two trends can be observed: any factor that broadens the spread of the Helmholtz corner results in a further extension of the slipping phase, and any factor that decreases the effective impedance at the bowing point (particularly at higher frequencies) allows the sticking phase to persist for a longer period of time, perhaps because it acts as a cushion against any disturbances arriving at the bow ahead of the main Helmholtz corner. Factors that influence the spread of the Helmholtz corner (the "corner rounding", as it was

[2] If we hadn't done so, a smaller minimum bow force for a case would have been automatically translated into a smaller average spectral centroid.

[3] A larger bow force is needed to feed mode energy into the system and to compensate for the added damping of the finger, thus making the Helmholtz motion sustainable.

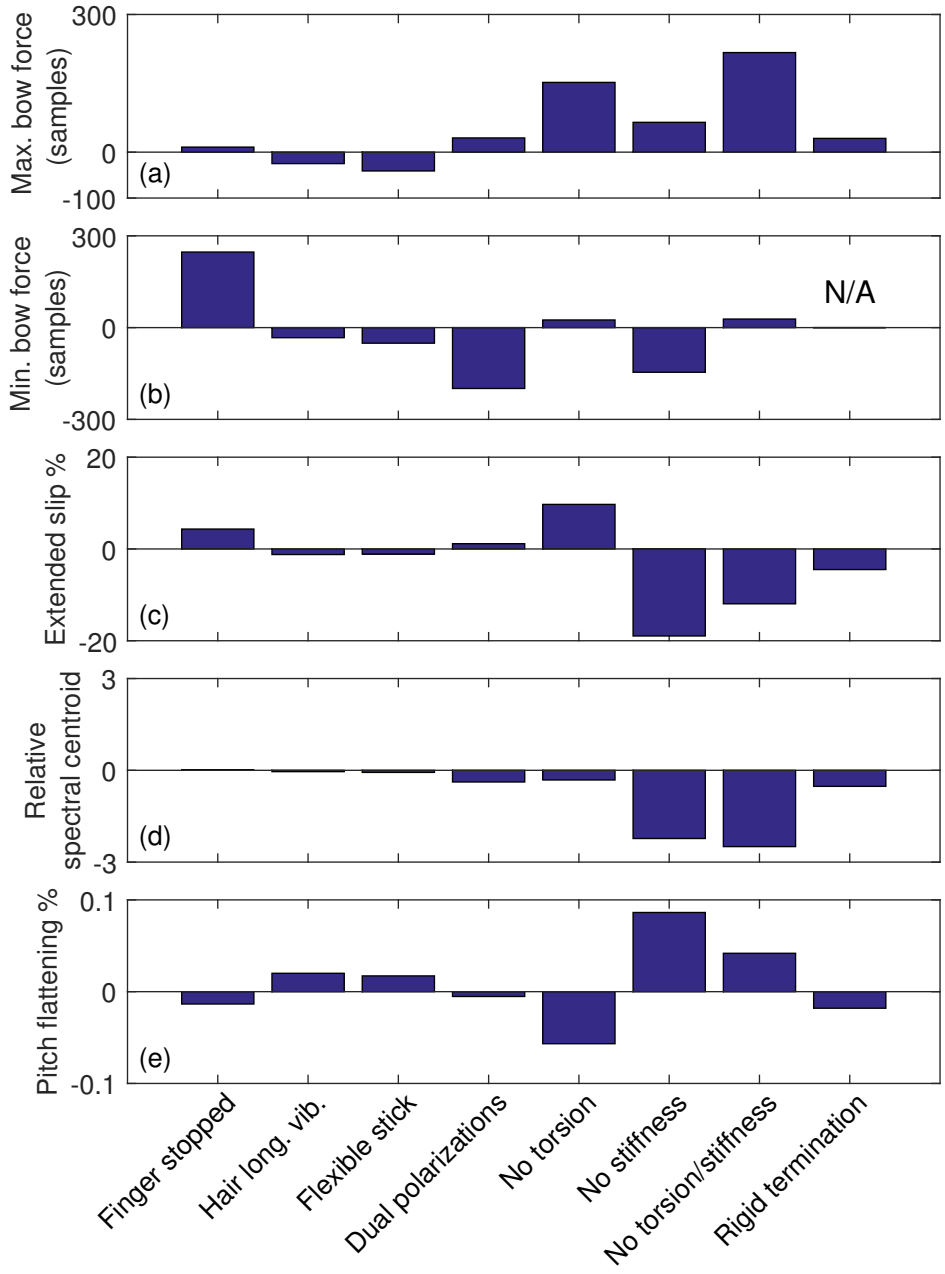

Fig. 5.4 The comparison of the maximum bow force (a), minimum bow force (b), increase in the slip-to-stick ratio as a percentage of its theoretical value (c), spectral centroid relative to the fundamental frequency (d), pitch flattening as a percentage of the fundamental frequency (e) relative to their value for the base case. Different cases shown on the horizontal axis are defined in the text.

called in earlier literature [95]) are as follows: damping by the finger leads to more rounding and a longer slipping phase, while removing the string's bending stiffness and turning the bridge to a rigid termination results in a sharper corner and shorter slipping phase. For the effective impedance, adding the longitudinal vibration of the bow hair, with or without a flexible bow-stick, shortens the slipping phase, and removing the torsional vibrations of the string further extends the slipping phase.

Among different options, the stiffness of the string has the biggest effect on the spectral centroid. It is not clear how the string's stiffness results in more high frequency content in the bridge force. Given the importance of the pitch flattening, from the player's and the listener's point of view, it has been more thoroughly discussed in Sec. 5.1.3. It is worth noting that the trend and amplitude of change in all calculated metrics for the "No torsion/stiffness" case can be approximated by adding the changes when the torsion and stiffness are individually excluded from the model, so we did not see any evidence for the interaction between the two other than the ripple structure mentioned earlier in Sec. 5.1.1.

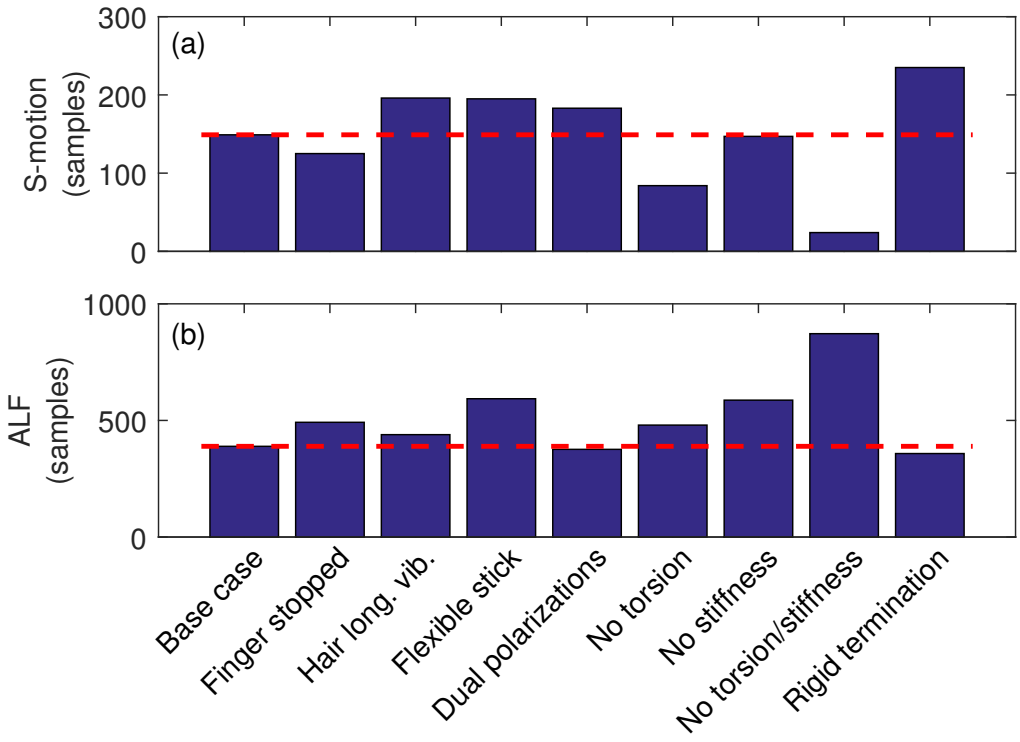

Fig. 5.5 Comparing the total number of S-motion (a) and ALF note (b) samples for different cases defined in the text.

Figure 5.5 investigates the effect of different physical details on the occurrence of the S-motion and the ALF notes. The base case is also added to the plot. The vertical axis shows the total number of occurrence for the corresponding regime, and the dashed red line marks

the total number for the base case. The most striking observation in Fig. 5.5a is that the exclusion of the torsional motion significantly reduces the number of S-motion occurrences. The effect is even stronger if both torsional motion and the bending stiffness are excluded. It should be noted that in our simulations the string starts from a perfect Helmholtz motion. A transition to the S-motion would require a high-frequency excitation at the bowing point which apparently is provided, in large part, by the torsional motion of the sting and the precursor waves. Turning the bridge to a rigid termination also significantly increases the number of S-motion samples.

Looking at the number of ALF notes in Fig. 5.5b, the biggest deviation from the base case is for the "No torsion/stiffness" case with almost double the number of ALF notes. The longitudinal compliance of the bow hair, especially if coupled with the flexible bow-stick, acts as a cushion against untimely disturbances, thus making the ALF notes more stable. This is consistent with what Mari Kimura, a violinist and composer best known for her use of ALF notes, suggests on how to play the ALF notes: *"The first secret is maintaining loose bow-hair [...]. You don't want a lot of tension [...]. You need enough elasticity on the bow-hair that you can really grab the string" [134].*

A further investigation into the stick-slip frequency of the "No torsion/stiffness" case reveals a structure in the frequency of the ALF notes. Figure 5.6b shows the amount of pitch flattening for all Helmholtz occurrences as well as the ALF notes. Given the broad range used for the plot (up to 400% flattening), all the Helmholtz occurrences are more or less painted with the same color. For the ALF notes, however, at least four distinct straps can be detected with almost the same frequency within each strap, and spaced by samples of raucous motion from the neighbor straps (a similar observation was made on experimental results of [133]). Figure 5.6a shows the same plot for the base case. The same "modes[4]" of ALF note can be still identified, but they are more sparse and less structured compared to the "No torsion/stiffness" case. This suggests that bending stiffness and torsional motion make it harder and less reliable to play ALF notes on a string.

5.1.3 Pitch flattening

The factors affecting the stick-slip frequency of the string can be classified into two general categories: (a) asymmetric pattern of stick and slip arising from the hysteresis loop in the F_F-v plane (causing pitch flattening), and (b) slight deviation of the string mode frequencies from being perfectly harmonic. There are also static and dynamic alterations of the tension which were earlier discussed in Secs. 3.3.3 and 2.2.3. Both of these latter effects uniformly

[4] "Mode" here refers to the number of times that the Helmholtz corner is reflected at the bow before it can trigger a slip.

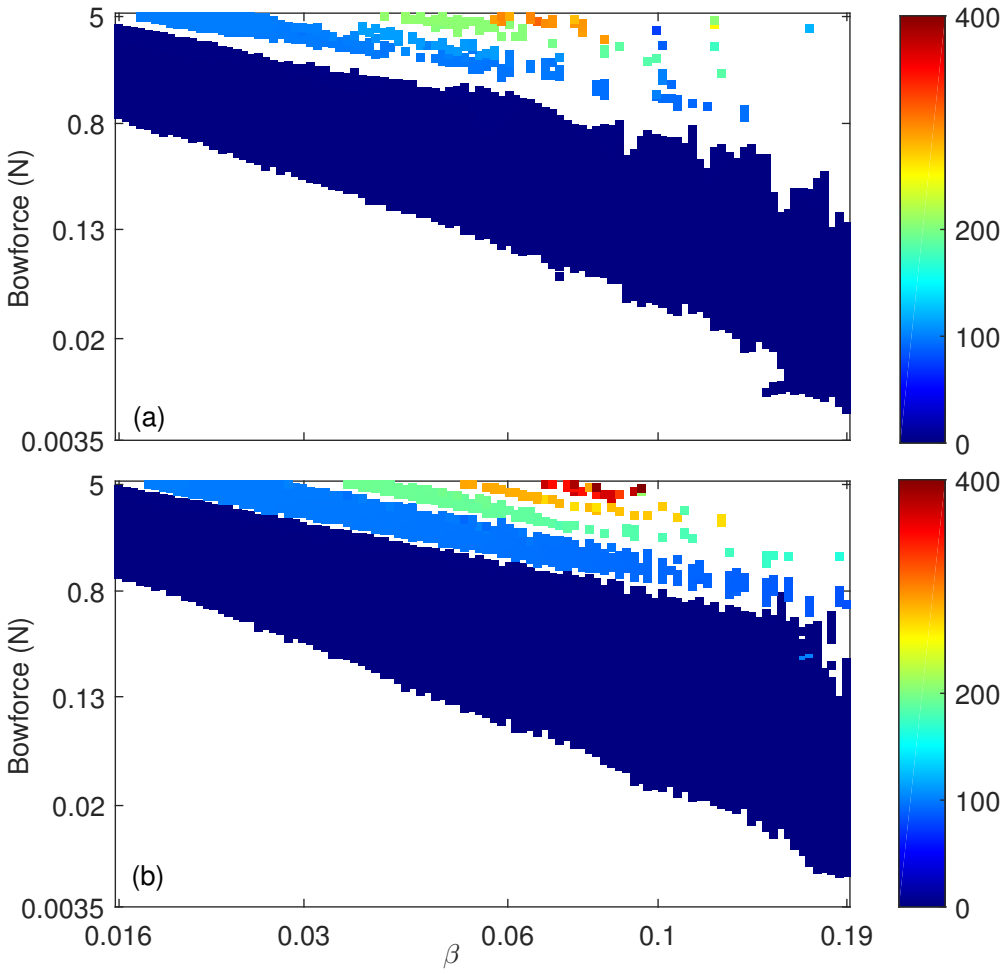

Fig. 5.6 The pitch flattening as a percentage of the fundamental frequency plotted in the β-bow force plane for the base case (a) and the "No torsion/stiffness" case (b). The range for the pitch flattening is widened to 400% to show different modes of the ALF notes.

scale the frequencies of the string modes up and down, and with that the stick-slip frequency of the bowed string. The pitch deviation from the alterations of the tension is not further discussed in here.

The physical explanation for pitch flattening was first provided by McIntyre and Woodhouse [34]. Given the fact that a realistic traveling corner is not perfectly sharp, it takes a finite amount of time (with the same time-scale as the width of the finger-side reflection function) for the string to make the complete transition from one state to another. If the bow force is large enough to create the Friedlander's ambiguity range (discussed in Sec. 3.1.2), there will be a difference between the values of v_h at which slipping and sticking are triggered. In that situation, the velocity should make a bigger jump in transition to slipping, which means a bigger delay compared to when sticking recommences. The net effect would be a lower pitch compared to the case for an ideal Helmholtz motion. This argument is based on the velocity-dependent friction model and a single contact point; nonetheless, it has been argued by Boutillon [131] that any hysteresis loop in F_F-v plane traversed in an anticlockwise direction leads to flattening. It has been shown by Woodhouse [32] that this is the case for the thermal friction model[5] as well.

The second class of effects altering the stick-slip frequency have to do with the slightly inharmonic modes of a realistic string. The main contributors to such inharmonicity are a) the bending stiffness of the string which skews the frequency of higher string modes toward higher frequencies, and (b) the perturbation of the string modes because of their coupling to the body modes. Both of these effects are thoroughly discussed in Chap. 2. Once the string is bowed, and assuming it settles to the Helmholtz regime at all, the stick-slip enforces the higher modes to vibrate in integer multiples of the stick-slip frequency. That frequency itself is set in such a way that the total reactive power produced by the modes that are driven above their natural frequencies are balanced with the reactive power produced by the ones which are driven below their natural frequencies [131]. This argument is only valid if the bow does not contribute any reactive power, which would be the case if the bow force is smaller than the limit needed to create the ambiguous range on the friction curve. If not the case, the contribution from the hysteresis loop should be also considered in the calculation for the balance of the reactive powers [131], which indeed provides a quantitative measure for the pitch flattening mentioned in the previous paragraph .

Looking back at Fig. 5.4e, we can see that the inclusion of the longitudinal bow hair vibrations has resulted in more flattening while removing the torsional motion of the string has resulted in less flattening. This is consistent with our earlier assumption that both of

[5] A minor difference is that the thermal model does not predict any threshold for the normal bow force to create flattening effect.

the compliance of the bow hair in the bowing direction and the torsional motion of the string reduce the effective impedance at the bowing point which creates a larger hysteresis loop thus more flattening. Exclusion of the flexible body from the model has also reduced the amount of flattening, likely because the flexibility of the body adds to the corner rounding. Unexpectedly, adding to the intrinsic damping of the string results in less flattening.

Excluding the bending stiffness of the string results in more flattening. This well matches our predictions because all higher modes of a stiff string have higher frequencies compared to the same modes for a perfectly flexible string (assuming the frequency of the first mode is the same for both cases), therefore the compromise between the modes of a stiff string pushes the stick-slip frequency higher. A close comparison of the base case with the case with no bending stiffness reveals an interesting pattern shown in Fig. 5.7. This figure shows the percentage of pitch flattening for the "No stiffness" case relative to the same metric for the base case. For the reason mentioned above, the majority of data points has positive values which can be confirmed from a positive value for the "No stiffness" case in Fig. 5.4e. Interestingly however, close to the maximum bow force, where the pitch flattening gains significance, most of the data points have negative values. The dark blue samples can be attributed to the ripple structure earlier shown in Fig. 5.2c, and lack thereof for the "No stiffness" case, but even the data points between those dark blue samples have mostly negative values. This suggests that pitch flattening caused by the spatial spread of the corner on a stiff string outweighs the pitch sharpening caused by the string's inharmonicity. This also suggests that pitch flattening becomes a more sensitive function of the normal bow force when the bending stiffness of the string increases. Musically, this makes the undesirable effect of the flattening more severe as it is very likely that a player uses a range of bow forces when playing a single note in a repertoire (think of a "martelé", for example). A more uniform distribution of pitch flattening across the β-bow force plane could be more easily, and perhaps automatically, compensated by the player by placing his/her finger slightly above or below the "theoretical" position.

Lastly, we look at how pitch flattening is affected by the interactions of the string with a strong body mode. To make the analysis easier to interpret, and similar to what we've done in Chap. 4, a single body mode with an effective mass of 300 g is considered, and the unperturbed frequency of the string is increased in small steps from slightly below, to slightly above the body mode frequency. All string and body parameters are the same as ones used to calculate Fig. 4.22. The frequency of the first string mode is expected to decrease if it falls below the body mode frequency (i.e. 172 Hz), and it is expected to increase if it falls above the body mode frequency (see the analytical discussion in Sec. 2.2.3). The frequency of the other string modes remain unchanged and very close to integer multiples of

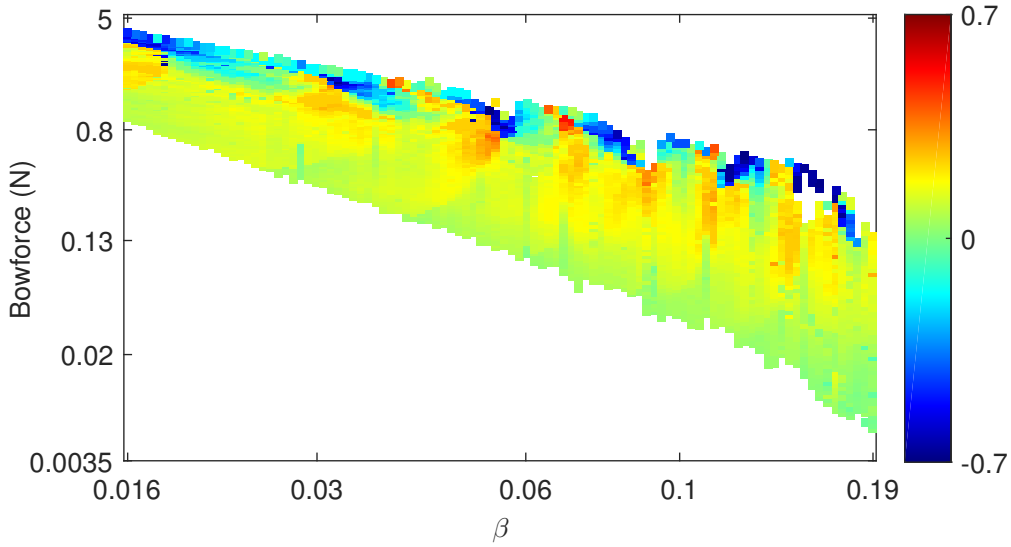

Fig. 5.7 The percentage of pitch flattening for the "No stiffness" case relative to the same metric for the base case.

the unperturbed frequency of the first string mode (recall that the bending stiffness of the string is not included in the model). Figure 5.8 shows the pitch flattening for 12 values of relative body-string frequencies, shown on top of each subplot. The color scheme only varies up to a flatting of 0.4% and any value above that is shown with the same dark-red color.

Within each subplot, the distribution of the flattening is very similar to what we have seen earlier in Fig. 5.3b. Looking across different subplots there is an anti-symmetric pattern on the two sides of the body mode. The appearance of the negative values for the bottom four subplots is particularly interesting because if it wasn't for the body mode, all the simulated samples were expected to show a positive pitch flattening rather than a pitch sharpening. It is encouraging, then to see that the stick-slip frequency of a bowed string follows the move of a single string mode frequency when the frequencies of all other string modes are kept almost unchanged. That said, the range of variations caused by the body mode alone is limited to 0.2% which merely reaches the threshold for human pitch discrimination (roughly at 0.2% [120]). Given the fact that the modeled body mode has parameters comparable to the strongest body mode of an actual cello, it seems safe to conclude that the pitch flattening caused by the body modes would hardly be noticeable by a player. More importantly, the effect is consistent across all the points of the same played frequency, therefore the player may easily compensate for that by adjusting the position of his/her finger.

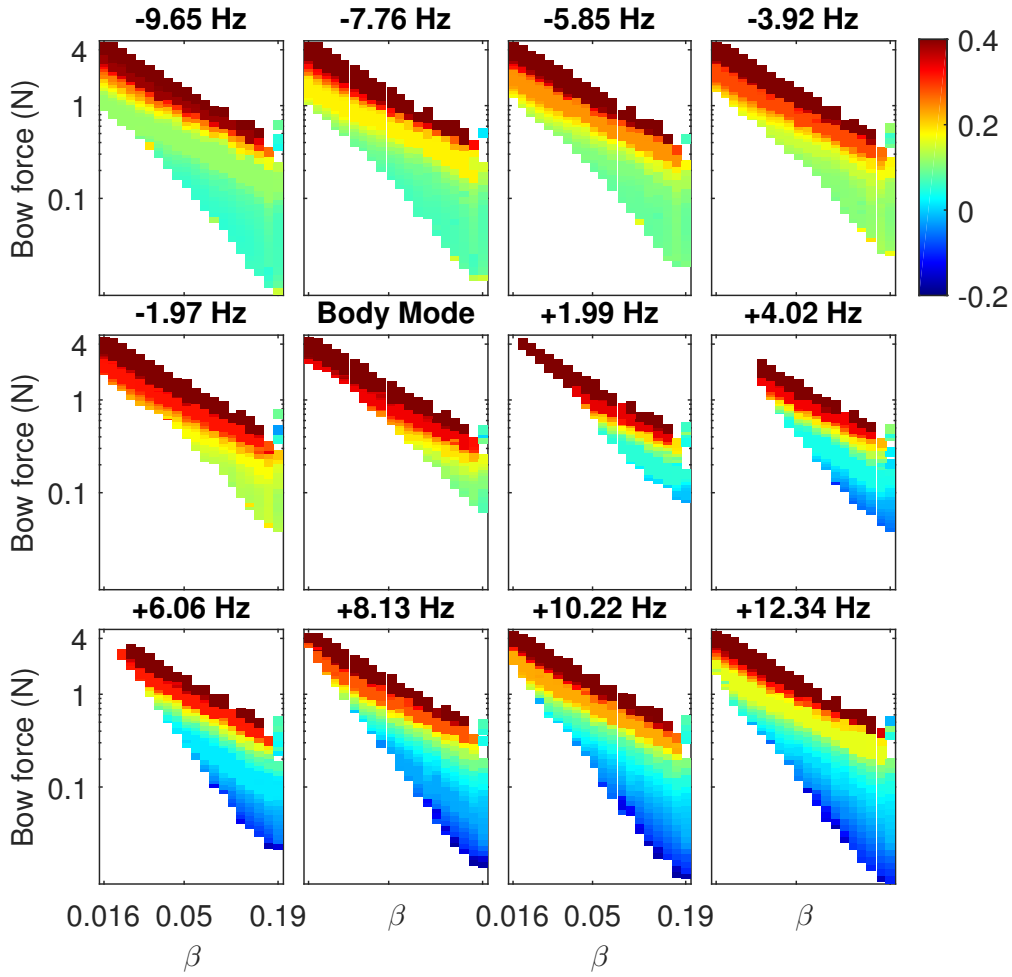

Fig. 5.8 The amount of pitch flattening as a percentage of deviation from the frequency of the first string mode. The static tension alteration in response to the normal and lateral bow force (see Sec. 3.3.3) is also taken into account. The simulations are made for a damped and perfectly flexible D_3 cello string terminated at a single-resonance body at 172 Hz and with an effective mass of 300 g. The torsional vibrations of the string were excluded from the simulations. The number on top of each subplot shows the relative frequency of the played note with respect to the body resonance.

5.1.4 Fluctuations of the bow force and the bow speed

We speculated earlier that the main effect of the longitudinal and the transverse flexibility of the bow hair is to add a fluctuating component to the nominal bow speed and bow force respectively. In this section, we will take a closer look at the amplitude of those fluctuations, their frequency content, and their distribution across the β-F_N plane. Figures 5.9a and 5.9b show the amplitude of fluctuations as a percentage of the nominal values for the bow force and bow speed. The figure is calculated base on the data from the "Dual-polarizations" and "Hair long. vib." cases of an open D_3 string whose results were presented in Sec. 5.1.2. Amplitude of fluctuation is defined here as half the peak-to-peak value within the last period of the simulated data.

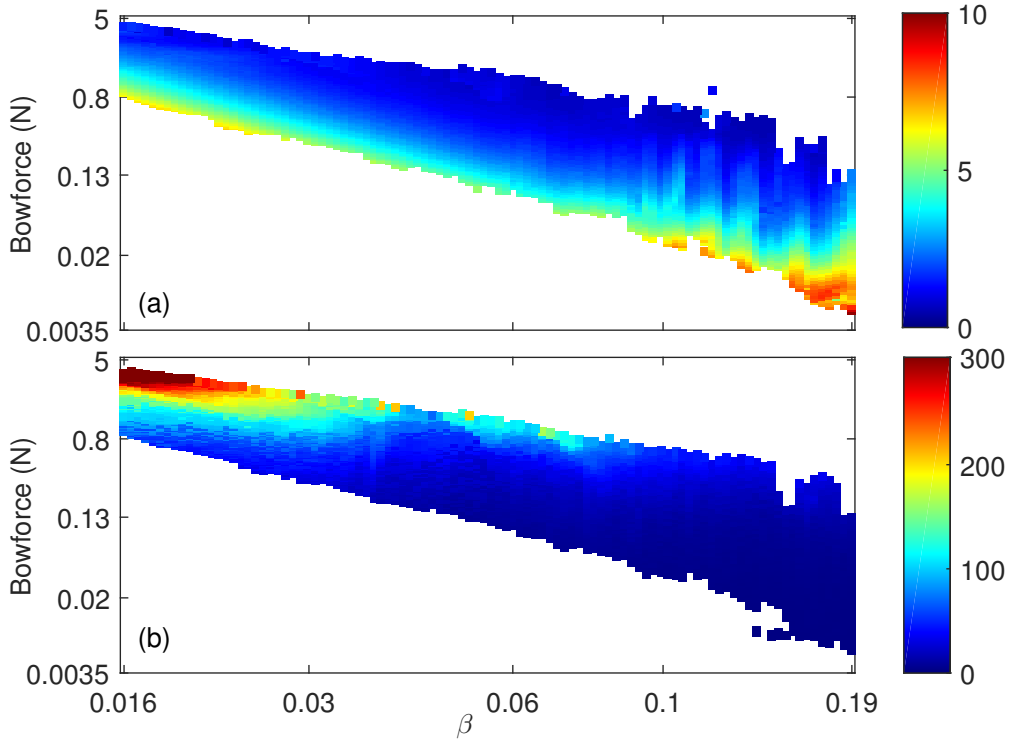

Fig. 5.9 The amplitude of fluctuations as a percentage of the nominal values for (a) the bow force and (b) the bow speed, based on the data from the "Dual-polarizations" and "Hair long. vib." cases of an open D_3 string.

To interpret these results it is useful to look at the chain of events leading to perpendicular-to-bow vibration of the string, with associated bow force fluctuations. The force that a bowed string applies to the bridge is approximately a sawtooth wave, which excites the body modes. The vibration of the string in the Y' direction is primarily driven by the motion of the bridge notch in that direction. Suppose the m^{th} harmonic falls close to the frequency of a strong body mode, with a spatial angle with respect to the bowing direction θ'_{Mk}. Note that the

strength of the harmonic components in the bridge force is roughly inversely proportional to the harmonic number, which gives the higher harmonics a relative disadvantage.

The frequency of the m^{th} harmonic in the bridge force will be close to the frequency of the m^{th} string mode in the perpendicular-to-bow direction, so the string vibration in the second polarisation is likely to occur predominantly in that mode. Keeping the vibration pattern of the m^{th} string mode in mind, and given that m is likely to be small enough that $\beta < 1/2m$, the farther the bow is placed from the bridge, the larger the amplitude of the perpendicular-to-bow velocity of the string at the bowing point, and hence the amplitude of the bow force fluctuation, is likely to become. On the other hand, the initial excitation force at the bridge is inversely proportional to β, and so keeping all other parameters the same, playing farther from the bridge would tend to result in a smaller bow force fluctuation. These two effects tend to cancel each other out, so that the contours in Fig. 5.9a are roughly horizontal, but the second effect wins out so that increasing β while keeping the bow force the same reduces slightly the percentage of bow force fluctuation. The exact physical properties of the hair ribbon and the contact position on the bow also affect the magnitude of bow force fluctuations, but in general these effects are of minor importance in comparison.

Figure 5.9a also shows that the relative amplitude of bow force fluctuations increases with reducing bow force. This is not unexpected: the absolute amplitude of the bridge force is independent of the bow force to the first order of approximation, and so is the amplitude of bow force fluctuation. Percentage-wise, this results in an increase in the bow force fluctuation with decreasing nominal bow force. The maximum fluctuation amplitude obtained for the simulated string is around 10% of its nominal value. Figure 5.10a shows the effective bow force in the time domain for a sample from Fig. 5.9a with $\beta = 0.016$ and $F_N = 3.5$ N. It can be seen that the bow force fluctuation mostly corresponds to the 3rd harmonic of the bowed string (around 440 Hz). The coupling apparently happens through a relatively strong body mode at 433 Hz, with a spatial angle of $\theta'_{Mk} = 19.27°$, a Q factor of 53, and an effective mass of 180 g.

The analysis of the fluctuating bow speed is relatively more straightforward. The bow hair is excited in its longitudinal direction by the fluctuating friction force acting between the string and the bow. The response of the bow hair is a superposition of its forced and transient responses to the perturbation force at the bow, thoroughly discussed in Sec. 4.3.1. Figure 5.10b shows the effective bow speed in the time domain for a sample in Fig. 5.9b with $\beta = 0.016$ and $F_N = 3.5$ N. The fluctuations just after the stick-to-slip transition are confirmed to be mostly the transient response of the bow hair to the sudden drop in the friction force, as they have a dominant frequency of around 1950 Hz. Based on the chosen β for this particular simulation, the Schelleng ripples appear at a frequency of 9176 Hz.

The fluctuations close, but before, the stick-to-slip transition are mostly the precursor waves preceding the main Helmholtz corner arriving from the finger side, a consequence of the string's bending stiffness.

Looking at Fig. 5.9b, the amplitude of fluctuations generally increases with increasing bow force. It is striking how large the fluctuations are compared to the nominal bow speed. Their amplitude is at least 3 times the nominal bow speed for any bow force larger than 4 N, and the effective bow speed experiences negative values within every cycle for virtually all samples with $\beta < 0.03$. It is surprising how small of an impact they made on the Schelleng diagram of the "Hair long. vib." case, as compared to that of the base case. The fluctuations of the effective bow speed scale with the characteristic impedance of the string, so one would expect even larger fluctuations when a C_2 string is bowed, for example.

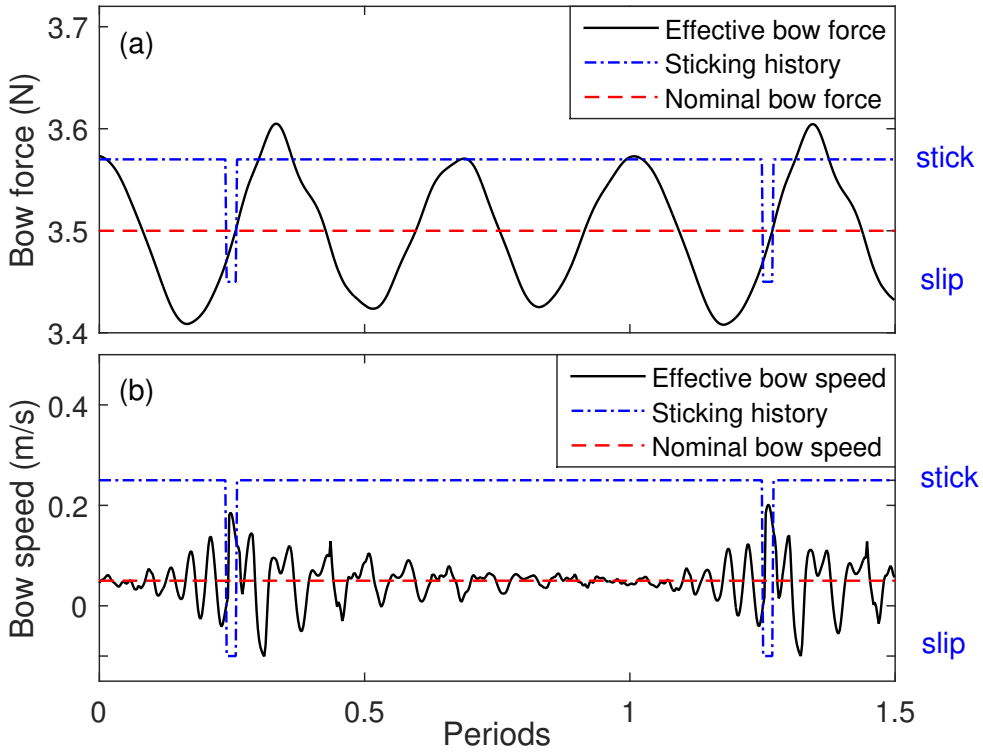

Fig. 5.10 A sample of the fluctuating effective bow force for the "Dual-polarizations" case (a) and the fluctuating effective bow speed for the "Hair long. vib." case (b). The stick-slip history of the string is overlaid for relative phase comparison. For both cases $\beta = 0.016$, $F_N = 3.5$ N, and $v_b = 5$ cm/s. The red dashed lines show the nominal values of the bow force and bow speed.

A closer look into the bow force fluctuations

In light of the results presented earlier in the section, it is encouraging to obtain a more general understanding of the fluctuating bow force and its potential effect on the minimum bow force. Recall that the results presented in Fig. 5.4 showed that for the particular case of an open D_3 string, adding the second polarization resulted in a significantly smaller minimum bow force. Qualitatively, the effect of the second polarisation on the minimum bow force would be expected to depend on the timing of the bow force oscillations relative to the moment within the cycle when the perturbation force at the bowing point reaches its maximum value: this is the critical moment for determining the minimum bow force.

Time-domain simulations of four cases are compared to investigate how this effect varies with the properties of the body modes and over different frequencies. The chosen base case is one that was also considered to obtain the results presented in Fig. 5.8: the single-polarization vibrations of a damped but perfectly flexible D_3 cello string terminated at a single-resonance body at 172 Hz and with an effective mass of 300 g. For simplicity, the torsional motion of the string is also excluded. All other cases include the second polarization of string motion. The body mode is inclined with respect to the bowing direction by $\theta'_M = +20°$ in one case, and by $\theta'_M = -20°$ in the other, both with the same adjustment to maintain the effective mass in the bowing direction at 300 g (see Fig. 2.4 for the definition of a positive angle). To monitor the effects caused by variations in bowing-point admittance (discussed in Sec. 4.2.2), a fourth case is considered that is the same as the case with $\theta'_M = +20°$ except the fluctuations of the bow force are not considered in the calculation of friction.

Given that for all dual-polarization cases the coupling happens via a single mode whose frequency is also close to the played note, the second polarization of the string mainly responds to the fundamental frequency of the string. Figure 5.11 shows the relative timing for the oscillations of the bow force with respect to the string vibrations in the bowing direction for the $\theta'_M = +20°$ case. This relative timing indicates where the fluctuating bow force reaches its maximum with respect to the time that the stick-to-slip transition happens within each cycle. The number is normalized to the period of the string and is shown in absolute terms, therefore it ranges from 0 to 0.5. The frequencies shown on top of different subplots are the relative frequencies of their fundamental to the frequency of the body mode at 172 Hz, indicated by the word “Body Mode”.

It can be seen that the bow force reaches its maximum at a time close to the stick-to-slip transition for the frequencies below the body mode, and it reaches its maximum value at

around the middle of the sticking phase for the frequencies above it.[6] The same pattern is expected for the perturbation force at the bowing point: the body acts like a spring (in-phase vibration) at frequencies below its mode frequency and like a mass (out-of-phase vibration) at frequencies above it. Based on the argument given above, a body mode with $\theta'_M > 0$ should reduce the minimum bow force at all frequencies (because it produces a larger value for the effective bow force when the perturbation force reaches its maximum). The corresponding computations for the $\theta'_M = -20°$ case resulted in an exact reversal of the relative timing, so the prediction would be an increase in minimum bow force at all frequencies.

Figure 5.12 shows how well those predictions work. The relative number of double-slip/decaying occurrences for each played note of the three double-polarization cases are compared to that for the base case in Fig. 5.12: a larger number of such samples indicates a relatively larger minimum bow force. As expected, the $\theta'_M = +20°$ case has a significantly smaller number of double-slip/decaying samples than the base case; the opposite holds for the $\theta'_M = -20°$ case. The minimum bow force for the case with $\theta'_M = +20°$ but a constant bow force remains very close to that of the single polarization case except at the relative frequency +1.99 Hz: this gives assurance that the two other cases mostly capture the influence of bow force fluctuations.

It should be noted that the effect of θ'_M will be negated by reversing the bowing direction (i.e. from up-bow to down-bow). For a real instrument at lower frequencies, the center of rotation for the bridge is usually close to the bridge foot on the treble side. As a result, for ergonomically possible bow inclinations the body modes generally have slightly positive angles for the lowest string (e.g. C_2 for the cello) and negative angles for all other strings.

5.1.5 Effect of the nominal bow speed

So far in our simulations we have considered the nominal bow speed to be a constant 5 cm/s that falls on the low end of bow speeds used in real playing (one full stroke with a cello bow would last 12 s). Based on Schelleng's argument (Eqs. (4.4) and (4.5)), both the minimum and the maximum bow forces should scale up and down proportional to the bow speed. A small deviation from proportionality may be expected because of the variations in the dynamic friction coefficient, but numerically the variations are very small, and only become noticeable in large β values. Contrary to that prediction, Schoonderwaldt et al. [22] found in their experiments on D_4 and E_5 violin strings that while the maximum bow force scales

[6] There is a large deviation from this behavior for large bow force values at all frequencies, and the same spot showed the largest amount of bow force fluctuation within each subplot. The initial guess in that regard is that a larger bow force increases the tension of the bow hair ribbon and increases its mode frequency to match an integer subharmonic of the bowed note. Curiously, the same qualitative effect was observed when the static tension alteration of the bowhair was not accounted for in the model.

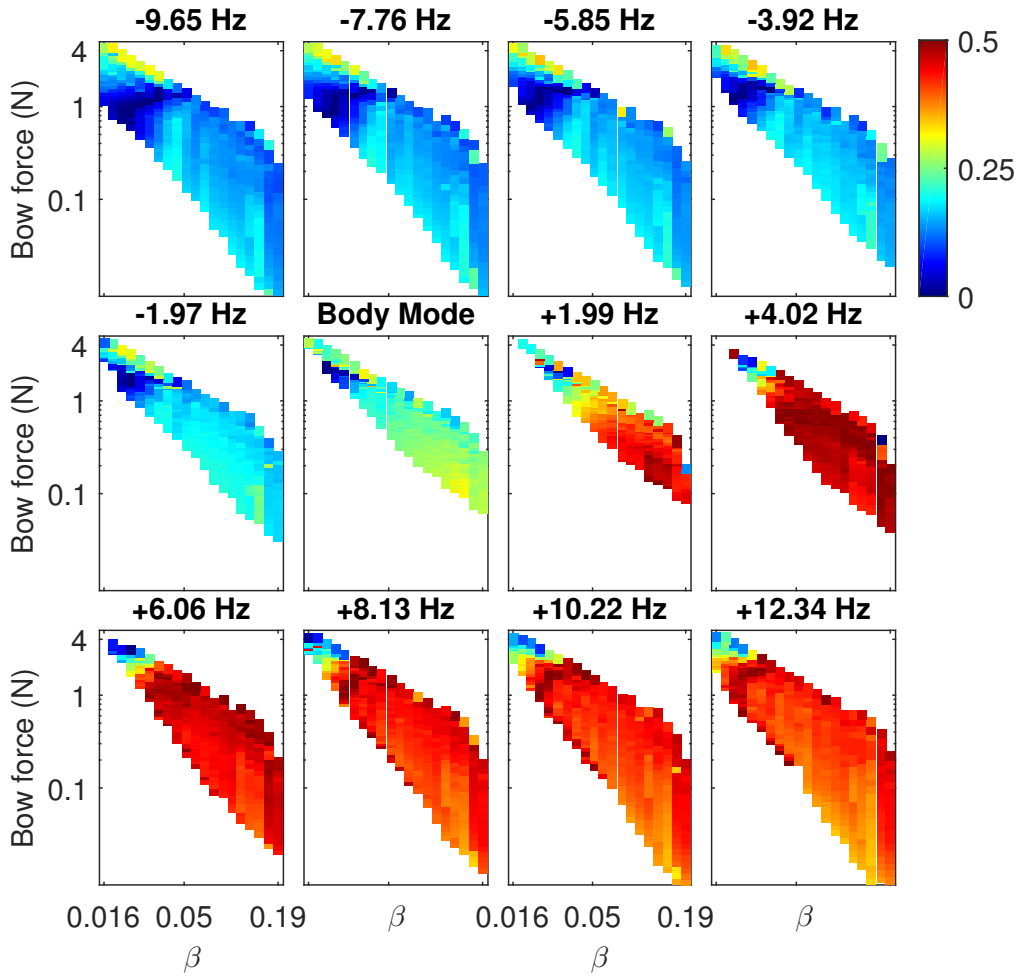

Fig. 5.11 The phase of the effective bow force fluctuations normalized to the period of the string and relative to the stick-to-slip transition. The simulations are made for a damped and perfectly flexible D_3 cello string terminated at a single-resonance body at 172 Hz with an effective mass of 264.9 g inclined by $+20°$ with respect to the bowing direction. The torsional vibrations of the string were excluded from the simulations. The number on top of each subplot shows the relative frequency of the played note with respect to the body resonance.

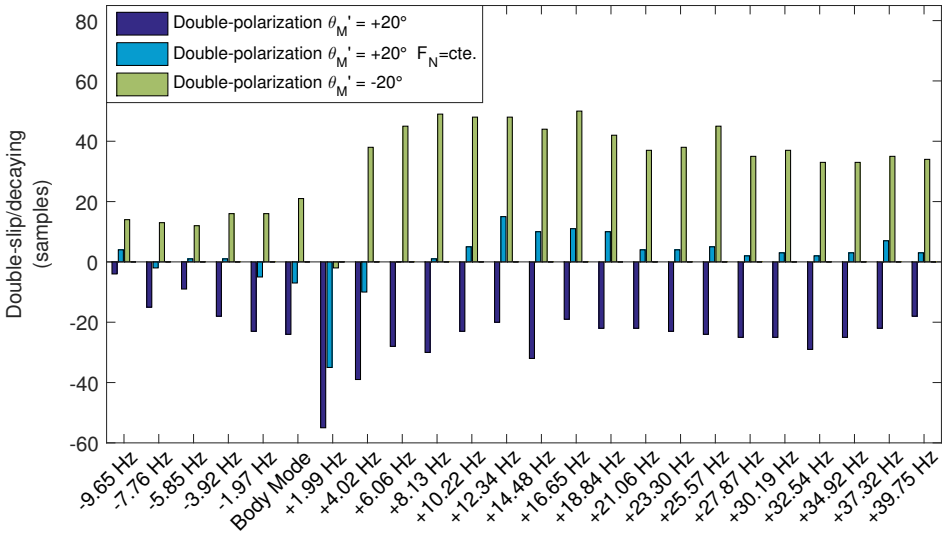

Fig. 5.12 The relative number of double-slip/decaying samples out of a total of 600 simulated samples for each string frequency. The numbers are for the three cases of double-polarization with respect to the single-polarization base case. The double-polarization cases include $\theta'_M = +20°$, $\theta'_M = -20°$, and $\theta'_M = +20°$ but without considering the fluctuations of bow force. The horizontal axis shows the frequency of the simulated note relative to the body mode frequency. See the text for the description details of the simulations.

with bow speed, the minimum bow force does not follow a particular trend. If anything, their results suggested that the minimum bow force remains almost unchanged when the bow speed takes different values of 5, 10, 15, and 20 cm/s.

This gave us the motivation to perform a corresponding set of simulations to see if this surprising independence of the minimum bow force from the bow speed is captured by our bowed-string model as well. Figure 5.13 shows the results of such simulations. In accordance with the original study, the bow speed varied from 5 cm/s to 20 cm/s and the Schelleng diagram was plotted. The base case model is used for all plots with their only difference being in their bow speed (i.e. Fig. 5.13a is the same as Fig. 5.1a). Approximate best fit representations of the minimum and maximum bow force limits in Fig. 5.13a were found to be $0.00028/\beta^2$ and $0.067/\beta$ respectively. Those limits are shown by red diagonal lines in Fig. 5.13a.; the red lines in other subplots show the same limits, scaled according the bow speed of the corresponding subplot.

The simulated data suggests a slightly less steep minimum bow force limit than -2 consistently across different bow speeds. This may be due to the fact that the simulated note falls below the body resonance which, according to our discussions in Chap. 4, would create such effect. Aside from that, the predicted bow force limits are accurately scaled with the

bow speed. This suggests that the surprising trend observed in experiments can not be predicted by our refined model of the bowed string, thus is likely due to the detailed frictional behavior of the rosin not included in our model. It should be noted that the experiments were performed with a real bow sitting on its full width over the strings, but it is highly unlikely that the flexibility of the bow or its finite-width can produce such a large effect.

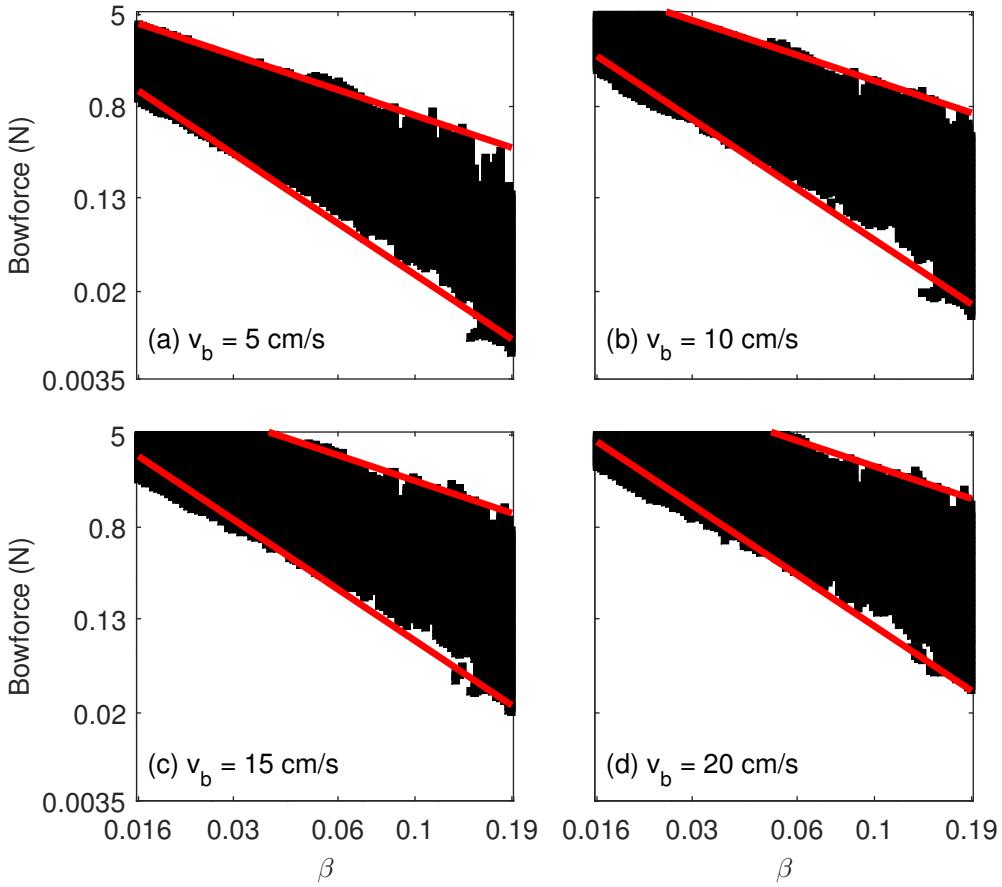

Fig. 5.13 Schelleng diagram as a function of the nominal bow speed, only Helmholtz samples are shown with black squares. (a) is for $v_b = 5$ cm/s, (b) is for $v_b = 10$ cm/s, (c) is for $v_b = 15$ cm/s, and (d) is for $v_b = 20$ cm/s. All other parameters of the model were the same as the base case. The red diagonal lines in (a) are best fits to the minimum and maximum bow force ($0.00028/\beta^2$ and $0.067/\beta$ respectively), which are scaled according to the bow speed and plotted in (b) to (d).

5.1.6 Comparison with experimental results

Galluzzo [21] experimentally measured the Schelleng diagram for an open D_3 cello string. He found the best fit to the maximum and minimum bow forces to be $0.13/\beta$ and $0.00086/\beta^2$ respectively. Here we will see how the results of our bowed string simulation model compares

with experiments. The experiments were made on a synthetic-core "Thomastic Dominant" string, whereas the parameters of our model are measured for a steel-core "D'Addario Kaplan Solutions". In this regard the parameters of the model are adjusted to better represent the experiments. The tension and bending rigidity of the string were set to 111 N and 3×10^{-4} N/m^2, and a larger η_F was chosen to represent the higher damping of the nylon core. We did not have any data on the body of the instrument on which the experiments were performed, therefore, we used the same model of the body used in our previous simulations. The model of friction was based on the reconstructed friction curve, earlier presented in Eq. (3.6). Recall that the "old" friction model (Eq. (3.5)) was used in all previous simulations of the thesis.

The simulation results are shown in Fig. 5.14 with the Helmholtz occurrences represented by black squares, ALF notes by green squares, and S-motion by cyan squares. The experimentally-found bow force limits are shown by red diagonal lines for comparison. It can be seen that both limits are underestimated by a factor of 2 on average. It could be argued that the mismatch at the minimum bow force (both the value and the slope) is caused, to some extent, by the fact that two different cello bodies were used in the simulations and the experiments, but the mismatch of the maximum bow force and particularly the fact that the simulations predicted many samples of ALF below the experimental maximum bow force limit shows how unrealistic the model of the friction is.

5.2 The transients of a bowed string and the Guettler diagram

While scientifically relevant, sustaining a bowed note is hardly a challenge for experienced players, instead they are more concerned with the transients of a bowed note and the formation of the Helmholtz motion in the first place. Schumacher and Woodhouse [30, 31] were the first to study the transients of a bowed string in a systematic manner. In their simulations, a string which was initially at rest was bowed when either the bow force or the bow speed were kept constant and the other started from an initial value and reached a different asymptotic value. Regardless of how the parameters change over the duration of the simulations, all of their simulations can be classified as "switch-on" transients, meaning both the bow force and the bow speed start from a non-zero value with the string initially at rest.

Being a professional player himself, Guettler [135] pointed out that in actual playing condition either (or both) of those parameters start from zero while the other one is kept approximately constant. A constant bow speed and an increasing bow force is normally limited to the "string crossing" and the "bouncing bow" techniques, while for the majority of the simpler gestures the force is kept almost constant and the bow accelerates roughly uniformly from zero. Focusing on the second case, Guettler argued that a relevant parameter space

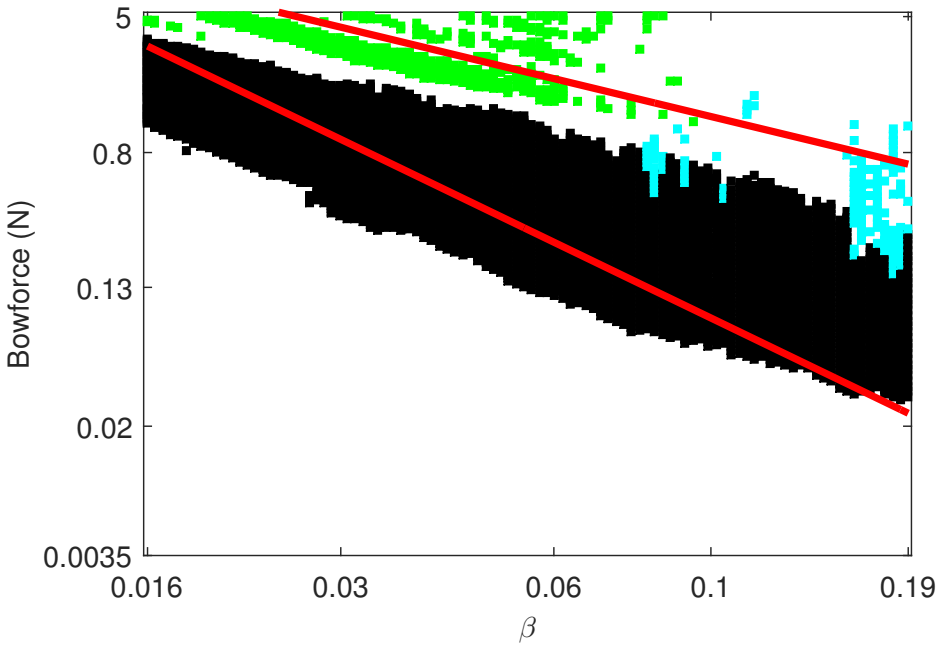

Fig. 5.14 Schelleng diagram according to simulations based on the reconstructed friction curve of Eq. (3.6). The minimum and maximum bow force limits obtained from experimental results in [21] are shown by red diagonal lines.

to study the transients of a bowed string is the F_N-a plane (a representing the bow acceleration). He also devised analytical relations to find the region within which the Helmholtz motion is achieved with no delay, which he called the region of a "perfect transient".

In order to understand the conditions that lead to a perfect transient, Guettler analyzed the chain of events that occurs for the case of a constantly accelerating bow. Before the first slip, the bow pulls the string sideways in a quasi-static manner, the friction force builds up until it reaches the limiting static friction and the first slip is triggered. The sudden change in the friction force following the first slip sends two waves toward the nut and the bridge called waves '1' and '2', respectively. For a perfect transient, wave 2 is the so-called Helmholtz corner and it is supposed to travel between the bridge and the nut, and trigger a stick or slip every time it passes underneath the bow. Wave 1, on the other hand, has the wrong sign and timing and so it should bounce back and forth between the bow and the nut. Similar to the argument we made about the subharmonics in Sec. 4.3.1, wave 1 traverses a shorter length of the string compared to wave 2 which traverses the full length of the string, therefore it can catch wave 2 from behind. In Guettler's idealized model it was assumed that $1/\beta$ is an integer, and as a result wave 1 will merge into wave 2 after $1/\beta$ periods. For a realistic string, however, such a coincidence of waves 1 and 2 is unlikely. Guettler summarized the conditions for a perfect transient:

1. The bow should press against the string sufficiently hard to avoid the untimely slip when wave 1 arrives at the bow from the finger side for the first time.

2. The bow should press against the string sufficiently lightly to allow for the timely slip when wave 2 arrives at the bow from the finger side.

3. Given that wave 1 has an opposite sign to wave 2, and recalling that wave 1 will catch wave 2 from behind after $1/\beta$ periods, wave 1 is in danger of sufficiently canceling out wave 2 at this point, so that the $1/\beta$ slip may not occur. This gives a second upper limit for the bow force.

4. Guettler's model showed that the perturbation force at the bowing point sometimes reaches a large value after around $1/(3\beta)$ periods. The bow should then press hard enough against the string to avoid this increased force from triggering an untimely slip. This gives a second lower limit for the bow force.

The region within the F_N-a plane for which the above conditions are met becomes a wedge pointing toward the origin. If the bow force is too high (or the acceleration is too low) the attack would sound "choked/creaky" and if the bow force is too low (or the acceleration is too high) the attack would sound "loose/slipping". If the same diagram is plotted for

a larger bow-bridge distance, the wedge becomes wider and it tilts clockwise. Guettler confirmed these theoretical deductions by the results of a time-domain simulation.

A perceptual study by Guettler and Askenfelt [136] showed that a note with some pre-Helmholtz transients is still considered musically acceptable if the duration of the transients is shorter than 50 ms on the high bow force side, and 90 ms on the low bow force side. What it means for the players is that a perfect transient may be a mandatory requirement for low-pitched notes (e.g. the C_2 string of a cello or any string on a double-bass), but it sets too harsh a requirement for high-pitched strings like the ones of a violin. Indeed the players may deliberately choose a gesture that creates some pre-Helmholtz transient if the musical context demands so [136]. Nonetheless, Guettler's diagram still gives a very useful measure to study the transients of a bowed string, and even if a perfect transient is not intended, the notes with an acceptable length of pre-Helmholtz transients are expected to gather around Guettler's perfect transient wedge.

Experiments with a precisely controlled bowing machine [21] showed that the placement of samples with shorter pre-Helmholtz duration agrees very well with Guettler's predictions. The results of that experiment, performed on an open D_3 cello string and for eight values of β, are reproduced in Fig. 5.15. In each plot, the time taken to achieve Helmholtz motion relative to the time of the first slip at a given combination of bow force and acceleration is given by the shade of the pixel at the corresponding location in the F_N-a plane. White pixels indicate perfect transients, black pixels indicate that it took twenty or more period lengths to achieve Helmholtz motion, and shaded grey pixels indicate intermediate cases. Pixels with crosses ("×") indicate unsuccessful measurements for which there were less than 20 string periods left in the recorded data after the first slip. The results reproduced in Fig. 5.15 are obtained using a rosin-coated perspex rod in place of a real bow, but the same experiments repeated with a real bow agreed very well with the former [21].

5.2.1 The effect of model variations on the Guettler diagram

Following the approach taken for the steady-state vibrations, a Guettler diagram is plotted for several variations of the parameters of the bowed-string model. In addition to the base case, other cases considered are "Finger-stopped", "No torsion", "No stiffness", and "Rigid terminations", the description of which was given in Sec. 5.1.2. The simulations for each case are made on a grid of 300 × 300 data points, linearly spaced in the F_N-a plane. The chosen range of bow force is from 0.4 N to 3.2 N, and the chosen range of bow acceleration is from 0.08 m/s^2 to 3.2 m/s^2. The simulations are only made for a $\beta = 0.0899$. The results of these simulations are plotted in Fig. 5.16. The time taken to achieve Helmholtz motion relative to the time of the first slip at a given combination of bow force and acceleration is

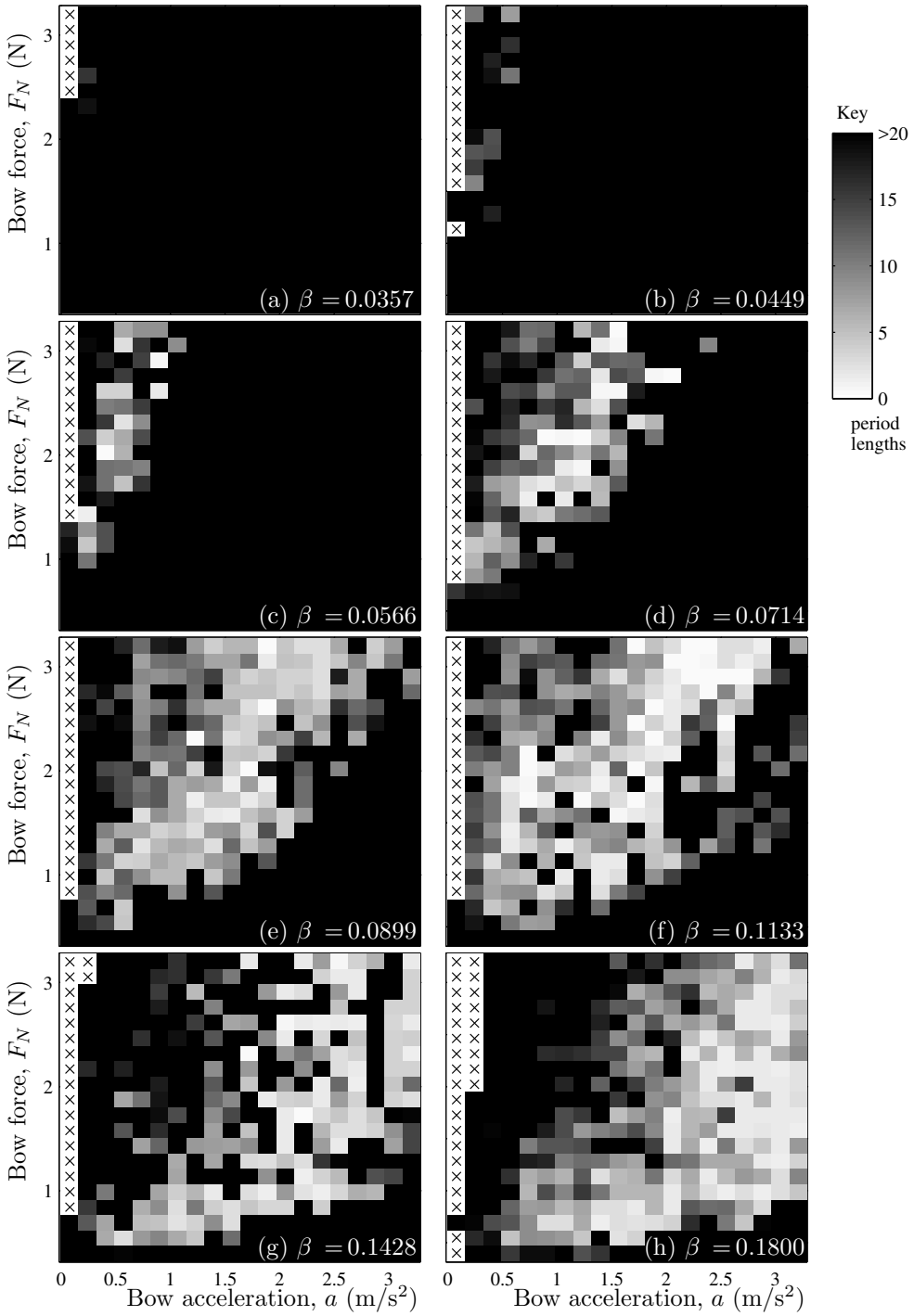

Fig. 5.15 Experimentally measured "Guettler diagrams", for eight different values of β. In each plot, the time taken to achieve Helmholtz motion relative to the time of the first slip at a given combination of bow force and acceleration is given by the shade of the pixel at the corresponding location in the N vs. a plane. White pixels with crosses ("×") indicate unsuccessful measurements, as described in the text. The vertical and horizontal scales of each plot are the same. (From [21])

given by the shade of each pixel. The data points for which the Helmholtz motion was not achieved, or more than 25 periods was taken to achieve the Helmholtz motion are shown by black pixels. Twenty five periods of pre-Helmholtz motion, corresponding to 170 ms on a D_3 string, is too long for a note to be considered musically acceptable: it is simply chosen so that the non-black pixels are not too rare to be studied. Fifteen periods would be a more realistic limit for musical acceptability. The blue pixels show the samples for which there were less than 25 string periods left in the simulated data after the first slip. Bearing in mind that the properties of the body and the string used in our simulations are different from that of the experiments reported by Galluzzo [21], all subplots in Fig. 5.16 are comparable to Fig. 5.15e. The starting points of the horizontal and vertical axes are numerically different in both figures, which should be considered when extrapolating the tip of the Guettler wedge to the origin of the plot. The total number of successful samples is smaller for all simulated cases compared to the experiments, which is consistent with the findings of Galluzzo [21] and could be associated with the inadequacy of the "old" friction model used in the simulations.

The existence of a radial structure in all subplots of Fig. 5.16 is immediately apparent. A strong similarity between waveforms falling on a $F_N/a = constant$ line was previously pointed out by Galluzzo when using the friction curve model of Eq. (3.5). The reason for such similarity was associated to the steep slope of that particular friction curve at low sliding speeds. The result would be that for a wide range of input parameters the effective μ_d becomes very close to 0.35 which leads to an approximately constant $(\mu_s - \mu_d)$. In that situation the waveforms look almost identical as long as the non-dimensional parameter $F_N/aZ_{0T}(L/c_0)$ is kept unchanged. This extreme similarity would vanish if other friction models are used; that said, there would still remain some similarities.

Figure 5.17 shows some further analysis on the results shown in Fig. 5.16. Guettler diagrams for the five cases are compared from different aspects, Fig. 5.17a shows the total number of samples which led to a Helmholtz regime in less than 25 string periods (out of a total of 90,000 samples in each subplot), Fig. 5.17b shows the average number of unsuccessful periods before a Helmholtz regime is established, Fig. 5.17c shows the mean angle of the lines that connect the successful samples to the origin in each subplot (this criteria is a measure for the orientation of the Guettler wedge), and Fig. 5.17d shows the tip angle of a Guettler wedge that can fit 90% of the successful samples in each subplot.

For four out of five cases, roughly $1/4^{th}$ of the samples are classified as successful. The exception is the case with no torsion which shows a surprisingly small number of Helmholtz samples. In fact the Helmholtz samples are so rare that the subsequent numbers for that particular case have become unreliable. The situation might be eased to some extent if a less "twitchy" friction model is used. In any case, our finding is in clear contrast to Serafin's

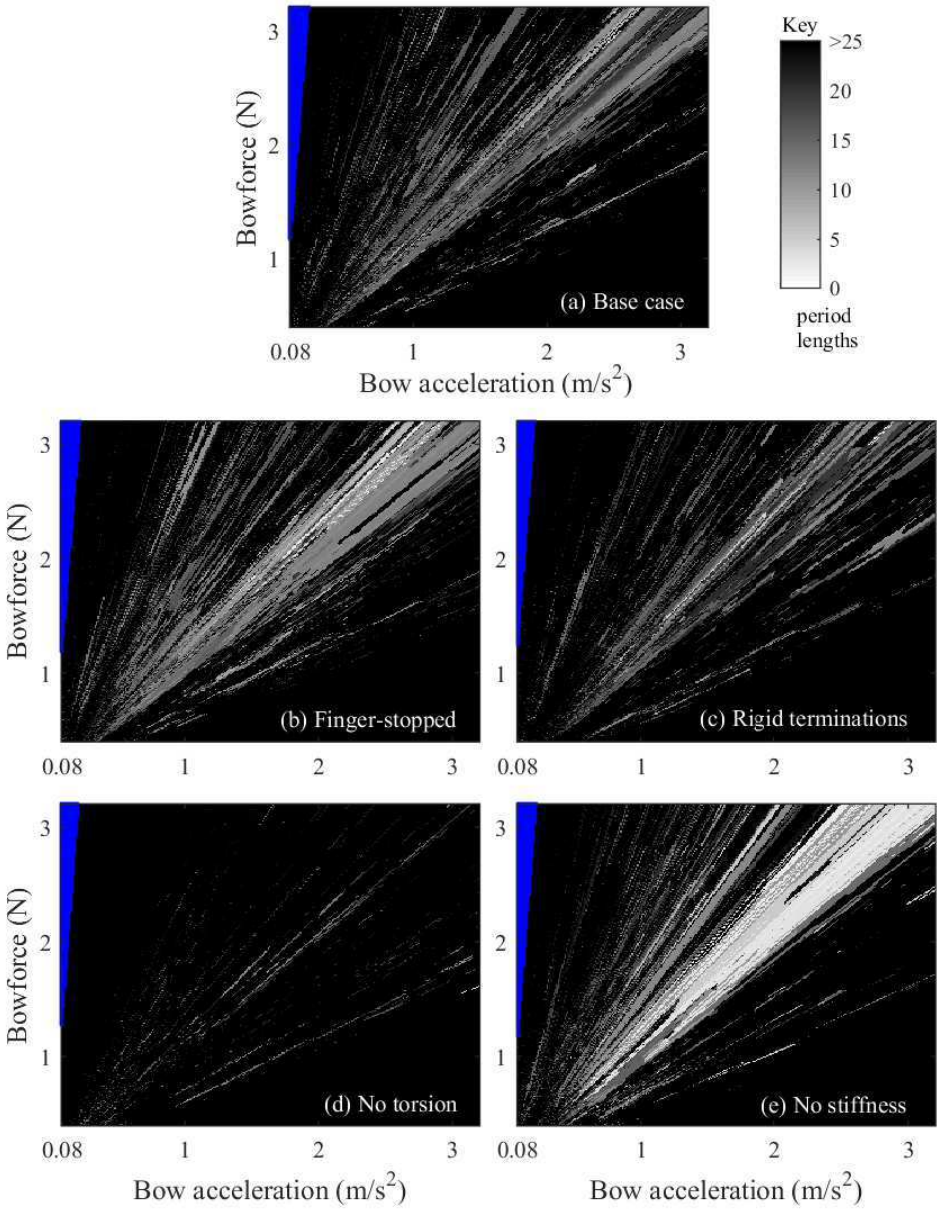

Fig. 5.16 Simulated "Guettler diagrams" for an open D_3 cello string with different variations of the model. In each plot, the time taken to achieve Helmholtz motion relative to the time of the first slip at a given combination of bow force and acceleration is given by the shade of the pixel at the corresponding location in the N vs. a plane. Pixels with blue color indicate unsuccessful simulations, as described in the text. The vertical and horizontal scales of each plot are the same.

suggestion based on her steady bowing results: *"The good news for synthesizer builders is that the added expense of torsional wave simulation (which basically adds a coupled "second string") does not appear to improve playability. Since torsional waves are not prominent in the radiated sound either, it seems warranted to leave them out of synthesis models, even in the highest quality instances"*[137].

Turning the bridge into a rigid termination point has reduced the number of Helmholtz samples and has made their formation slightly more delayed. It is not clear how the flexibility at the bridge can help the formation of Helmholtz motion as in Guettler's argument any factor that weakens wave '2' with respect to wave '1' should do the opposite.

The "Finger-stopped" case shows a larger number of Helmholtz occurrences which are also achieved within a shorter period of time. Such a significant difference between the two cases is a confirmation of our earlier speculation made in Sec. 2.2.1 that even though the intrinsic damping of a string may be very small compared to the damping induced by the coupling to the instrument's body, it may make a significant difference for the waves that are trapped between the finger and the bow. That is evidently the case for wave '1' of Guettler's argument. Our observation is also in accordance with the experience of the players that a finger-stopped string is generally more playable than an open string [36].

The most interesting case of all is the one with no bending stiffness. The number of successful samples are increased with respect to the base case, almost as much as they were increased for the "Finger-stopped" case. A much larger improvement is made to the pre-Helmholtz duration: the average number of unsuccessful periods is reduced from 17.49 for the base case to 14.13. More to this point, the successful samples are more densely clustered around the center-line of the Guettler wedge which would practically make the formation of the Helmholtz motion more reliable and more rigorous from the player's point of view. Putting this together with our earlier results on steady bowing, one can conclude that the string's bending stiffness is detrimental both to the formation and to the stability of the Helmholtz motion, and as such it is advisable to the string makers to produce strings with as little bending stiffness as possible.

5.2.2 Bowing point as the player's interface

When thinking about the playability of an instrument, one should also consider that the bowing point on the surface of the string is the interface of the instrument from the player's point of view.[7] In that capacity many features that may, or may not, directly affect the formation or stability of the Helmholtz motion may contribute to the player's ability to

[7]Strictly speaking, the interface is the grip on the bow but we have considered the bow as an extension of the player. Some points regarding the ergonomic features of a bow are discussed in Sec. 3.2.2.

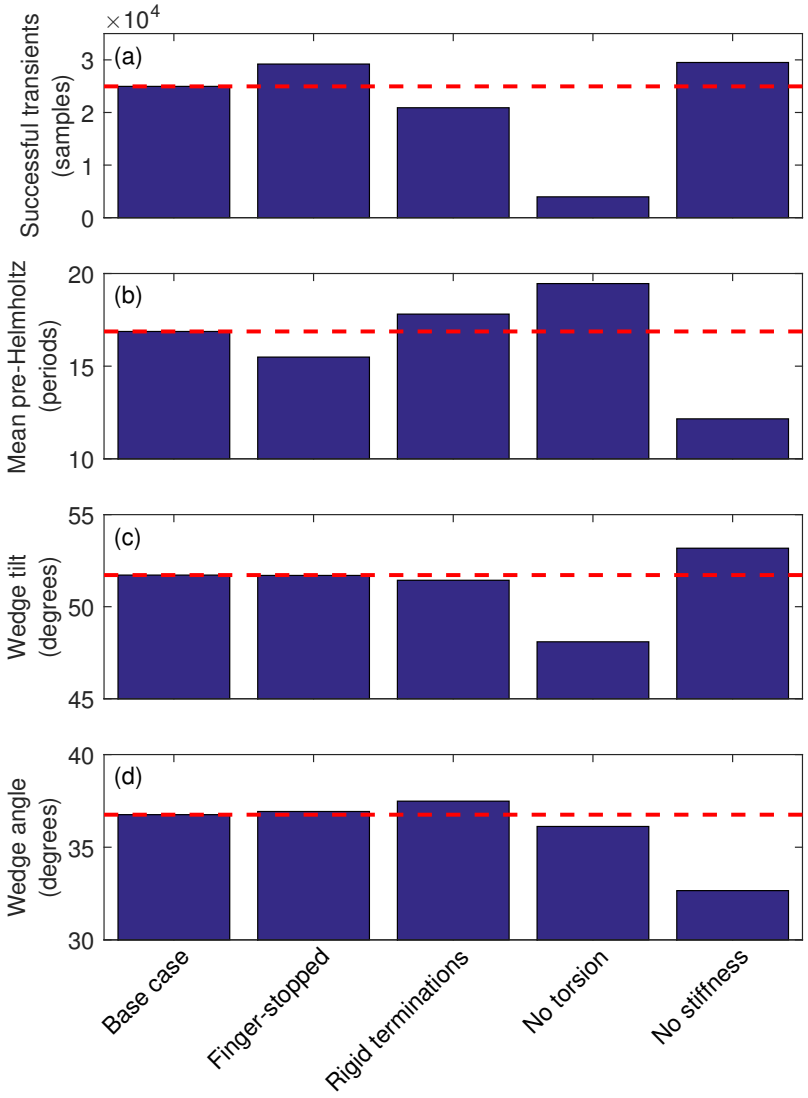

Fig. 5.17 A comparison of different metrics related to the Guettler diagrams for several cases shown on the horizontal axis and defined in the text. (a) The number of successful transients (out of a total of 90,000 in each subplot) which led to the Helmholtz regime in less than 25 string periods, (b) the average number of unsuccessful periods before a Helmholtz regime is established, (c) the mean angle of the line that connects the origin to the successful samples that is a measure for the orientation of the Guettler wedge, and (d) the tip angle of a Guettler wedge that can fit 90% of the successful samples in each subplot.

execute the intended gesture. This line of research is in its infancy and researchers are still trying to pin down the definition of different terms (e.g. "cushion" and "resistance") used by players and makers to describe a particular combination of bow, string, and instrument body.

One particular feature of a bowed string which cannot be captured by the Schelleng or the Guettler diagrams but affects the ability of the player to play a series of rapid notes is the static deflection of the bowing point in response to a unit lateral force.[8] If the string is too compliant (or wobbly) the player needs to displace the bowing point by a large amount before the reaction force of the string reaches the limiting static friction that is considered the onset of the note. Given the physical constraints of a human player, excessive compliance at the bowing point may delay the onset of the note for too long and make the exact timing of it hard to control.

If the amount of lateral force is small compared to the static tension of the string, the static stiffness at the bowing point can be found from $\frac{T_0}{\beta(1-\beta)L^2}$. If that assumption does not hold (which is highly unlikely based on the data presented in Fig. 3.5), the change in the static tension of the string should also be considered, which itself depends on the longitudinal stiffness of the string (i.e. ES) in a way formalized in Eq. (3.16). Two other factors that may contribute to such wobbliness are the torsional stiffness of the string and its bending stiffness, the latter through the quasi-evanescent waves mentioned in Sec. 2.2.2.

Another relevant parameter to the interface of the player with the string is the transversal compliance of the bow hair at the contact point with the string. Tilting, which is used continuously by string players (in particular violinists), not only reduces the effective width of the bow hair, but also changes the compliance. Tilting increases the compliance in the transversal direction, and makes it easier to control low bow forces by the right hand by allowing a little larger pivoting motion at the frog for a certain small change in bow force. On the other hand, to apply a large amount of bow force the player may use the full width of the bow and play close to the frog to give himself/herself more room before the bow hair ribbon bottoms out on the bow stick.

5.3 Summary of findings

In this chapter, we looked at different metrics of a bowed string as well as their dependence on different parameters of the model. The metrics that are studied are the increase in the slip-to-stick ratio as a percentage of its theoretical value, the spectral centroid relative to

[8] This feature is discussed by Guettler in an unpublished document that can be accessed from http://knutsacoustics.com/files/String-stiffness.pdf. The author believes some aspects of the arguments made there are subject to debate.

the fundamental frequency, and the pitch flattening as a percentage of the fundamental frequency, as well as the more familiar minimum and maximum bow forces. Many aspects of the results are in good agreement with previous experiments conducted by Galluzzo [21] and Schoonderwaldt [133], at least qualitatively. We also looked into the transients of a string initially at rest when it is bowed by a constant bow force and a bow speed uniformly accelerating from zero (a.k.a. the Guettler diagram). Our simulations of the Guettler diagram suggested that the torsional motion of the string is extremely helpful to the formation of the Helmholtz motion, so are the flexibility at the bridge and the intrinsic damping of the string but to a lesser extent. The bending stiffness of the string is a strong barrier in the formation of the Helmholtz motion.

Chapter 6

Conclusions and future work

6.1 Main findings of the thesis

In this thesis we described the development of a highly refined physics-based model of a bowed string and its subsequent use to investigate several aspects of a bowed string, particularly its playability. Building on an earlier simulation model of a bowed string, introduced in [28], different aspects of the model are replaced by more accurate alternatives and several new features were added to make the model more realistic.

In Chap. 2, the development of the plucked-string model was described in details and this later serves as a platform to make the model of the bowed string. In accordance with the main interest of the thesis, the cello is chosen as the main subject of Chap. 2, nonetheless most of the arguments and the approaches taken are applicable to the plucked strings of the guitar and any instrument of the violin family. After a review of the relevant physics involved and their underlying theories, different methods are proposed to include some of those physics in our particular modeling scheme. The motivation to study a plucked string first was that the damping and dispersion properties of a simulated string, as well as its interaction with the body modes, could be readily investigated from a plucked response and be compared to experimental data, a luxury which was not available in the case of a bowed string due to the constant feeding of the energy by the bow and the mode lock-in phenomenon [54] that enforces perfectly harmonic partials. There were also some questionable assumptions involved with the tribology behavior of the rosin that might influence the results, hence weakening their link to experimental data.

Among the details that were discussed were the frequency-dependent damping of the string, its bending stiffness, its out-of-plane vibrations, its nonlinear vibrations, and its coupling to the body modes, the sympathetic strings, and the after-lengths. The broad range of topics that are covered as well as the depth of the theoretical discussions offered,

make Chap. 2 (and Chap. 3) a good starting point for anyone interested in the modeling of the vibrating string, regardless of the intended modeling approach. Several physical parameters were reported for a full set of "D'Addario Kaplan Solutions" cello strings as well as a set of "Cleartone 12-53 Phosphor Bronze" steel guitar strings. Those parameters are also general and can be used readily by other researchers.

In the later part of Chap. 2, the synthesized plucked responses were compared to their experimental counterparts as well as the designed values, which confirms the accuracy of the model and its parameters. The accuracy with which the coupling of the string to the body modes (and to the sympathetic strings) is modeled is evaluated by comparing the bridge admittance measured on an actual instrument to the same quantity obtained from our model when the strings were either damped or free to vibrate. Moreover, the plucked responses of the simulated open C_2 and D_3 strings were compared to their experimental counterparts. Aside from a minor difference for the D_3 and at higher frequencies, the match was satisfyingly good.

In Chap. 3 we looked into the new physical details that emerge from the interaction of the bow with the string, namely the tribology of the rosin, the torsional motion of the string, tension alterations of the string and the bow hair ribbon when one is pushed against the other, and the flexibility of the bow hair ribbon in its longitudinal and transverse directions. The finite-width of the bow hair ribbon was discussed but it has not been included in the current version of our model.

The main unresolved issue in regards to the modeling of a bowed string still [3] remains the friction behavior of the rosin. Although a thermal friction model of the rosin is also included in our model, the simulations of the subsequent chapters were made using the classic velocity-dependent friction model. Earlier studies have pointed to some serious concerns in regards to the thermal model [21], at least the latest version at the time of this study.

In Chap. 4 we demonstrated a particular application of our bowed-string model in validating a revised relation for the minimum bow force. After a review of the available literature on the bow force limits (Schelleng's predictions [23] later improved by Woodhouse [24]), some experimental results were presented that weakened one of the underlying assumptions used in deriving earlier relations for the minimum bow force. The key point was that the force at the bridge no longer resembles a perfect sawtooth wave when the fundamental frequency of the string is close to a strong body resonance. It rather becomes a skewed sawtooth whose fundamental is relatively weaker than expected when the played note falls below a strong body resonance, and stronger than expected if the played note falls above a strong body resonance.

Taking one step back, a more robust assumption was made that assumed an ideal stick-

slip at the bowing point rather than a perfect sawtooth-shaped excitation force at the bridge. Using the standard transmission line theory, the bridge force from a perfect stick-slip assumption was calculated which qualitatively matched our earlier experimental findings. The approach taken by Woodhouse [24] to calculate the minimum bow force was repeated using the modified bridge force in place of the ideal one. The revised prediction of minimum bow force showed some fundamentally different results compared to ones obtained from the original relation.

The most significant difference between the two (considering a single-resonance body for simplicity) was that according to the original relation, the largest value for minimum bow force should be observed at the frequency of the body mode, whereas the revised relation predicted that the maximum bow force always occurs above that frequency. More interestingly, the amount by which the frequency of the peak value is shifted upward increases as the bow-bridge distance decreases. In terms of the Schelleng diagram, this implies that the minimum bow force limit would be curved downward for string frequencies below the body resonance, thus extending the playable range toward lower beta values. The opposite happens for the string frequencies above the body resonance.

Based on the same transmission line model, we argued that in contrast to the predictions made by Gough [128], the second polarization of the string may not contribute a sharp peak to the bowing-point admittance under typical circumstances. That said, we did not rule out the possibility that it can contribute to the playability by adding a fluctuating component to the effective bow force. We also showed that the sympathetic strings and their interactions with the body modes affect the minimum bow force to a large extent, and as such they should be considered an important component in the calculation of the minimum bow force. A simple recipe is offered to modify the bridge admittance in a way that includes the effect of the sympathetic strings.

The bowed-string model was used to evaluate the accuracy of our earlier predictions in regards to the minimum bow force, which confirmed the advantages of the revised relation over the original one. A surprising observation from the simulations was that the inclusion of the string's torsional motion made a very small impact on the minimum bow force. This was in contrast to the assumption made so far by other researchers [22, 99]. The reason for this observation was tracked down to the fact that the frequency of the first torsional mode of a string is typically around 5 times larger than that of the first transverse mode, as a result, the torsional degree of freedom makes little contribute to the admittance at the bowing point within the frequency of the first harmonics of the bowed string. Finally, it was shown that the impedance at the bowing point cannot be directly used to predict the minimum bow force unless one precisely knows the velocity that the string would have at

the bowing point if it was bowed.

In Chap. 5 the bowed-string model was used to investigate a broader range of features. Several variations of the model were considered (based on the physical details which were included) and their results were compared to that of a base case. The base case simulated the single-polarization vibrations of a damped and stiff D_3 cello string, terminated at a realistic multi-resonance bridge, and bowed by a rigid rod. It also included the torsional motion of the string.

The steady state vibrations of different cases were compared to that of the base case for different features including the increase in the slip-to-stick ratio as a percentage of its theoretical value, the spectral centroid relative to the fundamental frequency, and the pitch flattening as a percentage of the fundamental frequency. The minimum and maximum bow forces as well as the number of ALF and S-motion occurrences were also considered. Our results showed that:

- Adding noise to the bow force and bow speed creates a patchy region in the lower-right side of the Schelleng diagram that is in accordance with earlier experimental observations [21].

- The samples with the same amount of extended slipping phase were laid out almost parallel to the minimum bow force limit, and the samples with the same amount of pitch flattening were laid out almost parallel to the maximum bow force limit. The spectral centroid was almost exclusively a function of the bow force (i.e., a larger bow force typically led to a higher frequency for the spectral centroid).

- A ripple structure along the β axis was observed on both pitch flattening and slip extension plots. The structure disappeared if either, or both the torsional motion of the string or its stiffness were excluded from the model, and for that reason the structure was associated to an interaction between the two.

- Adding to the intrinsic damping of the string made a minimal effect on the maximum bow force, but it significantly increased the minimum bow force. Including the longitudinal vibrations of the bow hair reduced both the minimum and the maximum bow forces by a small amount. Removing the torsional motion of the string shifted the Helmholtz region upward, and removing the bending stiffness expanded the Helmholtz region from both top and bottom sides. Turning the bridge into a rigid termination point moderately increased the maximum bow force, and as expected, reduced the minimum bow force by a very large amount.

- Adding to the intrinsic damping of the string led to a longer slipping phase. Removing the string's bending stiffness and turning the bridge to a rigid termination point resulted in a shorter slipping phase. Including the longitudinal vibrations of the bow hair shortened the slipping phase, and removing the torsional vibrations of the string further extended it. Based on these observations it was concluded that any factor that increases the spatial spread of the Helmholtz kink results in a further extension of the slipping phase, and any factor that decreases the effective impedance at the bowing point (particularly at higher frequencies) allows the sticking phase to persist for a longer period of time, thus shortening its duration.

- Removing the bending stiffness of the string significantly reduced the spectral centroid. The difference between the spectral centroid of other cases was negligible.

- Longitudinal vibrations of the bow hair resulted in more flattening and removing the torsional motion of the string resulted in less flattening. Exclusion of the flexible body from the model and adding to the intrinsic damping of the string both resulted in less flattening. As was expected, excluding the bending stiffness of the string resulted in more flattening in general, but interestingly, it resulted in less flattening at very large bow forces.

- When the frequency of the played note was varied in close proximity to a strong body resonance, repulsion between the first string mode and the body mode decreased the stick-slip frequency for the frequencies below the body mode, and increased it for the frequencies above the body mode. However, the pitch deviation caused only by such repulsion was outweighed by the flattening close to the maximum bow force, therefore it may be considered negligible for practical purposes.

- At least four distinct regions of ALF note were observed above the maximum bow force limit with each area representing a particular "mode" of ALF regime, hence a distinct pitch. Those areas had a clear structure when both torsional motion of the string and its stiffness were excluded from the model, but they became less structured as more physical details were included in the model. Flexibility of the bow hair resulted in more frequent occurrence of ALF notes.

- Excluding the torsional motion of the string significantly reduced the number of S-motion occurrences, the effect being even stronger if the bending stiffness of the string was excluded as well. Turning the bridge into a rigid termination point significantly increased the number of S-motion samples.

- The case with a flexible bow hair and a flexible bow-stick produced very similar results when compared to the case of a flexible bow hair but a rigid bow-stick. This led to the conclusion that the properties of the bow-stick make a very small difference in the vibrations of a bowed string. The only significant difference between the two cases was the number of ALF notes that was noticeably higher when the bow-stick was made flexible.

- For our base case, the bow force fluctuations due to the perpendicular-to-bow motion of the string amounted to as much as 10% of its nominal value. The fluctuations were dominantly at a frequency close to a string mode frequency which fell close to a body mode that is also angled with respect to the bowing direction as close as possible to 45°.

- The amplitude of the bow speed fluctuations due to the longitudinal flexibility of the bow hair was as much as 300% of its nominal value. The dominant frequency components of bow speed fluctuations were the first mode frequency of the bow hair in its longitudinal directions, as well as the frequency components present in the perturbation force at the bowing point. The effect of the longitudinal bow hair vibrations on the bow force limits was relatively small.

- Three different cases, all with a single body resonance, were investigated to identify how the bow force fluctuations affect the bow force limits. We concluded that a body mode with a positive angle (defined in Fig. 2.4) reduces the minimum bow force at all frequencies, it increase the maximum bow force at the frequencies below the body resonance, and it decrease the maximum bow force at the frequencies above the body resonance. The opposite happens for a negative mode angle, or if the bowing direction is reversed.

- Four different nominal bow speeds were used for the base case and the upper and lower bow force limits were calculated from simulated results. In accordance with the theoretical predictions, the limits linearly scaled with the bow speed.

- Many aspects of our results, regarding the steady state vibrations of a bowed string, were in good agreement with previous experimental observations reported by Galluzzo [21] and Schoonderwaldt [133].

The transients of an open D_3 string were investigated using the Guettler diagram plotted for the base case compared to those of four other cases for which (a) the torsional motion of the string was excluded, (b) the string was made perfectly flexible, (c) the bridge was turned

into a rigid termination point, and (d) the intrinsic damping of the string was increased to reflect finger stopping by the player. Excluding the torsional motion of the string and turning the bridge into a rigid termination point made the formation of the Helmholtz motion harder, with a much stronger effect caused by the exclusion of the torsional motion. Increasing the intrinsic damping of the string helped the formation of the Helmholtz motion to some extent, but the biggest improvement resulted when the bending stiffness of the string was removed. Removal of the bending stiffness not only increased the number of successful transients, but it also significantly reduced the average duration within which the Helmholtz regime was achieved. In addition, the successful transients of a perfectly flexible string were gathered in a smaller region of the Guettler diagram which would help the player to form the Helmholtz regime more reliably and more rigorously.

We argued that the static stiffness of the string surface at the bowing point is an important contributor to the player's ability to execute a series of rapid notes. To the first order of approximation, such stiffness depends on the static tension of the string, its length, and the bow-bridge distance. Some secondary factors are the torsional stiffness of the string, its bending stiffness, and the stiffness along its length.

6.2 Future directions

The application of the bowed-string model developed in this study is, by no means, limited to what was described in Chaps. 4 and 5. The model can be used as a general tool in conducting systematic experiments which, for different reasons, cannot be done on an actual instrument.

As was mentioned earlier, the main unresolved issue in the modeling of a bowed string is the friction behavior of the rosin. Our model can serve as an excellent platform to test newer friction models once they become available. Aside from a better friction model, accounting for the nonlinear vibrations of the string, the quasi-evanescent field around the bowing point, and the finite-width of the bow are possible improvements to the model.

The only aspect of this study which looked at the transients of a bowed string was the particular case of the Guettler diagram. It would be interesting, and very straightforward to investigate other types of transients such as martelé, spiccato, or indeed more complex gestural inputs from an actual player acquired by motion capturing techniques [109, 110, 111, 112].

The exact stick-slip frequency of a bowed string is of interest both for musical reasons (i.e. pitch flattening) and for musical acousticians in calculating the minimum bow force. We conducted a detailed analysis of the pitch flattening using our model (presented in Sec. 5.1.3),

and it would be interesting to compare those results with the theoretical predictions made by Boutillon [131], and to possibly extend those predictions using the theoretical framework offered in Sec. 4.2.

A practically important regime of vibration that was not analyzed in this study is the double/multiple flyback regime (it has been defined in Sec. 3.4.1). Our simulation model, and especially its animation tool (see some examples at this link[1]), can be used in identifying the gestural inputs that lead to a double/multiple flyback regime, and in providing some guidelines on how to avoid it in the first place. Another possibility in this regard is to initialize the model with double flyback and check its stability region on the β-F_N plane, in the same way as was done for the Helmholtz motion on the Schelleng diagram.

In the course of this study a large collection of high speed video recordings was gathered which were not fully analyzed due to time constraints. Although many high frequency features are hard to capture by the displacement of a vibrating string (velocity and acceleration are better suited for that purpose), image processing techniques can be applied to extract some useful qualitative, and even quantitative data from those recordings [138]. Some samples of the high-speed recordings are available at this link[1].

Given the extensive number of physically accurate features in our model, it may be used as a reference to conduct perceptual studies and to investigate how much simplification can be made on the modeling of a particular physical detail before the change in the synthesized sound becomes noticeable to human subjects. This would provide useful information for people in the sound synthesis domain to decide whether it is worthwhile to implement a specific detail in their real-time models or it can be eliminated in order to improve computational efficiency.

[1] http://mt.music.mcgill.ca/~hosseinm/research/mus_acc/thesis_mat/

References

[1] G. Weinreich, "What science knows about violins–and what it does not know," *American Journal of Physics*, vol. 61, no. 12, pp. 1067–1077, 1993.

[2] H. Helmholtz, *On the sensations of tone*. Dover Publications (English translation of the German edition was published in 1954), 1877.

[3] J. Woodhouse and P. M. Galluzzo, "The bowed string as we know it today," *Acta Acustica united with Acustica*, vol. 90, no. 4, pp. 579–589, 2004.

[4] G. Bissinger, "Structural acoustics of good and bad violins," *The Journal of the Acoustical Society of America*, vol. 124, no. 3, pp. 1764–1773, 2008.

[5] J. Woodhouse, E. K. Y. Manuel, L. A. Smith, A. J. C. Wheble, and C. Fritz, "Perceptual thresholds for acoustical guitar models," *Acta Acustica united with Acustica*, vol. 98, no. 3, pp. 475–486, 2012.

[6] H. Mansour, V. Fréour, C. Saitis, and G. P. Scavone, "Post-classification of nominally identical steel-string guitars using bridge admittances," *Acta Acustica united with Acustica*, vol. 101, no. 2, pp. 394–407, 2015.

[7] J. Curtin, "Bridging the divide : A conversation with professor Jim Woodhouse," *The Strad*, Aug 2005.

[8] C. E. Gough, "Violin plate modes," *The Journal of the Acoustical Society of America*, vol. 137, no. 1, pp. 139–153, 2015.

[9] C. E. Gough, "A violin shell model: Vibrational modes and acoustics," *The Journal of the Acoustical Society of America*, vol. 137, no. 3, pp. 1210–1225, 2015.

[10] G. Bissinger, "Parametric plate-bridge dynamic filter model of violin radiativity," *The Journal of the Acoustical Society of America*, vol. 132, no. 1, p. 465, 2012.

[11] J. Woodhouse, "On the synthesis of guitar plucks," *Acta Acustica united with Acustica*, vol. 90, pp. 928–944, 2004.

[12] J. Woodhouse and R. S. Langley, "Interpreting the input admittance of violins and guitars," *Acta Acustica united with Acustica*, vol. 98, no. 4, pp. 611–628, 2012.

[13] N. McLachlan, B. K. Nigjeh, and A. Hasell, "The design of bells with harmonic overtones," *The Journal of the Acoustical Society of America*, vol. 114, no. 1, pp. 505–511, 2003.

[14] H. T. Nia, A. D. Jain, Y. Liu, M.-R. Alam, R. Barnas, and N. C. Makris, "The evolution of air resonance power efficiency in the violin and its ancestors," in *Proceedings of the Royal Society of London A: Mathematical, Physical and Engineering Sciences*, vol. 471, p. 20140905, The Royal Society, 2015.

[15] M. A. Pyrkosz and C. Van Karsen, "Coupled vibro-acoustic model of the Titian Stradivari violin," in *Topics in Modal Analysis I, Volume 7*, pp. 317–332, Springer, 2014.

[16] M. Schleske, "Empirical tools in contemporary violin making: Part I. Analysis of design, materials, varnish, and normal modes," *Catgut Acoustical Society Journal*, vol. 4, no. 5, pp. 50–64, 2002.

[17] F. Durup and E. V. Jansson, "The quest of the violin bridge-hill," *Acta Acustica united with Acustica*, vol. 91, no. 2, pp. 206–213, 2005.

[18] J. Woodhouse, "On the "bridge hill" of the violin," *Acta Acustica united with Acustica*, vol. 91, no. 1, pp. 155–165, 2005.

[19] M. Pyrkosz, C. Van Karsen, and G. Bissinger, "Converting ct scans of a stradivari violin to a fem," in *Structural Dynamics, Volume 3*, pp. 811–820, Springer, 2011.

[20] S. A. Sirr and J. R. Waddle, "Use of CT in detection of internal damage and repair and determination of authenticity in high-quality bowed stringed instruments," *RadioGraphics*, vol. 19, no. 3, pp. 639–646, 1999.

[21] P. M. Galluzzo, *On the playability of stringed instruments*. Thesis, Engineering Department, University of Cambridge, Cambridge, UK, 2003.

[22] E. Schoonderwaldt, K. Guettler, and A. Askenfelt, "An empirical investigation of bow-force limits in the schelleng diagram," *Acta Acustica united with Acustica*, vol. 94, no. 4, pp. 604–622, 2008.

[23] J. C. Schelleng, "The bowed string and the player," *The Journal of the Acoustical Society of America*, vol. 53, no. 1, pp. 26–41, 1973.

[24] J. Woodhouse, "On the playability of violins. Part II: Minimum bow force and transients," *Acustica*, vol. 78, pp. 137–153, 1993.

[25] A. Zhang and J. Woodhouse, "On the playability of wolf note," in *International Symposium on Musical Acoustics (ISMA 2014), Le Mans, France*, pp. 32–37, 2014.

[26] C. Fritz and D. Dubois, "Perceptual evaluation of musical instruments: State of the art and methodology," *Acta Acustica united with Acustica*, vol. 101, no. 2, pp. 369–381, 2015.

[27] C. Saitis, *Evaluating violin quality: Player reliability and verbalization*. PhD thesis, Dept. of Music Research, McGill University, Montreal, Quebec, Canada, 2013.

[28] M. E. McIntyre, R. T. Schumacher, and J. Woodhouse, "On the oscillations of musical instruments," *The Journal of the Acoustical Society of America*, vol. 74, no. 5, pp. 1325–1345, 1983.

[29] J. Woodhouse, "On the playability of violins. Part I: Reflection functions," *Acustica*, vol. 78, no. 3, pp. 125–136, 1993.

[30] R. T. Schumacher and J. Woodhouse, "The transient behaviour of models of bowed-string motion," *Chaos: An Interdisciplinary Journal of Nonlinear Science*, vol. 5, no. 3, pp. 509–523, 1995.

[31] R. T. Schumacher and J. Woodhouse, "Computer modelling of violin playing," *Contemporary Physics*, vol. 36, no. 2, pp. 79–92, 1995.

[32] J. Woodhouse, "Bowed string simulation using a thermal friction model," *Acta Acustica united with Acustica*, vol. 89, no. 2, pp. 355–368, 2003.

[33] J. Woodhouse and A. R. Loach, "Torsional behaviour of cello strings," *Acta Acustica united with Acustica*, vol. 85, no. 5, pp. 734–740, 1999.

[34] M. E. McIntyre and J. Woodhouse, "On the fundamentals of bowed string dynamics," *Acustica*, vol. 43, no. 2, pp. 93–108, 1979.

[35] R. Pitteroff and J. Woodhouse, "Mechanics of the contact area between a violin bow and a string. Part I: Reflection and transmission behaviour," *Acta Acustica united with Acustica*, vol. 84, no. 3, pp. 543–562, 1998.

[36] J. Curtin and T. D. Rossing, "Violin," in Rossing [139], pp. 209–244.

[37] C. E. Gough, "Musical acoustics," in *Handbook of Acoustics* (T. D. Rossing, ed.), pp. 533–667, Springer, New York, 2007.

[38] J. Woodhouse, "The acoustics of the violin: a review," *Reports on Progress in Physics*, vol. 77, no. 11, pp. 1–42, 2014.

[39] J. Woodhouse, "On the synthesis of guitar plucks," *Acta Acustica united with Acustica*, vol. 90, no. 5, pp. 928–944, 2004.

[40] B. Taylor, "De motu nervi tensii," *Royal Society of London Philosophical Transactions Series I*, vol. 28, pp. 26–32, 1713.

[41] O. Darrigol, "The acoustic origins of harmonic analysis," *Archive for history of exact sciences*, vol. 61, no. 4, pp. 343–424, 2007.

[42] D. Bernoulli, "De vibrationibus et sono laminarum elasticarum," *Commentarii Academiae Scientiarum Imperialis Petropolitanae*, vol. 13, pp. 105–120, 1751.

[43] J. D'Alembert, "Recherches sur la courbe que forme une corde tendue mise en vibrations," *Histoire de l'Académie Royale des Sciences et Belles Lettres*, vol. 3, pp. 214–249, 1747.

[44] J. O. Smith, *Physical audio signal processing: For virtual musical instruments and audio effects*. W3K Publishing, 2010.

[45] C. V. Raman, "On the mechanical theory of bowed strings and of musical instruments of the violin family, with experimental verification of results: Part I," *Bulletin of the Indian Association for the Cultivation of Science*, vol. 15, pp. 1–158, 1918.

[46] S. H. Crandall, "The role of damping in vibration theory," *Journal of Sound and Vibration*, vol. 11, no. 1, pp. 3–18, 1970.

[47] R. Pitteroff and J. Woodhouse, "Mechanics of the contact area between a violin bow and a string. Part II: Simulating the bowed string," *Acta Acustica united with Acustica*, vol. 84, no. 4, pp. 744–757, 1998.

[48] M. Van Walstijn, "Parametric fir design of propagation loss filters in digital waveguide string models," *Signal Processing Letters, IEEE*, vol. 17, no. 9, pp. 795–798, 2010.

[49] C. Valette, "The mechanics of vibrating strings," in *Mechanics of musical instruments* (A. Hirschberg, ed.), pp. 115–183, Springer-Verlag, Vienna, 1995.

[50] L. Cremer, "Das Schicksal der 'Sekundärwellen' bei der Selbsterregung von Streichinstrumenten (translated: The fate of 'secondary waves' arising from self-excitation of stringed instruments)," *Acta Acustica united with Acustica*, vol. 42, no. 3, pp. 133–148, 1979.

[51] L. Cremer, *The physics of the violin*. Cambridge, MA: The MIT Press, 1984.

[52] E. Ducasse, "On waveguide modeling of stiff piano strings," *The Journal of the Acoustical Society of America*, vol. 118, no. 3, pp. 1776–1781, 2005.

[53] H. Jarvelainen and M. Karjalainen, "Perceptibility of inharmonicity in the acoustic guitar," *Acta Acustica United with Acustica*, vol. 92, no. 5, pp. 842–847, 2006.

[54] M. T. Bengisu and A. Akay, "Stability of friction-induced vibrations in multi-degree-of-freedom systems," *Journal of Sound and Vibration*, vol. 171, no. 4, pp. 557–570, 1994.

[55] A. H. Benade, *Fundamentals of musical acoustics*. London: Oxford University Press, second ed., 1976.

[56] N. H. Fletcher, "Mode locking in nonlinearly excited inharmonic musical oscillators," *The Journal of the Acoustical Society of America*, vol. 64, no. 6, pp. 1566–1569, 1978.

[57] W. L. Coyle, P. Guillemain, J. Kergomard, and J. P. Dalmont, "Predicting playing frequencies for clarinets: a comparison between numerical simulations and simplified analytical formulas," *The Journal of the Acoustical Society of America*, submitted 2014.

[58] X. Boutillon and G. Weinreich, "Three-dimensional mechanical admittance: Theory and new measurement method applied to the violin bridge," *The Journal of the Acoustical Society of America*, vol. 105, no. 6, pp. 3524–3533, 1999.

[59] J. Woodhouse and P. E. Courtney, "The admittance matrix of a cello," in *Stockholm Music Acoustics Conference 2003 (SMAC 03)*, vol. 3, pp. 107–110, 2003.

[60] J. Woodhouse, "Plucked guitar transients: Comparison of measurements and synthesis," *Acta Acustica united with Acustica*, vol. 90, no. 5, pp. 945–965, 2004.

[61] A. Zhang and J. Woodhouse, "Reliability of the input admittance of bowed-string instruments measured by the hammer method," *The Journal of the Acoustical Society of America*, vol. 136, no. 6, pp. 3371–3381, 2014.

[62] C. E. Gough, "The theory of string resonances on musical instruments," *Acustica*, vol. 49, no. 2, pp. 124–141, 1981.

[63] L. Rayleigh, *The theory of sound (two volumes)*. New York: Dover Publications, second ed., 1877.

[64] R. J. Clarke, "The analysis of multiple resonance in a vibrating mechanical system by the use of the electrical transmission line analogy," *Acta Acustica united with Acustica*, vol. 40, no. 1, pp. 34–39, 1978.

[65] G. Weinreich, "Coupled piano strings," *The Journal of the Acoustical Society of America*, vol. 62, no. 6, pp. 1474–1484, 1977.

[66] H. Fletcher and L. C. Sanders, "Quality of violin vibrato tones," *The Journal of the Acoustical Society of America*, vol. 41, no. 6, pp. 1534–1544, 1967.

[67] N. H. Fletcher and T. D. Rossing, *The physics of musical instruments*. Springer Verlag, 1998.

[68] B. Bank and L. Sujbert, "Generation of longitudinal vibrations in piano strings: From physics to sound synthesis," *The Journal of the Acoustical Society of America*, vol. 117, no. 4, pp. 2268–2278, 2005.

[69] G. V. Anand, "Large-amplitude damped free vibration of a stretched string," *The Journal of the Acoustical Society of America*, vol. 45, no. 5, pp. 1089–1096, 1969.

[70] J. Miles, "Resonant, nonplanar motion of a stretched string," *The Journal of the Acoustical Society of America*, vol. 75, no. 5, pp. 1505–1510, 1984.

[71] K. A. Legge and N. H. Fletcher, "Nonlinear generation of missing modes on a vibrating string," *The Journal of the Acoustical Society of America*, vol. 76, no. 1, pp. 5–12, 1984.

[72] T. Tolonen, V. Välimäki, and M. Karjalainen, "Modeling of tension modulation nonlinearity in plucked strings," *Speech and Audio Processing, IEEE Transactions on*, vol. 8, no. 3, pp. 300–310, 2000.

[73] H. A. Conklin, "Generation of partials due to nonlinear mixing in a stringed instrument," *The Journal of the Acoustical Society of America*, vol. 105, no. 1, pp. 536–545, 1999.

[74] B. Bank and L. Sujbert, "Efficient modeling strategies for the geometric nonlinearities of musical instrument strings," in *Proceedings of Forum Acusticum*, 2005.

[75] C. H. Hodges, J. Power, and J. Woodhouse, "The use of the sonogram in structural acoustics and an application to the vibrations of cylindrical shells," *Journal of Sound and Vibration*, vol. 101, pp. 203–218, 1985.

[76] S. M. Saw, "Influence of finger forces on string vibration," thesis, Engineering Department, University of Cambridge, Cambridge, UK, 2010.

[77] C. W. Farrow, "A continuously variable digital delay element," in *Circuits and Systems, 1988., IEEE International Symposium on*, pp. 2641–2645, IEEE, 1988.

[78] J. S. Abel and J. O. Smith, "Robust design of very high-order allpass dispersion filters," in *Proceedings of the International Conference on Digital Audio Effects, Montreal, Quebec, Canada*, pp. 13–18, 2006.

[79] J. S. Abel, V. Valimaki, and J. O. Smith, "Robust, efficient design of allpass filters for dispersive string sound synthesis," *Signal Processing Letters, IEEE*, vol. 17, no. 4, pp. 406–409, 2010.

[80] J. O. Smith, *Introduction to digital filters: with audio applications*, vol. 2. W3K Publishing, 2007.

[81] A. S. Phani and J. Woodhouse, "Experimental identification of viscous damping in linear vibration," *Journal of Sound and Vibration*, vol. 319, no. 3, pp. 832–849, 2009.

[82] E. Fouilhe, G. Goli, A. Houssay, and G. Stoppani, "Vibration modes of the cello tailpiece," *Archives of acoustics*, vol. 36, no. 4, pp. 713–726, 2011.

[83] B. Scherrer, *Physically-informed indirect acquisition of instrumental gestures on the classical guitar: Extracting the angle of release.* Thesis, Dept. of Music Research, McGill University, 2013.

[84] W. Reinicke, *Die Übertragungseigenschaften des Streichinstrumentensteges.* PhD thesis, Technical University of Berlin, 1973.

[85] D. Chadefaux, J. L. Le Carrou, and B. Fabre, "A model of harp plucking," *The Journal of the Acoustical Society of America*, vol. 133, no. 4, pp. 2444–2455, 2013.

[86] G. Cuzzucoli and V. Lombardo, "A physical model of the classical guitar, including the player's touch," *Computer Music Journal*, vol. 23, no. 2, pp. 52–69, 1999.

[87] G. Evangelista and F. Eckerholm, "Player-instrument interaction models for digital waveguide synthesis of guitar: Touch and collisions," *Audio, Speech, and Language Processing, IEEE Transactions on*, vol. 18, no. 4, pp. 822–832, 2010.

[88] D. Chadefaux, J. L. Le Carrou, B. Fabre, and L. Daudet, "Experimentally based description of harp plucking," *The Journal of the Acoustical Society of America*, vol. 131, no. 1, pp. 844–855, 2012.

[89] C. V. Raman, "Experiments with mechanically-played violins," *Proceedings of the Indian Association for the Cultivation of Science*, vol. 6, pp. 19–36, 1920.

[90] F. G. Friedlander, "On the oscillations of a bowed string," in *Mathematical Proceedings of the Cambridge Philosophical Society*, vol. 49, pp. 516–530, Cambridge Univ Press, 1953.

[91] J. B. Keller, "Bowing of violin strings," *Communications on Pure and Applied Mathematics*, vol. 6, no. 4, pp. 483–495, 1953.

[92] M. E. Mclntyre, R. T. Schumacher, and J. Woodhouse, "Aperiodicity in bowed-string motion," *Acustica*, vol. 49, no. 1, pp. 13–32, 1981.

[93] G. Weinreich and R. Causse, "Elementary stability considerations for bowed-string motion," *The Journal of the Acoustical Society of America*, vol. 89, no. 2, pp. 887–895, 1991.

[94] J. Woodhouse, "On the stability of bowed string motion," *Acta Acustica united with Acustica*, vol. 80, no. 1, pp. 58–72, 1994.

[95] L. Cremer and H. Lazarus, "Die Ermittlung der Richtcharakteristik von Streichinstrumenten bei Gegebener Schwinungsform des Körpen," in *Proceedings of the 6th International Congress on Acoustics, Tokyo*, vol. 2, p. 3, 1968.

[96] L. Cremer, "Der Einfluss des 'Bogendrucks' auf die selbsterregten Schwingungen der gestrichenen Saite," *Acustica*, vol. 30, no. 3, pp. 119–136, 1974.

[97] J. O. Smith, *Techniques for digital filter design and system identification with application to the violin*. Thesis, Electrical Engineering Department, Stanford University, Stanford, CA, 1983.

[98] B. Stough, "E string whistles," *Catgut Acoustical Society Journal*, vol. 3, no. 2, pp. 28–33, 1999.

[99] R. T. Schumacher, "Measurements of some parameters of bowing," *The Journal of the Acoustical Society of America*, vol. 96, no. 4, pp. 1985–1998, 1994.

[100] S. Serafin, J. O. Smith, and J. Woodhouse, "An investigation of the impact of torsion waves and friction characteristics on the playability of virtual bowed strings," in *IEEE Workshop on Signal Processing to Audio and Acoustics*, pp. 87–90, 1999.

[101] C. E. Gough, "Violin bow vibrations," *The Journal of the Acoustical Society of America*, vol. 131, no. 5, pp. 4152–4163, 2012.

[102] A. Askenfelt, "Observations on the violin bow and the interaction with the string," in *International Symposium on Musical Acoustics (ISMA 1995), Dourdan, France*, 1995.

[103] A. Askenfelt and K. Guettler, "Bows and timbre - myth or reality?," in *International Symposium on Musical Acoustics (ISMA 2001), Perugia, Italy*, pp. 273–276, 2001.

[104] K. Guettler, "Bows, strings, and bowing," in Rossing [139], pp. 279–299.

[105] A. Askenfelt and K. Guettler, "The bouncing bow: An experimental study," *Catgut Acoustical Society Journal*, vol. 3, no. 6, pp. 3–8, 1998.

[106] E. Schoonderwaldt, K. Guettler, and A. Askenfelt, "Effect of the width of the bow hair on the violin string spectrum," in *Stockholm Music Acoustics Conference 2003 (SMAC 03)*, pp. 91–94, 2003.

[107] E. Maestre, C. Spa, and J. O. Smith, "A bowed string physical model including finite-width thermal friction and hair dynamics," in *International Computer Music Conference*, 2014.

[108] E. Schoonderwaldt, "On the use of skewness in violin bowing: Should the bow be straight or not?," *Acta Acustica united with Acustica*, vol. 96, no. 4, pp. 593–602, 2010.

[109] E. Maestre, J. Bonada, M. Blaauw, A. Perez, and E. Guaus, "Acquisition of violin instrumental gestures using a commercial emf tracking device," in *Proceedings of the International Computer Music Conference*, vol. 1, pp. 386–393, 2007.

[110] M. Marchini, R. Ramirez, P. Papiotis, and E. Maestre, "The sense of ensemble: A machine learning approach to expressive performance modelling in string quartets," *Journal of New Music Research*, vol. 43, no. 3, pp. 303–317, 2014.

[111] E. Schoonderwaldt, "The player and the bowed string: Coordination of bowing parameters in violin and viola performance," *The Journal of the Acoustical Society of America*, vol. 126, no. 5, pp. 2709–2720, 2009.

[112] E. Schoonderwaldt and M. Demoucron, "Extraction of bowing parameters from violin performance combining motion capture and sensors," *The Journal of the Acoustical Society of America*, vol. 126, no. 5, pp. 2695–2708, 2009.

[113] J. H. Smith and J. Woodhouse, "The tribology of rosin," *Journal of the Mechanics and Physics of Solids*, vol. 48, no. 8, pp. 1633–1681, 2000.

[114] H. Lazarus, *Die Behandlung der Selbsterregten Kippschwingungen der Gestrichenen, Saite mit Hilfeder Endlichen Laplacetransformation*. Thesis, Technical University of Berlin, 1972.

[115] J. H. Smith, *Stick-slip vibration and its constitutive laws*. Thesis, Engineering Department, University of Cambridge, Cambridge, UK, 1990.

[116] J. Woodhouse, R. T. Schumacher, and S. Garoff, "Reconstruction of bowing point friction force in a bowed string," *The Journal of the Acoustical Society of America*, vol. 108, no. 1, pp. 357–368, 2000.

[117] D. C. B. Evans, J. F. Nye, and K. J. Cheeseman, "The kinetic friction of ice," *Proceedings of the Royal Society of London. A. Mathematical and Physical Sciences*, vol. 347, no. 1651, pp. 493–512, 1976.

[118] D. Tabor, "Junction growth in metallic friction: The role of combined stresses and surface contamination," *Proceedings of the Royal Society of London. Series A, Mathematical and Physical Sciences*, vol. 251, pp. 378–393, 1959.

[119] H. Herz, "Über die Berührung fester elastischer Körper.," *J. reine und angewandte Mathematik*, vol. 92, pp. 156–171, 1882.

[120] B. C. J. Moore, *An Introduction to the Psychology of Hearing (5th ed.)*. Academic Press, 2003.

[121] K. Guettler, "Wave analysis of a string bowed to anomalous low frequencies," *Catgut Acoustical Society Journal*, vol. 2, no. 6, pp. 8–14, 1994.

[122] R. J. Hanson, F. W. Halgedahl, and K. Guettler, "Anomalous low-pitched tones from a bowed violin string," *The Journal of the Acoustical Society of America*, vol. 97, no. 5, pp. 3270–3270, 1995.

[123] M. E. McIntyre and J. Woodhouse, "A parametric study of the bowed string: the violinist's menagerie," *Catgut Acoustical Society Journal*, vol. 42, pp. 18–21, 1984.

[124] H. Mansour, J. Woodhouse, and G. Scavone, "Time-domain simulation of the bowed cello string: Dual-polarization effect," in *Proceedings of Meetings on Acoustics*, vol. 19, p. 035014, Acoustical Society of America, 2013.

[125] S. Ramo, J. R. Whinnery, and T. Van Duzer, *Fields and waves in communication electronics*. John Wiley & Sons, 2008.

[126] W. E. Kock, "The vibrating string considered as an electrical transmission line," *The Journal of the Acoustical Society of America*, vol. 8, no. 4, pp. 227–233, 1937.

[127] J. C. Schelleng, "The violin as a circuit," *The Journal of the Acoustical Society of America*, vol. 35, pp. 326–338, March 1963.

[128] C. E. Gough, "The resonant response of a violin G-string and the excitation of the wolf-note," *Acta Acustica united with Acustica*, vol. 44, no. 2, pp. 113–123, 1980.

[129] R. M. Foster, "A reactance theorem," *Bell System Technical Journal*, vol. 3, no. 2, pp. 259–267, 1924.

[130] M. Hancock, "The mechanical impedance of violin strings - Part I," *Catgut Acoustical Society Newsletter*, vol. 23, pp. 17–26, 1975.

[131] X. Boutillon, "Analytical investigation of the flattening effect: the reactive power balance rule," *The Journal of the Acoustical Society of America*, vol. 90, no. 2, pp. 754–763, 1991.

[132] B. Lawergren, "Harmonics of s motion on bowed strings," *The Journal of the Acoustical Society of America*, vol. 73, no. 6, pp. 2174–2179, 1983.

[133] E. Schoonderwaldt, "The violinist's sound palette: spectral centroid, pitch flattening and anomalous low frequencies," *Acta Acustica united with Acustica*, vol. 95, no. 5, pp. 901–914, 2009.

[134] J. Reel, "Mari Kimura on subharmonics: The violinist continues to explore the world below G," in *Strings*, vol. 107, 2009.

[135] K. Guettler, "On the creation of the helmholtz motion in bowed strings," *Acta Acustica united with Acustica*, vol. 88, no. 6, pp. 970–985, 2002.

[136] K. Guettler and A. Askenfelt, "Acceptance limits for the duration of pre-helmholtz transients in bowed string attacks," *The Journal of the Acoustical Society of America*, vol. 101, no. 5, pp. 2903–2913, 1997.

[137] S. Serafin, *The sound of friction: real-time models, playability and musical applications*. PhD thesis, Music Department, Stanford University, Stanford, CA, 2004.

[138] C. Z. Zhang, G. M. Zhang, B. Y. Ye, and L. D. Liang, "Three dimensional motion tracking of a point on a bowed violin string using high speed videography," *Acta Acustica united with Acustica*, vol. 100, no. 3, pp. 574–582, 2014.

[139] T. D. Rossing, ed., *The Science of String Instruments*. Springer, New York, 2010.